PhD THESIS
in FLUID DYNAMICS

Pollutant dispersion in urban canopy

study of the plume behaviour through an obstacle array

Valeria GARBERO

DIASP, Politecnico di Torino - LMFA, Ecole Centrale de Lyon

Abstract

The dispersion of pollutants in urban areas is a very actual topic and the approach of modelling depends on the involved atmospheric processes, which are commonly classified with regard to their spatial scale. In the current study we focused on the dispersion at the neighborhood scale, where the air flow is very complex, as it depends strongly on the detailed surface characteristics, i.e. the form of the buildings or their orientation with regard to the wind direction. The aim of this work is thus to investigate the plume behaviour through an obstacle array and to point out how the dispersion mechanisms are affected by the geometrical layout of the obstacles and by the incident wind direction.

The study has been performed by means of wind tunnel experiments and, to a lesser degree, numerical simulations. An idealized neighborhood was simulated by an obstacle array, whose spacing between the obstacles and whose orientation with regards to the incident wind have been varied. The numerical simulations were performed by Fluent using the standard $\kappa-\varepsilon$ turbulence model. The velocity measurements were conducted through the hot-wire anemometry and the laser Doppler anemometry, while the concentrations of a passive scalar released from a point source were detected by means of the Flame Ionization Detector.

Initially we focused on the flow dynamics occurring through the obstacles for the different array configurations. Two different flow regimes took place, the wake interference flow and the skimming flow, depending on the aspect ratio of the street perpendicular to the wind direction, rather than the usual *lambda* parameters defining the dimensionless frontal and plan areas.

Then we investigated the influence of the array configurations on the dispersion mechanisms and we point out that the different observed flow regimes corresponded to different dispersion patterns. The skimming flow suppressed the dispersion mechanisms, since the pollutant exchange is only related to the turbulent diffusion, and the plume appeared to be confined within the main street. Concerning the wake interference flow and any tilted incident wind orientations, the vertical and horizontal plume spreadings appeared to be enhanced, since an advection mechanism contributes to the pollutant exchanges. Further, the horizontal concentration profiles within the array appeared highly asymmetrical and showed a *step* distribution, suggesting that the dispersion mechanisms are strongly influenced by the presence of the obstacles and that the intersection plays a fundamental role in the dispersion processes.

Regarding the dispersion above the array, although the concentration profiles are well described by Gaussian curves, the usual Gaussian approach is totally inappropriate as it parameterizes the standard deviations as function of the geometrical characteristics of the urban canopy and does not take into account the orientation regards with the incident wind direction.

Another approach was proposed to describe the dispersion in urban areas that went over the usual methods and implemented the main findings concerning the physical processes which have been obtained during various Thesis works. The urban dispersion model SIRANE is an operational model that has been developed as tool for the monitoring and the management of the urban air quality. SIRANE was applied to the studied array configurations and seemed to simulate quite well the measured dispersion patterns. The agreement between numerical

and experimental results is encouraging, as it means that the main dispersion mechanisms are represented, even if some improvements have to be taken into account.

Contents

Introduction

Air pollution originated in human activities and became a serious problem during the last 200 years, when growing population and industrialization produced vast quantities of contaminants. In general, air quality tends to be worst where most air pollutants are emitted, that is in highly industrial and urban areas. However, atmospheric motions transport the pollutants elsewhere and soon regional problems such as acid rain were recognized. Most recently, global problems such as climate change and stratospheric ozone depletion have been widely publicized.

Dealing with air pollution problems means to know pollutants sources and the characteristic of the emitted contaminants, to understand the atmospheric transport and diffusion in the atmosphere and finally to evaluate the reponse of the various receptors. Assessing and managing air pollution is currently a very active area of environmental research and the dispersion modelling is certainly a primary tool for air quality study.

The modelling of the dispersion mechanisms depends on the scale we are interested in. At each scale there are various physical processes that are described through mathematical models to form a nested model, in a hierarchy of complexity. The scale of atmospheric motions and related phenomena have been usually classified into four categories according to their horizontal dimensions. The classification proposed by Oke (1987) is summarized in Table 1:

Microscale	10^{-2} to $10^{3}m$
Local scale	10^{2} to $5 \cdot 10^{4}m$
Mesoscale	10^{4} to $2 \cdot 10^{5}m$
Macroscale	10^{5} to $10^{8}m$

Table 1: Atmospheric dispersion scales according to Oke's classification

Our research aims at improving the current understanding of the dispersion mechanisms in urban areas and at developing tools for air quality management purposes. The urban air pollution involves physical and chemical processes over a wide range of space and time scales. A classification concerning the urban dispersion scales has been proposed by Britter and Hanna (2003) and is summarized in Table 2:

Street	up to 10^{2} or $2 \cdot 10^{3}$ m
Neighborhood	up to 10^{3} or $2 \cdot 10^{3}$ m
City	up to 10^{4} or $2 \cdot 10^{4}$ m
Regional	up to 10^{5} or $2 \cdot 10^{5}$ m

Table 2: Urban dispersion scales according to Britter and Hanna

Most studies focused on the largest scales, where buildings tend to behave merely as rough-

ness elements and conventional dispersion theory is applicable. Flow and short range dispersion around single building is largely investigated as well. It is in the intermediate scale, where the number of buildings is large enough so that the wakes of individual obstacles interact and the local effects can not be neglected anymore, that knowledge is most incomplete. While at regional scale the mean synoptic meteorologic patterns are given and urban area represents a perturbation, causing deceleration and deflection of the flow as well as changes to the surface-energy budget and thermal structure, at the city and neighborhood scales, the geometrical details of the surface are no longer negligible.

Our study focus on the neighbourhood scale and investigates the variations in flow and dispersion due to the geometrical layout of the buildings and to their orientation with regards to the incident wind direction. There are many other aspects that could affect the dispersion in urban areas, i.e. the traffic induced turbulence or the thermal fluxes, but experimental difficulties and the necessity to reduce the number of degrees of freedom limited our investigation to few parameters.

Chapter 1

Flow and dispersion in urban areas

1.1 Essentials on atmospheric flows and turbulent dispersion

Since transport and diffusion of pollutants, as well as their chemical transformation and removal processes, occur in the atmosphere, we will discuss shortly the structure of the atmosphere and the dynamics of atmospheric flows, as well as the lineament of turbulent dispersion, in order to introduce the essentials to describe the peculiarity of flow and dispersion in urban areas.

1.1.1 Similarity theory in neutral boundary layers

The atmospheric boundary layer (ABL), also known as the planetary boundary layer (PBL), is the region of the lower atmosphere (troposphere) that is directly influenced by the presence of the earth's surface. Its depth and structure is determined by the physical and thermal properties of the underlying surface in conjunction with the dynamics and thermodynamics of the lower atmosphere. The ABL is the layer where the turbulent exchanges of momentum, heat and mass take place and the energy for turbulent exchanges is provided by the large vertical wind shear and the thermal effects of surface heating. We limit our dissertation to atmospheric flows with negligible thermal fluxes and focus on the neutral boundary layer dynamics.

The atmospheric flows are highly turbulent and their dynamics is governed by the fundamental laws of conservation of mass, energy and momentum. One characteristic of the turbulent flows is the irregularity, or the randomness, that makes a deterministic approach to turbulence problems impossible. A statistical methods was introduced and Reynolds suggested a decomposition of the variables into a mean and a fluctuating part. Applying Reynolds' averaging and assuming several reasonable conditions that are valid in the ABL, the governing equations can be simplified to a set of equations for the mean motions in the turbulent boundary layer. Unfortunately, the number of unknowns is larger than the number of equations and if we introduce new equations for these unknowns, even more unknowns appear. This fact is called *closure problem* and is apparently associated with the nonlinear nature of turbulence. While no exact solution has been found to date, approximations called *closure assumptions* can be made to allow approximated solution of the equations.

Similarity theory can be viewed as a type of zero-order closure, because any closure assumptions has to be made. The similarity theory provides empirical relationship describing the vertical behaviour of non-dimensionalized mean flow and turbulence property as function of relevant variables. It is generally assumed that the turbulent velocity field in the atmospheric boundary layer can be divided into different regions, where the flow variables can be described by some form of similarity solutions, if appropriate scales are chosen. We first consider the neutral surface layer over a flat and homogeneous surface, that is typically the 10% of the entire boundary layer. In the fully turbulent and homogeneous surface layer, the momentum flux is observed to be nearly constant with height and is related to the surface stress τ_0. An appropriate similarity hypothesis is that the mean velocity gradient and turbulent quantities depend only on the height above the surface and on the kinematic momentum flux or surface stress τ_0. This implies that the influence of other possible variables, such as the surface roughness, the geostrophic wind and the boundary layer height, is indirectly taken into account through τ_0. The plausible similarity hypothesis for the mean velocity gradient

$$\frac{\partial \overline{u}}{\partial z} = f(z, \tau_0/\rho) \tag{1.1}$$

leads to z and $u_* \equiv (\tau_0/\rho)^{1/2}$ as the only appropriate length and velocity scales and also to a constant dimensionless wind shear

$$\frac{z}{u_*}\frac{\partial \overline{u}}{\partial z} = \frac{1}{k} \tag{1.2}$$

which follows from dimensional analysis. The constant k is the von Karman constant, which is an empirical constant with a value of about 0.40.

The above similarity prediction has been verified by many observations of velocity profiles. The integration of Eq. 1.2 with respect to z gives the well-known logarithmic velocity profile law:

$$\frac{\overline{u}}{u_*} = \frac{1}{\kappa} \ln\left(\frac{z}{z_o}\right) \tag{1.3}$$

where z_0 is the surface roughness parameter, named *roughness length*. Eq. 1.3 is valid only for $z >> z_0$ and $z << z_i$, where z_i is the boundary layer height. The roughness length is a constant of integration and identify the height at which the mean velocity would reach zero, assuming Eq. 1.3 to be valid down to the wall level. In this description the wall influence is thus reflected in one scalar and this follows directly from the assumption that the flow can be considered homogeneous in the $x - y$ planes.

The logarithmic law can be obtained in other ways, by keeping however two essential hypothesis:

1. the flow is homogeneous in the horizontal planes and the only relevant length scale in this region is z, the distance from the wall;

2. the fluctuating velocity field has only one velocity scale to which all velocity components are proportional, no matter how they are defined.

It is worth noting that the Eq. 1.2 also follows from the mixing-length and eddy viscosity theories. The gradient-transport theory or eddy-viscosity theory (K-theory) is a first order turbulence closure approximations that assumes the turbulent fluxes to be related to the mean velocity gradients, in direct analogy with molecular exchanges. Thus the turbulent momentum fluxes can be expressed as

$$\overline{u'w'} = -\nu_t \frac{\partial \overline{u}}{\partial z} \tag{1.4}$$

where ν_t is called the eddy diffusivity or turbulent viscosity in analogy with molecular viscosity. The gradient-transport relations are based on the analogy between molecular and turbulent exchange processes that is rather weak. In fact, unlike molecular viscosity, turbulent viscosity cannot be regarded as fluid properties, but is actually a property of the flow. In an attempt to specify eddy viscosity as a function of geometry and flow parameters, Prandtl further extended the analogy between molecular and turbulent transfer processes to the hypothetical mechanisms of such transfer and assumed

$$\nu_t \propto l_m \, \sigma_u \tag{1.5}$$

where σ_u is a turbulent velocity scale and l_m is the mixing length. Prandtl's mixing length theory is found to be very unsatisfactory to describe momentum transfer, as far as momentum is not transferred unaltered by advection from a region to another of the flow field. However, the expressions for eddy viscosity are considered to be plausible relations, since they can be written from dimensional considerations alone. σ_u and l_m are two parameters describing the fluctuating part of the flow field and are related to the turbulence intensity and to the linear dimension of the coherent turbulent structures. Particularly in the neutral surface layer the relevant velocity and length scales are the friction velocity u_* and the height z and then we can write:

$$\sigma_u = k_1 u_*$$

$$l_m = k_2 z$$

where k_1 and k_2 are two unknown constants. Substituting these relations into 1.3 we obtain:

$$\nu_t = k z u_* \tag{1.6}$$

As the Reynolds stresses varies so slowly that they can be considered effectively constant, we can assert

$$-\overline{u'w'} = \tau_0/\rho = {u_*}^2 \tag{1.7}$$

Substituting the expressions for eddy viscosity and turbulent flux in Eq. 1.4, the Eq.1.2 is obtained and the logarithmic law can be derived by integration.

The logarithmic law has been shown to agree well with a range of experimental data and has long been considered a successful result of the theory. Anyway the solidity of the log-law is due to more general and abstract reasons. In fact, the only essential proposition deals with the existence of a region in the flow field where the only significative length scale is z, the distance from the wall, and the only significative velocity scale is u_*, the friction velocity. The flow field we are considering is determined on the top by a velocity U_∞, imposed at the boundary layer height δ, and is limited at the bottom by the presence of a rigid surface which imposes the no-slip condition $\overline{u} = 0$. The solid boundary, in case of rough wall, is characterized by a typical length z_0, known as *roughness length*[1]. The assumption that in a region of the flow the only relevant length scale is the distance z from the wall is equivalent to assume that, in this region, δ and z_0 do not have any influence on the flow dynamics. The log-law region is therefore an intermediate region whose dynamics is determined by turbulent structures which are big enough not to be influenced by z_0 and too small to be influenced by the whole boundary layer height δ. The existence of the intermediate region requires that the inner and the outer scales should be separated by several orders of magnitude, i.e. $\delta \gg z_0$. There is an evident analogy between the log-law region for wall bounded turbulent flows and the inertial domain of the homogeneous and isotropic turbulence. This is the reason why the log-law region is usually called the *inertial layer* (Blackadar and Tennekes, 1968). The inertial layer is thought as the region of overlap between the region near the wall - the so called inner layer, where the appropriate length and velocity scales are respectively z_0 and u_* - and the outer layer, where U_∞ and δ are the appropriate scales. The process of obtaining the limiting behaviour of the law of the wall (inner layer) and the defect law (outer layer) is called *asymptotic matching* and gets once again the logarithmic law.

These considerations provide the basis of the *boundary layer theory*, a description of the boundary layer which relies on universal relations. We give a brief recall on the way the theory is extended in order to take account the thermal fluxes, even if they are neglected in the current work. Thermal fluxes between earth and atmosphere alter radically the structure of the planetary boundary layer, whose depth δ varies periodically during the day. The physical parameters that influence the flow field are the already mentioned variables - δ, z_o, u_* - and the convective thermal flux F_c. To take in account the effect of this term on the boundary layer structure, Monin and Obukhov proposed an extension of the similarity theory (Monin and Obukhov, 1954), by introducing a new length scale $\mathcal{L}$, the*Monin-Obukhov height*. The Monin-Obukhov height is defined as the distance from the wall at which the thermal production of turbulent kinetic energy equals the mechanical production. By the definition of similarity theory, every parameter describing the turbulent flow in the ABL, non-dimensionalized by its relevant scaling

[1] z_0 represents the effect of wall roughness but it can not be interpreted directly as the height of the roughness elements because the effect of wall roughness depends also on the spacing, orientation and organization of the roughness elements.

variable, can be described by a universal function of

$$\zeta = \frac{z}{L}$$

which is independent on the surface, height and velocity.

When $z < |L|$, mechanical turbulence dominates, while for $z > |L|$ buoyancy effects become more important. Thermal effects are not so relevant in the dispersion processes at the neighborhood scale, as long as they take place well below the Monin-Obukhov height.

1.1.2 Turbulent dispersion

The pollutant mass conservation applied to a control volume allows to determine the *advection-diffusion* equation

$$\frac{\partial c}{\partial t} = -\frac{\partial}{\partial x_j}\left(u_j c - D_m \frac{\partial c}{\partial x_j}\right) \tag{1.8}$$

which describes the temporal and spatial evolution of the instantaneous scalar concentration c within the turbulent flow field [2]. $u(x, y, z, t)$ is the instantaneous wind velocity, D_m is the molecular diffusion coefficient. By applying the Reynolds average operator and neglecting molecular diffusion, Eq. 1.8 becomes

$$\frac{\partial \overline{c}}{\partial t} = -\frac{\partial}{\partial x_j}\left(\overline{u_j' c'} + \overline{u}_j \overline{c}\right) \tag{1.9}$$

where $\overline{u_j' c'}$ is the turbulent flux of the passive scalar and $\overline{c}$ is the mean scalar concentration. In mathematical terms, as long as the tensor $\overline{u_j c}$ is unknown, Eq. 1.9 can not be solved and the whole problem of turbulent dispersion appears undetermined. The usual approach to the turbulence closure problem is to relate the unknown tensor to other known flow variables. Boussinesq (Boussinesq, 1897) pointed out the analogy between the effect of thermal motion of molecules on the instantaneous concentration c of a scalar field and the effect of the turbulent flux $\overline{u_j c}$ - expressed by the correlation of the fluctuating part of the velocity field and of the fluctuating part of the scalar field - on the averaged concentration $\overline{c}$. The previous analogy suggested to model the turbulent fluxes as the molecular fluxes by the Fick's law

$$\overline{u_j' c'} = -K_{ji} \frac{\partial C}{\partial x_i} \tag{1.10}$$

where K_{ji}, the turbulent diffusion tensor, depends on the fluctuating part of the velocity field and is generally varying with time and space coordinates. The turbulence closure problem now concerns the determination of K_{ji}. The assumption 1.10 is the simplest way of treating the mathematical problem and is referred to as the first-order closure or K-theory; although the analogy establishes a link too strict between the molecular thermal motion and the turbulent fluctuation, it is commonly used. By assuming Fick's closure, the advection-diffusion equation becomes

$$\frac{\partial \overline{c}}{\partial t} = -\frac{\partial}{\partial x_j}\left(-K_{ji}\frac{\partial \overline{c}}{\partial x_i} - \overline{u}_j \overline{c}\right) \tag{1.11}$$

The advection-diffusion equation can be solved analytically for simple boundary conditions. For a continuous point release of strength $\dot{M}_q(kg/s)$, the spatial evolution of the passive scalar concentration is described by the gaussian distribution

$$\overline{c}(x, y, z) = \frac{\dot{M}_q}{2\pi\sigma_y\sigma_z\overline{u}} \exp\left(-\frac{y^2}{2\sigma_y^2}\right) \exp\left(-\frac{z^2}{2\sigma_z^2}\right) \tag{1.12}$$

[2] The pollutant is considered a passive scalar and the source term is not taken into account

if the following condition are verified:

- the flow is stationary in statistical terms
- the flow is homogeneous and the mean velocity $\overline{u}$ is uniform
- the turbulent diffusion tensor is constant and diagonal, that is the turbulent fluxes in one direction are proportionally to the mean concentration gradient in that direction

$$\begin{bmatrix} K_{xx} & 0 & 0 \\ 0 & K_{yy} & 0 \\ 0 & 0 & K_{yy} \end{bmatrix}$$

- the turbulent flux in the stream-wise direction x is negligible in comparison to the flux of the mean motion, i.e. $\overline{uc} >> \overline{u'c'}$

The standard deviations of the gaussian distribution are related to the turbulent diffusion by means of the relation

$$\sigma_z = \sqrt{2K_{zz}t} \quad \text{and} \quad \sigma_y = \sqrt{2K_{yy}t}$$

In order to have a better estimate of the scalar concentration field one can give a finer parametrization of the tensor K, or introduce a higher-order closure hypothesis. However, the common approach is to focus on the parametrization of the standard deviations rather than the turbulent diffusion tensor. A large number of diffusion experiments were conducted to evaluate empirically the plume diffusion parameters for use in simple Gaussian models. Briggs (1973) attempted to synthesize these differen set of diffusion data in proposing interpolation formulas for both open country and urban areas. Briggs' interpolation formulas describe the dispersion curves for the various Pasquill stability classes; in Table 1.1 the formulas concerning the neutral stability condition are shown.

	σ_y	σ_z
Open terrain	$0.08x(1+0.0001x)^{-1/2}$	$0.06x(1+0.0015x)^{-1/2}$
Urban areas	$0.16x(1+0.0004x)^{-1/2}$	$0.14x(1+0.0003x)^{-1/2}$

Table 1.1: Briggs' interpolation formulas

It has been pointed out that even under idealized conditions Gaussian diffusion models have large uncertainties due to natural variability and simplified model physics. Significant deviations from the idealized conditions, as the presence of obstacles over the terrain represents, introduce further limitations to the validity of such models.

The physical meaning of the first-order approximation - the Fick law - may be enlightened by a lagrangian approach to the same problem. Eq. 1.11 can be written in another way:

$$\frac{DC}{Dt} = -\frac{\partial}{\partial x_j}\left(\overline{u_j c}\right) \tag{1.13}$$

through the averaged continuity equation

$$\frac{\partial U_j}{\partial x_j} = 0$$

In equation 1.13,

$$\frac{D}{Dt} = \frac{\partial}{\partial t} + U_j \frac{\partial}{\partial x_j}$$

indicates the derivative with respect to time of a variable measured by means of an instrument moving within the fluid with the mean velocity U_j. Actually, Eq. 1.13 can be thought as directly obtained by averaging an ensemble of realizations, each of them ruled by the equation:

$$\frac{\partial c_t}{\partial t} = -\frac{\partial}{\partial x_j}\left((u_t)_j c_t\right) \tag{1.14}$$

whose solution is:

$$c_t = const.$$

along the trajectory

$$d\mathcal{Y}_i = \mathcal{V}_i dt$$

where $\mathcal{Y}_i$ indicates the displacement and $\mathcal{V}_i$ the lagrangian function of velocity of the fluid particles. The process we named turbulent dispersion is given by a statistical averaging of a class of trajectories of fluid elements that are wandering in space because of the stochastic nature of the velocity field, each of them keeping an invariant quantity - a sort of quantum - of contaminant. The process can therefore be modelled by reproducing a large number of trajectories with the same statistical features of the actual ones and the concentration can be computed simply by counting the number of end points of the trajectories in every volume cell. Taylor (1921) gave a first account of the lineaments of the lagrangian dispersion. We can consider a stochastic homogeneous motion in the $\mathcal{Y}$ direction with statistical structure given by the lagrangian autocorrelation function:

$$\overline{\mathcal{V}(t)\mathcal{V}(t+\tau)} = L(\tau)\sigma_{\mathcal{V}}^2$$

where $L(\tau)$ is the autocorrelation coefficient and $\sigma_{\mathcal{V}}^2$ is the variance of lagrangian velocities. The coefficient $L(\tau)$ varies only with the time delay τ because of the supposed stationarity of the process, in a statistical sense; it is equal to 1 for $\tau = 0$, as obvious, and goes to zero for a finite value of τ.

Now, if we have an ensemble of particles, emitted at the same point, we can compute the time variation of $\overline{\mathcal{Y}^2}$, the variance of the particle distribution along the $\mathcal{Y}$ axis. We write:

$$\frac{d\overline{\mathcal{Y}^2}}{dt} = 2\sigma_{\mathcal{V}}^2 \int_0^t L(\tau)d\tau$$

Integrating the previous equation we obtain the *Taylor equation* (Taylor, 1935):

$$\overline{\mathcal{Y}^2} = \sigma_{\mathcal{Y}}^2(T) = 2\sigma_{\mathcal{V}}^2 \int_0^T \int_0^t L(\tau)d\tau dt \tag{1.15}$$

where T is the flight time of fluid particles since the instant they were emitted. The Eq. 1.15 allows to relate the time evolution of the size of a pollutant puff to the statistical properties of the turbulent flow field.

To examine the asymptotical behaviour of $\sigma_{\mathcal{Y}}$, we consider the properties of the function $L(\tau)$:

$$\begin{cases} L(0) = 1 \\ \int_0^\infty L(\tau)d\tau = T_L \end{cases}$$

where T_L is the lagrangian macro scale. It is then possible to show that

$$\begin{cases} T << T_L & \Rightarrow \sigma_{\mathcal{Y}}^2 \sim \sigma_{\mathcal{V}}^2 T^2 \\ T >> T_L & \Rightarrow \sigma_{\mathcal{Y}}^2 \sim 2\sigma_{\mathcal{V}}^2 T_L T \end{cases}$$

For a short dispersion time, the puff size is proportional to T, whereas for a very long time the puff size tends to be proportional to $\sqrt{T}$. It is worth noting that the Fick's approximation gives a faithful description of the process in the limit :

$$\frac{T}{T_L} \to \infty$$

The dispersion model based on turbulent diffusion coefficient

$$K_{\mathcal{Y}} = \sigma_{\mathcal{V}}^2 T_L$$

represents actually asymptotic solutions of the dispersion problem.

1.2 Urban boundary layer

How does the presence of an urban area influence the atmospheric boundary layer?

An urban surface consists of buildings, trees and other roughness elements of varying length scales, resulting in a complex morphology that modifies flow and turbulence structure in the lowest part of the urban atmosphere. The air motion is slower compared to rural surface, while the mechanically generated turbulence increases. In addition to the enhanced roughness, the energy balance is altered because of the different thermal properties of a city: cement, asphalt and glasses reduce the albedo [3] and limit the evaporation processes, increasing the solar radiation absorption, while human activities act as further heat sources. Consequently, the air temperature above the urban area is higher than the temperature in the rural and suburban surroundings and a particular microclimate occurs known as *urban heat island*(Oke, 1988a).

At regional scale, the complexity of urban geometry is synthesized in one parameter only, the roughness length z_o (Wieringa, 1993). This means that a town is considered as a region with uniformly distributed drag forces and the problem is to parameterize small scale geometry details in order to give an evaluation of z_o. At city or district scale, the geometrical details of the surface are no longer negligible and what could be seen as a rough surface becomes a region occupied by densely packed obstacles. Urban geometry reveals all his complexity, due to the structure and orientation of buildings, whose influence on the flow can not be expressed by just one parameter. The problem now is to investigate the flow and the dispersion within and above a group of obstacles (MacDonald *et al.*, 2000; Davidson *et al.*, 1996; Perkins and Belcher, 1997; Hanna *et al.*, 2002). As we are interested in the lower region of the urban boundary layer, where mechanically generated turbulence dominates regards to thermal generated turbulence, a plausible assumption is to neglect the thermal fluxes and consider a neutral urban boundary layer. The neutrally stratified atmospheric boundary layer above a town cannot be divided vertically in the usual way of the similarity theory:

- the **inertial layer**, whose typical scales are roughness length z_o and friction velocity u_*;
- the **outer layer**, whose typical scales are the boundary layer depth δ and the friction velocity u_*.

The description of the vertical structure of the urban boundary layer requires two other regions (Fig. 1.1), in order to take into account more precisely the effect of the buildings:

- the **urban canopy**, where the flow is strongly inhomogeneous and the wakes of the various obstacles interact;
- the **roughness sub-layer**, where the turbulence structure is fully three-dimensional and depends explicitly on the properties of the roughness elements (Raupach, 1981)

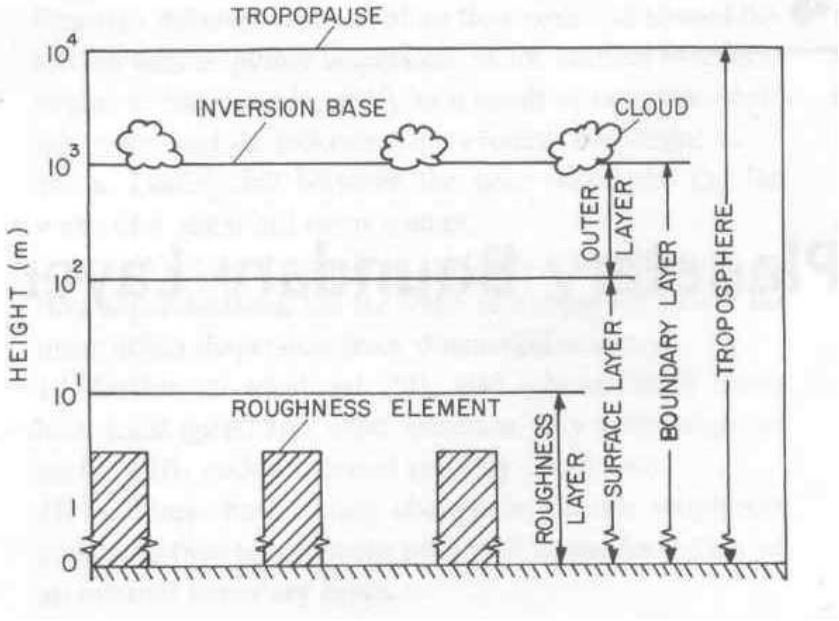

Figure 1.1: Vertical structure of the urban boundary layer in neutral conditions.

In the *urban canopy*, the flow is directly affected by orientation and position of each single building. Related to wind direction and street geometry, semi-permanent recirculating regions arise within the urban canopy. Immediately above the urban canopy, there is a region, the roughness sub-layer, where the flow is dynamically influenced by length scales associated with roughness elements; the flow is there non-homogeneous in the horizontal planes. This region extends up to the so called *blending height* z_*, which is far enough from the canopy so that wakes of buildings merge with each other. Above the blending height, the flow field feels the presence of obstacles as a unique element of aerodynamic drag, uniformly distributed on the whole surface. Then the inertial region takes place, where the logarithmic law applies. A new parameter appears, the *displacement height* d, which takes into account the upwards displacement of the entire flow due to the presence of the obstacles. We define the origin of z for a rough surface as Z=z-d, which allows to shift vertically the virtual plane where the mean velocity goes to zero. The mean velocity profile in the inertial layer becomes

$$\frac{U}{u_*} = \frac{1}{k} \ln \frac{z-d}{z_o} \tag{1.16}$$

The key parameters z_0 and d can be estimated by means of several approaches. Land-use methods are used in most applied dispersion models and a description of urban land-use types have been proposed by Grimmond and Oke (1999). More precise estimates of z_0 and d can be made using information about building sizes and spacing. A first approximation is given by relations that take into account the mean obstacle height $\hat{\mathrm{H}}$ (Grimmond and Oke, 1999):

$$z_o = a\hat{H}$$

$$d = b\hat{H}$$

with $a \simeq 0.1$ and $b \simeq 0.7$. Otherwise, parameterizations are based on the lambda parameters, defined as

$$\lambda_p \equiv A_p/A_d$$

[3]the albedo indicates the ratio of reflected/scattered radiation to incident radiation

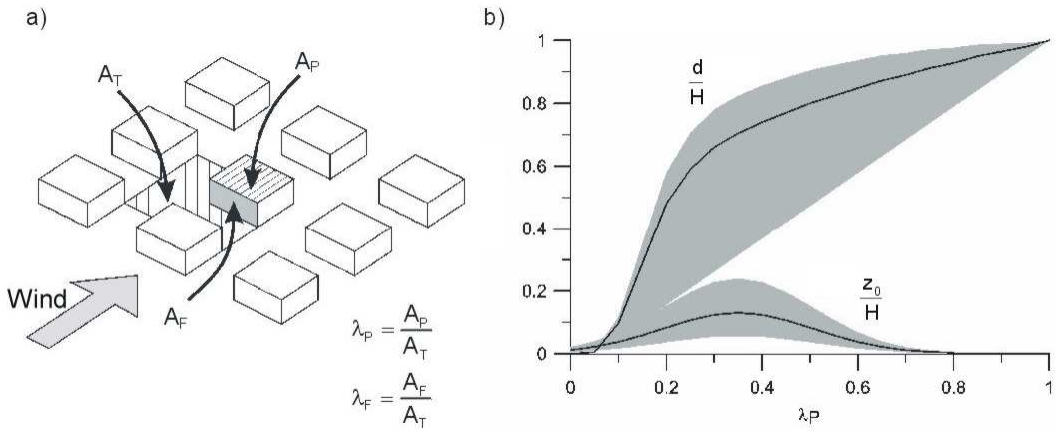

Figure 1.2: Variation of the displacement thickness d and of the roughness height z_o as a function of the porosity factor λ_p of a group of obstacles (Grimmond *et* Oke, 1999).

$$\lambda_f \equiv A_f/A_d$$

where A_d is the mean lot area, A_p the mean plan area occupied by obstacles and A_f the mean frontal area of roughness elements perpendicular to the wind direction, as shown in Fig.1.2. In Fig.1.2, d and z_o, normalized to the mean obstacle height, are plotted as a function of the porosity factor λ_p. It is worth noting that the porosity increase has two opposite effects on the drag exerted from the wall on the flow. For low values of $\lambda_p < 0.35$, the roughness length increases linearly with increasing obstacle density. For $\lambda_p > 0.35$, z_0 decreases with increasing λ_p as long as roughness elements placed at the wall begin to be enough densely packed to shelter each other. In an alternative way, d and z_o can be evaluated as a function of the *frontal area density* λ_f. Rotach (1994) suggested a method to evaluate the displacement height d based on *in situ* turbulence measurements in urban areas. More complex relations are also available in the literature for the determination of d and z_0 (Bottema, 1997), as function of several parameters describing the geometry of building groups. A critical review on the methods used to evaluate surface parameters can be found in Grimmond *et al.* (1999). Similar plots relating the effective roughness length to porosity parameters can be found in review works by Jimenez (2004) and Raupach *et al.* (1991).

A phenomenological description usually adopted to describe the flow field in the urban canopy identifies three different flow regimes, classified according to the aerodynamic interactions between the buildings. The key parameter is the obstacle aspect ratio H/S, defined as the ratio between the obstacle height, H, and the distance between them, S (Oke, 1987).

- the **isolated roughness** regime, for $0.15 < H/S < 0.2$: obstacles are sufficiently far that the flow has time enough to reach the dynamical condition it had before passing the previous. The flow field can be thought as a simple superposition of the flow fields around each isolated building. Recirculating regions develop downstream of the obstacle, whose length is about $6 - 7$ times the obstacle height, and upstream of the obstacle, even of a smaller extent. In terms of pollutant dispersion the wake behind a bluff body retain pollutants in his recirculating motion, exchanging mass with the surroundings flow by mean of an intermittent vortex shedding (Louka *et al.*, 2000).

- the **wake interference** regime, for $0.2 < H/S < 0.65$: buildings are sufficiently close to each other that the wakes generated by each building interact with the downstream buildings; the resulting flow pattern shows an increasing complexity.

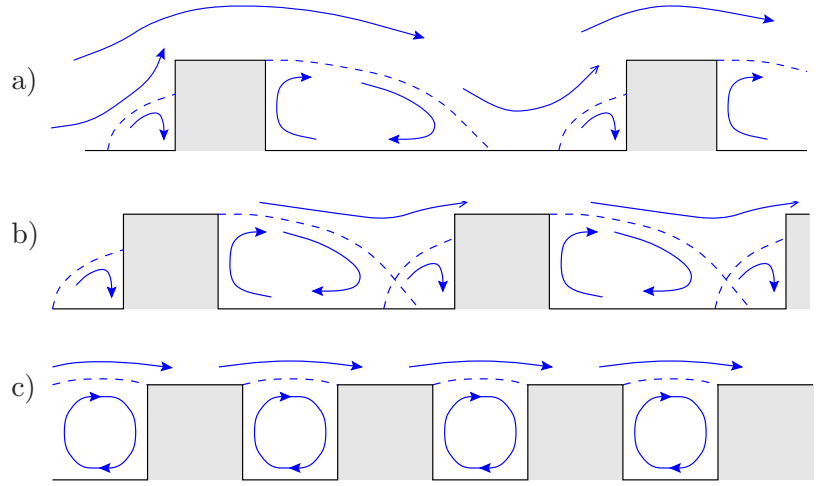

Figure 1.3: Flow regimes in a groups of obstacles : (a) Isolated roughness, (b) Wake interference, (c) Skimming flow (from Oke, 1988).

- the **skimming flow**, for $H/S > 0.65$: the buildings are so densely packed that steady recirculating regions develop within them and the flow above the buildings becomes relatively decoupled from the flow between the buildings and appears to skim over the top of the canopy. The number of vortex arising in the canyon depends on the street aspect ratio. Interaction between external flow and recirculating regions is reduced in comparison to the previous regime and it is controlled by the dynamics of a shallow shear layer, which develops at the external boundary of the cavity.

As the flow in the urban canopy and in the roughness sublayer is essential three-dimensional, the concept of spatial averaging has been introduced by Raupach et al. (1986) to cancel horizontal variations of the flow. The horizontal averages smooth the spatial variability of the canopy and incorporate all the dynamical effects of the the canopy into the averaged governing equations: new physically significant terms are introduced, accounting for dispersive fluxes and wake production. The averaging operator is denoted by angle brackets and can be defined as

$$\langle \Phi \rangle = \frac{1}{V} \int\int\int \Phi(x,y,z) dx dy dz \tag{1.17}$$

where Φ denotes a scalar field and V is an infinitesimally thin horizontal slab, large enough to include a number of canopy elements but not so large as to lose any spatial variation in the density of canopy elements. In analogy to the Reynolds decomposition of a time-dependent scalar flow variable into its mean and turbulent parts, the scalar field is decomposed into the spatial average and the departure therefrom:

$$\Phi = \langle \Phi \rangle + \Phi'' \tag{1.18}$$

$$\langle \Phi'' \rangle = 0 \tag{1.19}$$

Under the two operations of time and space averages, flow variables then have three components, which for the streamwise velocity u are:

$$u = \overline{u} + u' = \langle \overline{u} \rangle + \overline{u}'' + u' = U + \widetilde{u} + u' \tag{1.20}$$

where $U = \langle \overline{u} \rangle$ is the time and space averaged velocity, $\widetilde{u} = \overline{u} - U$ is the spatial variation of the time-mean flow and u' is the turbulent fluctuation.

By applying the space-averaging operator to the continuity equation and the Reynolds equation for mean momentum conservation - viscous stresses are neglected, the equations become:

$$\frac{\partial U_i}{\partial x_i} = 0 \tag{1.21}$$

$$\frac{\partial U_i}{\partial t} + U_j \frac{\partial U_i}{\partial x_j} = -\frac{1}{\varrho}\frac{\partial P}{\partial x_i} + \frac{\partial \tau_{ij}}{\partial x_i} - D_i \tag{1.22}$$

with

$$\frac{\partial \tau_{ij}}{\partial x_i} = -\frac{\partial}{\partial x_i}\langle \overline{u_i' u_j'} \rangle - \frac{\partial}{\partial x_i}\langle \widetilde{u}_i \widetilde{u}_j \rangle \tag{1.23}$$

The averaging procedure thus produces new terms in the momentum equation. Besides the spatially averaged Reynolds stress, there is a *dispersive stress* due to momentum transport by the spatial deviations from the spatially averaged wind and representing spatial correlation of time-averaged but position-dependent quantities (Wilson and Shaw, 1977); and there is a *form drag* D_i, which arises from spatially averaging the localized drag due to individual roughness elements. While dispersive stress is very small compared to Reynolds stress near the top of the canopy, as verified by Finnigan (1985) and Cheng (2002), and can be neglected, the drag term is important through the whole volume of the canopy.

1.3 Urban dispersion modelling

What are the approaches used to model dispersion in urban areas? How far has the research on flow and dispersion in urban areas gone?

The dispersion in urban areas has to deal with the peculiar effects of nonhomogeneous urban boundary layer and urban heat island. The interaction of the atmosphere with the urban canopy leads to complex localized mean flow patterns and enhanced turbulence around the buildings, where the majority of both sources and receptors of pollutants are situated. Simple analytical models such as the Gaussian solutions are applicable only to problems with simple boundary conditions, i.e. near flat terrain and uniform velocity field. Urban dispersion modelling is thus a difficult task as it involves complex terrain and a wide range of different scales. Different approaches to model urban dispersion are found in literature:

- **Experimental models**, as field experiments or scaled simulations in laboratory;
- **Numerical models**, models that solve flow and dispersion governing equations numerically for any given boundary conditions, using either Eulerian or Lagrangian approaches.
- **Parametric models**, mathematical models that express concentration values as a function of a set of variables and conditions

Field measurements provide the most direct and realistic way of simulating dispersion processes in actual urban environments and atmospheric conditions. However, the natural variability of the boundary conditions significantly complicates the process of understanding and isolating the effect of interest. Furthermore, experimental modelling in the field is typically the most time-consuming and expensive modelling method. Scaled modelling in the laboratory is carried out either in wind tunnel or water tank and is based on the theoretical assumption that flow and dispersion at model scale is dynamically similar to that in full scale. The advantage

of the wind tunnel modelling is that boundary conditions can be controlled accurately and reproducibly, conversely to what happens in open field. The main limitation is that a faithful representation of the turbulence variability is difficult to achieve.

Computational models are based on the numerical solution of the conservation/transport equations of flow and dispersion. The Computational Fluid Dynamics (CFD) modelling is divided in two categories:

1. Models that solve the Navier-Stokes equations directly, for the entire flow field (Direct Numerical Simulations, DNS), or for part of the flow (Large Eddy Simulations);

2. Models that solve the Reynolds Averaged Navier-Stokes equations (RANS simulations) by using turbulence model for turbulence closure (standard $k - \varepsilon$ model, RSM models)

The computational resources required for DNS and LES simulations are very high, while RANS methods are less demanding and therefore widely used to study flow and dispersion in urban areas. CFD modelling studies are providing realistic results, although there is much uncertainty about the range of its applicability. It is therefore necessary to validate CFD results carefully against wind tunnel and field data.

Parametric models are the simplest method to model dispersion phenomena and are either based on experimental data or analytical solutions. The empirical correlations or case-specific simplifying assumptions often limit the applicability and the confidence range of the model. For example, the Gaussian model - the most popular parametric dispersion model - is not applicable to near-field dispersion in the urban canopy, due to the complex boundary of the urban topography and the localized flow and turbulence, which invalidate the fundamental theoretical assumptions on which Gaussian models are based. While the dispersion of contaminants is fairly well understood in open, flat and homogeneous terrain, in more complicated urban environment many effects influence the pollutant dispersion as the turbulent flow interacts with obstacles possessing a large range of shapes, sizes and possible configurations. Thus some of the well-known traditional methods of dispersion estimation, such as Gaussian plume models, are expected to perform poorly in urban regimes without significant modifications, especially at smaller scales where the details of geometry and arrangement of buildings greatly affects the flow field. Concerning the largest scale as regional and city scales, buildings tends to behave as roughness elements and conventional dispersion theory is applicable with appropriate parameterizations.

1.3.1 Neighbourhood scale

The study of plume dispersion within a neighbourhood, because of its complexity, has been generally conducted by using physical models in wind tunnel or field experiments. Investigations are usually focused on dispersion through large idealized arrays of simple patterns; although they are necessarily simplifications of the real, complex urban environment, these simplified geometries allow a general understanding of the overall plume behaviour Britter *et al.* (2003) and provide some simple physical models. Through a controlled study of various idealised configurations the underlying physical mechanisms of flow and dispersion in urban terrain can be probed and the most relevant parameters are pointed out. A number of experimental studies of dispersion in large groups of regular obstacles appeared in the literature. Davidson *et al.*(1996) investigated the near-field plume behaviour emitted by point sources in relatively sparse array of cubes and verified an approximated Gaussian distribution for the concentration profiles. It is worth noting that the source was placed upwind of the first row of obstacles, which can influence the initial plume development. A key parameter in determining the plume dispersion behaviour is the plan area density of the buildings, related to the spacing between the obstacles and their height, that fixes the aerodynamic flow regimes occurring within the array. As mentioned

in the Section 1.2, three different flow regimes may occur depending on the building density: the isolated roughness flow, the wake interference flow and the skimming flow. Macdonald *et al.* (1997; 1998) examined the effect of the plan area density on plume dispersion in a wind tunnel and at a field site and expanded the study considering different obstacle width-to-height ratios. In these experiments, the measured concentration profiles exhibited a Gaussian distribution profile. Differently, Theurer et al. (1996) showed that, in more irregular arrays of buildings, Gaussian plume model may approximate concentration distribution only in far-field, i.e. for distance larger than a radius of homogenization, while in near-field dispersion depends strongly on the local arrangements of the obstacles and the assumption of a Gaussian plume gives erroneous results. Recently, Gailis (2006) performed wind tunnel simulations investigating the dispersion of a tracer within a large array of obstacles; the experiments modelled at 1:50 scale a large field study known as MUST (Mock Urban Setting Test) (Yee and Biltoft, 2004). The physical mechanisms involved in the development of a dispersing plume within an urban-like environment have been analyzed, by focusing on the description and mathematical modelling of concentration fluctuations within the plume, as well as the usual mean concentration results.

Pollutant dispersion modelling in urban neighbourhood has to deal with the modification of the atmospheric flow due to the presence of a city. As summarized by Roth (2000), the main effects are the presence of intense shear layers at the top of the urban canopy, the wake diffusion induced by buildings which enhances turbulent transport of momentum and pollutants and the drag induced by buildings. In order to model flow and dispersion phenomena two choices are available:

- a complete reconstruction of the urban geometry within the computational domain and the solution of the system of the governing equations by means of CFD codes;
- a parametrization of momentum and mass exchange processes that take place in the lower part of the boundary layer and in the urban canopy.

When a district of hundreds of streets is considered and a large amount of information on real urban geometries has to be taken into account, the application of CFD codes requires a very high computational cost. For operational purposes as air quality control and management, parametric models are required that implement simplified description of urban geometry and mass transfer phenomena. In this case, two main difficulties arise:

- characterize the lower part of the atmospheric boundary layer, where the flow dynamics are typically determined by the size and the density of the buildings and by the street geometry;
- parameterize the mass exchange between the recirculating region within the street canyons and the external flow and within the canopy itself.

In the last twenty years only few models for specific computations of pollutant concentration in an urban district have been developed.

The model SBLINE (Namdeo and Colls, 1996) assumes that the pollutant in each street is due to the contribution of two terms: the direct contribution of the sources placed in the street itself and the contribution due to sources located in the surrounding streets. The latter is taken into account by a Gaussian model, by supposing that the plume of pollutants is transported as if there were no buildings. The direct contribution of the street is computed with the model CPBM (Yamartino and Wiegand, 1986) which evaluates the mass exchanges at street intersections.

Similarly, ADMS-Urban (McHugh *et al.*, 1997) provides a module to compute mean concentration in the regions of the domain where street canyon effect arises. For each street canyon, concentration are computed as the sum of two component: the background concentration - due

to street canyon trapping effect - and the concentration related to the direct contribution of vehicles emissions within the street. The street canyon trapping effect is parameterized using the Danish Operational Street Pollution Model (Hertel and Berkowicz, 1989). This street canyon module is activated when street aspect ratio H/W is higher than 0.5, otherwise pollutant concentration are compute by mean of simple Gaussian plumes. The dispersion of pollutant emitted within the street is modelled by means of a Gaussian plume, whose transversal spreading is computed by relations that evaluate turbulent fluctuations within the canyon.

A completely different approach has been developed by Soulhac (2000) in the model SIRANE. The model assumes a decomposition between the external atmospheric flow and the urban canopy flow. SIRANE adopts a street-network approach to describe the urban geometry: the streets in a neighbourhood are modelled as a simplified network of segments connected by nodes, which represent the intersections. The flow within each street is driven by the component of the external wind parallel to the street and the pollutant is assumed to be uniformly mixed within the street. The model contains two main mechanisms for transport in and out of a street segment: diffusion across the interface between the air in the street and the overlying air and exchanges with other streets, at street intersections, due to the advection mechanisms. The dispersion of pollutant into the overlying air is taken into account using a Gaussian plume model.

At the neighbourhood scale dispersion studies require a refined knowledge of the flow within and above the urban canopy and the effect of individual building, as well as their interaction, has to be taken into account. We briefly review the most relevant outcomes about flow and dispersion at street scale, whose understanding is essential to study the phenomena at the larger scale.

1.3.2 Street scale

The most simplified geometry describing building structures and street configuration in the urban environment is the **street canyon**. The term street canyon ideally refers to a long straight street bounded by uniform parallel buildings, whose typical dimensions are expressed by the building height to street width ratio H/S.

When external winds are perpendicular to the canyon, three flow regimes may be identified, depending on the street canyon *aspect ratio* (Oke, 1988b): (i) *isolated roughness* flow (ii) *wake interference* flow and (iii) *skimming* flow. Although the emphasis has often been on the two-dimensional nature of the flow, by investigating a perpendicular flow over idealised infinitely long streets, it's worth noting that three-dimensionality belongs to real life and shouldn't be neglected: oblique winds and streets of finite length have to be taken into account. Concerning an oblique wind direction, Nakamura (1988) suggested a simple relationship between the direction of flow above the roof θ_{roof} and that near the floor θ_{canyon}, which indicates a "mirror like reflection" of the flow off the walls. When the flow above the roof is normal to the canyon axis, the flow near the canyon floor is directly opposite and the well-known across-canyon vortex originates within the street, while if the external wind is parallel to the street axis, it is efficiently channelled and the flow into the canyon has the same direction. When the flow above the roof is inclined respect to the canyon axis, a spiral vortex originates along the street-canyon, as the result of along-street channelling and across-street recirculation. In a first approximation, the angle of incidence on the windward wall is the same as the angle of reflection off the wall forming the return flow:

$$\theta_{canyon} = 180 - \theta_{roof} \quad 0^o \leq \theta_{roof} \leq 180^o \tag{1.24}$$

$$\theta_{canyon} = 540 - \theta_{roof} \quad 180^o \leq \theta_{roof} \leq 360^o \tag{1.25}$$

Closer inspection suggested that data were better explained if a cushioning at the wall occurred, producing the angle of reflection smaller than that of incidence.

Soulhac (2000) suggested that the movement in an infinite street resulted from the superposition of the longitudinal and transverse components and consisted in an irregular spiral. Although the longitudinal component is coupled to the transverse component and then its behaviour varies according to the angle, the street mean velocity U_{street}[4] can be regarded as proportional to the component of the external wind which is parallel to the street axis

$$U_{street} \propto cos(\theta_\infty) \tag{1.26}$$

Dobre *et al.* (**?**) performed flow field measurements in the proximity of an urban intersection in London, during the DAPPLE project field campaign; they demonstrated that flow within streets is the vector sum of a a channelling and a recirculation vortex, where the channelling depends linearly on the along-street component of the roof-top reference wind and the across-street recirculation vortex depends linearly on the component of the roof-top reference wind perpendicular to the street. The model decomposes the roof-top reference wind vector into two components, parallel to the street, $u_{R\parallel}$, and perpendicular, $u_{R\perp}$, and calculates the components of the wind vector on the floor of an infinitely long street as:

$$u_\parallel = u_{R\parallel}\, f_1(x/H, z/H, H/W) \tag{1.27}$$
$$u_\perp = u_{R\perp}\, f_2(x/H, z/H, H/W) \tag{1.28}$$
$$u_v = u_{R\perp}\, f_3(x/H, z/H, H/W) \tag{1.29}$$

where f_1, f_2, f_3 are dimensionless functions.

An impressive result is that the main large-scale features of the flow within a non-ideal street seem to be similar to those observed in idealised two-dimensional street canyons and are established at a short distance from the intersection. It is surprising because the intersection is supposed to modify the flow in the adjacent streets by inducing vortices near the corner. In that regards Soulhac (2000) detected a discrepancy between numerical and experimental results and explained it as the numerical simulations have been carried in an infinite street while the experimental measurements have been performed within a street of finite length.

Another constitutive element of the urban geometry is the **street intersection** that also plays an important role in pollutant dispersion in the urban canopy. Concerning pollutant emissions, the presence of the traffic lights induces increased emissions related to the residence time of vehicles at the stop and their acceleration when starting. Concerning pollutant dispersion, intersections are regions where important mass exchange phenomena between different streets take place. Furthermore, pollutant concentration measurements are often collected close to – or within – street intersections: the data analysis thus requires the understanding of the transport mechanisms in these locations (Ott, 1977; Scaperdas and Colvile, 1999).

Several in situ experiments were carried in street intersections in open areas, in order to evaluate the impact of crossing highways on pollutant emissions (O'Toole *et al.*, 1975; Rosas *et al.*, 1980; Bullin *et al.*, 1982). Semi-empirical models (IMM, MICRO2), based on a Gaussian model, were developed to estimate the concentrations near the crossroads (Benesh, 1978; Zamurs and Piracci, 1982; Griffin, 1983; Messina, 1983); however, as far as they do not explicitly consider the effects of the surrounding buildings, the outcomes of these studies cannot be transposed to the case of intersections in urban environment.

[4] the street mean velocity is calculated as the average of the mean velocity through a section of the street; only the longitudinal component plays a role

To date, different studies concerned the problem of air pollution concentrations in urban intersections. Wind tunnel experiments (Hoydysh and Dabberdt, 1994; Hoydysh *et al.*, 1995) were carried out within a network of perpendicular streets and concentration measurements were performed at the intersection using a quantitative gas-tracer method. The results of the study evidenced the key role of the street aspect ratio on the pollutant dispersion. Another wind tunnel experiment on pollutant dispersion in an intersection has been performed by Robins (2002) and showed that even small asymmetries in geometry or wind direction could lead to very different dispersion scenarios.

Some other studies investigated the flow and dispersion in urban intersection by means of numerical simulations. Hunter (1990) highlighted the presence of a vortex with a vertical axis at the end of the street – at the interface street-intersection – in case of a street axis perpendicular to the external flow direction. Scaperdas (1999) studied the flow and the dispersion within a real intersection in London by means of field measurements and CFD simulations, focusing on the dependence of the pollutant concentration field on the external wind direction. In another study, Gadilhe (1993) simulated the flow in a square of Nantes, analyzing the recirculating motions taking place within it.

Recently, Soulhac (2000) performed numerical simulations and wind tunnel experiments in order to understand the mass exchange mechanisms at street intersection. The influence of the wind direction on the streamlines topology was investigated and a parametrization of the mass transfers taking place at the intersection has been proposed and implemented in the SIRANE model.

1.4 Aim of the study

As pointed out previously, the dispersion of contaminants is fairly well understood in open, flat and homogeneous terrain, while the understanding for dispersion in an intrinsically more complicated urban environment appears to be lacking at present, especially at neighbourhood scale. In the urban regime, many new effects come into play as the turbulent flows interacts with group of obstacles, possessing a large range of shapes, sizes and possible configurations. The explicit details of geometry and arrangement of buildings greatly influences the flow and the dispersion pattern: height, width and length of the buildings, building shape, distance between the buildings, wind direction are some of the parameters affecting the flow field and the near-field dispersion. The necessity to improve either the understanding and the modelling of flow and dispersion in urban areas at the intermediate scale of district inspired our study.

The laboratory study of dispersion through large idealised arrays of obstacles is an important method of obtaining a better understanding of dispersion through a real urban environment, because it displays some of the characteristics of the real-world configurations but reducing the number of degrees of freedom. It is through a controlled study of a wide range of idealised configurations that the underlying physical mechanisms of flow and dispersion in urban areas can be probed and a quantitative description of the important processes developed.

So wind tunnel experiments were conducted to study the dispersion through a range of idealised configurations that represented simplified urban neighbourhood. Conversely to other experiments, the array consisted of identical blocks of width W=100 m, length L=100 m and height H=20 m, in order to represent a typical, even if idealized, European city.

The primary mean wind direction was normal to the front face of the obstacle array. In the primary wind direction, three different array layouts were investigated. The obstacles were aligned and initially spaced by $S_x = H$ in the lengthwise direction and $S_y = H$ in the spanwise direction, as showed in Figure 2.11-a. Then the spacing between the obstacles was varied and the other configurations were obtained: $S_x = H$ and $S_y = 2H$, shown in Figure 2.11-b, and

$S_x = 2H$ and $S_y = H$, shown in Figure 2.11-c. In addition to the primary direction, other wind directions were investigated, i.e. $\theta = 10^o, 25^o, 45^o$.

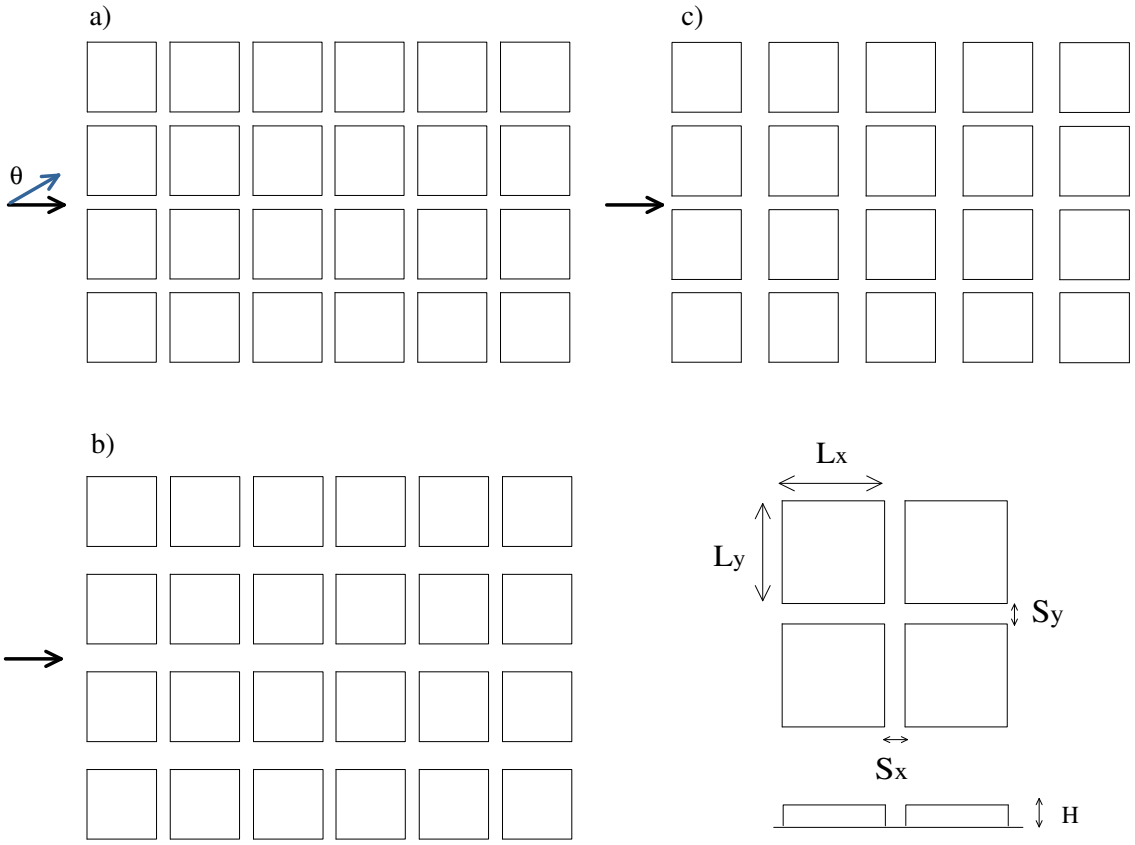

Figure 1.4: Geometry of the obstacle arrays: (a) $S_x = S_y = H$; (b) $S_x = H$ and $S_y = 2H$; (c) $S_x = 2H$ and $S_y = H$

Although the main problem we were interested in was to detect the overall plume behaviour through the array and to point out the influence of the wind direction and the obstacle spacing on the plume evolution, we also cared about the analysis of the flow field above and within the canopy. Numerical simulations have been performed to supply an exhaustive description of the flow dynamics within the street and the intersection, basic elements of the urban environment.

The aim of the study was to understand the fundamental mechanisms of the exchange processes and to enlighten the relevant parameters, in order to be able to model the phenomena in the most general way. Wind tunnel experiments and numerical simulations have been performed, whose set up is described in Chapter 2. The results are analyzed in Chapter 3 and an attempt to understand and explain the mechanisms is carried out. The outcomes are employed to improve an urban dispersion model, SIRANE, which has been developed at the LMFA of the Ecole Centrale de Lyon as a tool for the air quality management and control. In the Chapter 4, the operational model SIRANE is described and a first verification of the model is carried by comparing the experimental measurements and the SIRANE simulations. The subsequent validation of the model should consist in the application of SIRANE to a real neighborhood to evaluate if the implemented modelling, which has been developed on simplified geometries, well represent the complexity of the real phenomena. The final step will be the subject for a future work.

Chapter 2

Experimental and numerical methods and facilities

2.1 Wind tunnel experiments

The simulation of a full-scale model in laboratory studies has the potential to provide a very detailed and complete physical picture of flow and plume dispersion. Unlike the real atmosphere, whose behaviour is extremely variable and difficult to measure and characterise, the laboratory environment is strictly controlled and thus allows realizing certain configurations not encountered in a particular full-scale experiments. Because of the ability to control parameters in the laboratory, more stationary conditions can be simulated and a better convergence of the statistic of time series measurements is attained. Laboratory experiments also provide better defined boundary conditions when running computational models for validation or other purposes, which is of critical importance in complex calculations of computational fluid dynamics works.

The understanding of the fundamental aspects of dispersion in the atmosphere has not rested on the provision of an accurate scaled version of the atmospheric boundary layer in the wind tunnel, but rather on the provision of a fully developed turbulent boundary layer flow over a fully rough surface. Here, fully developed implies that stream-wise development is slow so that changes in structure over the fetch of interest are insignificant. In terms of its suitability for dispersion studies, Robins (1979) demonstrated that a fetch of about $6 - 7\delta$, where δ is the boundary layer depth, is needed for the development of a neutrally stable boundary layer and that thereafter stream-wise development is slow.

In order to correctly reproduce atmospheric boundary layers in a wind tunnel, some conditions have to be preserved.

2.1.1 Similarity

The geometrical similarity has to be ensured by the homogeneous scaling of all the involved lengths. A representative scaling requirement is that the Jensen number $Je = \delta/z_0$, defined as ratio of the boundary layer thickness and the aerodynamic roughness height, should be identical for the wind tunnel and field flows.

The dynamical similarity, involving the concept of similar flow patterns, is derived from the dimensional analysis of the Navier-Stokes equations governing fluid dynamics and implies that various nondimensional parameters must be matched between the model and real flows. Plate (1982) indicated that all these numbers can be exactly the same in model and prototype only if the model and the prototype are identical. In most cases, it is not necessary to consider every aspect of the fluid flow and it is only required to model the main feature of the boundary conditions. The most relevant characteristic number in the simulation of the urban boundary layer is the Reynolds number:

$$Re = \frac{\nu}{U\,L} \tag{2.1}$$

where U and L are the velocity and length scales respectively.

So, any atmospheric flow may be modelled by another flow provided that

- the characteristic dimensionless numbers Re are identical;
- the nondimensional boundary conditions are identical and thus the wind tunnel boundary layer exhibits velocity and turbulence intensity profiles similar to those of the atmospheric boundary layer.

The requirements for similarity of flow patterns have been discussed. The dispersion of a pollutant, assumed to be passive in the sense that it does not affect the governing equations, has

now to be considered. An additional parameter is derived by the molecular diffusion equation:

$$\frac{\partial C'}{\partial t'} + \mathbf{u}' \cdot \nabla' C' = \frac{1}{Re\, Sc} \triangle' C' \tag{2.2}$$

$Sc = \frac{\nu}{\alpha}$ is the Schmidt number and α the molecular mass diffusivity.

To summarize, if and only if the nondimensional coefficients and the boundary conditions are identical, the dispersion of the contaminant in a model will be identical to that in the atmosphere. It is generally impossible to simultaneously match all of the dimensionless parameters, but often it is only required to model certain aspects of the flow and certain similarity conditions may be relaxed.

2.1.2 Experimental set-up

The wind tunnel experiments were undertaken in the wind tunnel in the Laboratoire de Mecanique des Fluides et Acoustique de l'Ecole Central de Lyon. It is a recirculating wind tunnel measuring 24 m long x 7.4 m high x 7.2 m wide. It consists of a test section, a heat exchanger system that allows to maintain the desired temperature value ($\pm 0.5°$), an axial fan that produces a speed varying between 0.5 and 10 m/s, flow diverging and converging systems, an upwind grid that generates a homogenous turbulence; the working section is 14 m long x 2.5 m high x 3.7 m wide. The scheme of the wind tunnel is drawn in Figure 2.1.

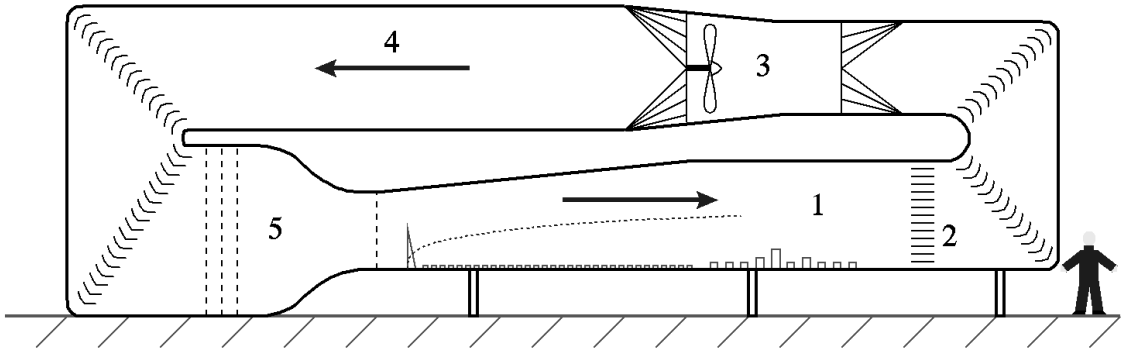

Figure 2.1: Wind tunnel at the Ecole Centrale de Lyon: **1** test section; **2** heat exchanger system; **3** fan; **4** diverging system; **5** converging system and generating turbulence grid

A neutrally stratified boundary layer of approximately 0.8 m has been generated by using spire arrays combined with floor roughness, as suggested by Irwin (1981). The spires were 500 mm high and allowed to thicken the boundary layer accelerating the streamwise development of the larger scale eddies in the boundary layer. The entire wind tunnel floor was overlaid with screw-covered rectangular obstacles, which acted as roughness elements in the first part of the wind tunnel (6-7 m) and simulated urban blocks downwind. In this way the development of an internal boundary layer due to roughness changes was avoided and the achievement of a fully developed boundary layer was accelerated. Further, this set up produced mean and turbulence velocity profiles that matched fairly well typical urban profiles. The photo in Figure 2.2 represents the experimental set-up.

The urban neighborhood was simulated by aligned building-like obstacles of height $H = 50$ mm and width and length $W = L = 250$ mm, at the scale factor 1:400. The ratio of the obstacle height H to the depth of the boundary layer δ was 1/16, ensuring a somewhat similar condition between the simulated and the real case. The reference free stream velocity U_∞ at the boundary layer height was set at 5 m/s and the characteristic Reynolds number Re=1.5 x 10^4 assured an

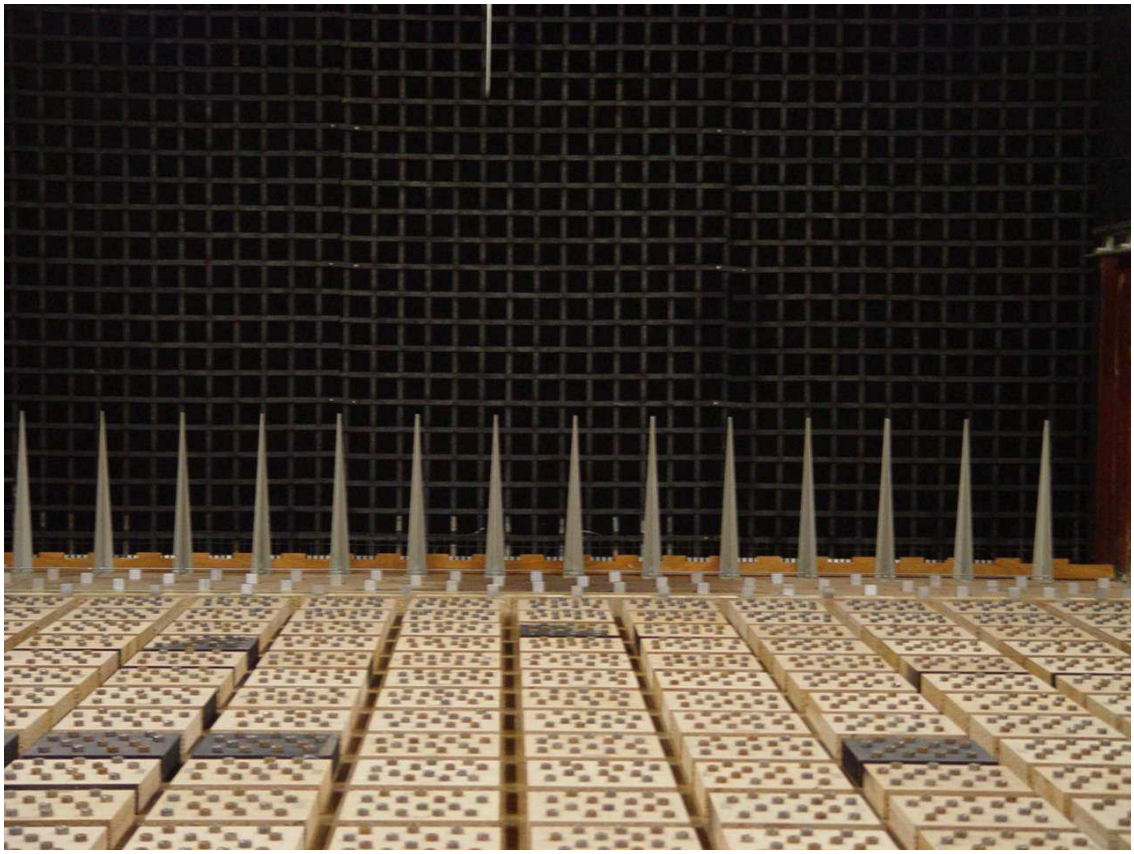

Figure 2.2: Experimental set-up: Irwin spires and floor roughness.

asymptotic behavior of the turbulent flow and the preservation of the dynamical and geometrical similarities.

The model was placed on a 3.7 m x 3.7 m rotating plate in the last part of the working section and could thus be oriented in any direction. The pollutant source was placed at the center of the turntable, so that it kept approximately the same positions respect to the wind tunnel if rotating the turntable. The source was placed within the obstacle array at height $H/2$. The primary coordinate system is solidal with the array and the origin matches the source position.

Figure 2.3 shows the experimental set-up for the investigated configurations, together with the source position, the rotating plate and the coordinate system. Configuration 1 consisted in obstacles aligned and equally spaced of a distance $S = H = 50$ mm. Configuration 2 and 3 were built by varying the spacing between the buildings in the spanwise and lengthwise direction. All the configurations were initially studied for a wind direction aligned with the x-axis, i.e. $\theta = 0^o$, to understand how the array layout affects the flow field and the dispersion pattern. Then, in order to study the influence of the wind direction, the turntable on which the group of buildings laid was rotated of the desired angle. The configuration 1 was investigated for $\vartheta = 10^o, 25^o$ and 45^o, while the configuration 2 for $\vartheta = 45^o$; the photo in Figure 2.4 shows the realization of the experiment in the wind tunnel.

Profiles of mean wind and turbulence intensity defining the inflow conditions and the velocity structure above the array were measured by means of crossed hot wire anemometer. Measurements of velocity within the high turbulence intensity regions below the canopy height were performed by means of the Laser Doppler anemometer. Various horizontal profiles of concentration, and some vertical profiles, were measured by Flame Ionisation Detector within the array, at height H/2, and above it, at height 2H, for different rows downwind the source. The sampling lines are indicated by the dashed line in Figure 2.3.

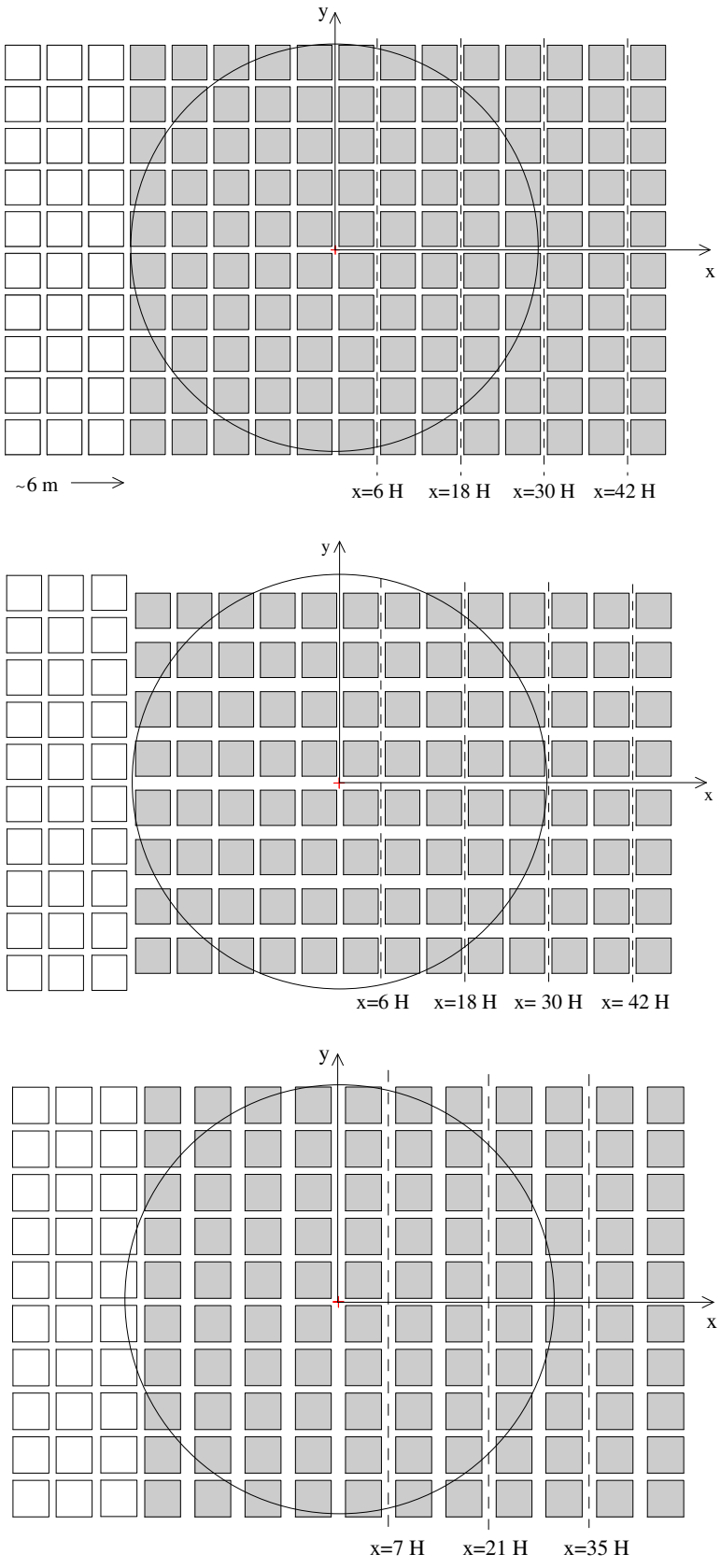

Figure 2.3: Diagram of the arrays as set up for the wind tunnel, including the source release position (+), the turntable and the sampling locations (dashed lines). (a) Configuration 1: $S_y = S_x$=H; (b) Configuration 2: S_x=H S_y=2H; (c) Conf 3: S_x=2H S_y=H

Figure 2.4: Experimental set-up representing the upwind roughness and the rotated array

2.1.3 Measurement techniques

Hot-wire anemometer and Laser Doppler anemometer

Mean wind speed and turbulence intensity were measured upwind the obstacle array, to verify they were consistent with typical urban flow profiles. Flow field measurements above the group of obstacles were performed with conventional hot-wire anemometry, a technique founded on the heat transfer principle: the hot wire, heated up by a constant current or maintained at a constant temperature, is cooled by the local flow and the heat lost to flow convection depends on flow velocity. By measuring the change in wire temperature under constant current or the current required to maintain a constant wire temperature, the heat lost can be obtained and can then be converted into a flow velocity in accordance with convective theory. Typically, the anemometer wire is made of platinum or tungsten and is $4 \sim 10\mu$ m in diameter and $1 \sim 5$ mm in length. The small size of the hot-wire element enables good spatial resolution of the velocity field and the correspondingly low thermal inertia also promises fast response, thus allowing the high-frequency fluctuations of a turbulent flow to be detected. In order to provide simultaneous measurements of two velocity components, two hot wires are arranged in a X configuration, oriented at $\pm 45^o$ to the direction of flow.

A constant temperature crossed hot wire has been used in the measurements and is shown in the Figure 2.5. The X-probe has been calibrated adopting the "full velocity vs yaw-angle" technique, as suggested by Browne (1989). A suitable code has been developed in Labview to perform X-probe calibration and to acquire and elaborate velocity measurements, i.e. mean velocities, velocity fluctuations and velocity correlations, as the Reynolds stress $-\rho\overline{u'w'}$.

Some authors pointed out that the hot wire anemometry technique seems to show some limitations in the correct measurements of velocity fluctuations and Reynolds stresses, when the local turbulent intensity $i_u = u'/\overline{u}$ is relatively high. Smalley (2001) and Legg (1984) suggested that the velocity fluctuation measurements are reliable when $i_u < 0.35$ and the Reynolds stress measurements when $i_u < 0.25$.

The X-wire probe may be subject to errors of several kinds: errors at high turbulence intensities due to short-term flow reversals in the streamwise direction and errors due to the contamination by lateral velocity fluctuations, which are estimated theoretically by Legg (1984). Further, the loss of high-frequency coherence due to the spatial separation of the wires may compromise the measurement, as suggested by Raupach (1986). The main limitation of the hot anemometer is that it is unable to detect reversal flow, as it does not recognize the direction of

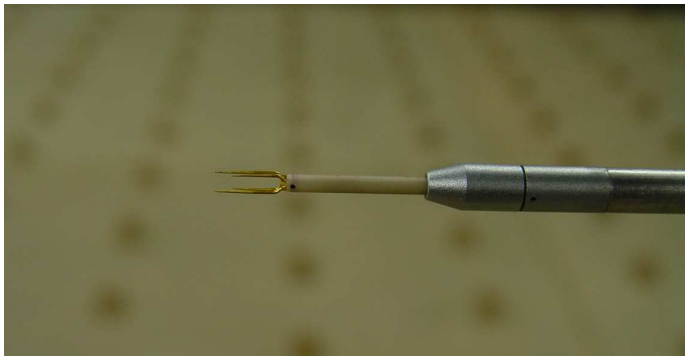

Figure 2.5: Crossed hot wire anemometer

the flow. Further, as the X-wire probe is mounted on a support, it does not allow to perform measurements in narrow spaces and therefore limits the investigation field between the obstacles. A non-invasive measurement method has been adopted in order to avoid these difficulties and investigate the turbulent flow field within the obstacles: the laser Doppler anemometry.

The laser Doppler anemometer measures the flow velocity by measuring the velocity of small particles transported by the flow. In LDA the laser beam is first divided into two beams with equal intensities. The beams are then directed to optical fibers which deliver them to the probe optics. Optics are used to guide the two laser beams into the measurement point, where the beams crossing with each other form interference fringes. The flow is seeded with small particles that follow the turbulent motion of the fluid. When these particles pass by the measurement volume they scatter light according to the Mie-theory. The intensity fluctuation of the scattered light depends on the velocity of the particle. Thus, the velocity of the flow is obtained by measuring the change in wavelength of the reflected laser light by means of the interference fringe pattern, as seen in Figure 2.6.

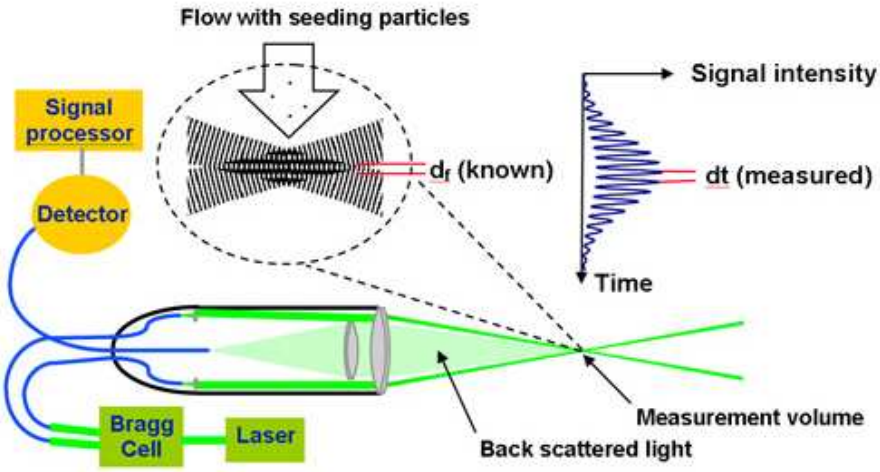

Figure 2.6: Description of the LDA working

The moving gear on which the measurement instrumentations were mounted is displayed in Figure 2.7, as well as the optics of the laser Doppler anemometer and the support for the hot-wire anemometry equipment. The positioning of the measurement point respect to the gear differed according as the measurements were carried out by the hot wire anemometer or by the laser Doppler anemometer, as shown in Figure 2.8-a. In order to evaluate the gear influence on the flow field, we measured the mean velocity for two different positions of the gear that correspond to the hot-wire measurements (A) and to the Laser Doppler measurements (B), as indicated in

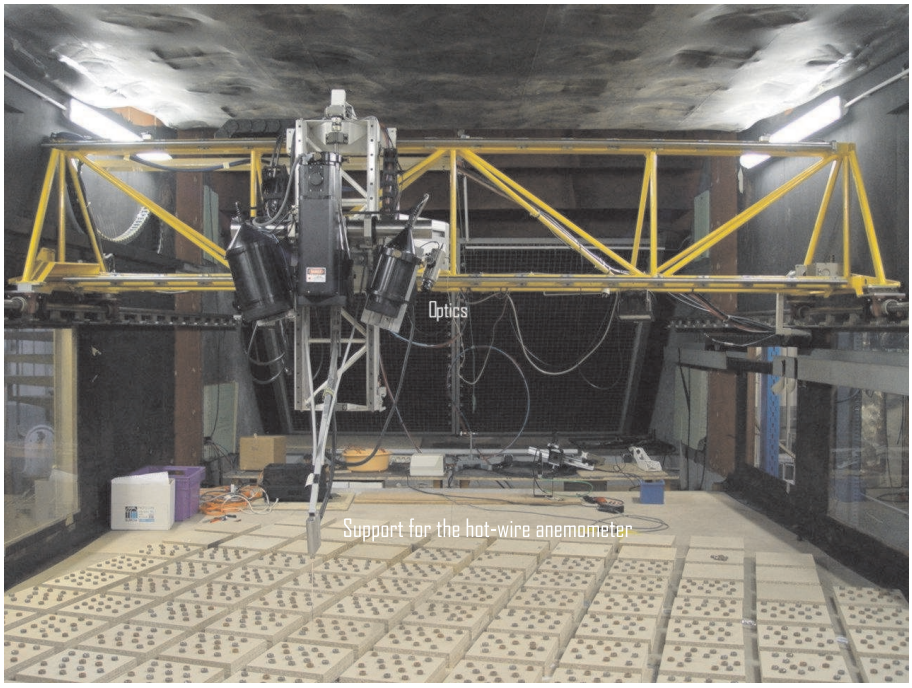

Figure 2.7: Instrumentation mounted on a moving gear

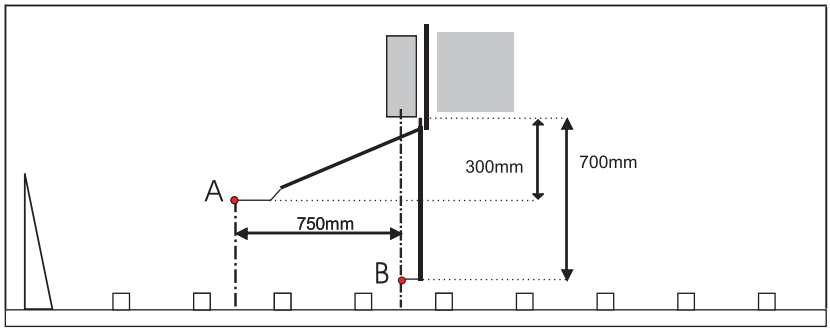

(a) The different relative positioning of the measurement point regards to the gear according to the measurement method: A refers to the hot wire measurements and B to the LDA measurements.

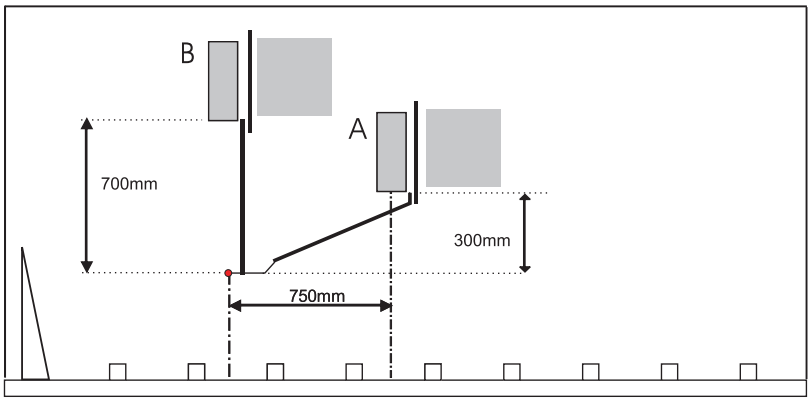

(b) The different relative positioning of the gear regards to the same measurement point: A refers to the hot wire measurement set up, while B to the LDA measurement set up.

Figure 2.8: Relative positioning of the measurement point regards to the gear

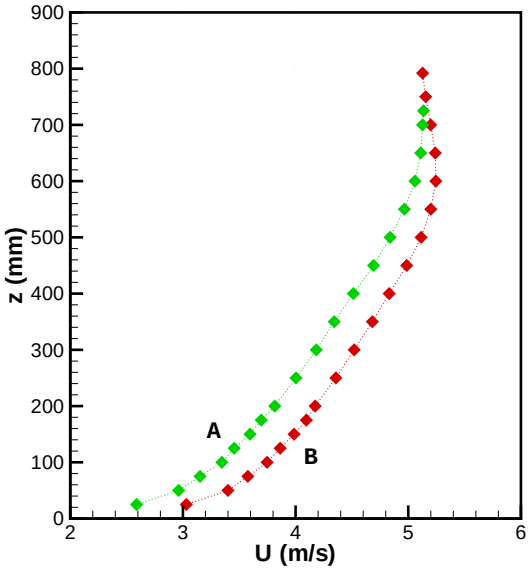

Figure 2.9: Vertical mean velocity profiles

2.8-b. Figure 2.9 shows that the vertical profiles are quite different and the mean velocity is higher at position B. This means that the presence of the gear during LDA measurements widely affects the flow field by modifying the wind tunnel effective section and accelerating the flow. The LDA measures a perturbed flow regards to the flow measured by the hot wire anemometer and it is important to take it into account in comparing and interpreting the results.

Flame Ionisation Detector

Concentration measurements were performed by detecting a passive gas tracer continuously discharged from an open-ended pipe 10 mm in diameter. Ethane (C_2H_6) was used as the tracer in the experiments, because its density is very similar to that of air and the releases had neutral buoyancy. The low release flow rate employed in the experiments ensured that the gas was quickly diluted and that passive diffusion started near the source.

The Flame Ionisation Detector (FID) measures hydrocarbons concentration in air. Air containing hydrocarbons is aspirated continuously by a tube, which is very thin not to perturb the flow, and is injected into a hydrogen flame. The amount of ions produced by the combustion is proportional to the concentration of hydrocarbons. A current is induced by the ions collected to an electrode that is proportional to the concentration of ethane in air.

Calibration was performed daily by subjecting FID to a series of known and controlled concentrations over an appreciable range and constructing a calibration curve. The FID was found to be linear over the range of operation, so that only a single calibration parameter defined the slope between FID output (millivolts) and measured concentration (ppm). Measurement problems might arise from the calibration procedure, as the calibration constant tended to drift significantly from one day to the next by possibly more than 10%.

Since FID provides instantaneous concentration values, a Labview code is employed to preprocess the data and extract meaningful statistics from the concentration time series. The data set consisted of 120 s samples of concentration time series sampled at 100 Hz. The 120 s averaging time seemed to be representative, since the scale of the turbulence generated within the array is of order H/U (typically about $0,5$ s) and is well averaged over two minutes. Because

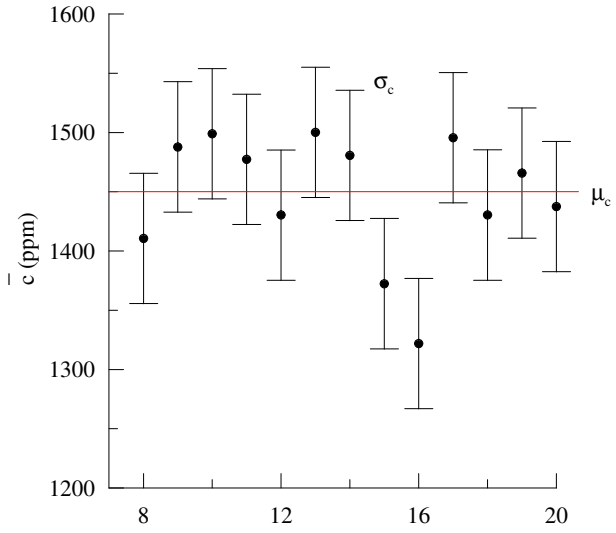

Figure 2.10: Uncertainty concerning the FID measurements

the pollutants recirculate in the wind tunnel and accumulate, the background concentration varies a lot before reaching a steady condition; it has been necessary to determine for each time series the zero-concentration level, i.e. the background concentration.

The statistics extracted from the time series include the mean, the standard deviation and the fluctuation intensity. A careful consideration of the uncertainties associated with the results was made, including an estimation of the intrinsic stochastic uncertainty of the statistical calculated from the finite length time series, as well as the uncertainty due to limitations of instrumentation and measurement errors. The uncertainty of the results was evaluated by the collection of repeated runs at the same sampling position[1], as shown in Figure 2.10. Different evaluations lead to consider the uncertainty of the FID measurements equal to $\sigma_c = 55$ ppm, which represents an acceptable error $(3 - 5\%)$ for the high near-field concentration values, while a more significative one $(10 - 15\%)$ for the lower far-field concentration values.

[1]The sampling time was assumed to be $T = 120$s, ensuring a meaningful time series

2.2 Numerical simulation

2.2.1 Numerical model

As complementary tool to explore the flow field in urban canopy, Computational Fluid Dynamics (CFD) simulations have been used. The Reynolds Averaged Navier-Stokes (RANS) equation methods are the current approach to simulate atmospheric flow in complex geometries, because of their reasonable computational costs. The Reynolds averaging process introduces into the governing equation system new unknown correlation terms and the turbulence models supply additional equations to solve the correlations and make the above governing equation system form a closed set. Different turbulence models have been developed: the standard $k-\varepsilon$ and the $k-\omega$ are turbulence closure model of the first order, while the Reynolds Stress Models (RSM) are higher order closure models.

The averaged Navier-Stokes equations and the continuity equation governing the motion of steady, incompressible and turbulent flow can be written as:

$$\overline{u_j}\frac{\partial \overline{u_i}}{\partial x_j} = -\frac{1}{\rho}\frac{\partial \overline{p}}{\partial x_i} + \frac{\partial}{\partial x_j}(\nu\frac{\partial \overline{u_i}}{\partial x_j} - \overline{u_i' u_j'}) \tag{2.3}$$

$$\frac{\partial \overline{u_i}}{\partial x_i} = 0 \tag{2.4}$$

In order to close the equation system, the standard $k-\varepsilon$ relates the unknown turbulent fluxes $\overline{u_i' u_j'}$ to the mean velocity gradients, using the concept of turbulent viscosity ν_t, analogous to its counterpart of viscous stress:

$$-\overline{u_i' u_j'} = -\nu_t(\frac{\partial \overline{u_i}}{\partial x_j} + \frac{\partial \overline{u_j}}{\partial x_i} + \frac{2}{3}\delta_{ij}k) \tag{2.5}$$

$$\nu_t = C_\mu \frac{k^2}{\varepsilon} \tag{2.6}$$

The turbulent kinetic energy k and the turbulent kinetic energy dissipation rate ε are computed by means of their transport equation. C_μ is an empirical constant, usually taken as 0.09. Such an approach does not give the details of turbulence but provides only mean values. Since we are interested in the simulation of the mean flow field and higher order solutions would require excessive computational efforts, it seems to be the best compromise in our case.

In our study we opted for the commercial CFD code FLUENT, which solves the equations for the conservation of mass, momentum, energy and scalars through a finite volume method. The domain is divided into discrete control volume cells using a computational grid mesh. Unstructured meshing supports variable volume cell sizes throughout the domain and allows to concentrate finer mesh in areas where is most critical resolving complex flows. Algebraic equations for discrete dependent variables such as velocities are constructed and solved.

For atmospheric flows the segregated solver using implicit discretization is appropriate and is being used for our study. The momentum equations are solved and then a pressure-correction is applied to update the pressure field so that the velocities calculated by the momentum equations satisfy the continuity equation. The solutions for energy, turbulence and other scalar equations follow separately. In the implicit discretization for a given variable the unknown value in each cell is calculated using both existing and unknown values from neighboring cells. Overall the software uses an algebraic multigrid method to solve the resultant system of equations for the dependant variable in each cell. The calculations continue and update all the cell properties until selected criteria for a converged solution is reached.

The solutions for the RANS governing equations require specific boundary conditions; inappropriate boundary conditions may be a significant source of errors. In a CFD simulation, the flow profiles of mean wind speed and turbulence quantities that are applied at the inlet plane of the computational domain are generally fully developed, equilibrium profiles and should be representative of the roughness characteristics of the upstream terrain. In order not to model explicitly the obstacles, wall functions are applied to the bottom of the domain that replace the overall effect on the flow as these obstacles. The wall boundary conditions involve physical modelling of the wall effect in terms of roughness, which is expressed as equivalent sand-grain roughness height k_s; two different ranges of k_s can be distinguished, one representing the roughness due to the obstacles over the terrain (large-scale roughness: 1 to 60 m), the other representing the surface of the obstacles themselves (small-scale roughness: 0 to 1 m).

A critical point in the dispersion modelling is the simulation of the atmospheric boundary layer, which has to be accurate near the ground surface to obtain reliable predictions of the related atmospheric processes. As pointed out by Blocken (2007), four requirements should be simultaneously satisfied:

1. A sufficiently high mesh resolution in the vertical direction close to the bottom of the computational domain (e.g. height of first cell < 1 m);
2. A horizontal homogeneous ABL flow that means the absence of streamwise gradients in the vertical profiles;
3. A distance y_p from the centre point of the wall-adjacent cell to the wall that is larger than the physical roughness height k_s of the terrain;
4. Knowing the relationship between k_s and the aerodynamic roughness length z_0 that results from matching the atmospheric boundary layer mean velocity profile and the wall function.

In Fluent, the first order matching to derive the roughness height k_s yields:

$$k_s = \frac{9.793\, z_0}{C_s} \tag{2.7}$$

where C_s is a constant whose value is in the range of 0 to 1, but generally assumed equal to 0.5. It is noticed that k_s is much larger than the aerodynamic roughness length: for urban areas, $z_0 \sim 0.1 \div 1$ m and consequently $k_s \sim 2 \div 20$ m. Then, in CFD simulations in urban environments, the third requirement $y_p > k_s$ implies that very large control volumes should be used, which is in conflict with the first requirements of high mesh resolution. Since no accurate solutions for near-ground flow can be obtained with large cell sizes, instead of simulating the urban boundary layer by means of large-scale roughness, we decided to explicitly model the roughness in all the computational domain. If the numerical domain is sufficiently large and appropriate boundary conditions are chosen, the second requirements is satisfied and the flow is in equilibrium with the roughness characteristics of the ground surface. Any internal boundary layer develops and the vertical profiles of the mean wind speed and turbulence quantities are maintained with downstream distance. Nevertheless, a large computational domain means a very time-consuming simulation. An interesting option could be to assume a periodic domain with periodical boundary conditions.

2.2.2 Numerical set up

The aim of the numerical investigation was to improve the understanding of the flow dynamics within the neighbourhood. Conversely to many authors, we were not interested to the spatially

averaged velocity profile within the obstacle canopy, but to the spatial inhomogeneity of the flow field due to the presence of the obstacles.

In order to simulate the experimental configurations, the numerical domain consisted of rectangular obstacles which covered the entire wind tunnel floor, acting as roughness in the first part of the wind tunnel and simulating urban blocks in the next part. The sand-grain roughness wall functions was used to model the small-scale roughness of the obstacle surface, set to $k_s = 0.01$ m. This value ensured a good agreement between the external velocity profile simulated by Fluent and that measured by the laser Doppler anemometer. Since the simulated array presented a geometrical periodicity, the computational domain could be represented by the single sub-element, as illustrated in Figure 2.11. A mass-flow rate was imposed at the inlet and a condition of symmetry was imposed on the top of the domain, whose height δ was sufficiently large as regard as the obstacle height H not to perturb the flow, i.e. $\delta = 11H$. Periodical conditions have been set between the inlet and the outlet and on the lateral boundaries. The numerical domain was opportunely meshed, as displayed in Figure 2.12.

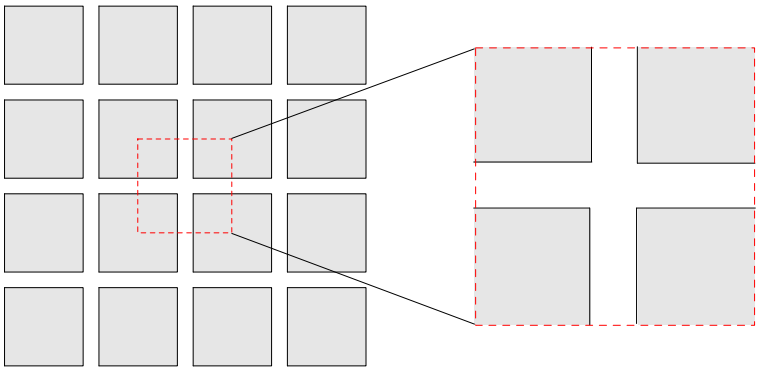

Figure 2.11: Geometrical periodicity of the array

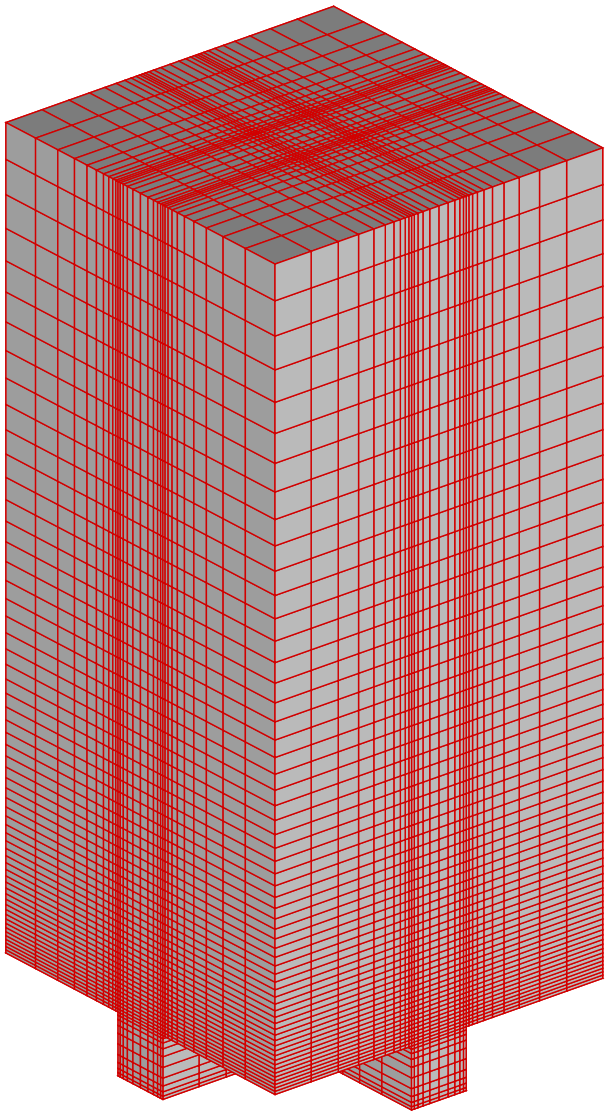

Figure 2.12: Numerical domain

Chapter 3

Flow and dispersion in a neighborhood

3.1 Flow above the array

In this Section we analyse the flow field above the array in order to evaluate if the wind tunnel boundary layer effectively simulates the main characteristics of a well-developed urban boundary layer. The evolution of the boundary layer is shown in Figure 3.1, where the vertical profiles of the flow variables are plotted at different distances from the entrance of the wind tunnel. The good matching of the curves demonstrates that the flow was fully developed since $x_r = 6640$ mm, that is the stream-wise development was slow so that changes in structure over the fetch were insignificant. The flow and dispersion measurements through the array were thus carried out in the downwind part of the working section, i.e. $x_r > 6640$ mm, where the boundary layer can be considered fully developed.

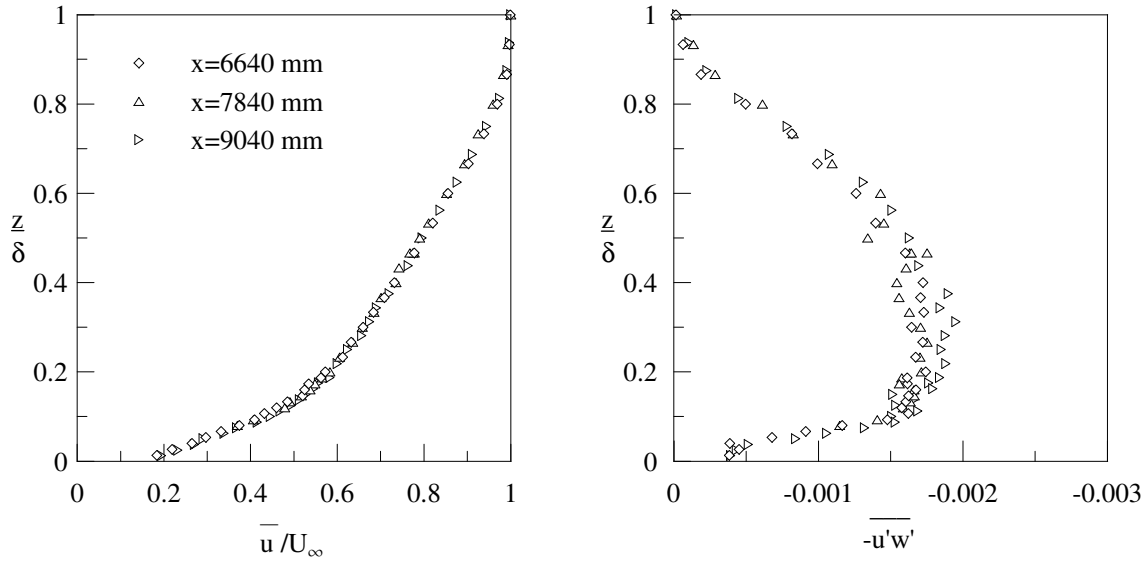

Figure 3.1: Boundary layer evolution along the streamwise direction from the entrance of the wind tunnel

Conversely, the horizontal homogeneity required by the similarity theory was not exactly satisfied. Figure 3.2 shows the horizontal profiles of the mean velocity components that reveal an unexpected horizontal component. The angle α is defined as the angle between the component $\overline{u}$ and $\overline{v}$ and points out the misalignment of the flow as regard to the axis of the wind tunnel. It's worth noting that all the variables are actually referred to the *wind tunnel reference system* $\{x_r, y_r, z_r\}$, x_r indicating the streamwise direction, y_r the transversal direction and z_r the vertical one. $\overline{u}$ is the component of the mean velocity along x_r, $\overline{v}$ the component along y_r and $\overline{w}$ the component along z_r.

Once ensured the boundary layer is totally developed, we verified that the simulated dynamical conditions represented an atmospheric urban boundary layer. The characteristic boundary layer parameters and the measured vertical profiles of flow variables have been compared to rough boundary layer profiles found in literature.

As discussed previously, we expected the surface layer over a rough boundary to be constituted of two parts. The inertial sublayer, where the height above the surface provides the only length scale and the logarithmic profile law describes the mean velocity profile, and the roughness sublayer, where the flow depends explicitly by individual roughness elements (Raupach *et al.*, 1980). We investigated the scatter of the vertical profiles of flow variables performed at different positions above the canopy to point out the horizontal inhomogeneity of the flow and then determine the extent of the roughness sublayer. We individuated 4 positions representing

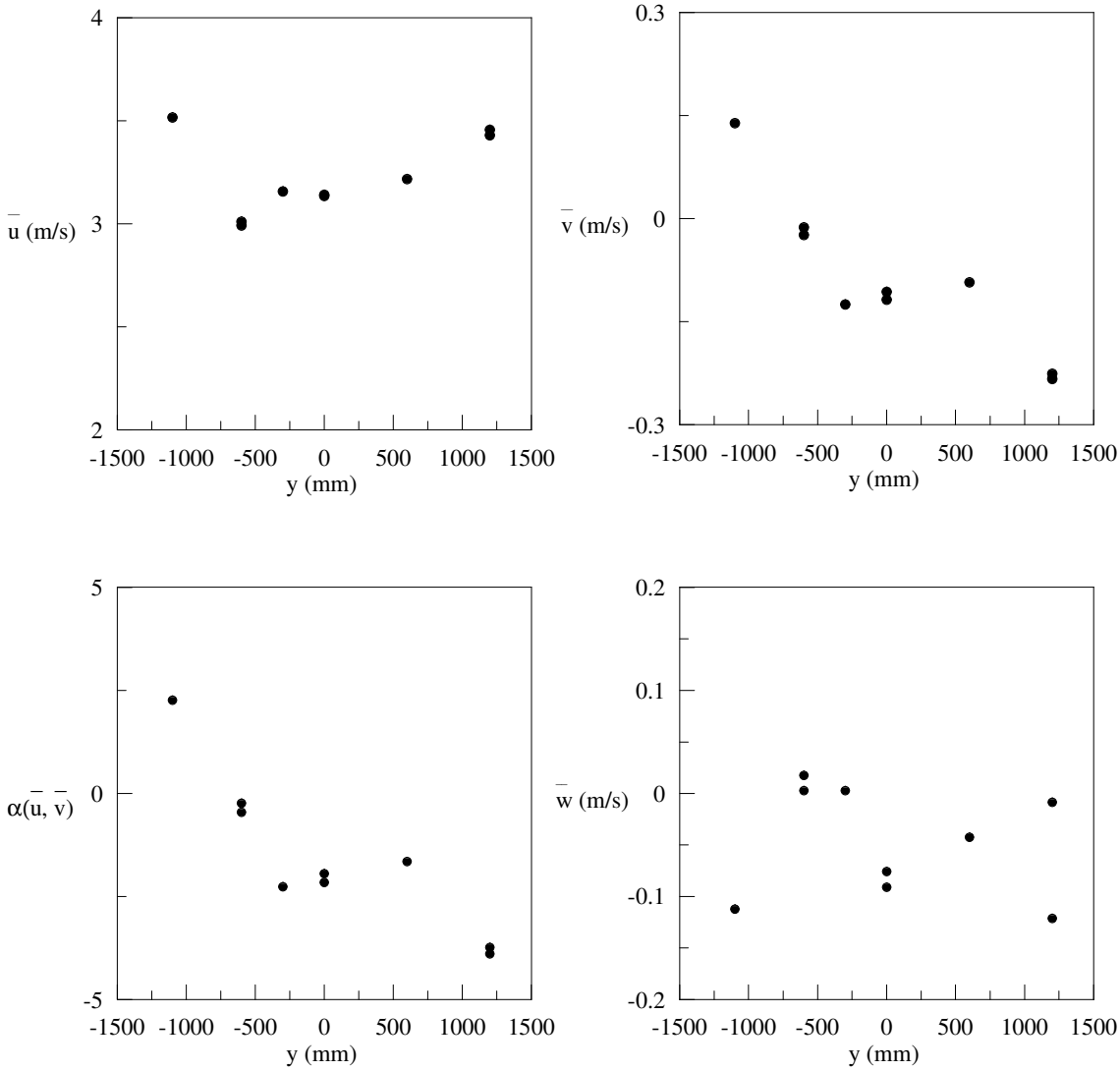

Figure 3.2: Horizontal inhomogeneity of the flow variables: a) Mean streamwise velocity component; b) Mean spanwise velocity component; c) Orientation of the velocity vector; d) Mean vertical velocity component

very different conditions:

- the center of the intersection: x=9040 mm, y=0 mm;
- the center of the longitudinal street: x=9190 mm, y=0 mm;
- the center of the transversal street: x=9040 mm, y=150 mm;
- the center of the obstacle: x=9190 mm, y=150 mm.

The measured flow variables are the streamline component of the mean velocity $\overline{u}$, the standard deviations σ_u and σ_w and the Reynolds stress $-\overline{uw}$.

In the Figure 3.3 the normalized profiles all collapse to common curves, although an increased scatter can be observed close to the surface. We estimated the horizontal scatter of the different profiles, in order to identify the roughness sublayer and eventually to determine its upper limit, referred to as the height of homogenization z_*. The spatial standard deviation over the 4 different positions was a representative measure of the spatial variability. For each flow variable j a vertical profile of the spatial standard deviation was defined, as follows:

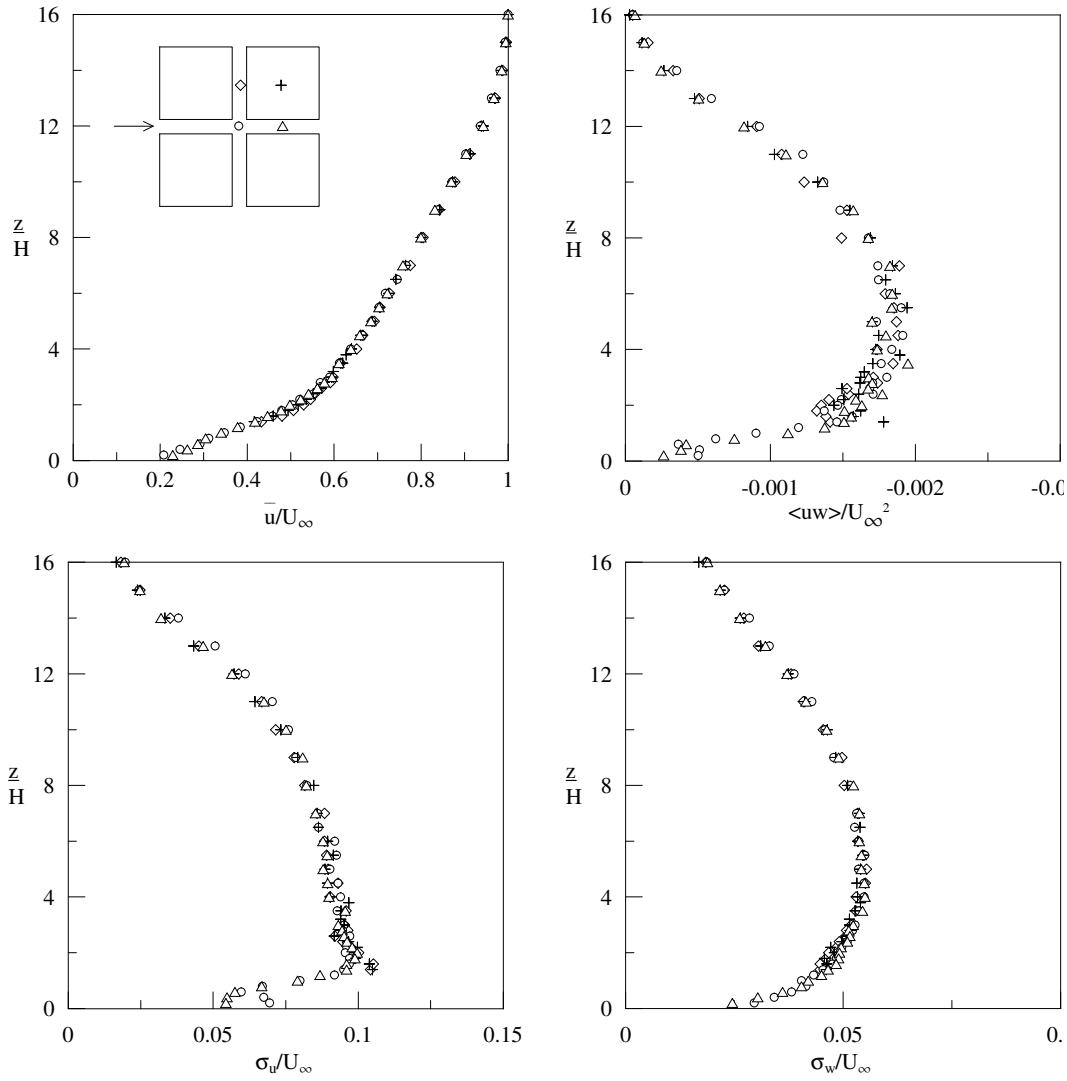

Figure 3.3: Vertical profiles of flow variables at different positions above the canopy

$$SSD_j(z) = \sqrt{\frac{\sum_{i=1,4}[x_i(z) - \overline{x}(z)]^2}{n}} \tag{3.1}$$

i indicates the positions where the profiles have been conducted.

The Figure 3.4 shows the vertical evolution of the spatial standard deviation for the flow variables $\overline{u}$, σ_u, σ_w and $\overline{uw}$. All the profiles show a higher scatter close to the obstacles, where the local effects were expected to be dominant and enlighten a horizontal inhomogeneous layer of height $z_* \simeq 2 - 3\mathrm{H}$. The roughness sublayer extends from $z = H$, the height of the canopy, to $z_* \simeq 2 - 3\mathrm{H}$, in agreement with data found in the literature (Raupach *et al.*, 1991). Above the height of homogenization z_*, the data represents a statistical scatter due to the measurement uncertainty, which can be introduced by the finite sampling period or by measurement errors. The measurement uncertainty can thus be evaluated for each flow variables as the mean of the standard deviations above the homogenization height: $SD_{\overline{u}} = 0.0035$ m/s, $SD_{\overline{w}} = 0.0055$ m/s, $SD_{u'} = 0.007$ m/s, $SD_{w'} = 0.0035$ m/s, $SD_{\overline{-u'w'}} = 0.001$ m/s.

The inertial sublayer has been defined as the overlap region in which the flow is independent of all lengths except Z=z-d. The asymptotic matching required that the inertial layer was free from all the influences governed by surface length scales and contextually that $Z << \delta$ (a

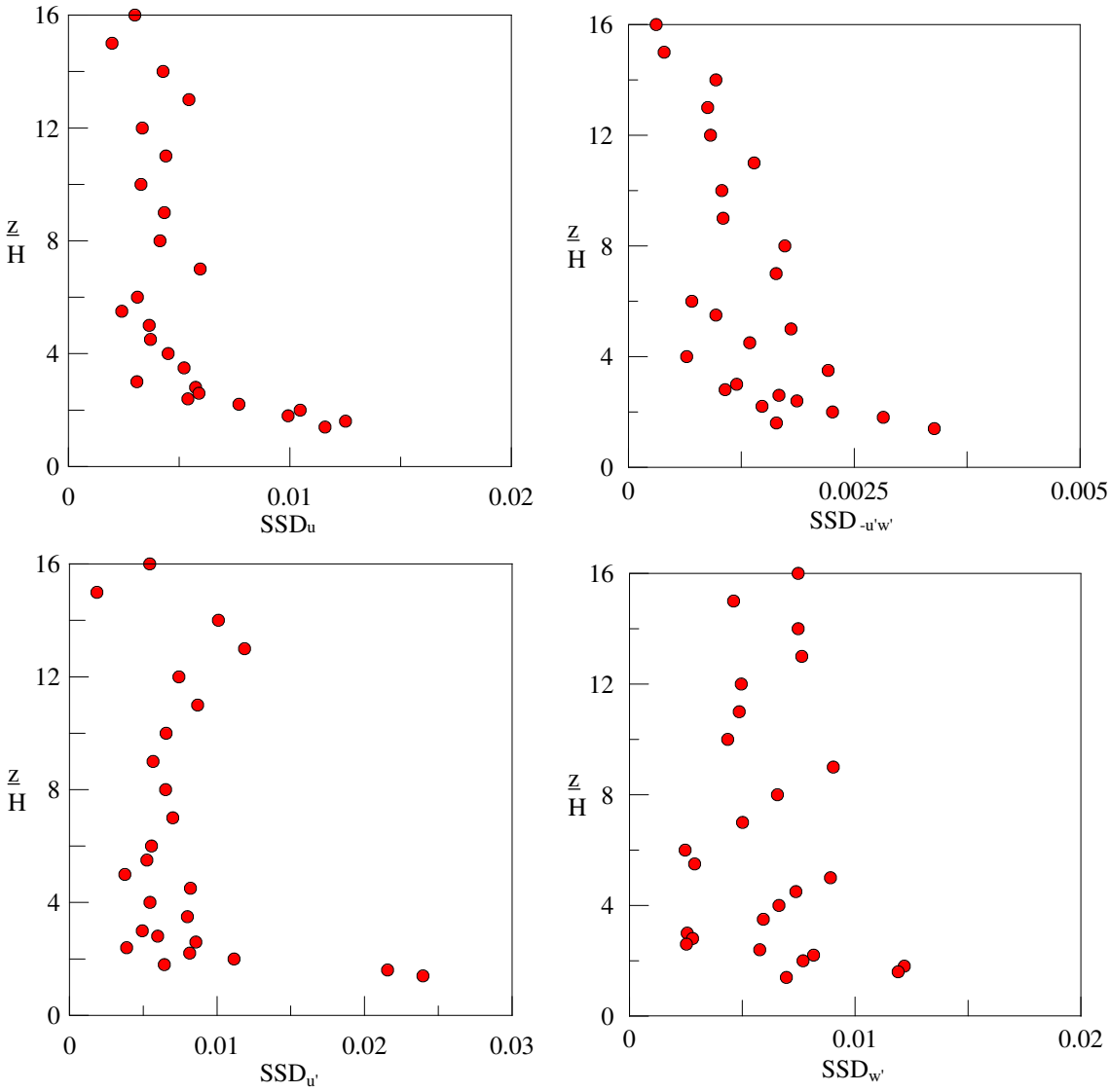

Figure 3.4: Measurements uncertainty estimated for each variable by SSD_j

real asymptotic matching should require $Z < 0.1\delta$). The lower height limit corresponds to the upper limit of the roughness sublayer $z_* \simeq 3\mathrm{H}$, while the upper height limit is imposed to be $Z = 0.1 \div 0.2\delta$.

The usual logarithmic law should describe the mean wind profile in the inertial layer:

$$\frac{U(z)}{u_*} = \frac{1}{k}\, ln\left(\frac{z-d}{z_0}\right) \tag{3.2}$$

where u_* is the friction velocity, z_0 the aerodynamic roughness and d the displacement height.

In literature several techniques have been developed to determine the values of these parameters. A reasonable estimate of u_* may be inferred from the Reynolds shear stress profile. Over most wall surfaces at relatively high Reynolds number, a constant-stress layer has been observed for $Z << \delta$, generally $Z \sim 0.1 \div 0.2\delta$. The typical distributions of the total stress, the Reynolds stress and the viscous stress across a boundary layer are shown in Figure 3.5. If the viscous stress can be neglected, that is for $Z >> \nu/u_*$, the surface stress reduces to the Reynolds stress. Thus the value of $-\overline{uw}$ at the plateau identifies the value of the surface stress at the wall $\tau(0) = \rho u_*^2$ (Antonia and Krogstad, 2001) and consequently it supplies an estimation

of the friction velocity u_*. The advantage of this approach is that it supplies an independent estimation of the friction velocity.

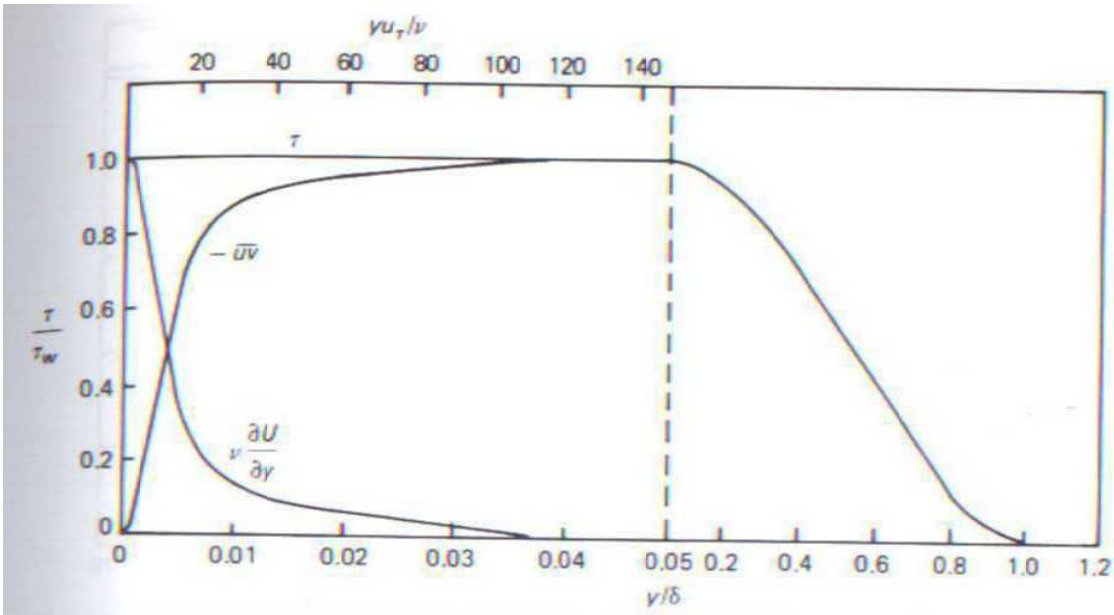

FIG. 21.12 Distributions of the total stress, Reynolds stress, and viscous stress across a boundary layer ($Re_\delta = 7 \times 10^4$). Note 30-fold change in abscissa scale at $y/\delta = 0.05$. Based on data in Refs. [223, 337].

Figure 3.5: Tritton (1988), p.337

Another approach is to estimate the parameters u_*, z_0 and d through a log-law fitting of the measured velocity profile. It is worth noting that the fitting has to be applied to the velocity profile of the inertial region and it is fundamentally wrong to extrapolate the logarithmic profile into the roughness sublayer, where no theoretical basis supports the validity of the logarithmic law. It is indeed important to evaluate correctly the depth of the inertial layer to avoid errors in the estimation of the parameters. Another reason for data uncertainty is the mathematical difficulty encountered when varying u_*, z_0 and d to obtain the best curve fit: the influence of these variables tend to be correlated, so that several combinations can give the same quality of fit to the data.

Our own approach consisted in estimating the friction velocity from the Reynolds stress profile: a constant-stress region has been detected for $2 - 3H < z < 5H$ that corresponded to a value $u_* = 0.21 m/s$. Then, we calculated the derivative of the logarithmic law

$$\frac{\bar{u}}{u_*} = \frac{1}{k}\, ln(z-d) - \frac{1}{k}\, ln(z_0) \tag{3.3}$$

$$\frac{\partial \bar{u}}{\partial z} = \frac{u_*}{k} \cdot \frac{1}{z-d} \tag{3.4}$$

Assuming the new variables $y = \bar{u}/u_*$ and $x = ln(z-d)$, the velocity profile becomes a straight line and the correct value of d should provide the theoretical slope $1/k = 2.5$ in the inertial layer. Unfortunately, an unsatisfactory value of the Von-Karman constant k has been obtained through a linear fit and this might be related to an incorrect evaluation of u_*. Several authors observed that the Reynolds stress may be underestimated, so we assumed a new value of the friction velocity, $u_* = 0.23$ m/s, that provides the right value of k for $d = 55$

mm[1]. We will explain below the reasons that could justify the Reynolds stress underestimation. We calculated the vertical gradient of the mean velocity profile and we compared it to the theoretical behaviour (Equation 3.4) to point out the extension of the inertial layer. The Figure 3.6-a suggests the extent of the inertial layer lies roughly between $z \simeq 2.5H$ and $z \simeq 4H$, that is $0.1\delta \leq Z = z - d \leq 0.25\delta$. The lower limit of the inertial sublayer, $z = 2.5H$, should matches the upper limit of the roughness sublayer, which has been derived equal to $z_* = 2 - 3H$, and it is encouraging it is verified.

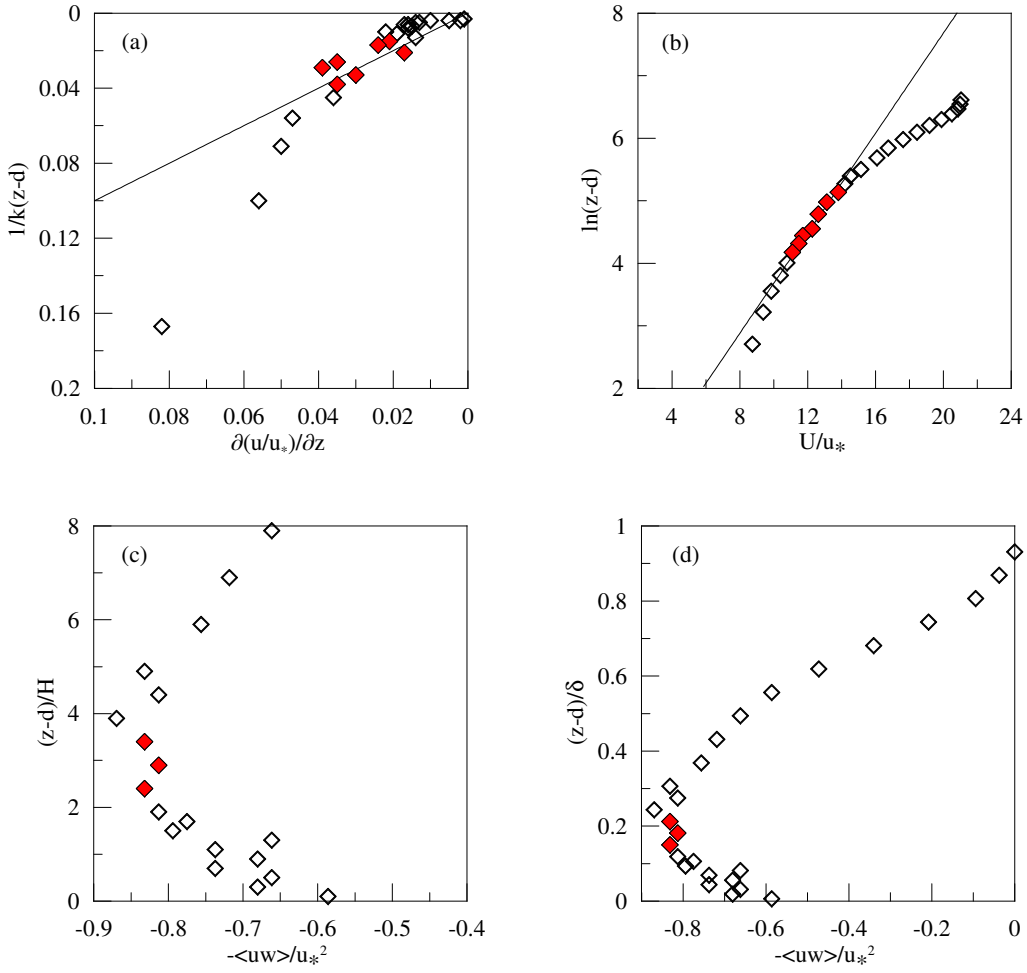

Figure 3.6: (a) Slope of the mean velocity profile; (b) Logarithmic law profile; (c) Reynolds stress profile close to the ground (d) Reynolds stress profile in the overall layer. The full symbols indicate the extension of the inertial layer defined as the logarithmic law region (a-b) and the constant-stress layer (c-d)

In Figure 3.6-b the mean velocity profile is fitted by a logarithmic law whose aerodynamical parameters are $u_* = 0.23$ m/s and $d = 55$ mm and the one parameter fit supplies $z_0 = 0.75$ mm, which corresponds to $z_0 = 0.3$ m at full scale. The characteristic boundary layer parameters are representative of an urban boundary layer. In the Figures 3.6-c and d, the Reynolds stress profile is normalized to the friction velocity and the constant-stress region is highlighted.

In evaluating the quality of the wind tunnel boundary layer, besides the values of the aerodynamical parameters, it is important to consider the structure of the flow. At sufficiently

[1]It is not surprisingly that the displacement height is higher than the obstacle height, because screws of height $1cm$ laid over the highly-packed obstacles

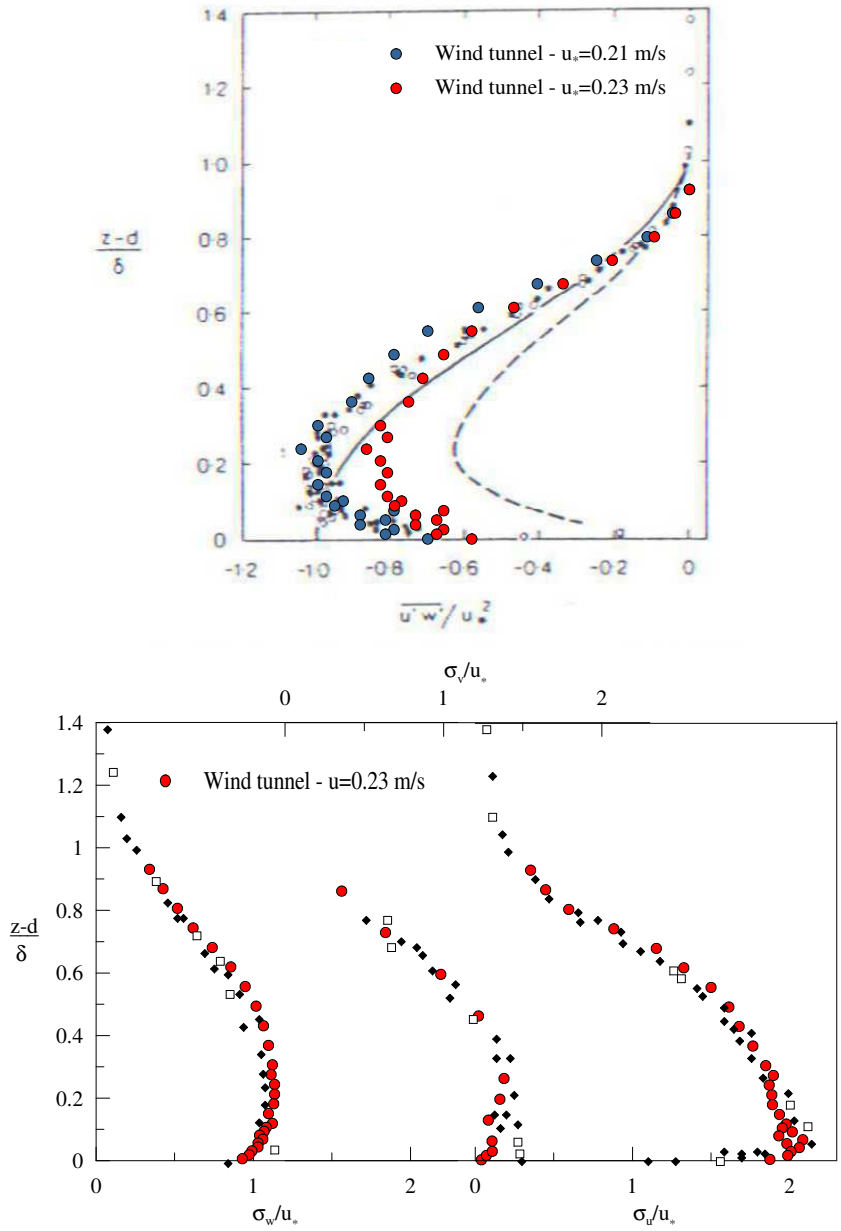

Figure 3.7: Comparison between the turbulence structure of the wind tunnel boundary layer and that by RAUPACH (1991)

high Reynolds numbers, rough-wall boundary layers have the same turbulence structure, scaling with height, boundary-layer thickness and friction velocity. The Reynolds number in our experiment is sufficiently high to compare the normalized vertical profiles of the flow variables to those of RAUPACH (1991). In Fig. 3.7 the profiles of the velocity fluctuations $\sigma_{\overline{u}}$, $\sigma_{\overline{v}}$ and $\sigma_{\overline{w}}$, non-dimensionalised by the friction velocity $u_* = 0.23$ m/s, show a very good agreement. Concerning the Reynolds stress, the profile is non-dimensionalised either by the maximum value of the Reynolds stress and by the friction velocity $u_* = 0.23$ m/s. If we assume the best estimation of the friction velocity is $u_* = 0.23$ m/s, as confirmed by the agreement of the velocity fluctuation profiles, it follows that the Reynolds stress have been underestimated or that the statement

$$-\overline{uw} = \rho \cdot u_*^2 \tag{3.5}$$

is not valid. In a recent paper, Cheng *et al.* (2007) demonstrated that the surface shear stress derived from drag measurements was about 25% larger than the Reynolds shear stress directly measured in the inertial sublayer. The 120^o X-wire data was checked by comparison with Laser Doppler Anemometer, so the observed discrepancy could not be attributed to measurement errors, but no argument was produced to justify the result. Raupach (1993) suggested that under not ideal conditions or with the x-axis of the coordinate system not in the direction of the mean wind, the vertical flux of lateral momentum can contribute to the Reynolds stress. The total stress is thus defined as the turbulent transport of horizontal momentum in the vertical direction and it is expressed as follows:

$$\tau = \rho(\overline{u'w'}^2 + \overline{v'w'}^2)^{1/2} = \rho \cdot u_*^2 \tag{3.6}$$

The contribution due to $\overline{v'w'}$ might be not negligible and cause a higher value of τ and thus of u_*. Concerning our experiment, evidences exist about the horizontal inhomogeneity of the flow related to a misalignment of the mean wind direction compared with the wind tunnel axis.

Another aspect about the Reynolds stress profile concerns the decreasing values observed as the surface approaches. Many authors explain this typical trend with a X-wire measurement error. X-wire measurements of velocity fluctuations and velocity correlations seem to be unreliable when the local turbulent intensity i_u is relatively high. Smalley (2001) and Legg (1984) suggested that X-wire measurements of velocity fluctuations are reliable if $i_u < 0.35$, while $i_u < 0.25$ is necessary for faithful measurements of Reynolds stress. Tutu and Chevray (1975) analyzed the possible sources of error in the X-wire measurements and estimated their effect on the values of $\overline{u}$ and $-\overline{uw}^{1/2}$, as shown in the Figure 3.8. We overlap to the figure the vertical profile of the turbulence intensity to estimate the error we make in this experiments. The region of the Reynolds stress decrease corresponds to an estimated error $E \sim 10\%$ that can partially explain the decrease.

Searching for a different explanation from the X-wire unreliability, some other authors speculated that the observed decrease of $-\overline{uw}$ near the wall could be due to the contribution from the dispersive stresses, related to the departures of the time-averaged velocity from the spatially averaged quantity. However, Raupach (1991) showed that the dispersive stresses are negligible in the region above the top of the canopy compared to the Reynolds stresses, while may be significant near the bottom of the canopy. The dispersive stresses do not give reason for the decreasing of the Reynolds stress in the roughness sublayer.

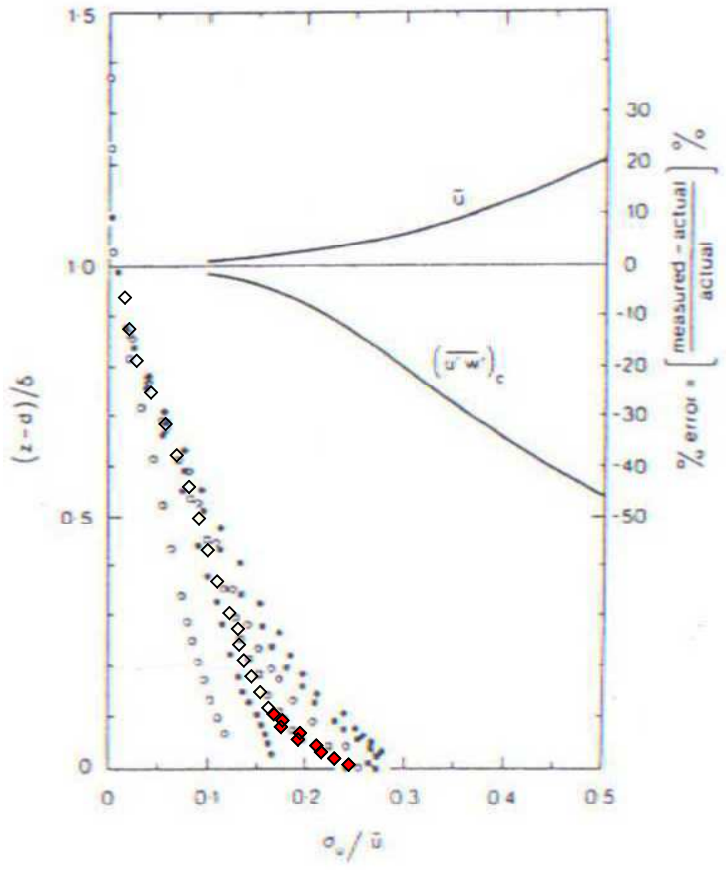

Figure 3.8: Evaluation of the X-wire measurement errors by Tutu et al. together with the turbulence intensity profile

3.2 Flow within the array

The aim of our study is to investigate the overall behaviour of the plume throughout arrays that represent simplified urban neighbourhood. Although the main interest is to evaluate the dispersion of pollutants, an important tool for understanding the mixing and transport of pollutants is to study the current flow dynamics within the canopy. The usual approach is to represent the dynamical effects of urban areas through an urban canopy model that estimates a spatially averaged wind velocity (Coceal, 2004; MacDonald, 2000). The strength of this approach is that it avoids the huge cost of resolving the flow around each individual building but it captures the variation in the mean wind as the density of the buildings changes. The urban canopy model resolves neighbourhood variations in mixing and transport, but in the present study we are interested in resolving the variations at the street scale. Numerical simulations have been conducted to compute the flow around the obstacles and were validated by means of experimental measurements. The results will be useful to understand the physical processes that control the mixing and transport of pollutants within the urban areas. The geometrical periodicity of the array allowed to focus on the flow within the two main elements of the neighbourhood, the street and the intersection.

3.2.1 Influence of the street aspect ratio

Initially, three different configurations were studied for an external wind direction perpendicular to the axis of the street. Although it is a very academic case, rarely observed in real world, it is useful to derive the main flow characteristics. The primary coordinate system is solidal to the neighborhood: the y-axis indicates the axis of the street and the x-axis the incident wind direction. The mean velocity is decomposed in the component parallel to the street axis U_{par}, in the component perpendicular to the street axis, U_{perp}, and in the vertical component W. As shown in Figure 3.9, the configurations differed in the street aspect ratio, that is the spacing to height ratio: configuration 1 was characterised by $S_x = S_y = H$, configuration 2 by $S_x = 2H$ and $S_y = H$, configuration 3 by $S_x = H$ and $S_y = 2H$.

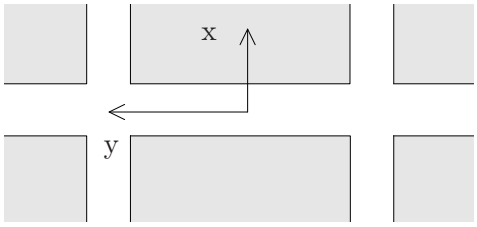

a) Configuration 1, $S_x = S_y = H$

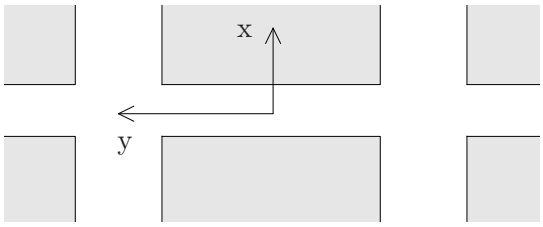

b) Configuration 2, $S_x = 2H$ and $S_y = H$

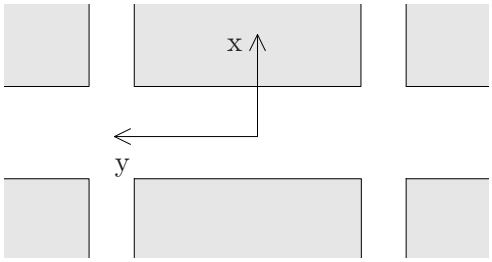

c) Configuration 3, $S_x = H$ and $S_y = 2H$

Figure 3.9: Main elements of the investigated array configurations: street and intersection

Direct flow field measurements were performed by the Laser Doppler Anemometer. The experimental data were not exhaustive and did not allow to determinate the full three dimensional

wind pattern, but they were useful to validate numerical simulations.

The description of the results will concern first the analysis of the flow field within the street perpendicular to the wind direction and then that of the flow into the street parallel to the wind direction. How the presence of the intersection affects the flow dynamics will be discussed.

Conversely to many studies that focus on the flow dynamics within street-canyon of infinite length, the studied street is characterised by a finite length $L = 5H$ and is connected at the ends to an intersection. The street of finite length presents three-dimensional aspects and it will be referred to as *3D street*. The street of infinite length will be referred to as *2D street*, since the flow behaviour should be independent on the coordinate parallel to the street axis. It is possible to extrapolate the influence of the intersection on the flow within the adjacent street by comparing the velocity profile within the *3D street* to the typical profile that occurs within the *2D street*. We will discuss experimental measurements and numerical simulations of the flow field within the *3D street* in configuration 1, which is characterised by equal width and height.

Initially, we recall the typical vertical profile of U_{perp} within a square street-canyon of infinite length representing a *2D street*. The value of the street height to width ratio, i.e. $H/S = 1$, makes a skimming flow regime occur. The obstacles are so densely packed that the external flow skims over the obstacles and a recirculating region is driven within the street-canyon. Figure 3.10 shows three different profiles of U_{perp}: two experimental profiles, one measured by Soulhac (2000) and the other by Salizzoni (2005), and a numerical profile calculated by Fluent. The wind tunnel experiments were conducted in different conditions, but a quite good agreement is reached by suitably non-dimensionalizing the velocity. Apparently, the friction velocity seem to be a better scaling (Fig. 3.10-a) rather than the velocity at roof height (Fig. 3.10-b). The fact that the non-dimensionalized experimental profiles are quite similar even if the boundary conditions are different seems to suggest that the flow field within the cavity is not decoupled by the external flow but depends on the turbulence characteristics, which are represented by the friction velocity. The numerical simulation well describe the mean velocity profile within the cavity.

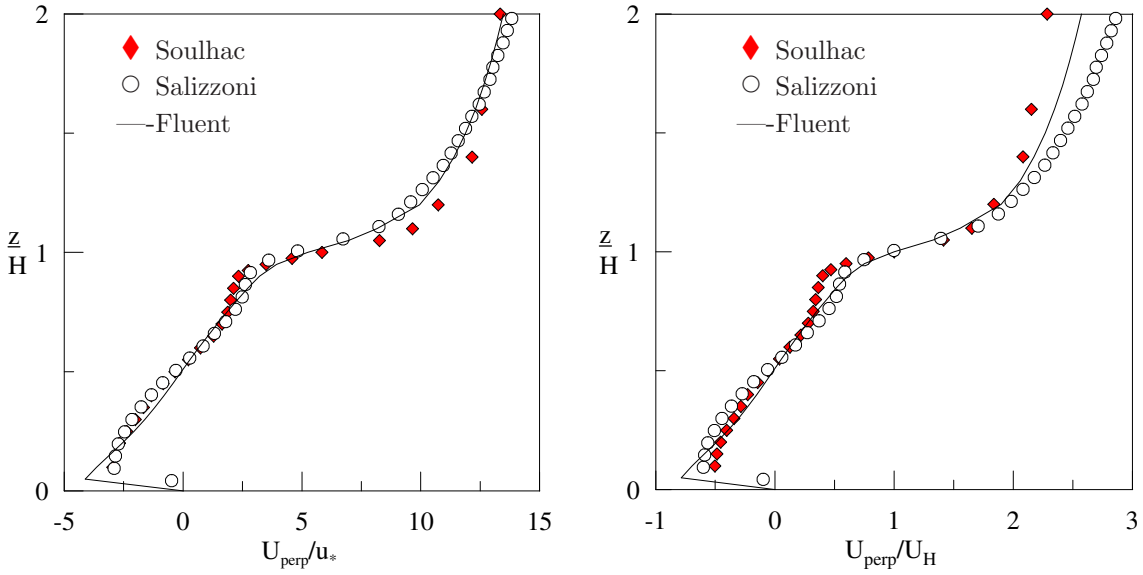

Figure 3.10: Vertical profiles of U_{perp} within a street-canyon

The typical recirculation motion occurring within the street-canyon is highlighted by displaying in Figure 3.11-a the vertical profile $U_{perp}(z)$ at the center of the street, i.e. $x = 0$, and the longitudinal profile $W(x)$ at z=H/2. In Figure 3.11-b the vector field is represented. A single

vortex occurs inside the square cavity, whose center is approximately in the center of the cavity. The profiles are non-dimensionalized by the friction velocity u_*, but it does not seem the best scaling for the W profile. Perhaps, an internal characteristic scale should have been searched, such the rotational velocity of the vortex as suggested by Soulhac (2000). The recirculating motion within the street-canyon is driven by the external flow and depends not only on the external flow conditions but also on the street aspect ratio and the wall roughness. The difference between the experimental profiles of the vertical velocity W may be due to a dissimilarity in the wall roughness value. Nevertheless, this is a very sensitive argument, accounting for the turbulent aspects as well as for the mean values, and is not the matter of our study. Salizzoni (2005) conducted an interesting wind tunnel study to evaluate how different conditions within and outside the canopy determine the velocity field within the canopy and to find appropriate velocity and length scales that characterise the mass exchange between the recirculating region and the external flow.

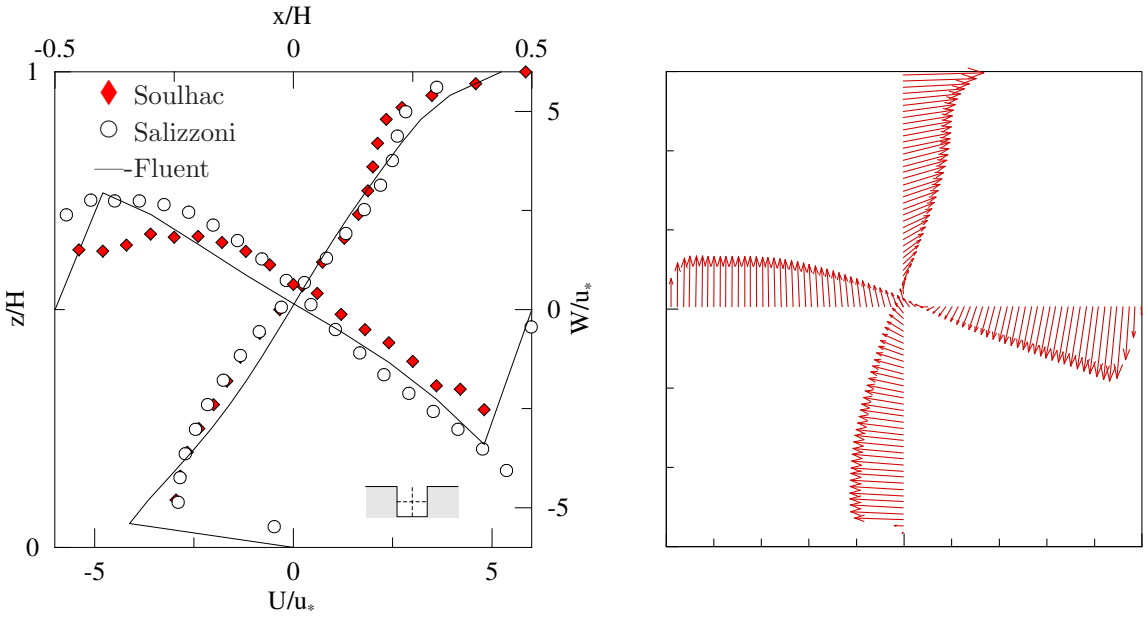

Figure 3.11: Recirculating motion within the street-canyon: velocity profiles and vector field

Once the flow field within a *2D street* of aspect ratio $S/H = 1$ has been described for a perpendicular external wind, we investigate the flow field within a *3D street* of aspect ratios $S = H$ and length $L = 5H$ by enlightening in what way it is modified by the presence of the intersection. The origin of the coordinate system is assumed to be the street center so that $y/H = 2.5$ identifies the end of the street. The velocity profiles have been performed at different positions along the axis of the street, i.e. y/H =0, 0.8, 1.6, 2.2, 2.4; the velocity component U_{perp} is non-dimensionalized by the velocity at roof level $U_H = U_{perp}$(z=H). Figures 3.12 a-d show both the experimental and the numerical results. It is worth noting that the typical $2D$ recirculating vortex persists along the street up to $y = 2.4H$, even if it is deformed approaching the intersection. At $y = 2.4H$, the perturbation due to the presence of the intersection becomes dominating and the across-street recirculating motion disappears. The velocity profiles describing the recirculating vortex do not superimpose each other but change along the street. This means that the perturbations originated by the presence of the intersection do not make the flow achieve an equilibrium state, introducing an important three-dimensional aspect. The numerical simulations well describe the mean flow field, ensuring that the numerical approach is an useful tool in analysing the mean flow field in a complex geometry.

The flow dynamics in a *3D street* is more complex than the flow dynamics in a *2D street*

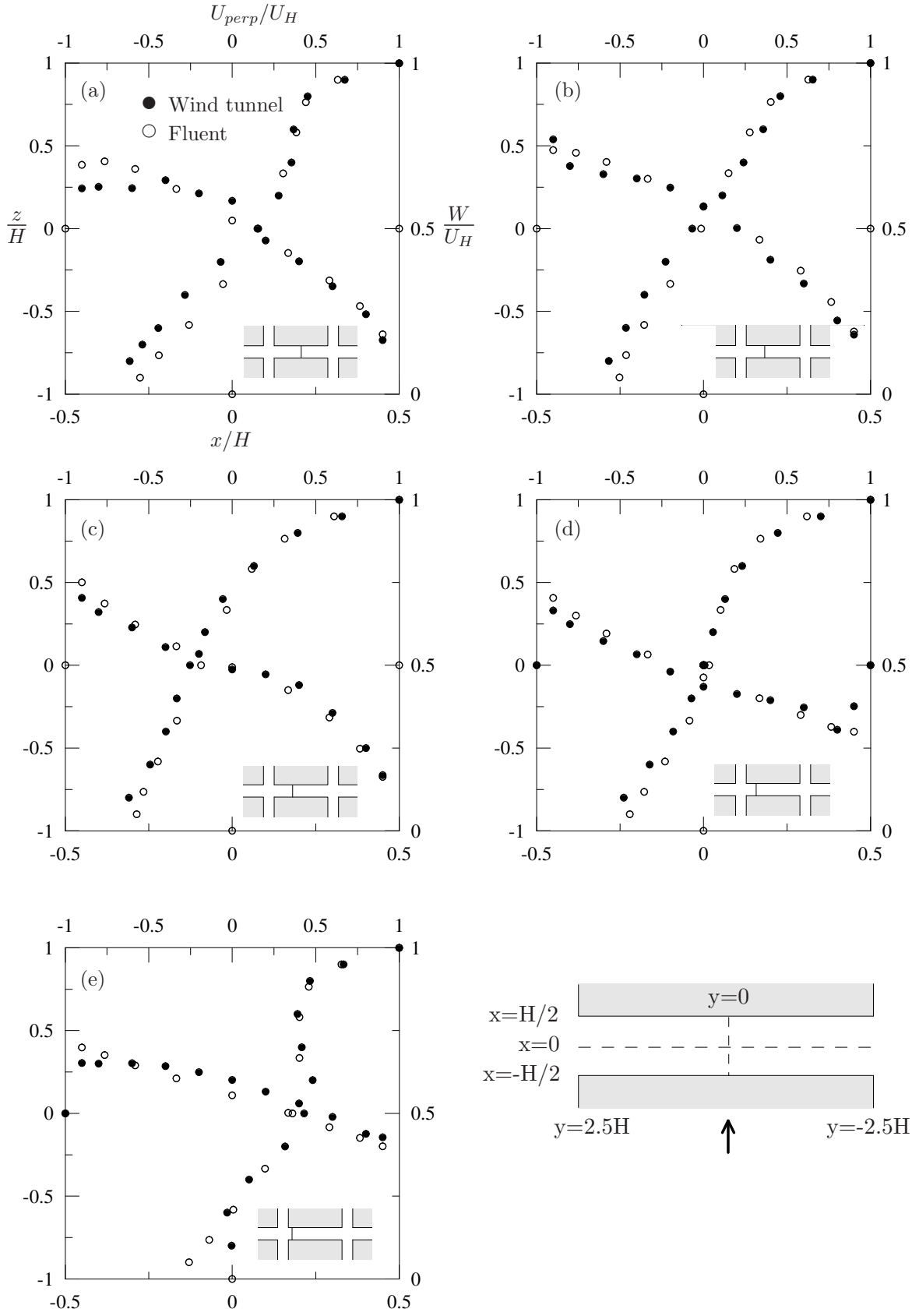

Figure 3.12: Experimental and numerical mean velocity profiles at different sections: (a) y/H=0; (b) y/H=0.8; (c) y/H=1.6; (d) y/H=2.2; (e) y/H=2.4.

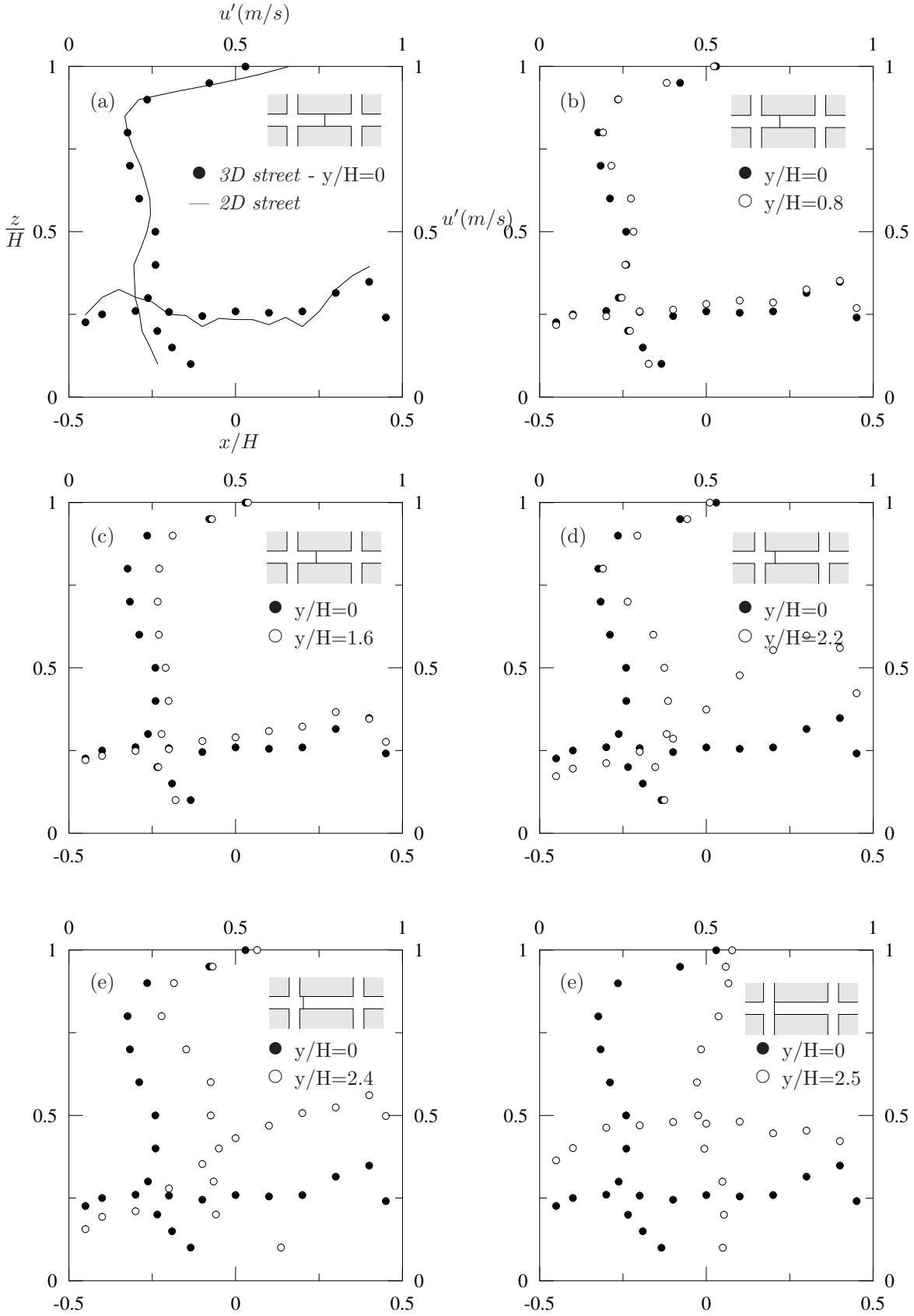

Figure 3.13: Experimental fluctuating velocity profiles. The profile at the center of the 3D street y/H=0 is compared to the profile within a 2D street (a) and to the profiles at different sections of the 3D street: (b) y/H=0.8; (c) y/H=1.6; (d) y/H=2.2; (e) y/H=2.4; (f) y/H=2.5

.

and can be thought as the result of two driving flows:

- the external flow that induces the conventional across-street recirculation vortex;
- the flow in the intersection that causes a vertical axis vortex close to the intersection.

The hypothesized flow dynamics is supported by the analysis of the fluctuating component u'. Figure 3.13 shows the measured profiles of u' at different position along the axis of the street. In Figure 3.13-a the profile at the center of the $3D$ street is compared to the profile within a $2D$ street-canyon and both presents a similar behaviour. The intensification of the velocity fluctuation at the interface between the street and the external flow, i.e. $z/H \sim 1$, points out the presence of a shear layer and thus of a driving flow. In the next figures, the u' profiles at different sections of the street, i.e. at $y/H = 0, 0.8, 1.6, 2.2, 2.4, 2.5$, are compared to the profile at the center to extrapolate the influence of the intersection. It is worth noting that the profiles begin to be altered at $y = 1.6H$, that is at a distance $\sim H$ from the interface. At the interface, i.e. $y = 2.5H$, the higher and constant values of the fluctuating component indicate the presence of a shear layer, as supposed.

Now we compute numerically the flow streamlines passing through appropriate rakes in order to analyse the vortical structure within the street. Two rakes were placed along the x-axis at the interface with the intersection at $z = H/2$ (rake A) and in the middle of the street at $z = H/2$ (rake B); a vertical rake (rake C) was placed at the interface between the street and the intersection at $x = 0$ and a horizontal one (rake D) along the y-axis at $z = H/2$. The flow streamlines passing through the rakes are projected on the x-y plane in Figure 3.14, while a three dimensional view is adopted in Figure 3.15. The vertical axis vortex occurs close to the intersection and interacts with the external wind driven vortex to form a single eddy, which extents for $y \sim H$. Then it evolves in an across-street recirculation vortex, whose horizontal axis becomes parallel to the street axis at $y \sim 1.5H$, when the perturbations due to the presence of the intersection are weakening. The transitional eddy close to the intersection is the result of the interaction between two driven flows, or in other terms it originates within a cavity characterised by two free surfaces.

It could be interesting to evaluate if and at what distance from the intersection the flow is no more perturbed and can be assumed two-dimensional. This is a parametrical study and the key parameters to investigate would be the length of the street, the aspect ratio and the size of the intersection, i.e.:

$$f = f(L/H, S_y/H, S_x/H) \tag{3.7}$$

Such an in-deep study is not the aim of our study and we restricted the investigation to explore the flow field within two other *3D streets* of the same length $L = 5H$. Configuration 2 preserved the aspect ratio of the street $S_y = H$ but varied the size of the intersection, while configuration 3 preserved the size of the intersection but varied the street aspect ratio $S_y = H/2$. The study was conducted by means of numerical simulations and the flow streamlines have been computed in order to understand the main flow characteristics. In Figure 3.16 the streamlines passing through the rakes A, B, C and D refer to configuration 2, while Figure 3.17 supplies a three dimensional view. It is worth noting that the main flow characteristics are quite similar within configuration 1 and configuration 2 and this means that the larger width of the crossing street S_x has a negligible influence on the flow within the street. A vertical axis vortex close to the intersection is driven by the flow within the intersection and interacts with the across-street recirculation vortex driven by the external flow. The resulting eddy evolves along the street and at a certain distance from the intersection becomes a stable recirculation vortex, typical of the skimming flow regime. Concerning the exchange mechanisms for a skimming flow regime,

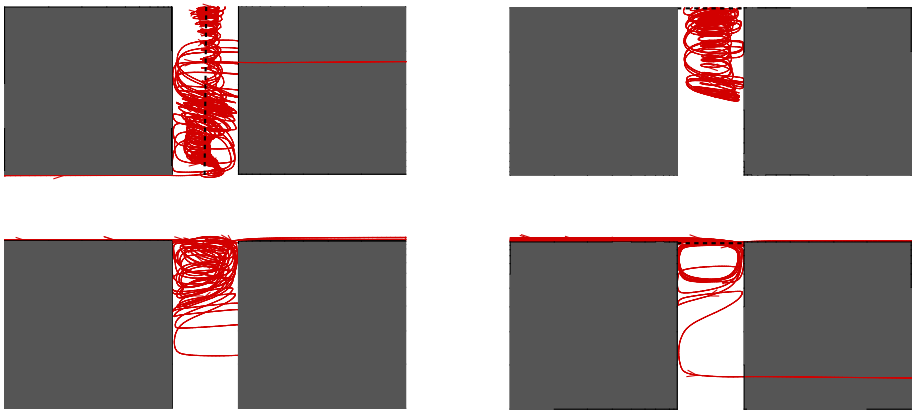

Figure 3.14: Projection of the flow streamlines passing through the rakes (dashed lines) on the x-y plane - configuration 1.

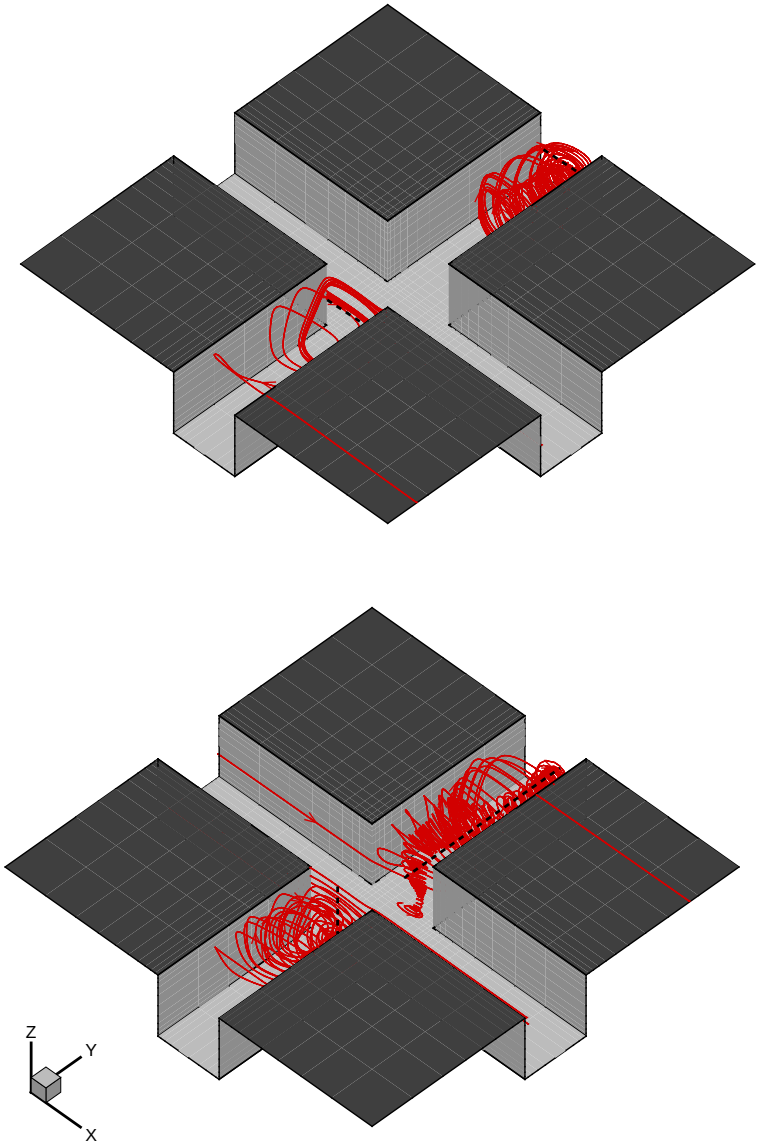

Figure 3.15: Flow streamlines passing through the rakes (dashed lines) within the 3D street - configuration 1.

the external flow appears to skim over the top of the obstacles and is relatively decoupled from the flow within the street reducing the interaction between external flow and recirculating regions. Analogously, we can suppose that the flow within the intersection is decoupled from the flow within the street and the exchange phenomena are suppressed. The key parameter that determines the structure of the flow is certainly the aspect ratio of the street, i.e. S_y, because it fixes both the size of the interface between the street and the intersection and the size of the interface between the street and the external flow. Ultimately, it sets the sizes of the exchange surfaces.

Conversely, the structure of the flow within the street in configuration 3 appears totally different. Figure 3.18 shows the flow streamlines on the x-y plane and Figure 3.19 the three-dimensional visualization. It is worth noting that the aspect ratio of the street doubled, i.e. $S_x = 2H$, and for such value a wake interference regime is supposed to take place within a street of infinite length. The wakes generated by the buildings interact and lead to the formation of complex flow patterns that are strongly coupled with the flow above. How the presence of the intersection modifies the expected flow regime? A vertical axis recirculation cell occurs close to the intersection but is confined in the upwind corner; then a strong interaction between the flow within the street and the flow within the intersection is observed as well as the expected interaction between the external flow and the flow within the street. The length of the street is too short respect to the aspect ratio to make the flow field establish and assume the characteristics similar to the wake interference flow within a two-dimensional cavity. A more complex vortical structure originates that amplifies the exchange processes. It is evident that the key parameter in determining the flow dynamics is the aspect ratio of the street perpendicular to the wind direction, S_y/H.

Numerical velocity profiles within the street of the different configurations have been compared in order to highlight the differences and the similarities. Figure 3.20 displays the vertical profile of U_{perp} and the horizontal profile of W at different sections along the street, i.e. $y/H = 0.8, 1.6, 2.2, 2.4$, while Figure 3.21 shows the profiles of U_{par} at the different sections. The flow field appears to be very similar for the streets of equal aspect ratio and the assumption that the size of the intersection does not have a significative effect is confirmed. Two different flow regimes are pointed out:

- in configuration 1 and 2, a vertical axis vortex occurs close to the intersection and evolves into a quasi two-dimensional recirculation motion;
- in configuration 3 the typical recirculating motion interacts with the mean flow coming from the intersection and forms a strongly three-dimensional vortical structures.

Regarding the exchange mechanisms between the external flow and the flow within the street, a deeper numerical investigation have been carried out and consisted in computing the streamlines through two rake lines. The rake lines were placed parallel to the street axis at roof height $z = H$, one upwind and the other downwind, i.e. $x = -H/2$ and $x = H/2$. In Figures 3.22 and 3.23, the upwind streamlines skim the square street without interacting with the flow within the street, while some downwind streamlines, especially in the center of the street, come from the street. This indicates a general decoupling of the flow but the presence of a weak mean flux directed towards the exterior, which will contribute, together with the turbulent fluxes, to the mass and momentum exchanges. Conversely, Figure 3.24 shows that the external mean flow penetrates into the cavity and interacts with the flow in the street, originating a complex mixing of vortices. More significative exchange mechanisms are expected as well as an enhanced mixing within the street.

Besides the exchange mechanisms taking place at the interface between the flow within the street and the external flow, a significative role in the dispersion phenomena is played by the

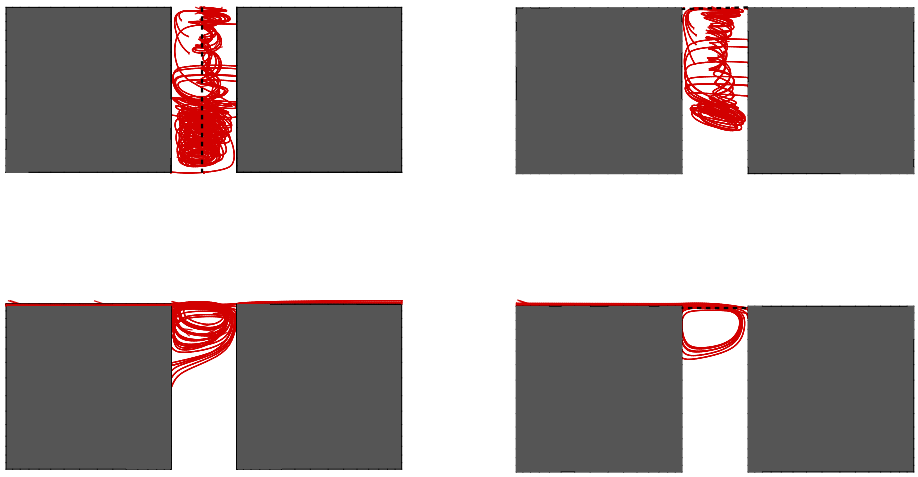

Figure 3.16: Projection of the flow streamlines passing through the rakes (dashed lines) on the x-y plane - configuration 2.

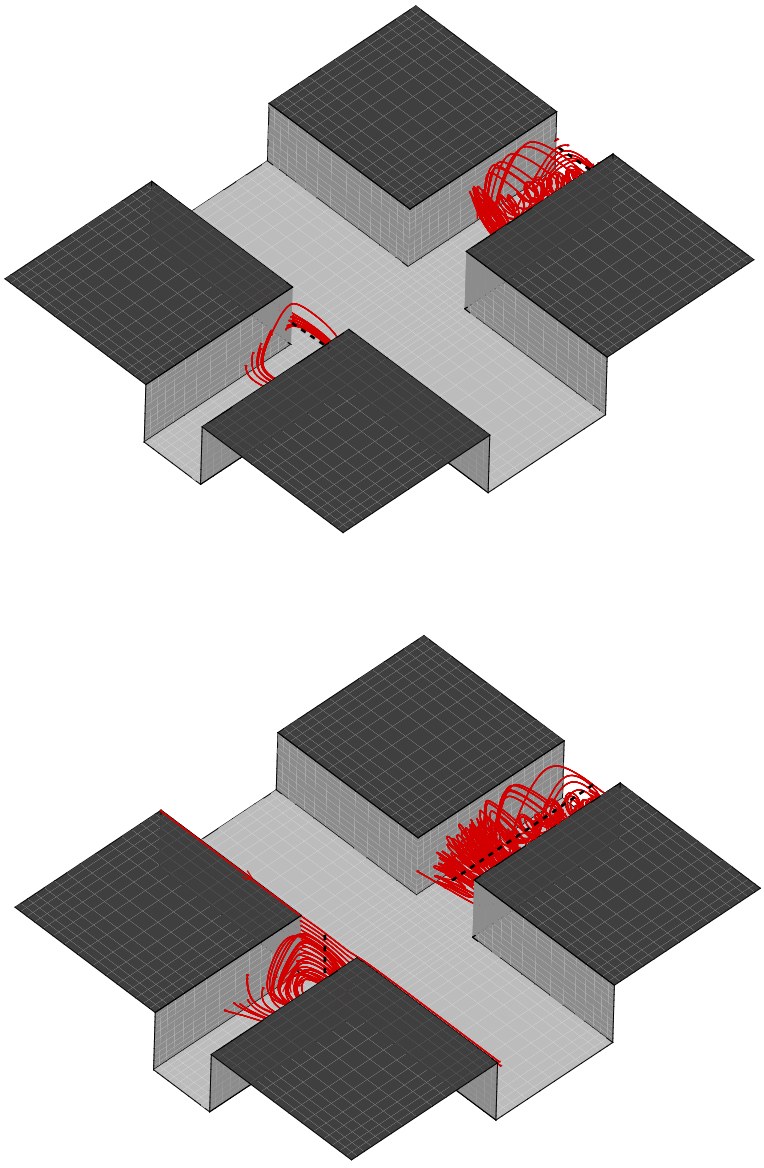

Figure 3.17: Flow streamlines passing through the rakes (dashed lines) within the 3D street - configuration 2.

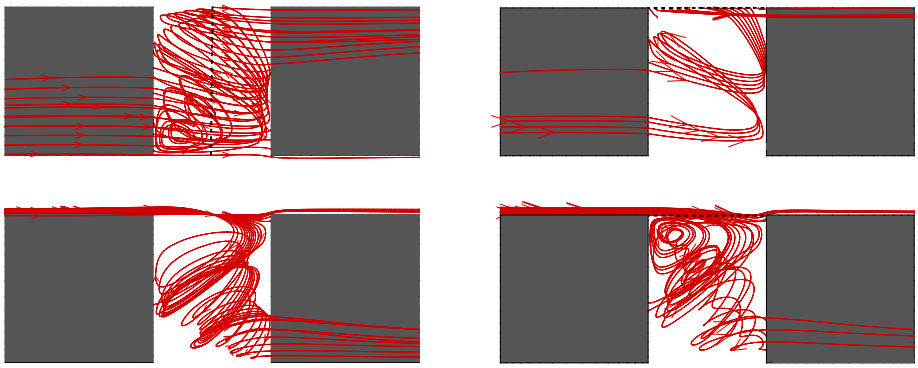

Figure 3.18: Projection of the flow streamlines passing through the rakes (dashed lines) on the x-y plane - configuration 3.

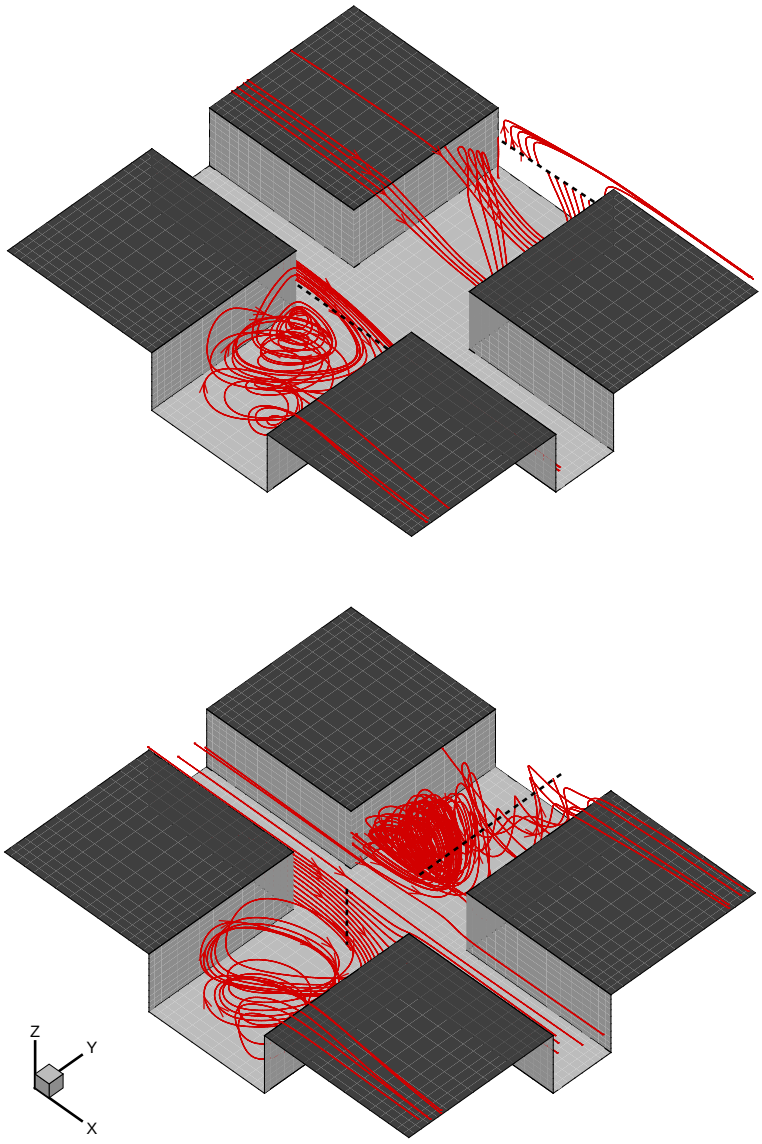

Figure 3.19: Flow streamlines passing through the rakes (dashed lines) within the 3D street - configuration 3.

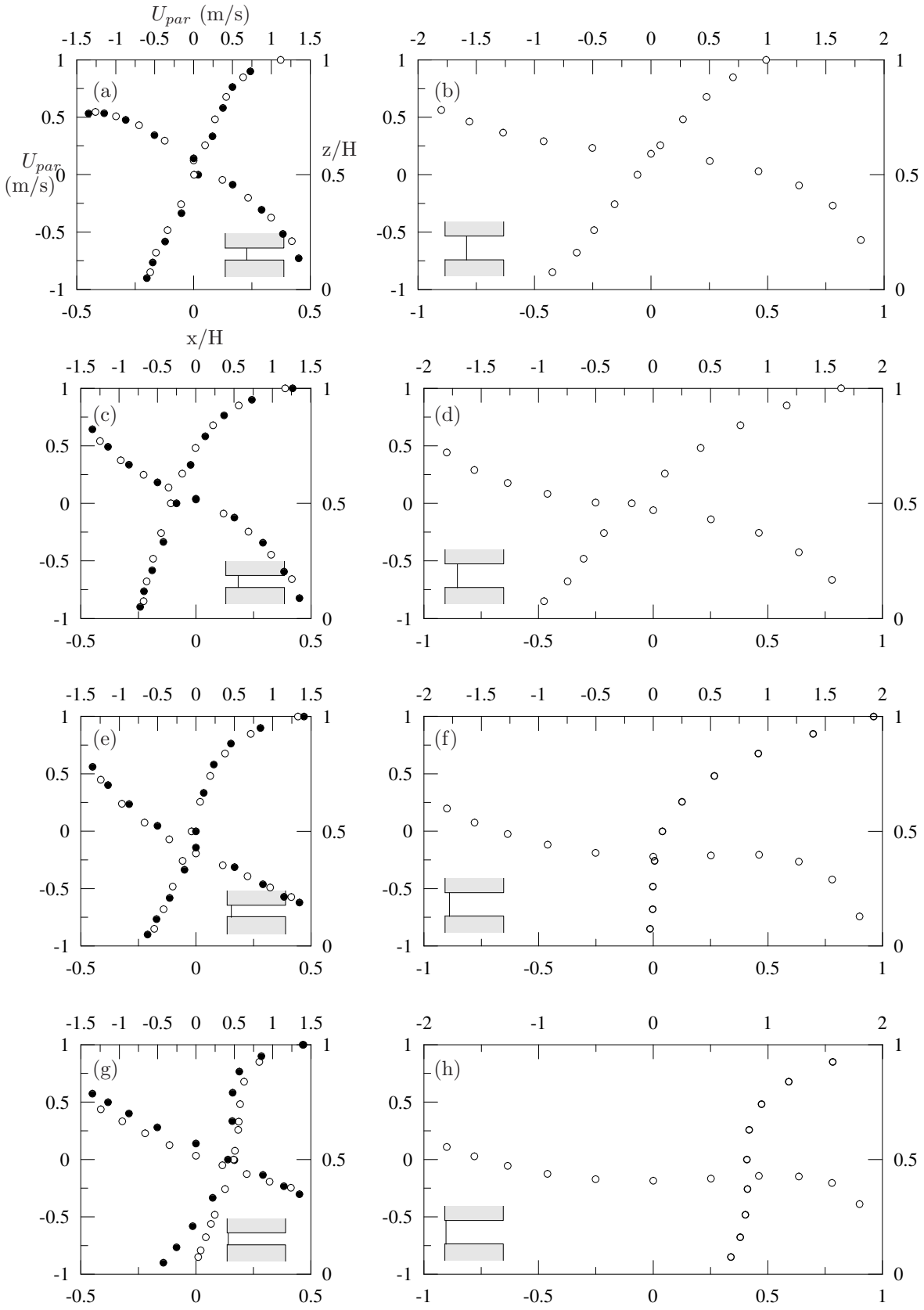

Figure 3.20: Numerical mean velocity profiles $U_{perp}(z)$ and $W(x)$ within the 3D streets. Figures on the left refer to the street $S_x/H = 1$ (• configuration 1; ∘ configuration 2), while figures on the right refer to the street $S_x/H = 2$ (∘ configuration 3). Various sections have been investigated: (a)-(b) y/H=0.8; (c)-(d) y/H=1.6; (e)-(f) y/H=2.2; (g)-(h) y/H=2.4

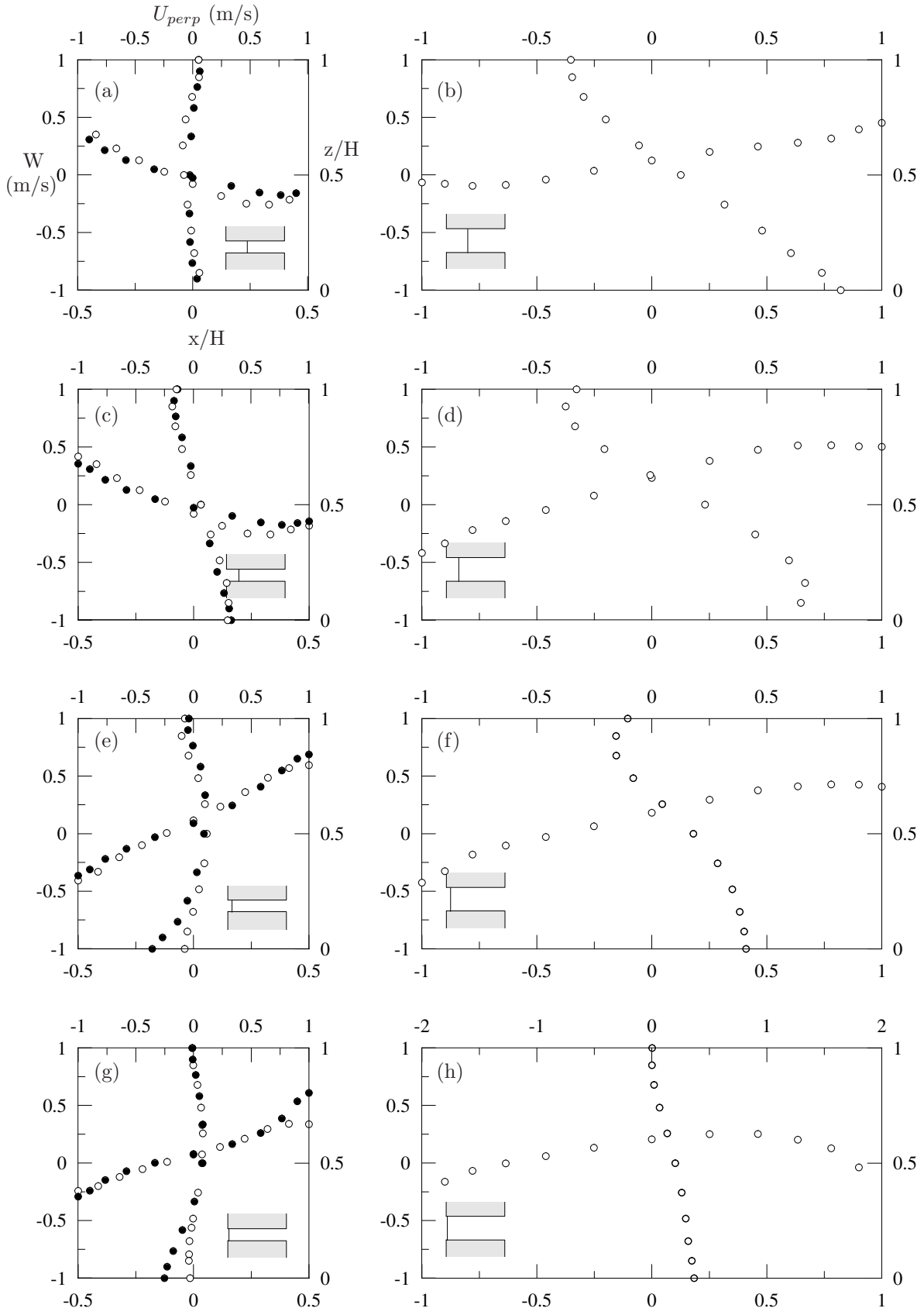

Figure 3.21: Numerical mean velocity profiles $U_{par}(z)$ and $U_{par}(x)$ within the 3D streets. Figures on the left refer to the street S_x/H=1 (• configuration 1; ∘ configuration 2), while figures on the r right refer to the street S_x/H=2 (∘ configuration 3). Various sections have been investigated: (a)-(b) y/H=0.8; (c)-(d) y/H=1.6; (e)-(f) y/H=2.2; (g)-(h) y/H=2.4.

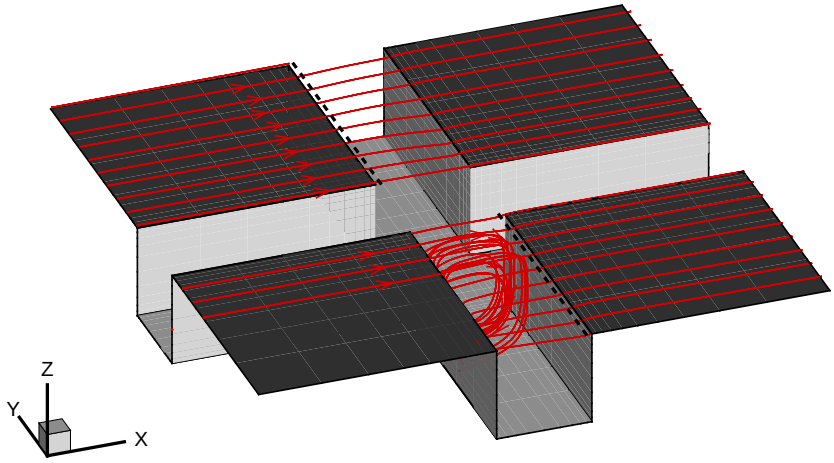

Figure 3.22: Flow streamlines passing through the rakes (dashed lines) within the 3D street - configuration 1.

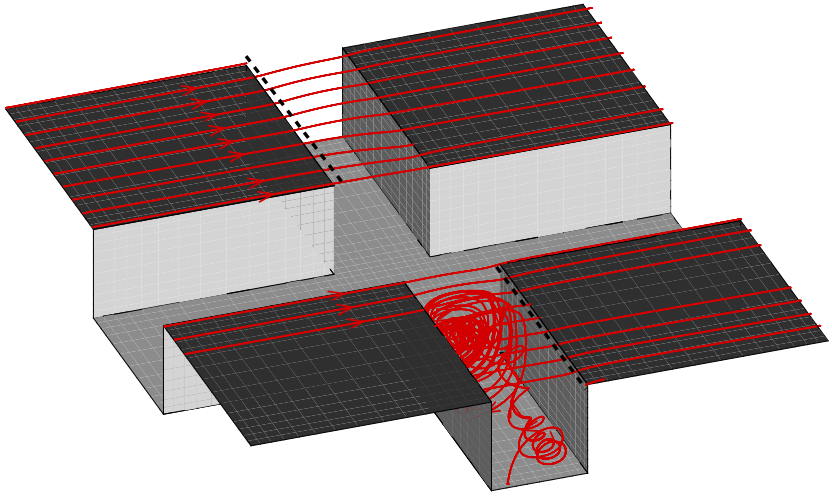

Figure 3.23: Flow streamlines passing through the rakes (dashed lines) within the 3D street - configuration 2.

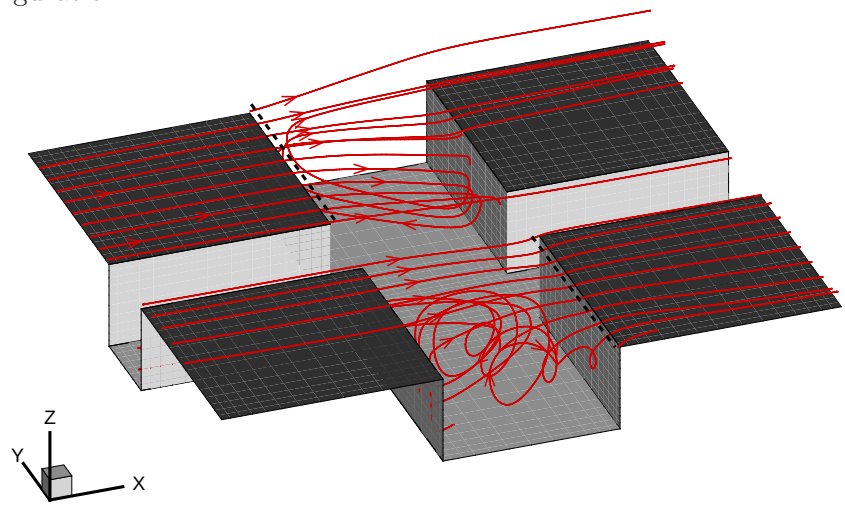

Figure 3.24: Flow streamlines passing through the rakes (dashed lines) within the 3D street - configuration 3.

intersection. In order to improve the understanding of the exchange mechanisms taking place at the interface between the intersection and the street, the flow within the intersection was investigated by means of numerical and experimental simulations.

In Figure 3.25, the numerical and experimental transversal profiles of the mean velocity are shown for the configuration 1 and 2, whose street aspect ratios are respectively $S_x = S_y = H$ and $S_x = H, S_y = 2H$. The mean velocity is decomposed in $\overline{u}$, the component of the mean velocity parallel to the x-axis, i.e. the direction of the external wind, and in $\overline{v}$, the along y-axis component, and is non-dimensionalised by the velocity at the boundary layer height U_∞. The profiles have been performed along the y-axis, at $z = H/2$ and $x = 0$, and the origin of the reference system matches the center of the intersection, $y = 0$. A strong channelling is observed within the intersection and a weak interaction with the flow within the street is suggested by the small values of $\overline{v}$ through the interface. The numerical results show a good agreement with the experimental measurements and support the use of the numerical approach to investigate the flow dynamics in complex geometries.

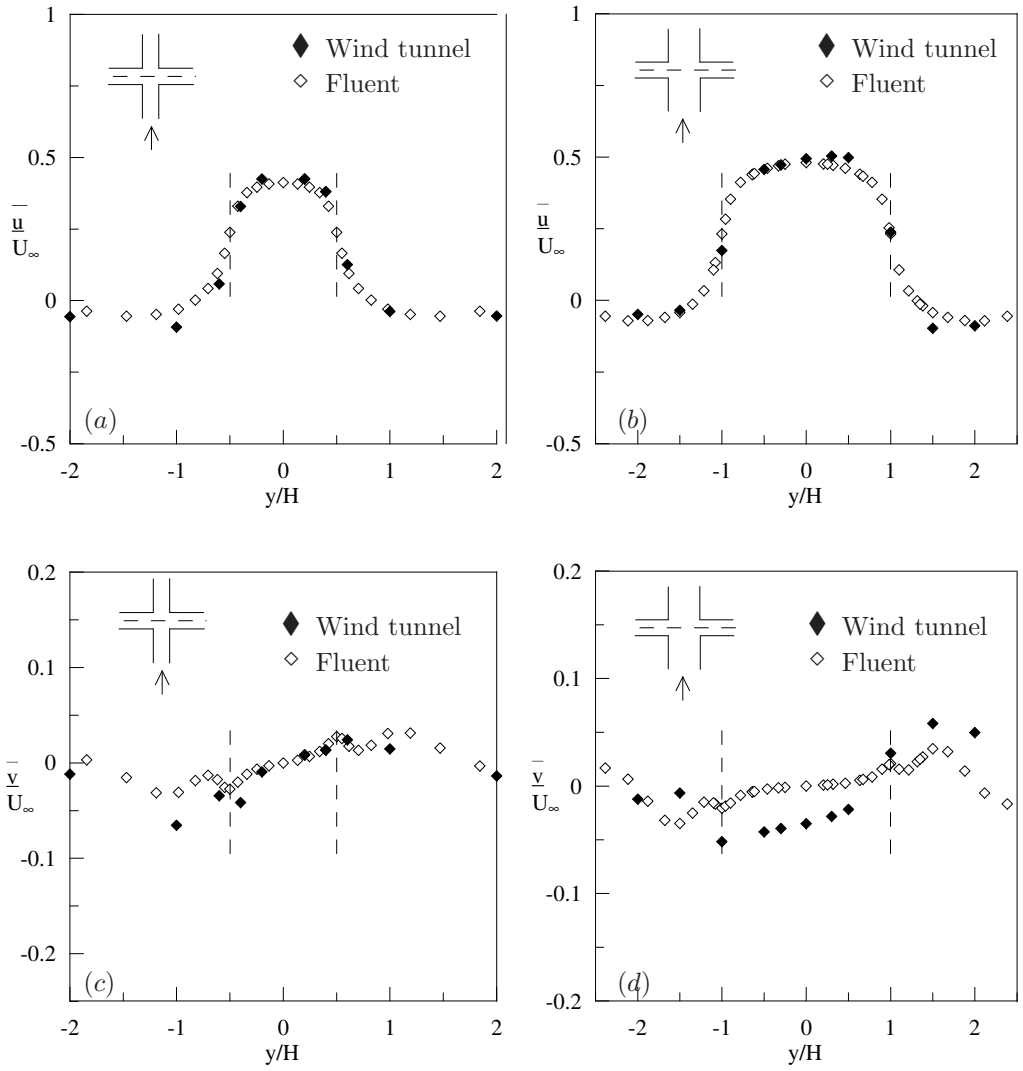

Figure 3.25: Mean velocity transversal profiles at street intersection: (a) and (c) refers to configuration 1, $S_x = S_y = H$; (b) and (d) refers to configuration 2, $S_x = HS_y = 2H$

In Figure 3.26 the numerical transversal profiles of the mean velocity within the configuration

3 are plotted. The profile $\overline{u}$ is similar to the profile of configuration 2, while the profile $\overline{v}$ points out a mean flow that penetrates into the lateral streets. The value of the aspect ratio of the lateral street is crucial:

- for $S_y = H$ a sort of skimming flow regime takes place and the interactions between the flow within the intersection and the flow within the street are reduced;
- for $S_y = 2H$ a sort of wake interference flow occurs and the interactions are enhanced.

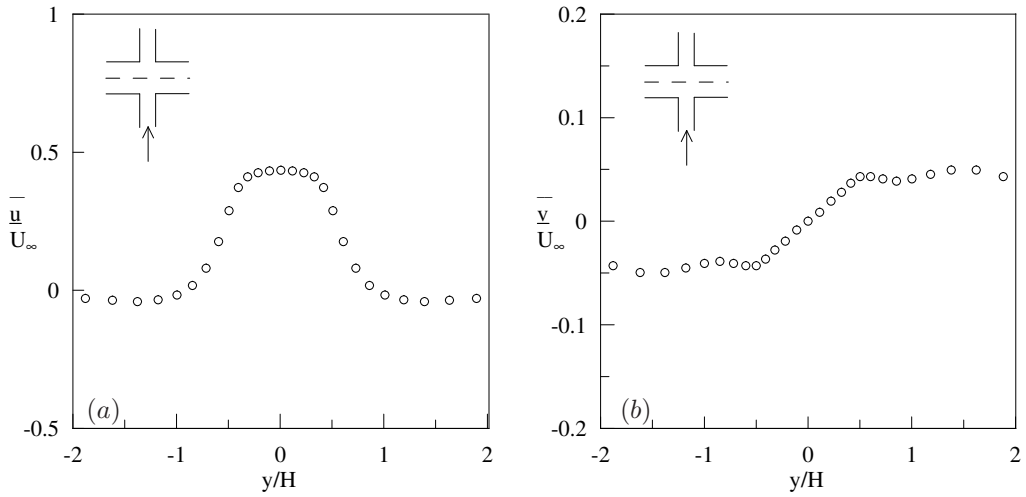

Figure 3.26: Numerical mean velocity transversal profiles at street intersection: (a) and (b) refers to configuration 3, $S_x = 2H S_y = H$

Numerical simulations were employed to visualize the main features of the flow field within different street intersections. The vector field is displayed for horizontal sections at different heights and the flow streamlines passing through rakes that are placed at the same height on the interface have been computed. The flow within the intersection preserves the direction of the external wind, even if close to the interface a weak mean flow directed towards the street is detected. The Figure 3.27 refers to configuration 1 and displays streamlines and velocity vector field on the x-y plane at the heights $z/H = 0.75, 0.7, 0.5, 0.25$. In the upper part of the intersection, i.e. $z/H \geq 0.75$, the streamlines go straight as driven by the external flow. As the bottom approaches, the velocity vectors at the interface indicate a mean motion into the street and the streamlines are captured into the vortical motion within the street. Figure 3.28 refers to configuration 2 at heights $z/H = 0.65, 0.6, 0.5, 0.25$ and shows a more limited interaction between the flow within the intersection and the flow within the street. This behaviour may be due to the larger size of the intersection that makes the flow less "aware" about the presence of the adjacent street. Figure 3.29 refers to configuration 3 at the heights $z/H = 0.85, 0.8, 0.5, 0.25$ and shows an emphasized interaction, because ever from $z/H = 0.8$ the flow penetrates into the adjacent streets. The highlighted motion appears only in the lower part of the intersection and this is due to the complex nature of the interface. In the upper part, the flow is mainly driven by the external flow, while in the lower part the presence of the intersection becomes dominant. The height that separates the lower and the upper part reveals the influence of the intersection on the flow.

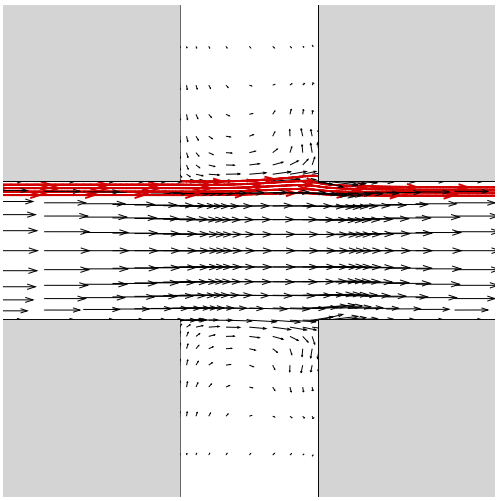

$z/H \geq 0.75$

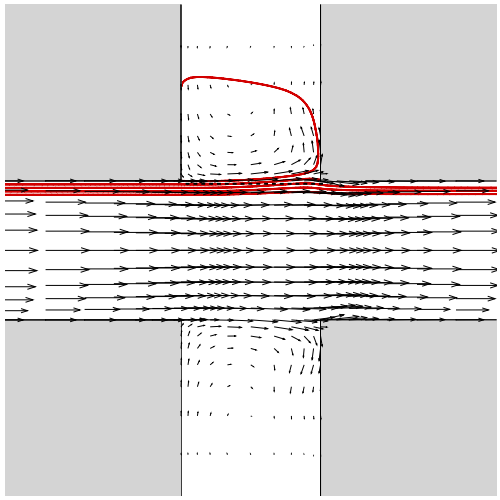

$z/H = 0.7$

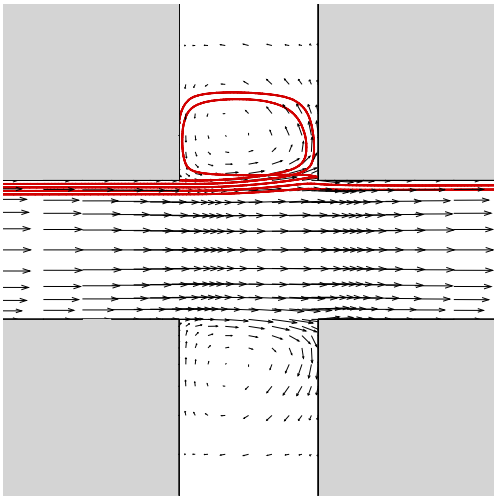

$z/H = 0.5$

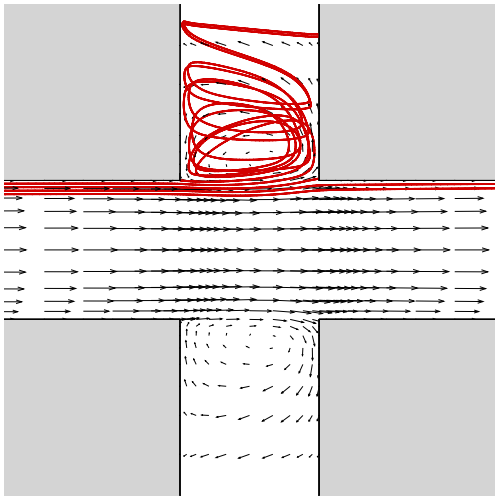

$z/H = 0.25$

Figure 3.27: Velocity vector field and streamlines at different heights - configuration 1.

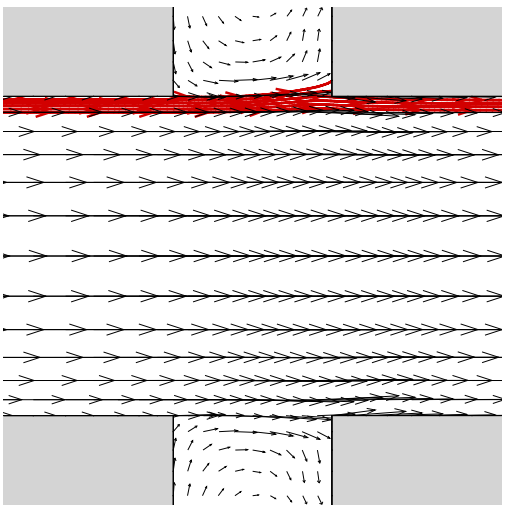

$z/H \geq 0.65$

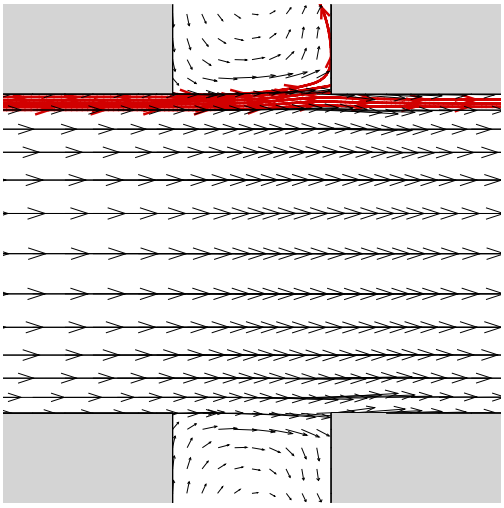

$z/H = 0.6$

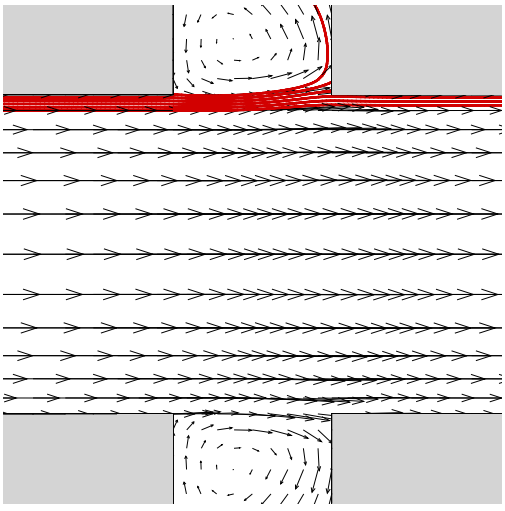

$z/H = 0.5$

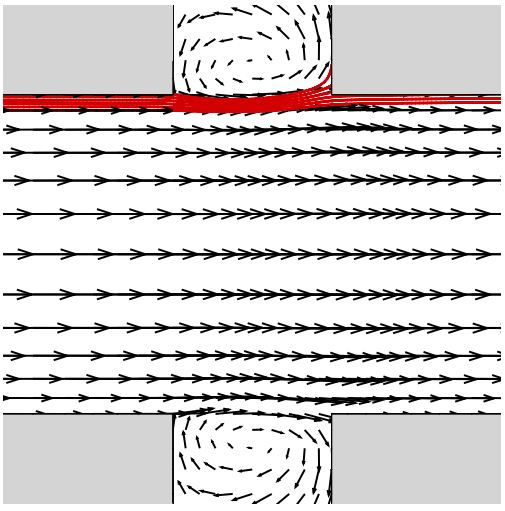

$z/H = 0.25$

Figure 3.28: Velocity vector field and streamlines at different heights - configuration 2.

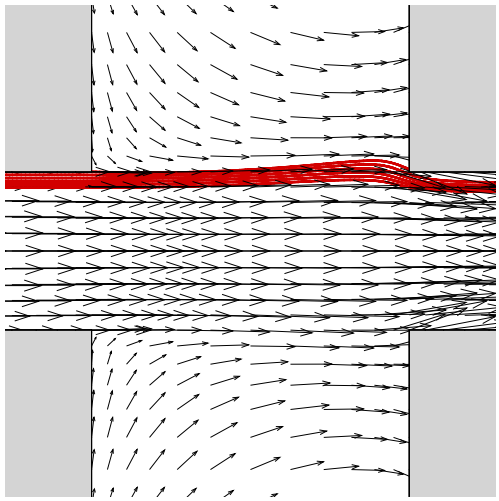

$z/H \geq 0.85$

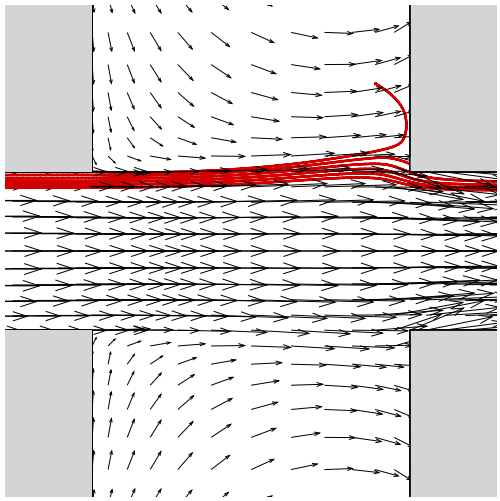

$z/H = 0.8$

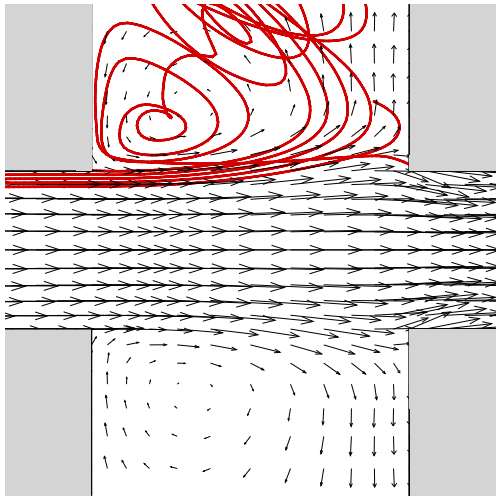

$z/H = 0.5$

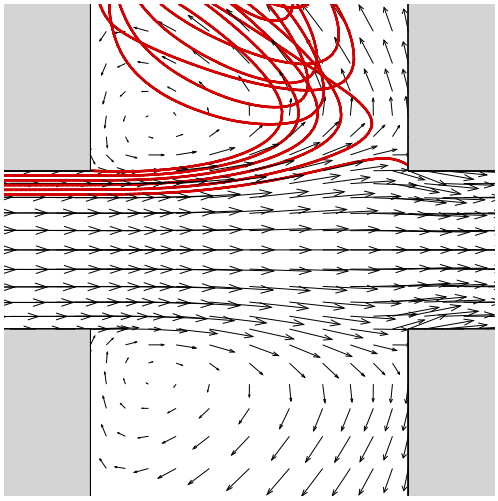

$z/H = 0.25$

Figure 3.29: Velocity vector field and streamlines at different heights - configuration 3.

3.2.2 Influence of the wind direction

In the previous section, we discussed about the influence of the geometrical layout on the flow dynamics within a canopy. The external wind was assumed parallel to the axis of the street, a very academic case rather than a common occurrence. So it would be interesting to evaluate the effect of the wind direction on the flow field within the canopy. A full analysis has already been conducted by Soulhac (2000), so we refer to his results and limit our investigation to measure mean velocity profiles along the street and within the intersection for different external wind directions, $\theta_\infty = 15^o, 30^o, 45^o, 60^o, 75^o$. The study was carried on configuration 1, which is characterised by street aspect ratios $S_x = S_y = H$, as shown in Figure 3.30.

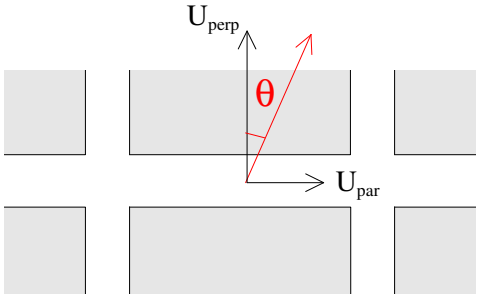

Figure 3.30:

The flow field in an infinite street for any wind direction is characterised by an helicoidal motion (Soulhac *et al.*, 2007; Dobre *et al.*, 2005), due to the superposition of an across-street recirculation vortex and an along-street channelling. The Figure 3.31 displays the hypothetical diagram of the mean flow field, obtained by CFD calculations.

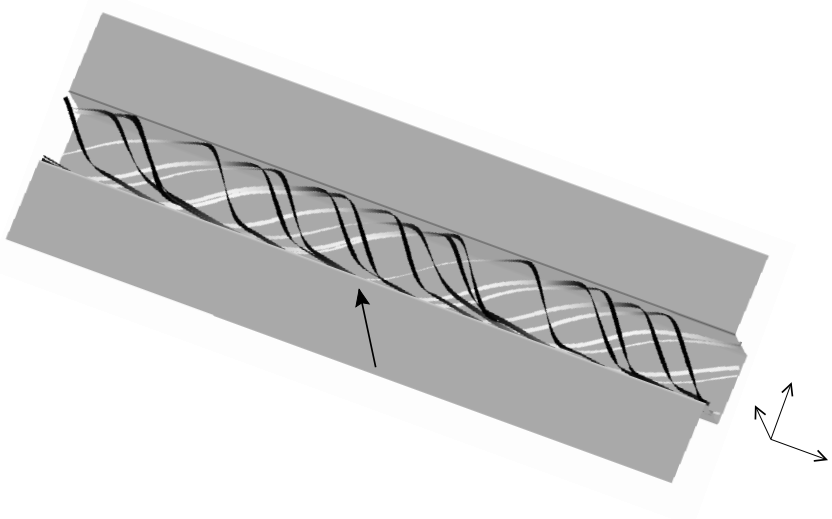

Figure 3.31: Helicoidal motion within a street of infinite length for any wind direction

Soulhac (2007) supposed a decoupling between transversal and longitudinal components and the mean velocity U_{street} through the street was calculated as:

$$U_{street} \propto U_{\infty} \cos(\theta_{\infty}) \tag{3.8}$$

where U_{∞} is the mean velocity at the boundary height and θ is the external wind direction.

What is changing in a street of finite length? Are the vortical structures preserved or they evolve? In Figures 3.32 and 3.33, experimental profiles of the mean velocity components, respectively U_{perp} and U_{par}, are plotted for different wind directions. For each wind direction the vertical profile performed at the center of the street, i.e. $y = 0$ and $x = 0$, was compared to the profiles performed at the ends of the street, i.e. $y = -2.4H$ and $y = 2.4H$ at $x = 0$, in order to investigate the influence of the intersection on the flow field. The Figure 3.32 suggests that an across-street recirculation vortex occurs far from the edges for angles $\theta_{\infty} = 0^o$ to 60^o, while it disappears for $\theta_{\infty} = 75^o$. It is evident the asymmetric dynamical configuration at the two ends of the street: at the left edge of the street, the positive values of U_{perp} indicate that a mean flow is penetrating into the street, while at the right edge, a vortical structure occurs, except for $\theta_{\infty} = 75^o$. Even if the flow dynamics is very complex, especially because of the presence of the intersection, a recirculating motion has been detected analogously to the the street of infinite length. The along-street channelling is pointed out by the positive values of the velocity longitudinal component U_{par}: in Figure 3.33 the vertical profiles at different positions along the street axis are shown and indicate that the presence of the intersection strongly affects the flow dynamics. In Figure 3.34, we represent the experimental vertical profiles of the angle that the velocity vector forms with the street axis, indicated as θ_{street}, at the center of the street for different values of θ_{∞}. Except for $\theta_{\infty} = 75^o$, the profiles indicate a helicoidal motion.

Besides the vertical profiles, we plot in Figure 3.35 the profiles of U_{perp} and U_{par} which have been performed along the axis of the street at $z = H/2$ for the external wind directions equal to $\theta_{\infty} = 0^o, 15^o, 30^o, 45^o, 60^o$.

It is a very hard task to verify if the channelling motion is related to the along-street component of the mean velocity, because the data lacking does not allow determining an exact value of the mean velocity through the street U_{street}. Although U_{par} varies both with z and with y, we roughly estimated the mean velocity through the street by calculating the average of the values U_{par} along the street at $z = H/2$:

$$U_{street} \simeq \int_{-2.5H}^{2.5H} U_{par}(y, x = 0, z = H/2)dy$$

The calculated U_{street} is compared to the theoretical value within a street of infinite length (Equation 3.8) in Figure 3.36 in order to evaluate the effect of the intersection on the mean velocity through the street. The mean velocity through a street of finite length is weakened, as if part of the energy of the flow was dissipated into the vortical structures that originate close to the intersection. This is an important result that adjusts the model proposed by Soulhac to calculate the velocity within the street.

Now, a short analysis will be carried on the the flow field within the intersection. The mean velocity profiles have been conducted along the y-axis at $x = 0$ and $z = H/2$; $\overline{u}$ is the component of the mean velocity parallel to the x-axis and $\overline{v}$ the component parallel to the y-axis. In Figure 3.37 the horizontal profiles of $\overline{u}$ and $\overline{v}$ are plotted for the external wind direction $\theta = 0^o, 15^o, 30^o, 45^o$. The channelling effect is evident for $\theta = 0^o$, while for the decreasing angles the $\overline{u}$ profile becomes smoothed and assume an asymmetrical shape. The $\overline{v}$ profiles demonstrate that a mean flow penetrates into the adjacent street whose strength depends on the external wind direction. In Figure 3.38 the velocity vector field on the x-y plane are visualized for the investigated wind direction.

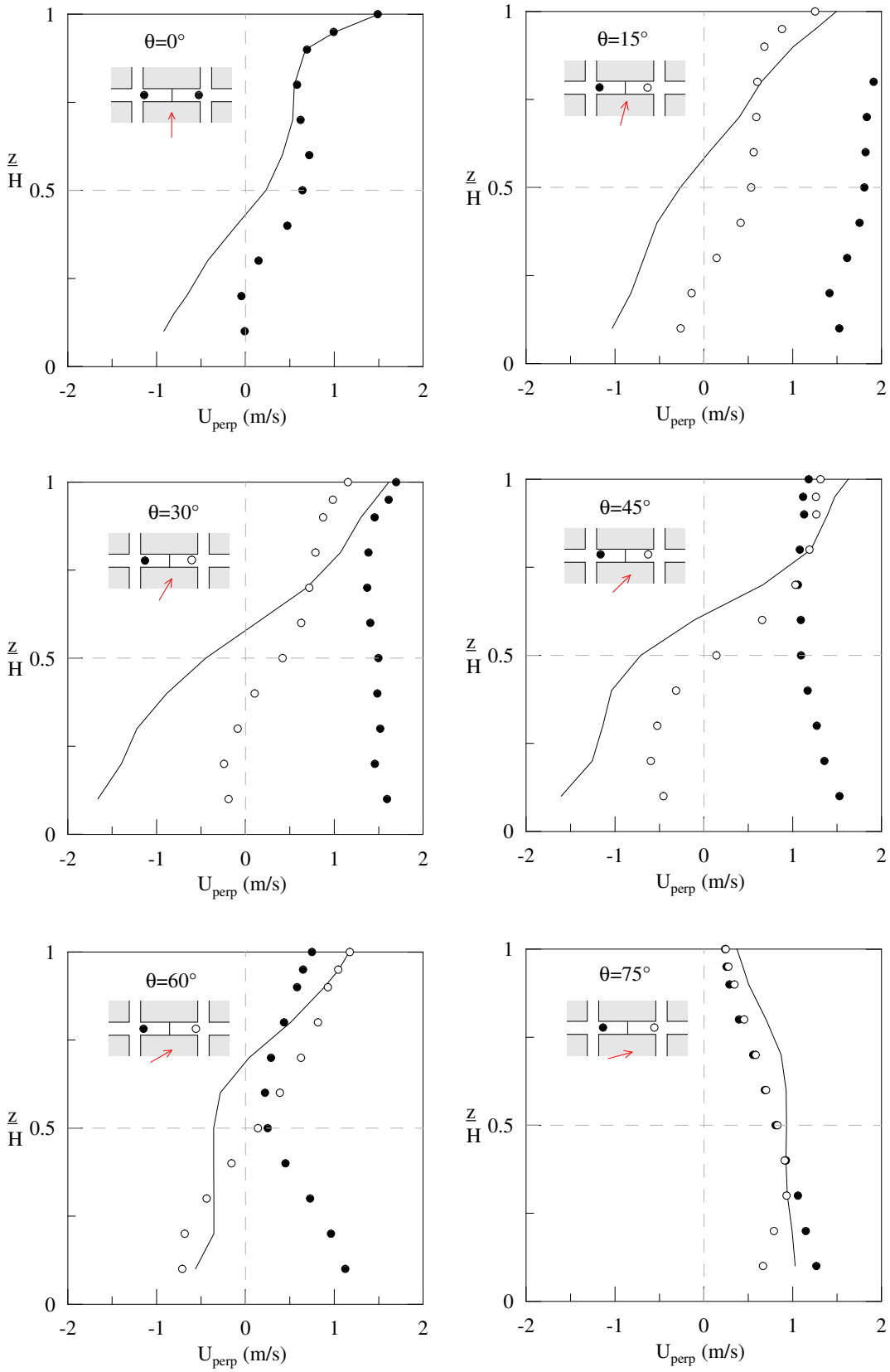

Figure 3.32: Experimental vertical profiles of the mean velocity component U_{perp} at the center and at the ends of the street for different external wind direction.

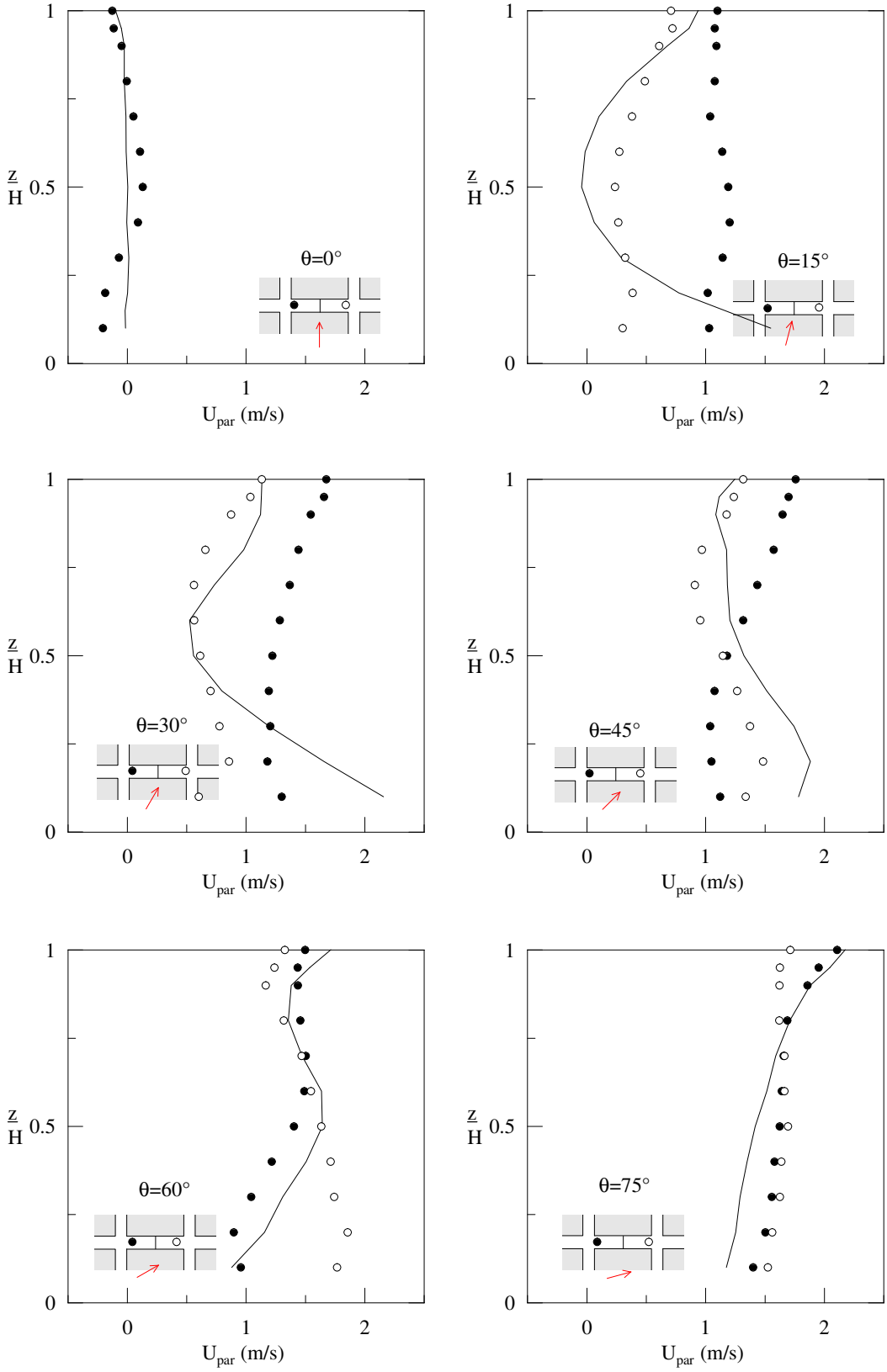

Figure 3.33: Experimental vertical profiles of the mean velocity component U_{par} at the center and at the ends of the street for different external wind directions.

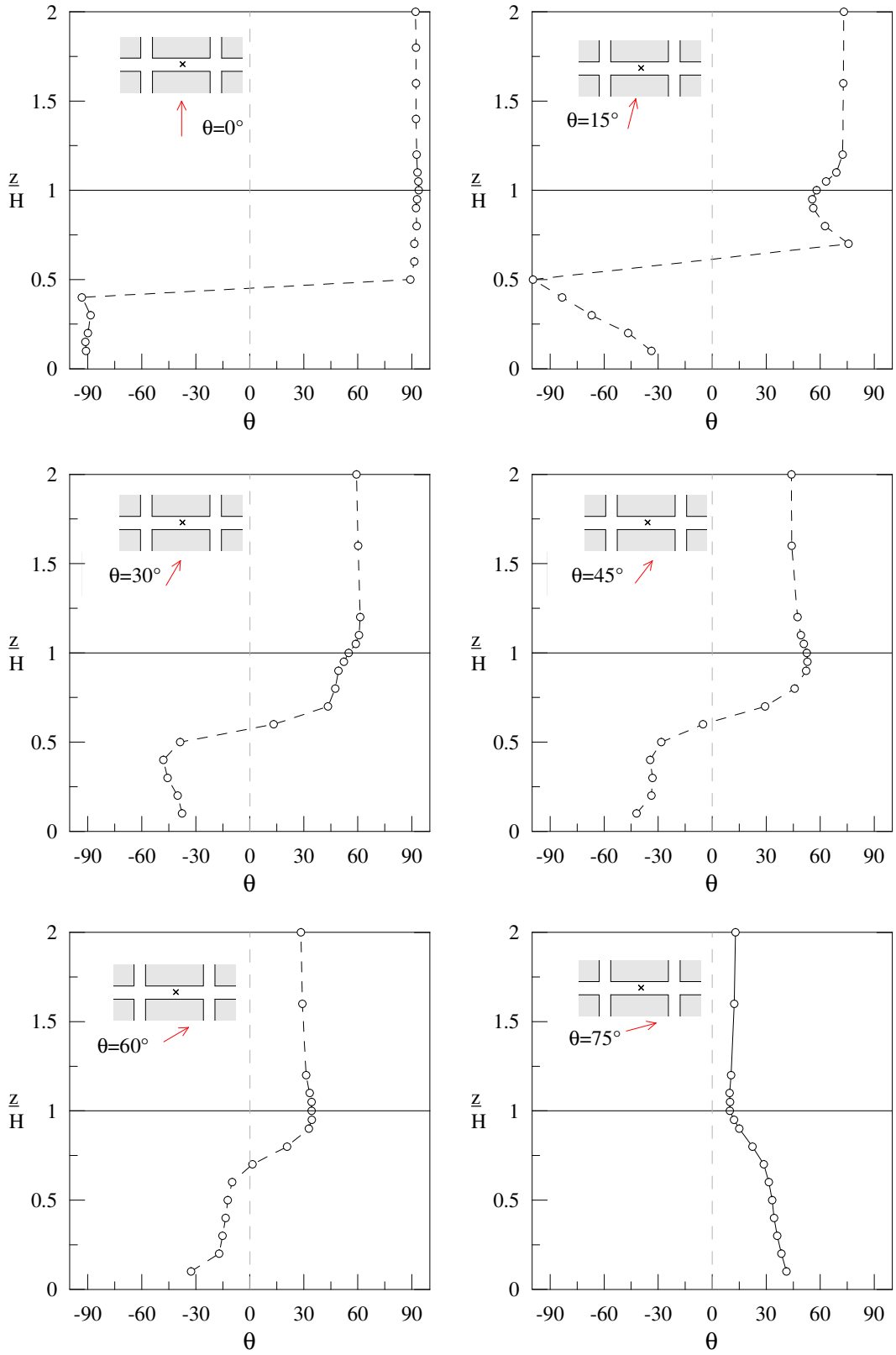

Figure 3.34: Experimental vertical profiles of the the mean velocity inclination θ respect to the axis of the street at the center of the street for different external wind directions.

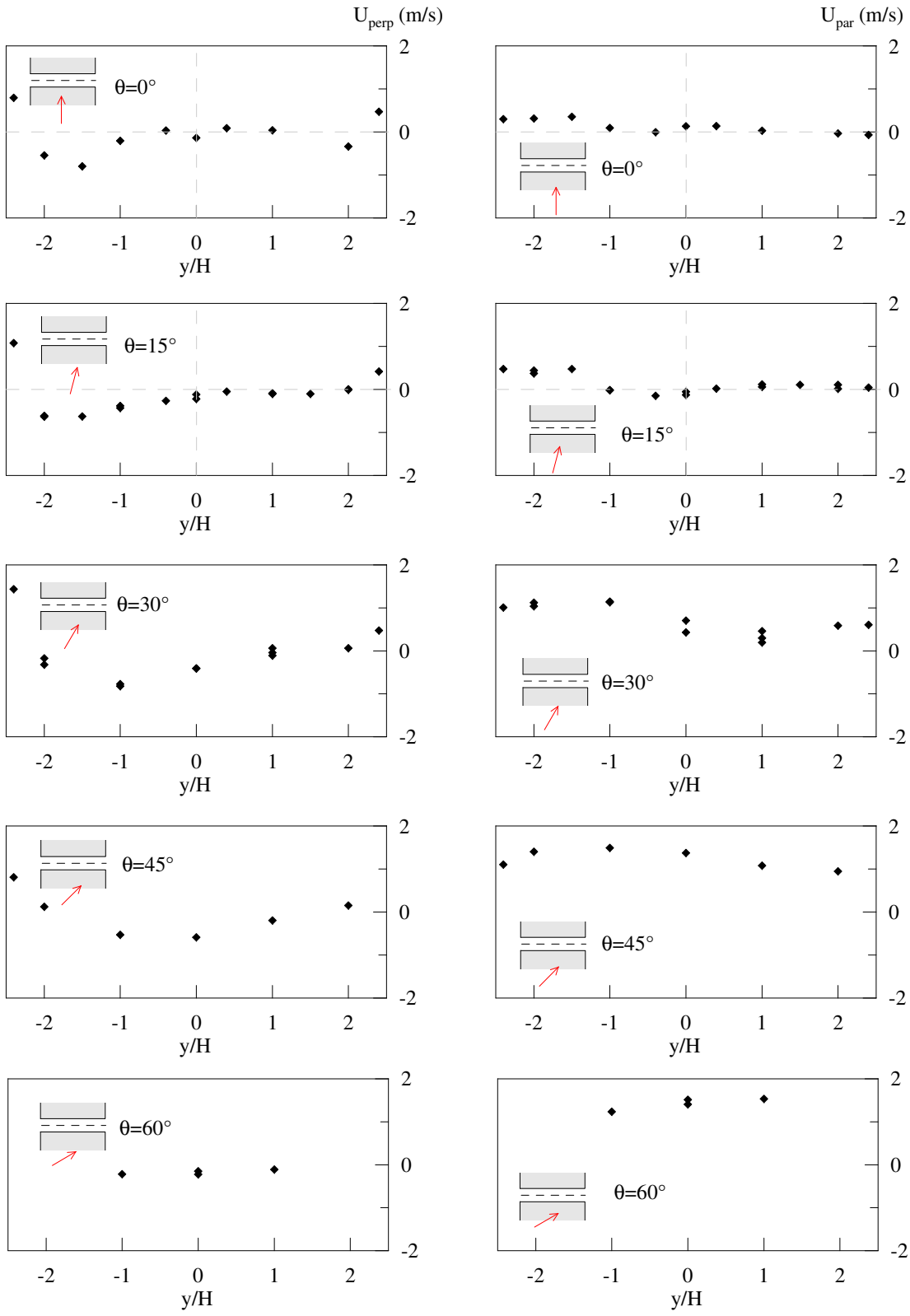

Figure 3.35: Experimental transversal profiles of the the mean velocity components U_{perp} and U_{par} along the street at $x = 0$ and $z = H/2$ for different external wind directions.

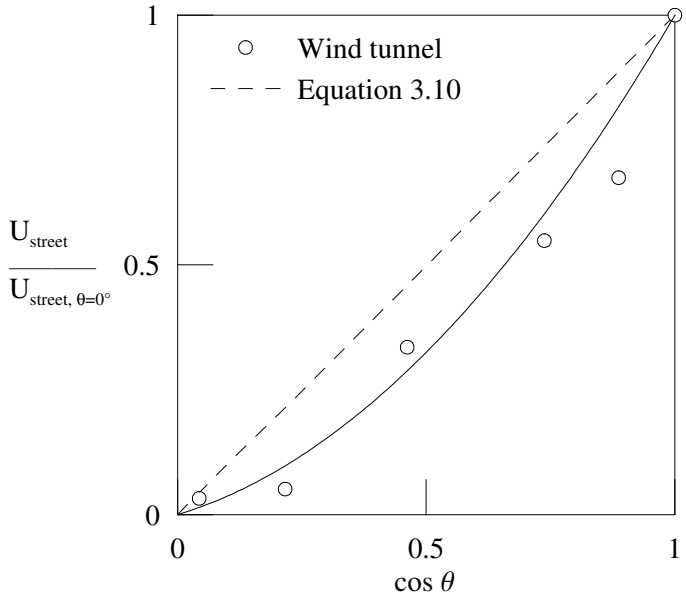

Figure 3.36: Mean velocity through a street as a function of the external wind direction θ: comparison between the experimental values and the theoretical behaviour expected within a street of infinite length.

Figures 3.39 shows the main flow characteristics according to the Soulhac's simulations. The experimental flow field pattern seems to validate the numerical study carried by Soulhac (2000) and thus his model on the exchange mechanisms at the intersection that will be described in the next chapter.

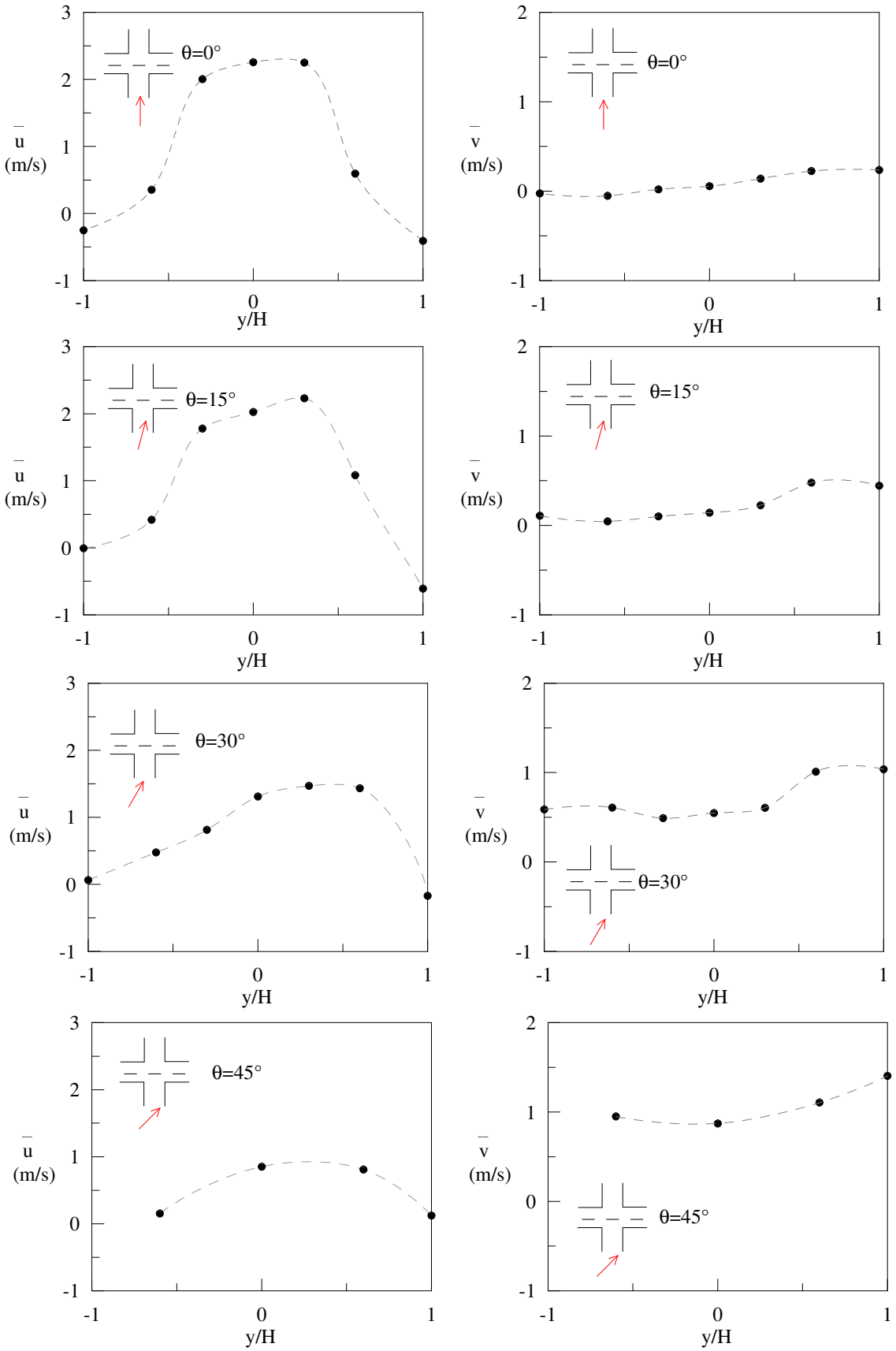

Figure 3.37: Experimental transversal profiles of the the mean velocity components $\overline{u}$ and $\overline{v}$ within the intersection at $x = 0$ and $z = H/2$ for different external wind directions. (g)-(h) $\theta_\infty = 45^o$.

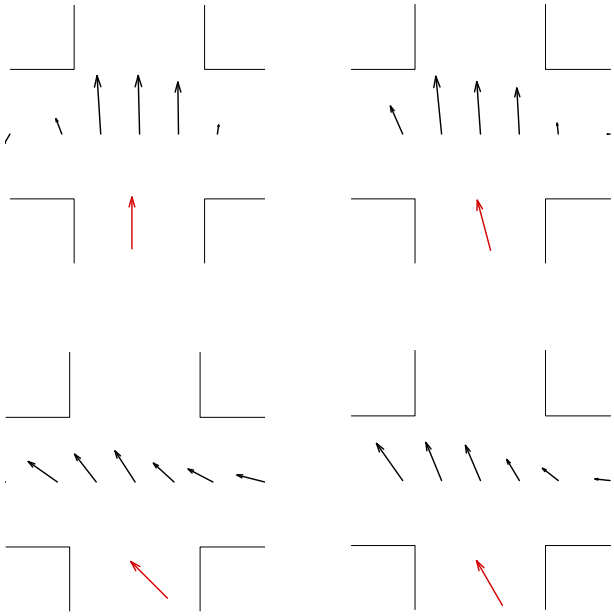

Figure 3.38: Experimental velocity vector field on the horizontal section for different external wind directions: $\theta_\infty = 0^o$, 15^o, 30^o and 45^o (clockwise) .

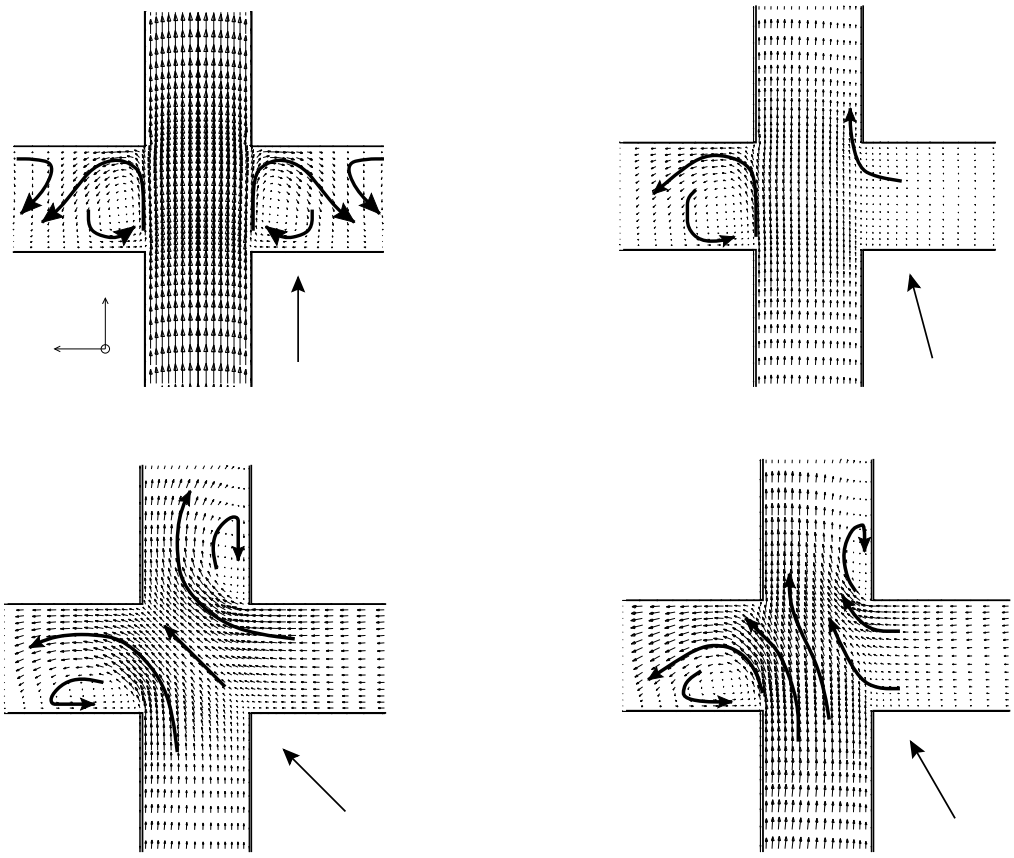

Figure 3.39: Numerically computed velocity vector field on the horizontal section for different external wind directions (SOULHAC, 2000): $\theta_\infty = 0^o$, 15^o, 30^o and 45^o (clockwise).

3.3 Dispersion through the array

While the dispersion of contaminants is fairly well understood in open, flat and homogeneous terrain, in more complicated urban environment many effects influence the pollutant dispersion, as the turbulent flow interacts with obstacles possessing a large range of shapes, sizes and possible configurations. Thus some of the well-known traditional methods of dispersion estimation, such as Gaussian plume models, are expected to perform poorly in urban regimes without significant modifications, especially at smaller scales where the details of geometry and arrangement of buildings greatly affects the flow field. As seen previously, the Gaussian plume model for a continuous point source in a uniform flow with homogeneous turbulence is

$$C(x,y,z) = \frac{Q}{2\pi\overline{u}\,\sigma_y\sigma_z}\, exp\left[-\frac{(y-y_c)^2}{2\sigma_y^2}\right]\left\{exp\left[-\frac{(z-z_c)^2}{2\sigma_z^2}\right] + exp\left[-\frac{(z+z_c)^2}{2\sigma_z^2}\right]\right\} \tag{3.9}$$

where Q is the emission rate, $\overline{u}$ is the mean transport velocity across the plume, σ_y and σ_z are the Gaussian plume dispersion parameters, y_c is the plume deflection and z_c is the effective height of release above the ground.

It is well known that even under idealized conditions Gaussian diffusion models have large uncertainties due to natural variability and simplified model physics. Significant deviations from the idealized conditions, as the presence of obstacles over the terrain represents, introduce further limitations to the validity of such models. Although theoretical basis do not support the use of the Gaussian diffusion models over complex terrain and flow conditions, Macdonald (1998) and Davidson (1996) demonstrated that the mean concentration distribution through an obstacle array can be modelled satisfactorily by suitably adapted Gaussian profiles.

Our experimental study has been carried out for a better understanding of the dispersion processes in complex terrain and for testing and validating more sophisticated dispersion models. We studied the dispersion through a dense group of obstacles that simulated an idealised urban neighbourhood and we looked at the effects of wind direction and obstacle layout pattern on the spreading of a passive scalar plume.

Concentration measurements were made by detecting the passive gas tracer released from the source through a Flame Ionisation Detector (FID). The mean concentrations were expressed in a standard dimensionless form:

$$K = \frac{CU_H LH}{Q} = \frac{CU_H 5H^2}{Q}\, 10^6 \tag{3.10}$$

where C is the measured mean concentration in ppm, Q is the emission rate in $m^3 s^{-1}$, H is the height of the obstacles, L is their length and U_H is the upwind velocity at height H.

Horizontal and vertical mean concentration profiles were recorded at various downwind distances within obstacle arrays; in order to evaluate the plume evolution, we calculated the moments of the measured concentration distributions. Concerning the horizontal distribution $K(y)$, we have:

$$y_c = \frac{\int_{-\infty}^{+\infty} y\, K(y)dy}{\int_{-\infty}^{+\infty} K(y)dy} \tag{3.11}$$

$$\sigma_y^2 = \frac{\int_{-\infty}^{+\infty} (y-\overline{y})^2 K(y)dy}{\int_{-\infty}^{+\infty} K(y)dy} \tag{3.12}$$

$$\beta = \frac{\int_{-\infty}^{+\infty} (y-y_c)^3\, K(y)dy}{\sigma_y^3} \tag{3.13}$$

$$K_{max} = max(K(y)) \tag{3.14}$$

The zero central moment corresponds to the centerline of the plume y_c, the standard deviations identify the lateral dispersion parameters σ_y, the third central moment or the skewness β characterizes the degree of asymmetry of the distribution. The skewness is a pure number that defines the shape of the distribution: a positive value of skewness signifies a distribution with an asymmetric tail extending out towards more positive y.

If the distribution K(y) was a Gaussian curve

$$K(y) = K_{y0}\, exp\left\{-\frac{(y - y_{c,gaus})^2}{2\sigma^2_{y,gaus}}\right\}$$

y_c and σ_y, as calculated by Equations 3.11 and 3.12, would match the Gaussian parameters $y_{c,gauss}$ and $\sigma_{y,gauss}$, while β would be zero.

Concerning the vertical distribution, since data exist only for $z > 0$ we have to make some assumptions in order to be able to calculate the distribution moments. Indeed, we suppose the distribution is symmetric regards to the ground. The standard deviation σ_z is calculated as follows:

$$\sigma_z^2 = \frac{\int_0^{+\infty} z^2 K(z) dz}{\int_0^{+\infty} K(z) dz}$$

If the distribution K(z) was a reflected Gaussian curve

$$K(z) = K_0 \left\{ exp\left[-\frac{(z - z_c)^2}{2\sigma^2_{z,gauss}}\right] + exp\left[-\frac{(z + z_c)^2}{2\sigma^2_{z,gauss}}\right]\right\} \tag{3.15}$$

the dispersion parameters would be related by the following relationship:

$$\sigma_z^2 = \sigma^2_{z,gauss} + z_c^2$$

It is worth noting that the vertical standard deviation we calculate is different from the usual standard deviation.

We will attempt to fit Gaussian profiles to the measured concentration distributions, the main motivation being simplicity rather than any deeper theoretical justification. Differently from the other authors, which derived the parameters of the distributions as the best fitting parameters, we calculated the moments of the distributions as previously described. The approach is different in so far as we do not assume a Gaussian distribution for the mean concentration profile but we verified it a posteriori, by plotting the normalized concentration K/K_{max} as function of $(y - y_c)/\sigma_y$ and by observing how it deviates from the Gaussian curve of parameters $y_c = 1$ and $\sigma_y = 1$, referred to as the unitarian Gaussian curve.

3.3.1 Open terrain

Initially, the plume was investigated in open terrain, where the Gaussian model should describe satisfactorily the dispersion. It is worth noting that the open terrain configuration was obtained by taking away the obstacles downwind the source and letting unchanged the array before the source, as shown in Figure 3.40, in order to preserve the upwind flow characteristics. The vertical profile was measured at ($x = 35H$,$y = 0$) from the source and is plotted in Figure 3.41-a together with the reflected Gaussian curve. The calculated dispersion parameter σ_z is plotted as function of the distance from the source in Figure 3.41-b. The transversal profiles were performed at z=H/2 and at z=2H, at distances downwind the source equal to x=21H and

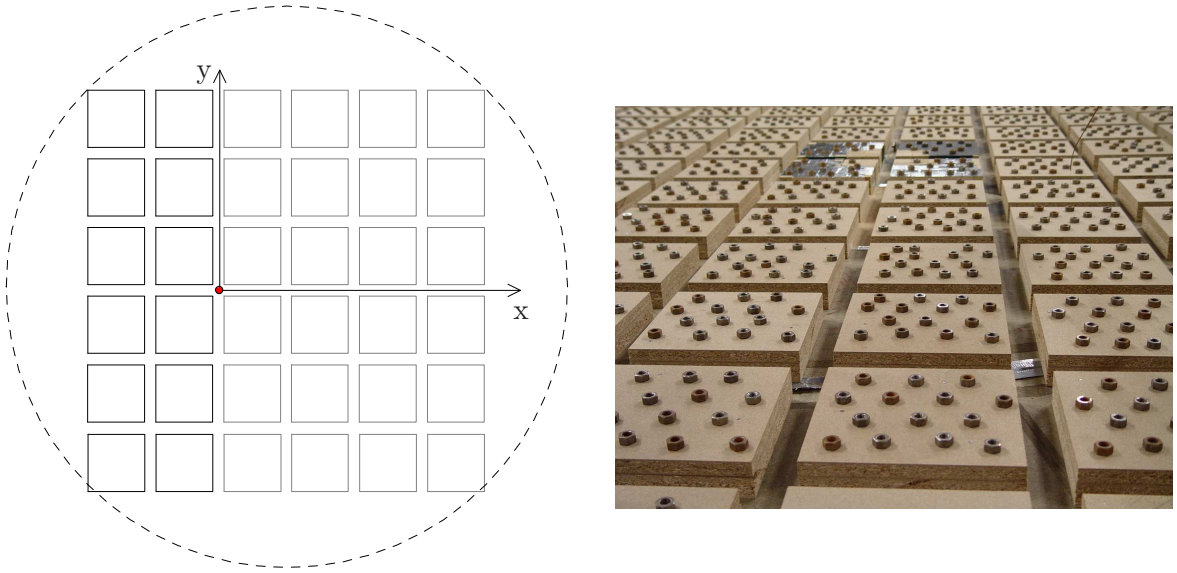

Figure 3.40: Obstacle array in the wind tunnel; the red circle represents the point source. The grey obstacles were taken away to obtain the open terrain configuration

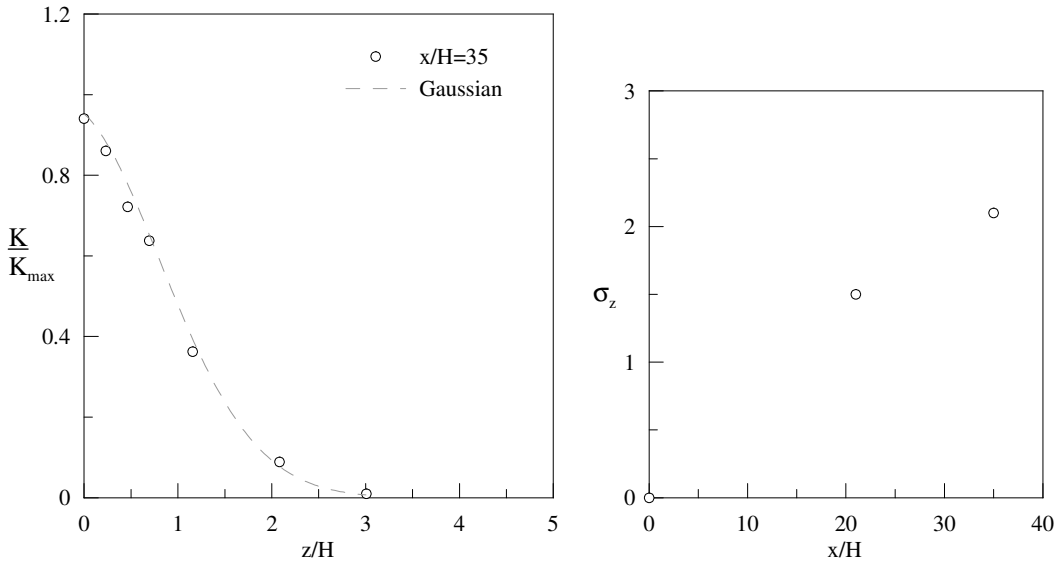

Figure 3.41: Evolution of the dispersion parameters in open terrain (wind tunnel)

x=35H. The normalized profiles are shown together with the unitarian Gaussian curve in 3.42-a, concerning $z = H/2$, and in 3.42-b, concerning $z = 2H$. The dispersion parameters K_{max}, y_c, σ_y and β which have been calculated for the horizontal profiles within and above the canopy are plotted as function of the distance from the source in 3.42-c to f. A first analysis of the data suggests that the Gaussian model well represents the dispersion in open terrain, as expected.

3.3.2 Obstacle array

Now, the pollutant dispersion in urban areas is taken into account by investigating the plume spreading through obstacle arrays for an external wind direction parallel to the x-axis, an academic case rather than a realistic one. Experimental difficulties have been encountered in aligning the wind direction to the street axis, because the flow was slightly deviated as regards the axis of the wind tunnel, as seen in section 3.1.

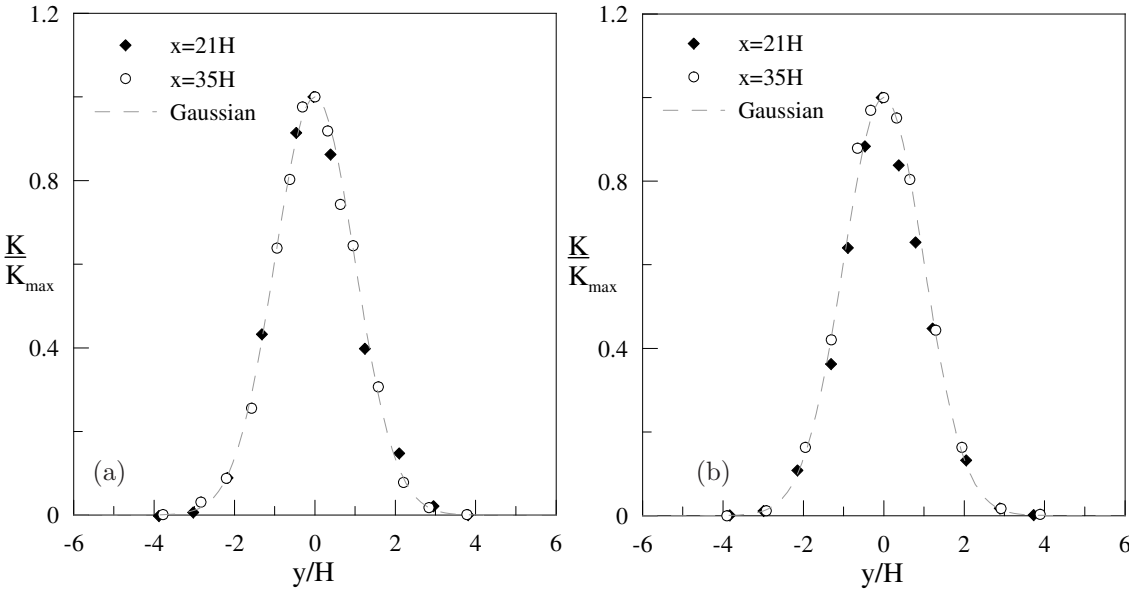

Normalized horizontal mean concentration profiles at various positions downstream the source and unitarian Gaussian curve (dashed line): a) within the canopy, at $z = H/2$ b) above the canopy, at $z = 2H$

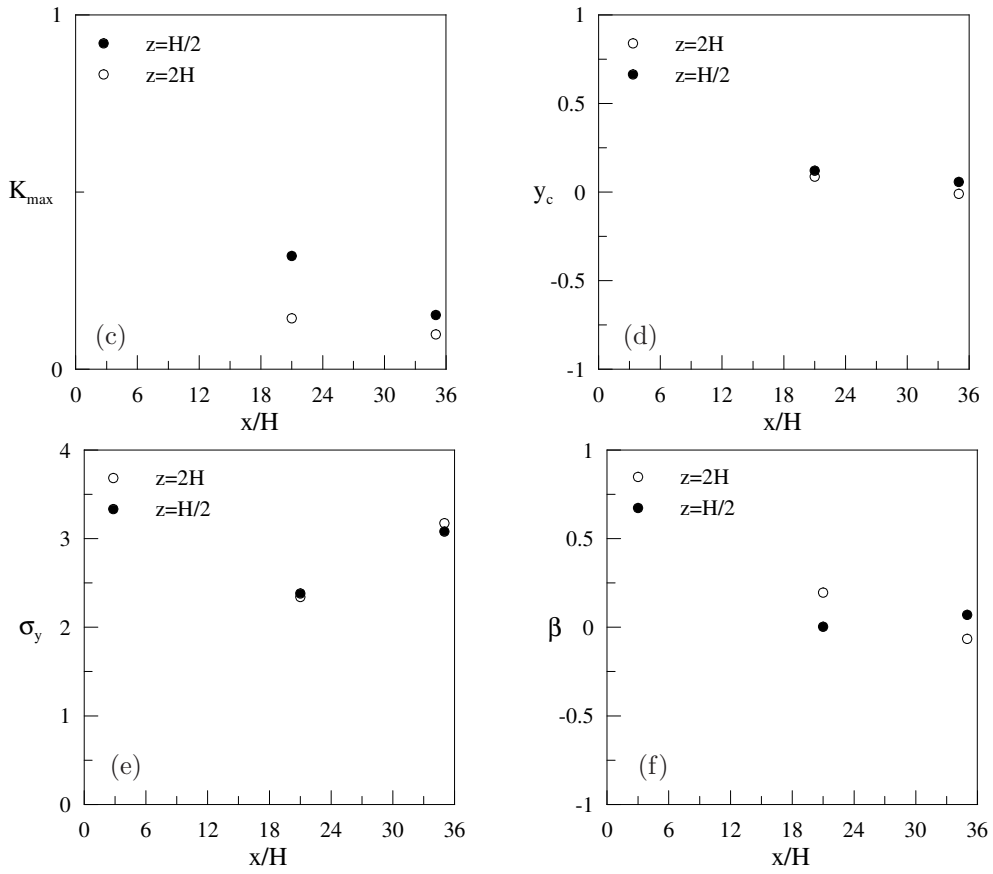

Moments of the horizontal mean concentration profiles at various positions downstream the source: c) mean concentration maximum; d) plume deflection; e) standard deviation; f) skewness.

Figure 3.42: Horizontal plume spreading in open terrain

Another source of error in the alignment could be the manual positioning of the obstacles that introduces local asymmetries in the array layout. As Robins et al. (2002) pointed out in a wind tunnel study at a simple intersection, small departures from symmetry, due to an off-set in the street alignment or to a change of orientation relative to the wind, were sufficient to modify significantly the exchanges between the streets. As result, the lateral concentration distribution that should be symmetrical for a theoretical aligned wind shows an asymmetrical profile, which is characterised by a plume deflection and by a non-zero value of the skewness. It is worth noting that the parameter that certifies an asymmetry in the exchange mechanisms due to the presence of the obstacles is the skewness β rather than the plume deflection y_c, which is related to the wind direction. So, different attempts were performed to obtain the theoretical condition of the wind aligned to the street axis by changing the angle θ between the array axis and the wind orientation. The initial value of θ is θ_0 and corresponds to the position of the array aligned with the wind tunnel. θ_0 is unknown and the ideal approach would be to rotate the street axis of a known infinitesimal $\delta\theta$ until the angle $\theta_0 + \delta\theta$ produce a symmetrical concentration distribution that would correspond to $\theta{=}\theta_0 + \delta\theta = 0^o$. Nevertheless, as the change in the wind orientation is obtained by rotating the overall array, as seen in Figure 3.43, in order to minimize the experimental efforts the dispersion pattern throughout the array has been investigated only for the angles θ_0, $\theta_0 + 2.5^o$, $\theta_0 + 5^o$.

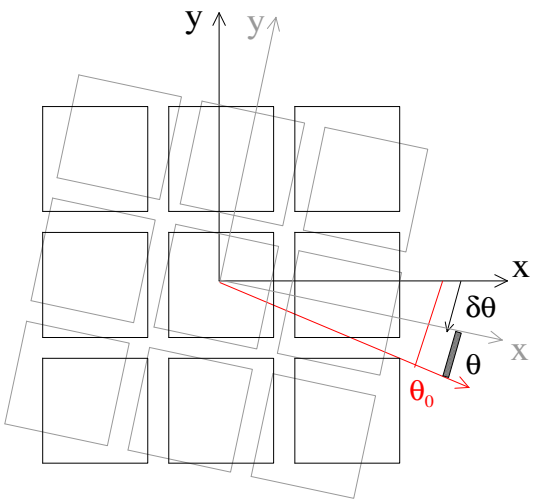

Figure 3.43: Rotation $\delta\theta$ of the array in order to align the array axis to the wind direction θ_0

In Figure 3.44 horizontal profiles of the mean concentration at the downstream positions $x/H = 6$ and $x/H = 12$ are plotted, which correspond to a wind orientation $\theta = \theta_0$ and $\theta = \theta_0 + \delta\theta$. In Figure 3.44-a the profiles correspond to $\theta = \theta_0$ and $\theta = \theta_0 + 2.5^o$ and the wind direction is evidently not aligned to the street axis for both the cases. Figure 3.44-b compares the profiles relative to $\theta = \theta_0$ and to $\theta = \theta_0 + 5^o$, the latest showing a rather symmetrical profile and suggesting that the best, even not perfect, alignment corresponds to $\theta = \theta_0 + 5^o$.

In order to evaluate the variability of the dispersion pattern due to a small change in the wind direction about the theoretical condition $\theta = 0^o$, we investigate the plume behaviour farther from the source: Figure 3.45 describe the plume evolution within the array for the wind orientation $\theta = \theta_0$ and $\theta = \theta_0 + 5^o$. In Figure 3.45-a the downwind evolution of the horizontal concentration profiles within the array are compared; the measurements have been performed at $z = H/2$. In Figure 3.45-b the plume centerline is plotted as function of the distance downwind the source and a linear fit calculates the deflection of the plume, which corresponds to -2^o for $\theta = \theta_0$ and to 0.5^o for $\theta = \theta_0 + 5^o$. The transition from a negative to a positive angle suggests that the theoretical condition $\theta = 0^o$ would occur between the two investigated wind orientations. The

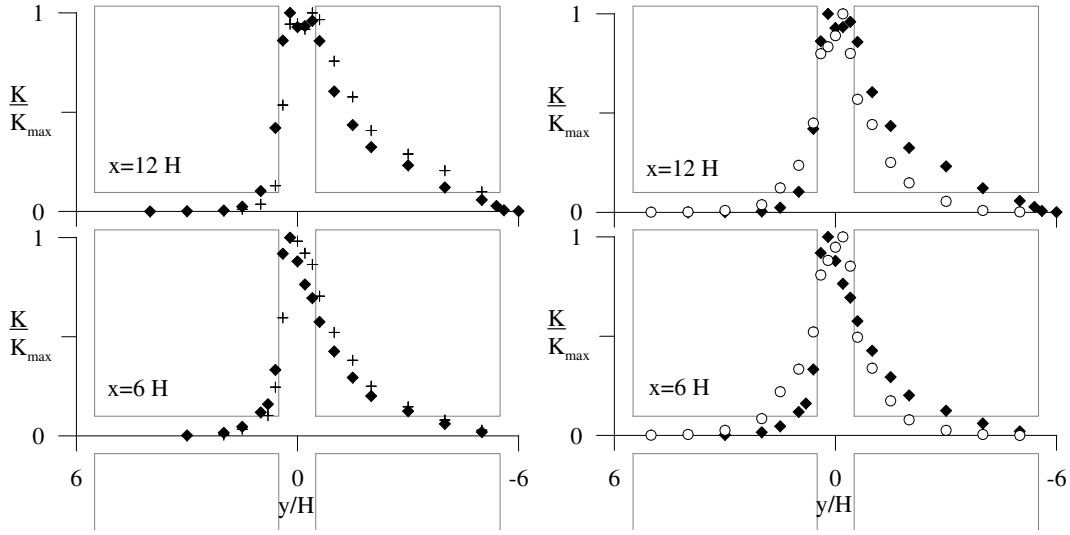

Figure 3.44: Horizontal mean concentration profiles at various positions downstream the source for small differences in the wind orientation θ. In the figure on the left: $\theta = \theta_0$ (⧫) and $\theta = \theta_0 + 2.5^o$ (+). In the figure on the right: $\theta = \theta_0$ (⧫) and $\theta = \theta_0 + 5^o$ (○)

same consideration may be inferred from the skewness behaviour, as negative values characterize the case $\theta = \theta_0$, while positive values characterize the case $\theta = \theta_0 + 5^o$ (Figure 3.45-d). The standard deviations of the distributions seem not to be affected by the slight difference in the wind orientation, as observed in Figure 3.45-c. A good approximation of the symmetrical case $\theta = 0^o$ is $\theta_0 + 5^o$, even if a significative uncertainty exists related to the high sensitivity of the exchange mechanisms to local asymmetries that makes impossible know the exact value of the angle θ. Thus we will consider that our experimental study describes the plume behaviour through the array for a wind direction equal to $\theta = 0^o \pm 2.5^o$.

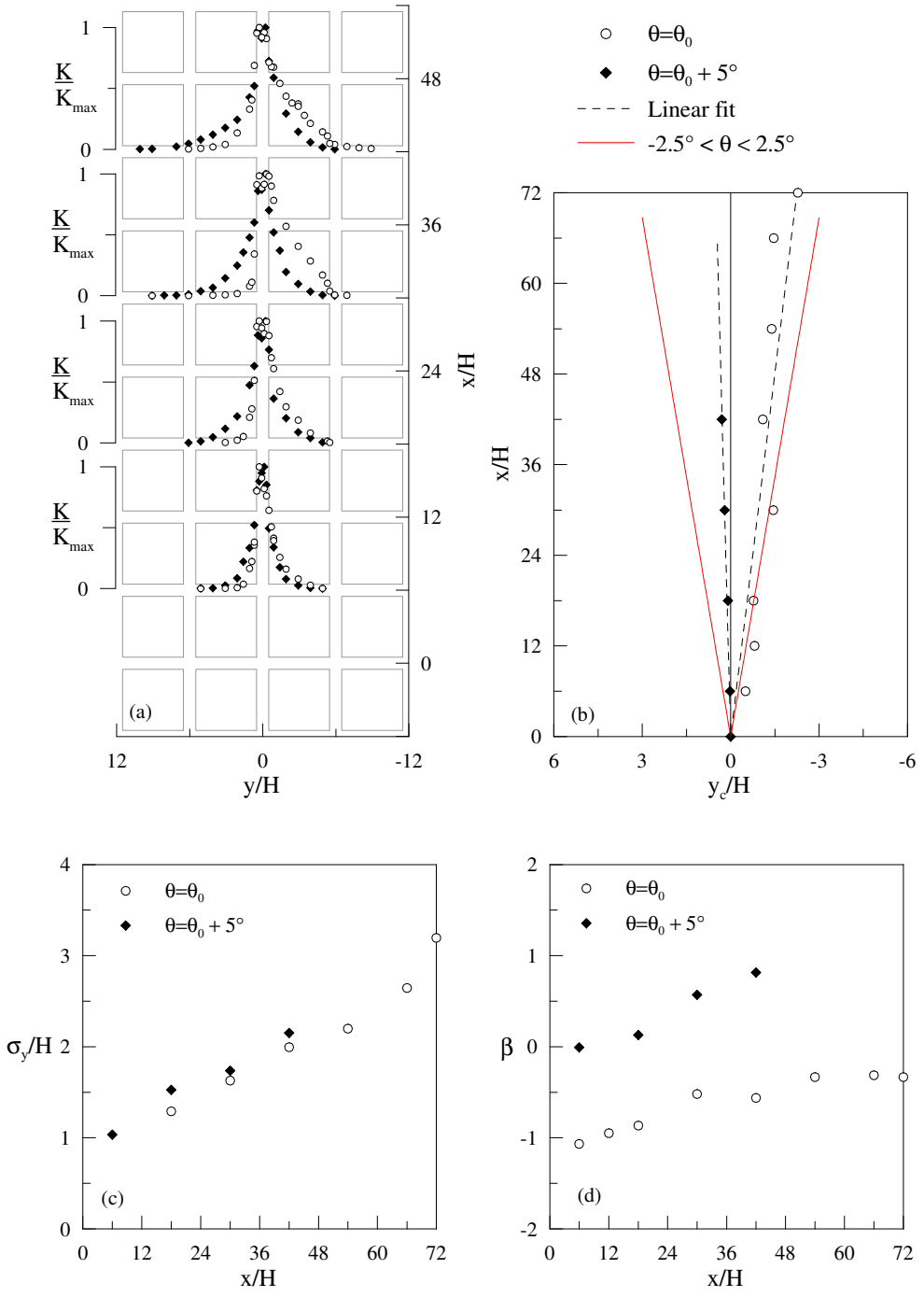

Figure 3.45: Evolution of the plume within the array for small changes in wind orientation, $\theta = \theta_0$ and $\theta = \theta_0 + 5^o$. a) Horizontal mean concentration profiles; b) Plume centerline; c) Standard deviations; d) Skewness.

3.3.3 Influence of the street aspect ratio

In order to study the effect of the geometrical layout on the dispersion pattern, the plume evolution through three different array has been investigated for a wind parallel to the street axis. As seen, a perfect alignment does not hold exactly and the wind direction is supposed to form an angle equal to $\theta = 0^o \pm 2.5^o$ with the street axis.

The first experimental configuration which has been studied is referred to as configuration 1 and consisted in obstacles equally spaced at a distance $S = H = 50$ mm (Figure 3.46-a). The resulting plan area density was equal to $\lambda_p = 69\%$. Other two different array configurations were taken into account by varying the spacing between the obstacles. Configuration 2 consisted of aligned obstacles which were spaced at distance S_y=2H and S_x=H (Figure 3.46-b). Configuration 3 was characterised by S_y=H and S_x=2H (Figure 3.46-c). It is worth noting that configuration 3 is the configuration 2 which has been rotated of 90^o. The plan area density was the same for the two configurations, λ_p= 59%, but smaller than that of configuration 1, so that it was possible to extrapolate on one hand the influence of the package density and on the other hand the effect of the geometrical layout on the plume spreading through the group of obstacles.

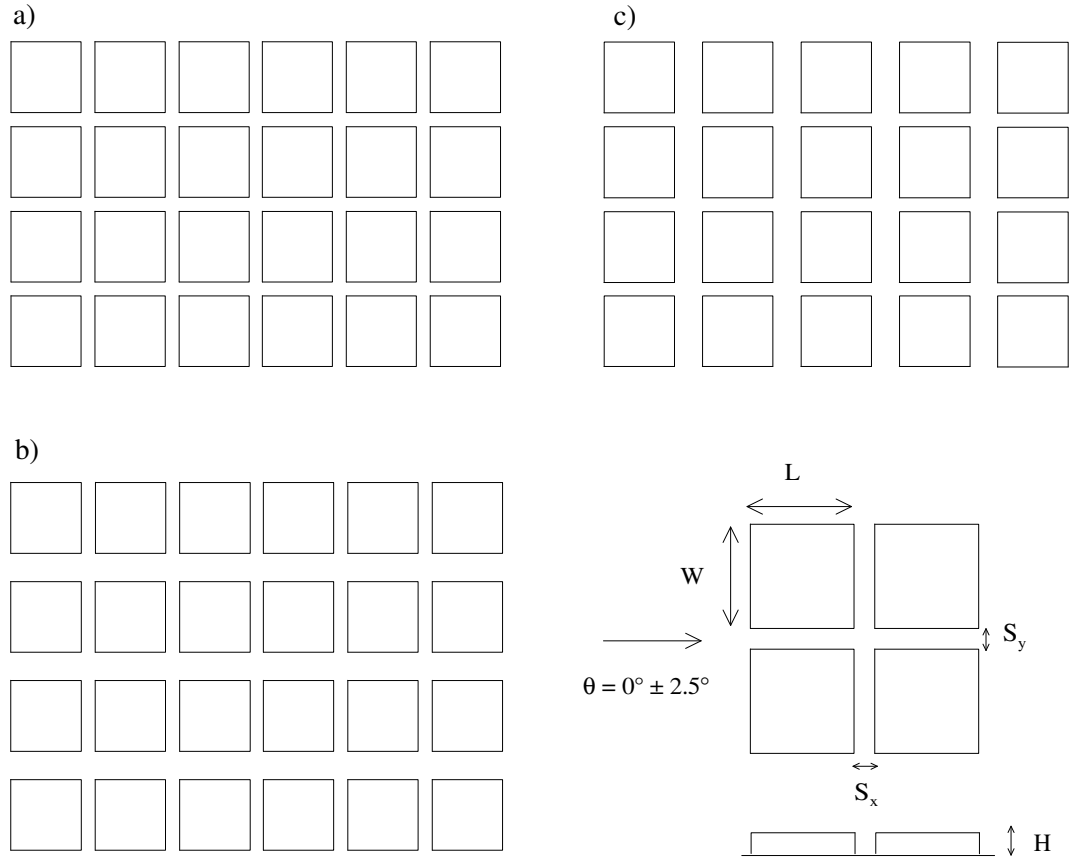

Figure 3.46: Geometrical layout of the obstacle array, $W = L = 5H$: a) Configuration 1, $S_x = S_y = H$; b) Configuration 2, $S_x = H$ $S_y = 2H$; c) Configuration 3, $S_x = 2H$ $S_y = H$

The plume behavior was investigated in the **configuration 1** by recording horizontal profiles of mean concentration, within the canopy at $z = H/2$ and above the canopy at $z = 2H$, and vertical profiles, at different distances downwind the source. In order to better visualize the plume spreading within the array, the horizontal profiles are synthesized in Figure 3.47. In Figure 3.47-a, the horizontal profiles at $z = H/2$ are normalized to the calculated distribution moments;

the profiles appear self-similar, suggesting that the adopted parameters are appropriate scales, but are not fitted by a Gaussian curve. Further, the concentration distribution seems to have a different behaviour by the streamwise street and the lateral street, indicating that the dispersion through the array is strongly affected by the presence of the obstacles. In Figure 3.47-b the downwind decay of the mean concentration maximum is plotted. The channelling mechanism is evident: the plume appears to be confined into the channel within which it is released and the spread of the plume into neighboring channels is inhibited. Coherent turbulent structures arise into the channels and limit the mass exchange in the lateral direction, which mainly relied on the mechanism of intermittency. Two dispersion mechanisms may be pointed out that reflect the flow dynamics within the array and explain the different observed behavior:

- the dispersion due to the mean flow advection that is associated to the channelling effect by the streamwise street
- the dispersion due to the turbulent mass exchange taking place at the interfaces that is related to the recirculating regions within the lateral streets

The overall plume spreading above the array is shown in Figure 3.48 and it is worth noting that the horizontal concentration distribution is described quite well by a Gaussian curve, suggesting that the local effect of the obstacles vanishes and the array acts on the plume as an overall roughness. In Figure 3.49-a the normalized vertical profiles of the mean concentration are plotted for different downwind positions, while Figure 3.49-b shows how the standard deviation of the vertical distribution evolves with the distance from the source. In Figure 3.49-c to f the moments of the horizontal distributions within and above the array are compared, in order to highlight the effect of the presence of the obstacles on the dispersion pattern. The plume centerline within the array matches the theoretical value $y_c = 0^o$, while above the array it seems to be slightly deflected. The skewness is positive both within and above the array, although it is more enhanced within the array because the presence of the obstacle originates an asymmetry in the exchange mechanisms that affects in great measure the profile within the array and to a small extent the distribution above the array. A consequence of the channelling effect is the reduced spreading of the plume within the array, since it is confined in the longitudinal channel, and therefore above the array.

In Figure 3.50 the mean concentration profiles which have been recorded within the **configuration 2** are plotted. In Figure 3.50-a the horizontal profiles at $z = H/2$ are normalized to the calculated distribution moments and appear self-similar, except for $x = 6$H. The concentration distribution at $x = 6$H, which corresponds to the first intersection, is narrower and a sharp cut occurs at the interface between the intersection and the lateral street, $y = H$ and $y = -H$: the effect of channelling is more important than in configuration 1 and the dispersion in the lateral street is more strongly inhibited. Concerning the profiles at the next downstream positions, the cut at the interface is less sharp, maybe because another mechanism contributes to increase the concentration within the lateral street, that is the vertical turbulent flux occurring at the interface between the external flow and the lateral street. Further, no Gaussian model is able to fit the entire experimental distribution, once again suggesting a decoupling between the longitudinal street and the lateral ones that is certainly associated to the decoupling of the flow field. In Figure 3.51-a the horizontal profiles at $z = 2H$ are normalized to the calculated distribution moments and they are quite well fitted by a Gaussian curve; in Figure 3.51 is visualized the overall plume behavior above the array. Finally, in Figure 3.52-a and b the vertical mean concentration distributions and the vertical dispersion parameter are plotted as function of the downstream position and indicate the plume is confined within the channel. In Figure 3.52-c to f the moments of the horizontal distribution within and above the array are compared. The plume deflection above the array differs from that within the array, but are both coherent with

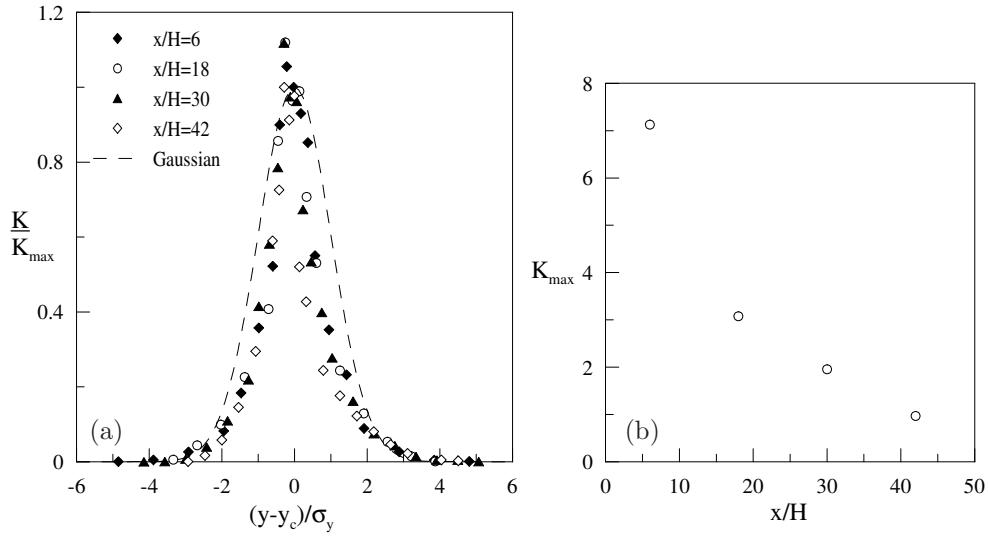

a) Normalized mean concentration profiles at various positions downstream the source and the unitarian Gaussian curve (dashed line); b) downwind decay of the maximum concentration value

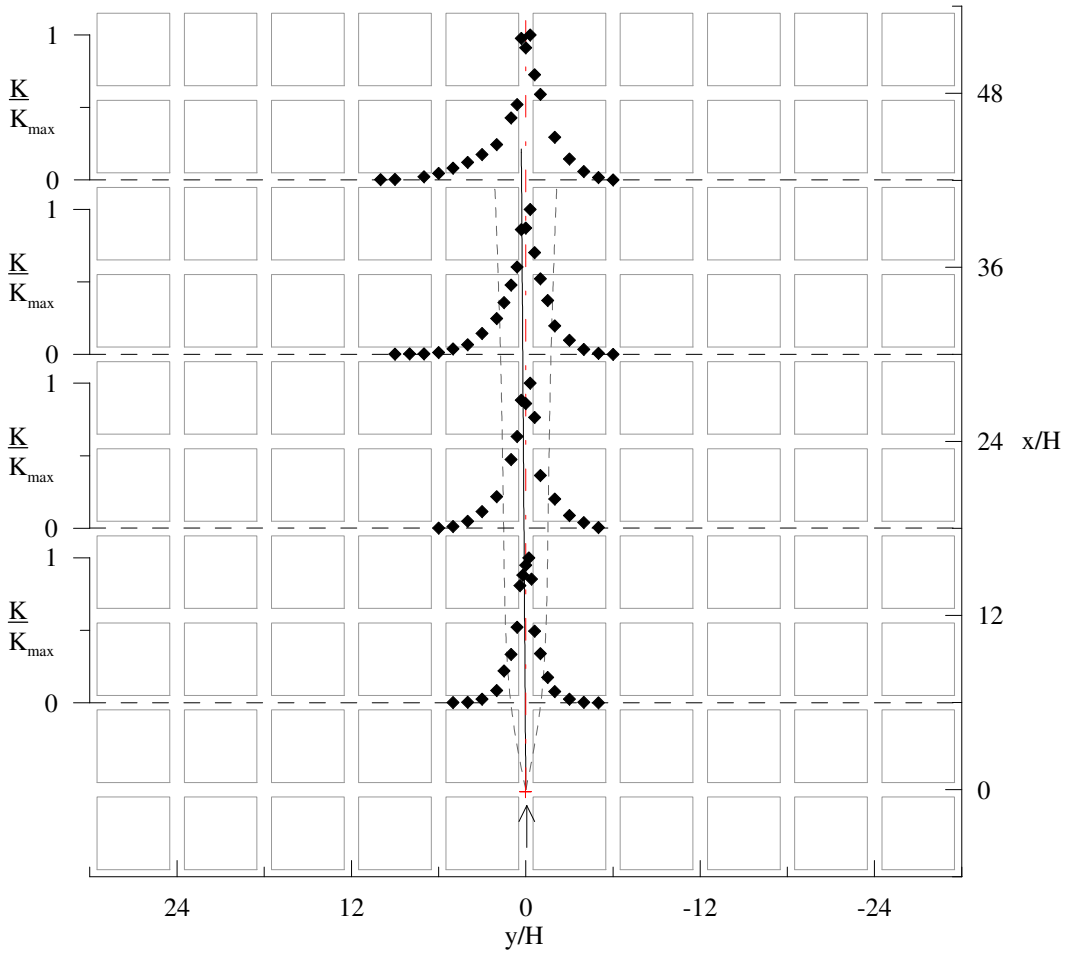

Evolution of the plume downwind the source (+). The solid line identifies the plume centerline y_c, the dashed lines identify the horizontal plume dimensions $y_c \pm \sigma_y$, the dashed dot line notices the wind direction.

Figure 3.47: Overall plume behaviour within the array (z=H/2), **configuration 1**

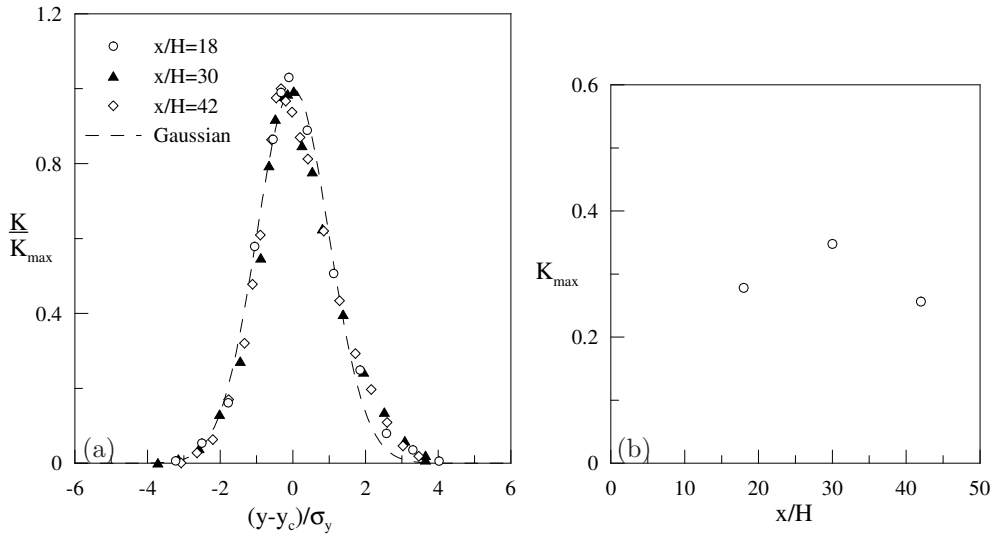

a) Normalized mean concentration profiles at various positions downstream the source and unitarian Gaussian curve (dashed line); b) downwind decay of the maximum concentration value

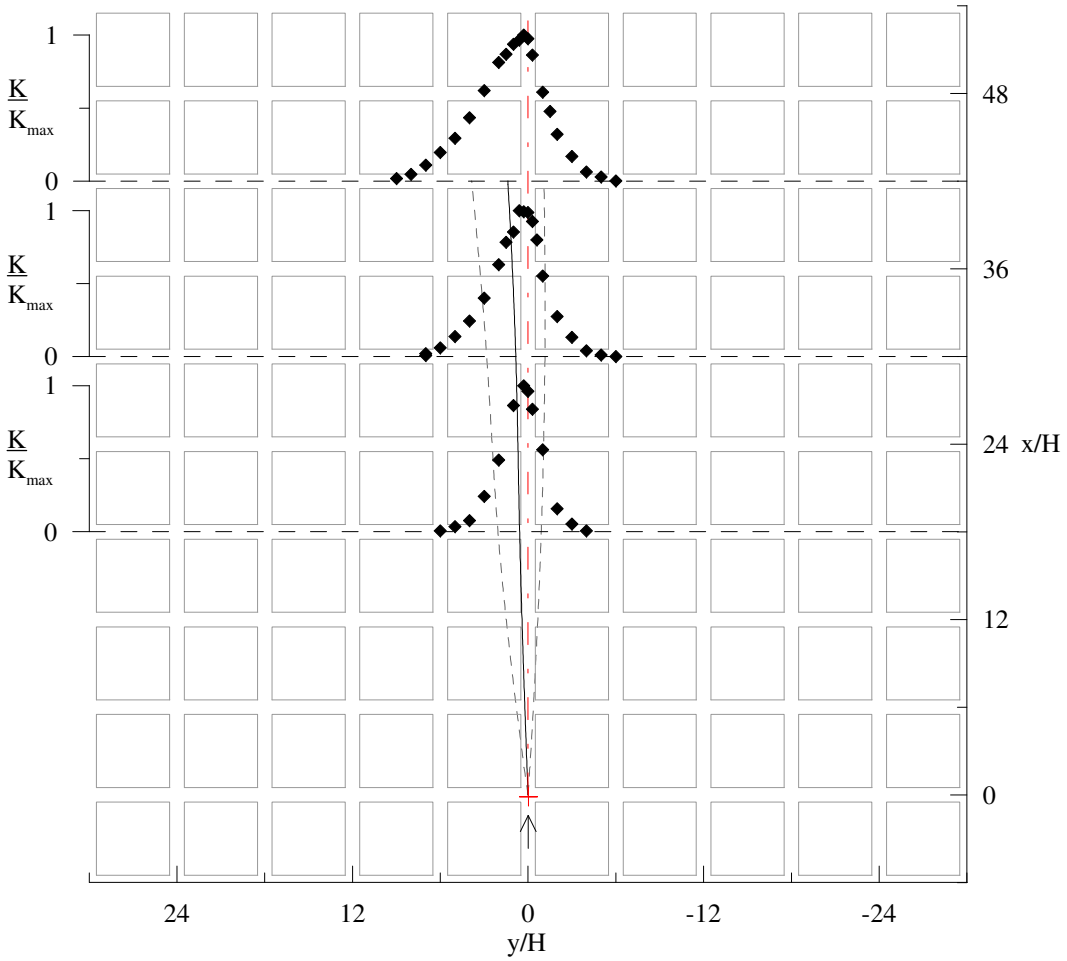

Evolution of the plume downwind the source (+). The solid line identifies the plume centerline y_c, the dashed lines identify the horizontal plume dimensions $y_c \pm \sigma_y$, the dashed dot line indicates the wind direction.

Figure 3.48: Overall plume behaviour above the array (z=2H), **configuration 1**

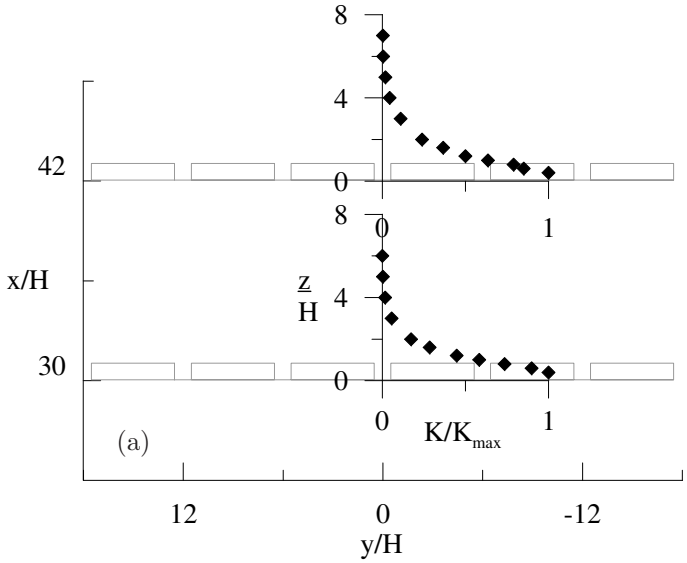

a) Normalized vertical mean concentration profiles at various positions downstream the source and unitarian Gaussian curve (dashed line);

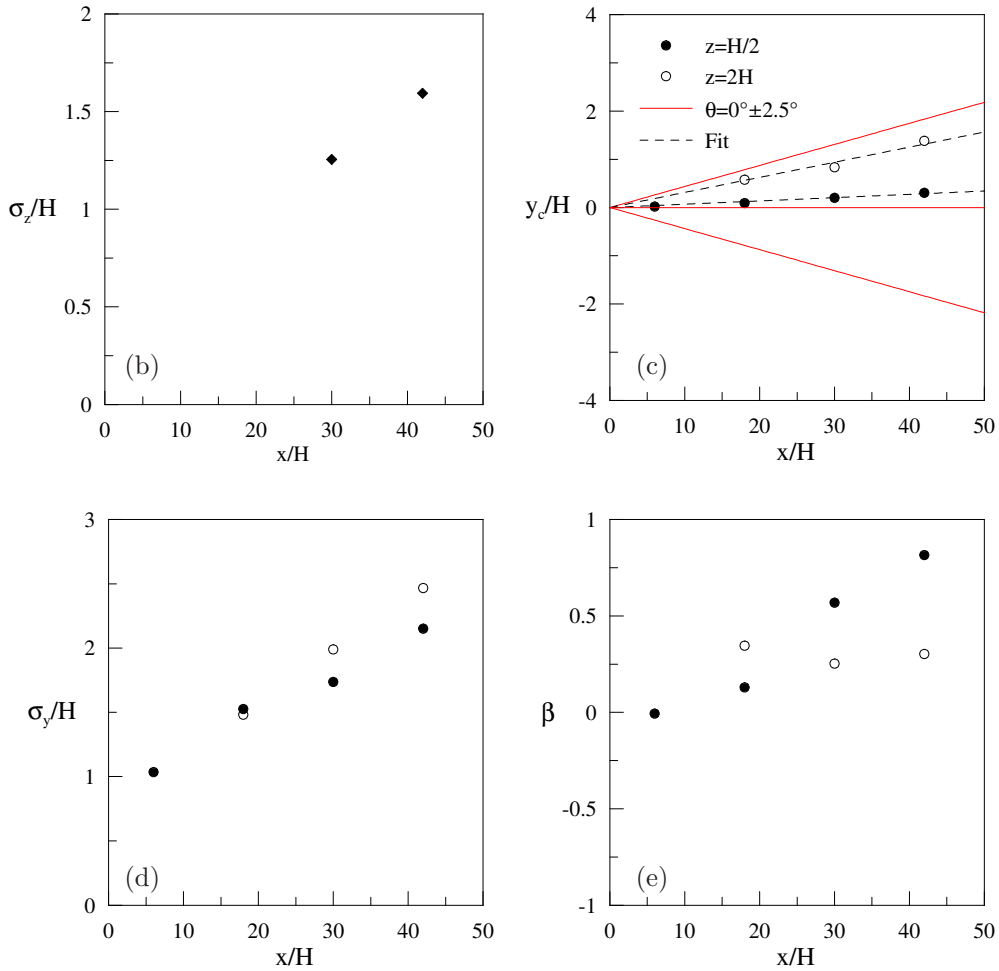

b) vertical dispersion parameter. Moments of the horizontal mean concentration distributions at various positions downstream the source: c) standard deviation; d) plume deflection; e) skewness.

Figure 3.49: Description of the plume, **configuration 1**

the hypothetical wind direction $\theta = 0^o \pm 2.5^o$. The reduced plume spreading within the array is a consequence of the significant effect of channelling.

Before summing up the influence of the geometrical layout on the plume spreading, the experimental data recorded at the **configuration 3** are presented. The overall plume spreading within the array is visualized in Figure 3.53, while the plume behaviour above the array is shown in Figure 3.54. In Figure 3.55 the normalized vertical profiles are plotted and the moments of the horizontal distributions within and above the array are compared.

The mean concentration horizontal profiles within the array, normalized to the calculated distribution moments, are coarsely self-similar and are quite well fitted by a Gaussian curve, conversely to what happened in the other configurations. The lateral streets are larger and a wake interference flow regime takes place that enhances the exchanges between the intersection and the lateral street and between the lateral street and the exterior. The lateral and vertical dispersion is thus enhanced, as well as the turbulent mixing within the lateral street. Further, there is no preferential direction of the exchange mechanisms and this may be the reason for the Gaussian distribution. The mean concentration horizontal profiles above the array are well described by a Gaussian model, meaning that the local effects of the obstacles vanished. An important deflection of the plume within and above the array is observed, which corresponds to an angle equal to 7^o. This behaviour may be explained by supposing that a plume deflection derives by an existing misalignment in the wind orientation and is amplified within the array by the asymmetry of the geometrical layout of the array, that is the lateral streets are larger than the wind-aligned streets and "propagates" above the array. The horizontal spreading shows similar values within and above the array, as a confirmation of the enhanced turbulent mixing. The skewness is small and the distribution can be considered rather symmetric, so that the current obstacle layout is thought not to impose a preferential direction in the dispersion mechanism.

The experiments of Hoydysh and Dabberdt (1994) confirms qualitatively the observed plume behaviour through the arrays. The experimental results refer to concentration measurements conducted by means of a visualization method. Figure 3.56-a corresponds to configuration 2 and it is worth noting that most pollutants are advected in the streamwise street and only few pollutants diffuse into the lateral streets. Figure 3.56-b corresponds to configuration 3 and conversely to the previous case most pollutants are advected within the lateral street. An asymmetry of the wind direction regards to the axis of the street is amplified by the asymmetrical layout and can explain the asymmetry of the plume. The asymmetry of the wind direction could be rather than an experimental effect an intrinsic characteristic of the mean wind that fluctuates about the mean value.

Now, we compare the results concerning the three different configurations and the open terrain, in order to study the effect of the array geometry on the plume spreading. In Figure 3.57 we plot the standard deviations σ_y and σ_z as function of the downstream positions from the source. It is worth noting that the arrays can be classified according if they enhance or not the plume spreading respect to the spreading in the open terrain configuration. The key parameter is S_x/H, which characterizes both the size of the exchange surface between the intersection and the lateral street and that of the exchange surface between the lateral street and the external flow. For $S_x = H$ (configurations 1 and 2) the channelled mean flow transports the pollutants within the longitudinal street and the plume appears to be confined, since the diffusion in the lateral streets is only due to the fluctuating component of the mean flow. For $S_x = 2H$ (configuration 3), the horizontal plume spreading is enhanced, as the pollutants dispersion into the lateral street is due both to diffusion and advection processes at the intersection. The dominant role of the intersection in the lateral dispersion has thus been pointed out. Concerning the vertical dispersion, the lateral streets seem to be the more effective in vertical pollutant exchanges and the larger the street the more enhanced is the vertical spreading. If the horizontal exchange is supported, the vertical exchange will be consequently strengthened. This picture

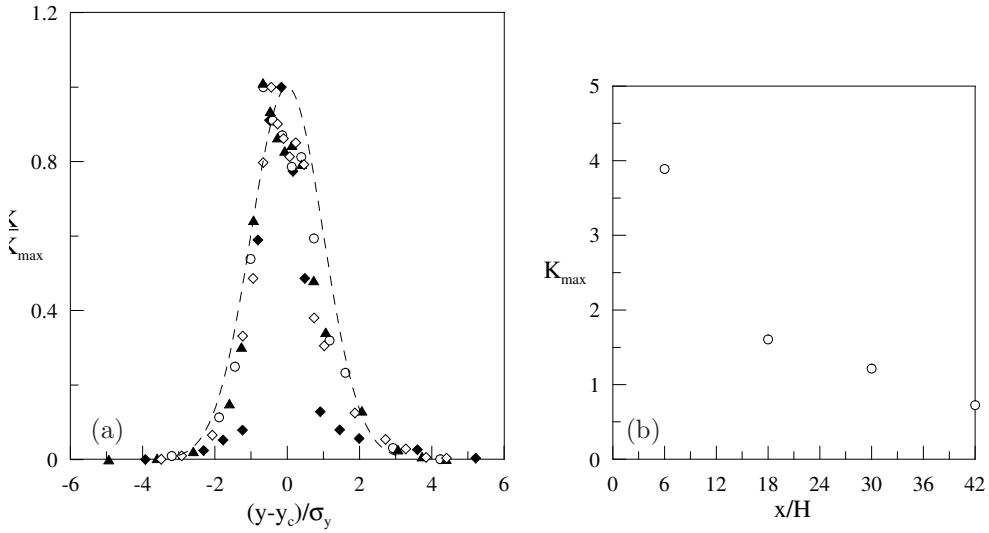

a) Normalized mean concentration profiles at various positions downstream the source and unitarian Gaussian curve (dashed line); b) downwind decay of the maximum value of the mean concentration profile

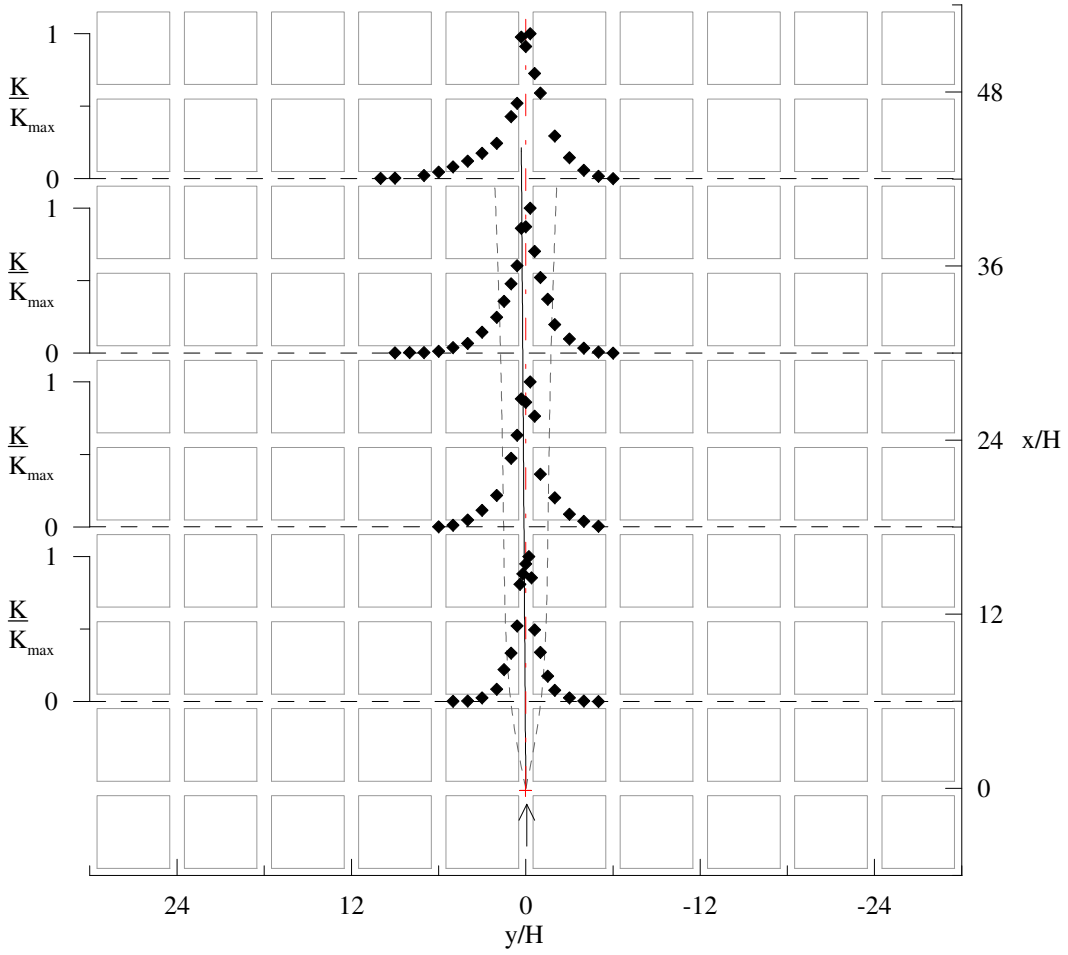

Figure 3.50: Overall plume behaviour within the array, **configuration 2**

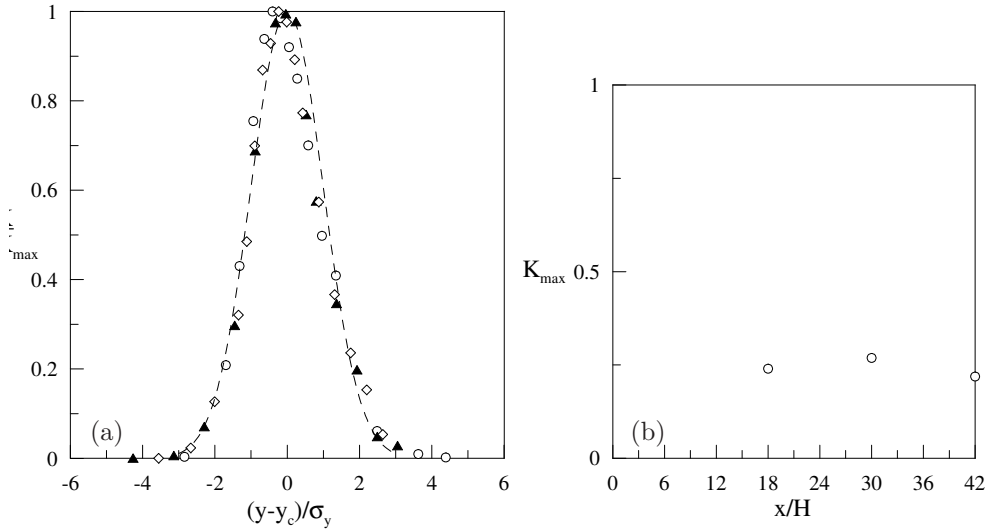

a) Normalized mean concentration profiles at various positions downstream the source and unitarian Gaussian curve (dashed line); b) downwind decay of the maximum value of the mean concentration profile

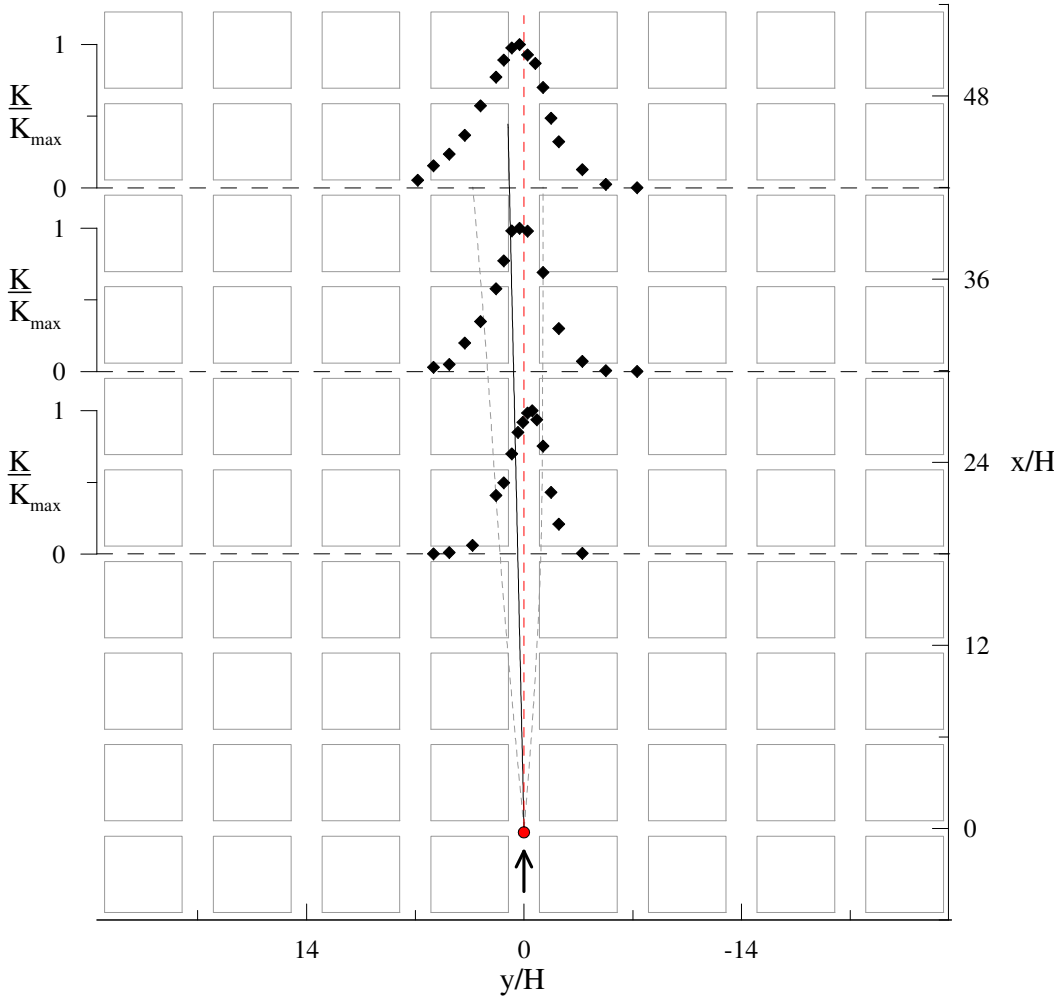

Figure 3.51: Overall plume behaviour above the array, **configuration 2**

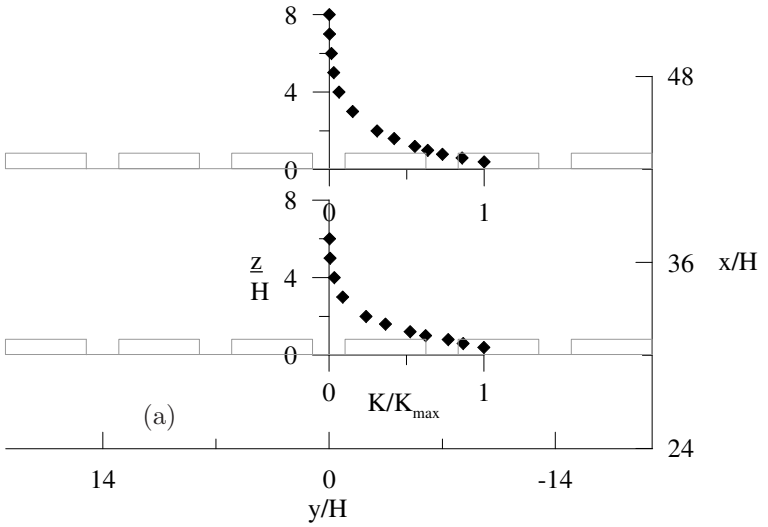

a) Normalized vertical mean concentration profiles at various positions downstream the source and unitarian Gaussian curve (dashed line);

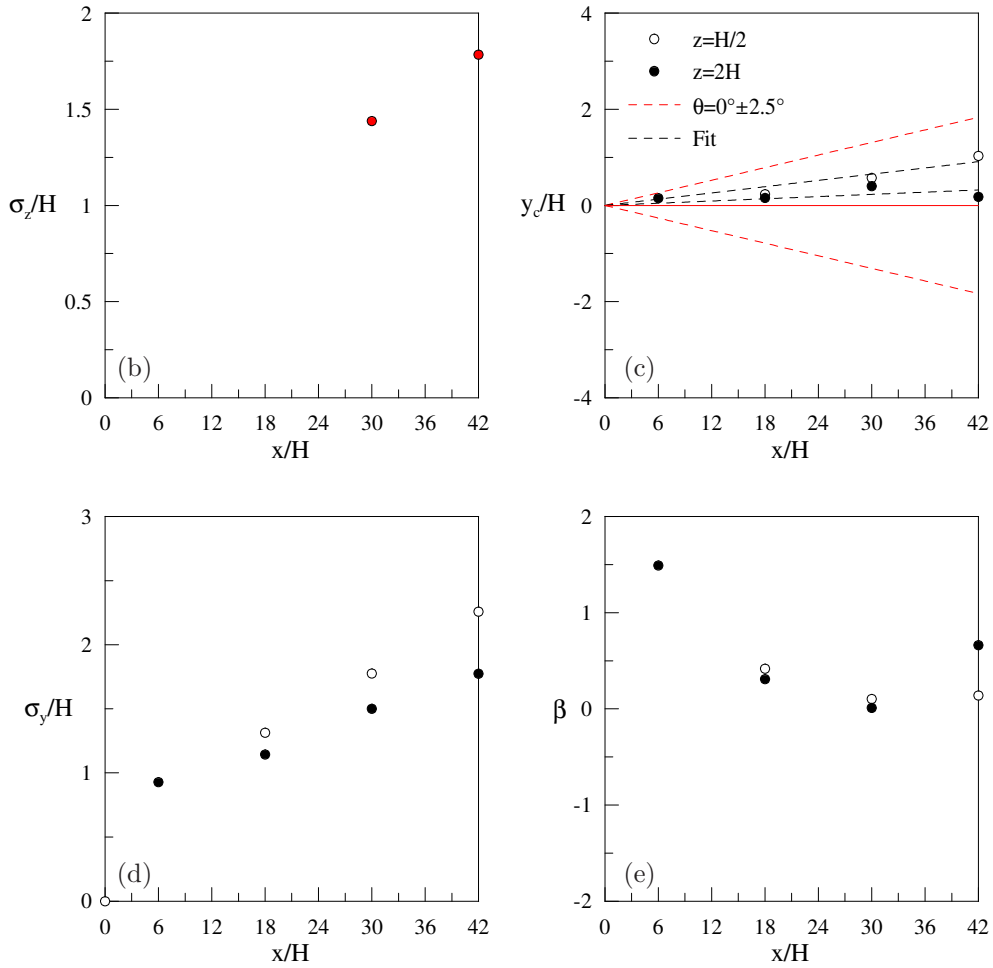

b) Evolution of the vertical dispersion parameter. Moments of the horizontal mean concentration profiles at various positions downstream the source: c) plume deflection; d) standard deviation; e) skewness.

Figure 3.52: Description of the plume, **configuration 2**

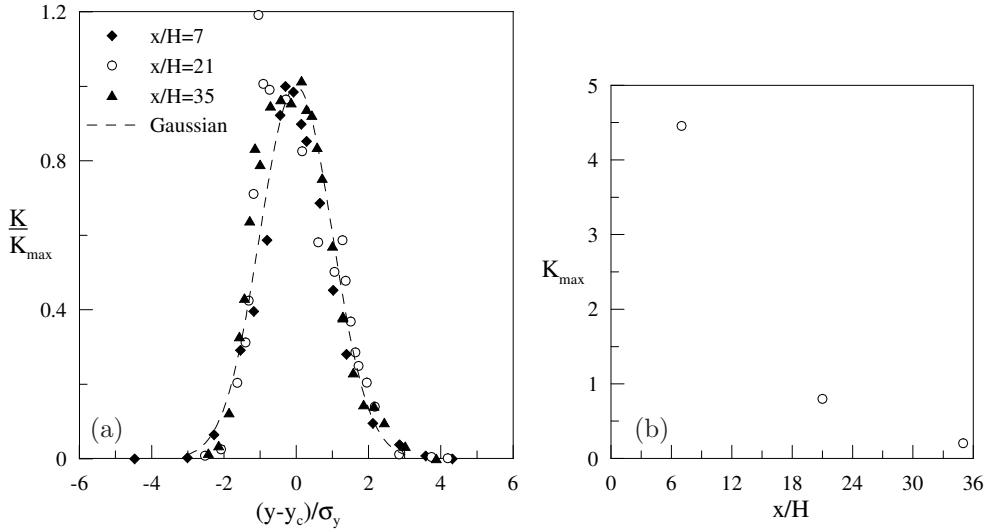

a) Normalized mean concentration profiles at various positions downstream the source and unitarian Gaussian curve (dashed line); b) downwind decay of the maximum value of the mean concentration profile

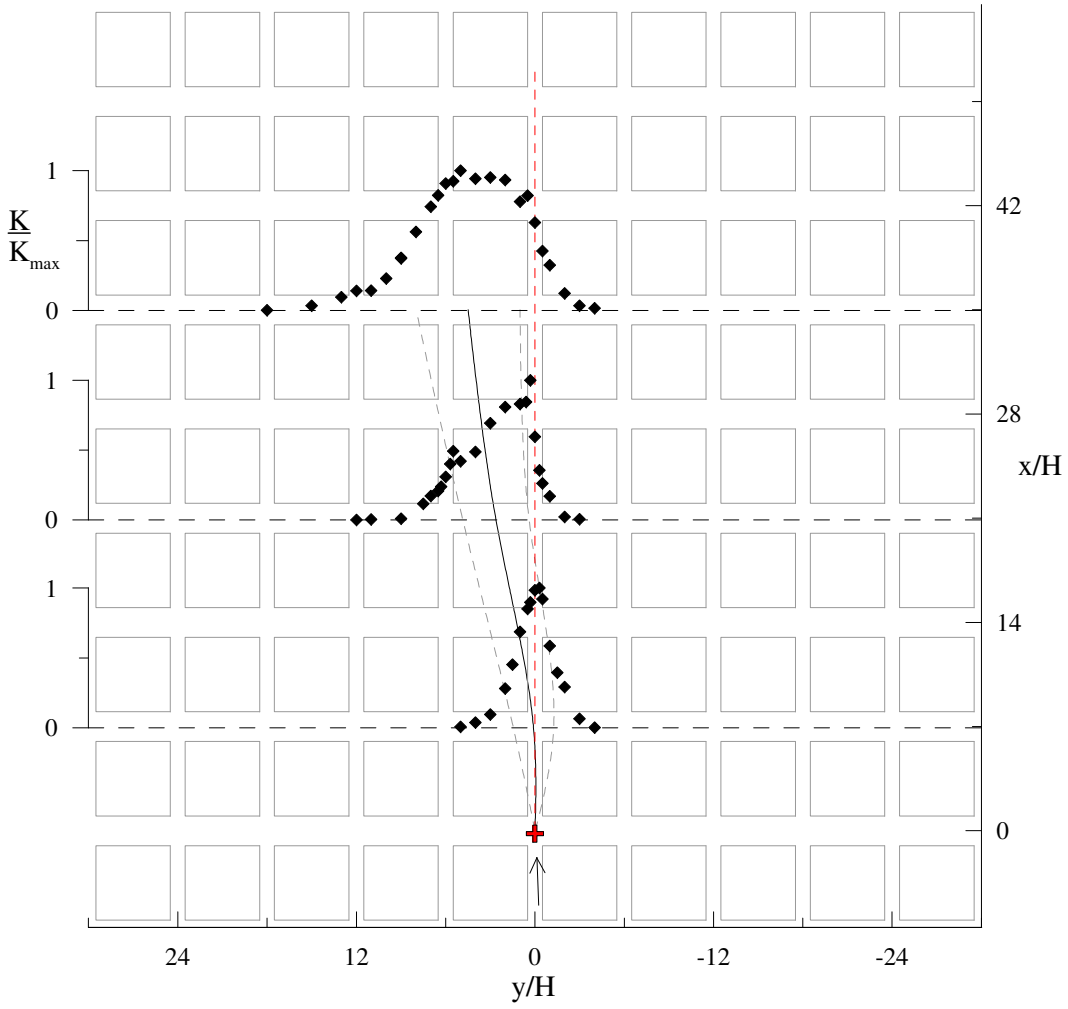

Figure 3.53: Overall plume behaviour within the array, **configuration 3**

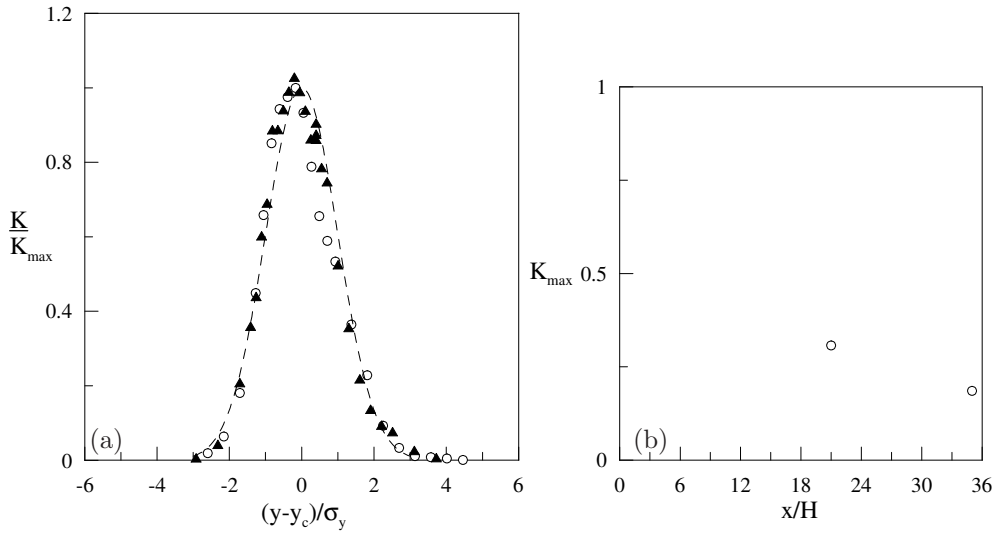

Normalized mean concentration profiles at various positions downstream the source and unitarian Gaussian curve (dashed line) (a) and downwind decay of the maximum value of the mean concentration profile (b)

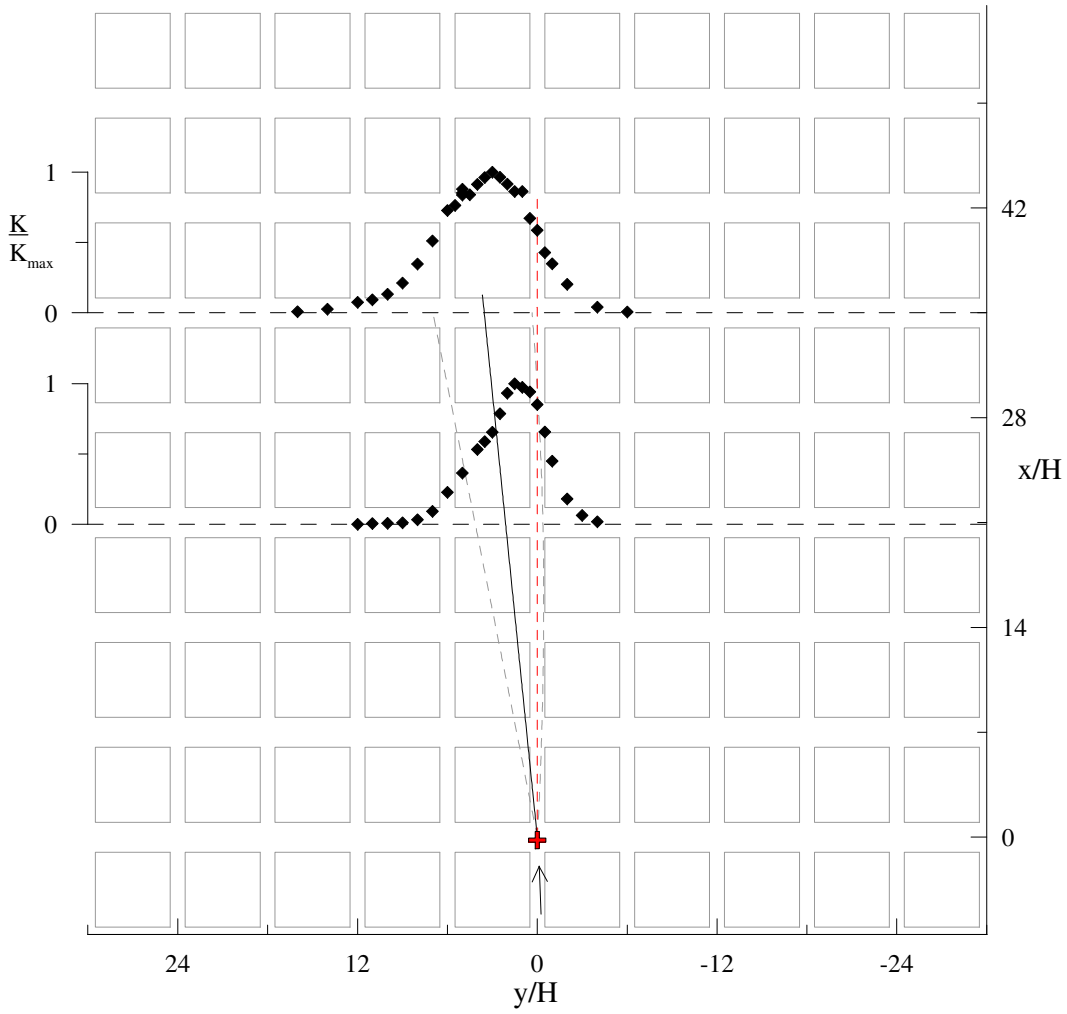

Figure 3.54: Overall plume behaviour above the array, **configuration 3**

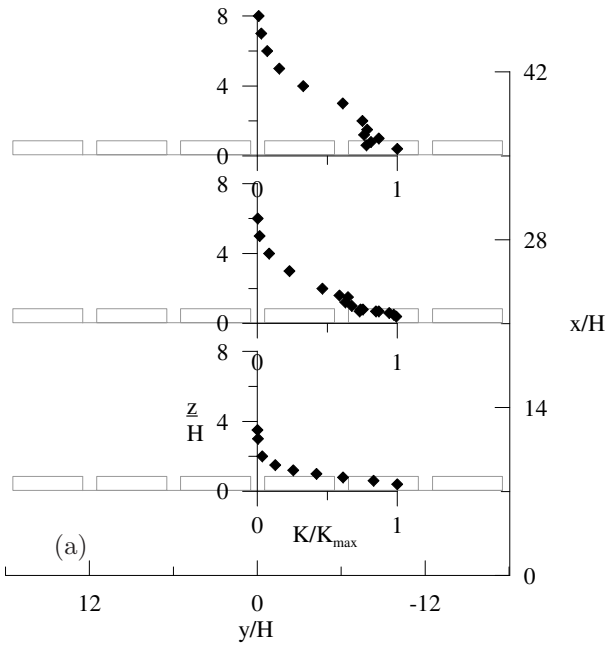

a) Normalized vertical mean concentration profiles at various positions downstream the source and unitarian Gaussian curve (dashed line); b) Evolution of the vertical dispersion parameter

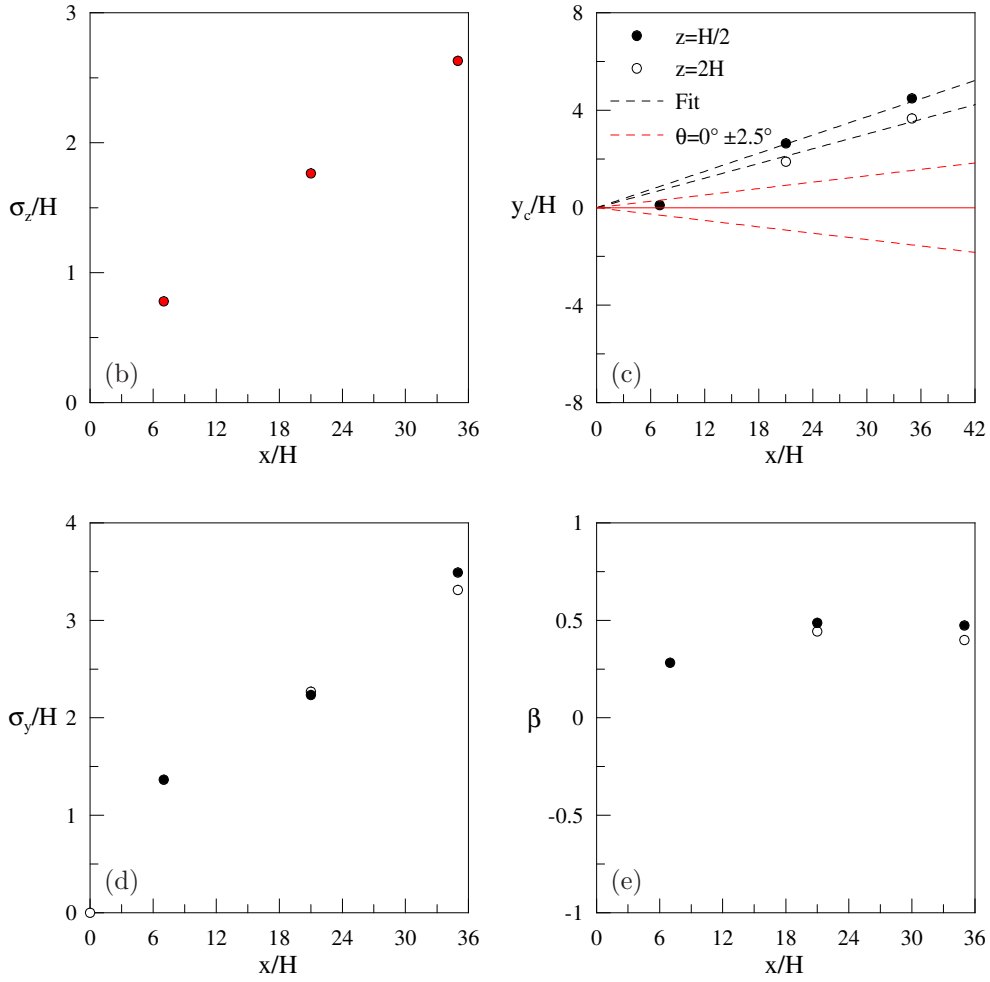

Moments of the horizontal mean concentration profiles at various positions downstream the source: b) mean concentration maximum; c) plume deflection; d) standard deviation; e) skewness.

Figure 3.55: Description of the plume, **configuration 3**

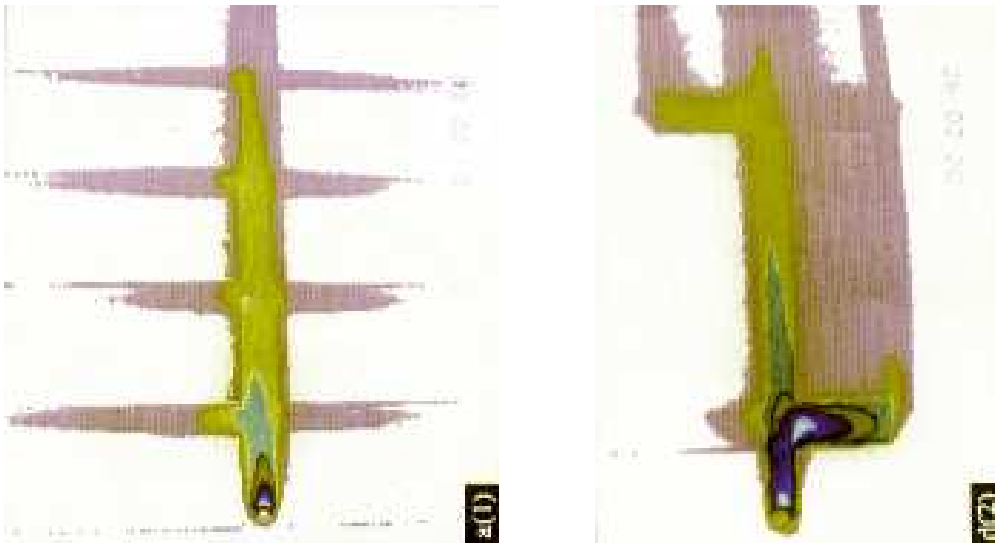

Figure 3.56: Experimental concentration field through an array according to Hoydysh et Dabberdt, Figure 2-a and 2-d.

is coherent with the flow dynamics which characterizes the three different configurations, as highlighted in the previous chapter, the skimming flow and the wake interference flow. The dispersion within the array is not isotropic due to the strong presence of the obstacles. Taking into account the configuration 2 and 3, identical arrays but different wind orientations produce totally different dispersion patterns. Therefore the effect of the obstacles on the dispersion is not only due to the geometrical configuration but mainly to the orientation of the wind regards as the neighbourhood. This contradicts the modelling approach of Briggs (Briggs, 1973) that attempted to synthesize different set of diffusion data in proposing interpolation formulas for both open country and urban areas. Briggs' interpolation formulas describe the dispersion curves for the various Pasquill stability classes and characterize urban areas as enhanced roughness terrain.

In Table 3.1 the formulas concerning the neutral stability condition are shown and are compared to the experimental values in Figure 3.57. According to Briggs the presence of urban areas increases the horizontal and the vertical spreading, in contradiction with the wind tunnel results for a street-aligned wind.

	σ_y	σ_z
Open terrain	$0.08x(1+0.0001x)^{-1/2}$	$0.06x(1+0.0015x)^{-1/2}$
Urban areas	$0.16x(1+0.0004x)^{-1/2}$	$0.14x(1+0.0003x)^{-1/2}$

Table 3.1: Briggs' interpolation formulas

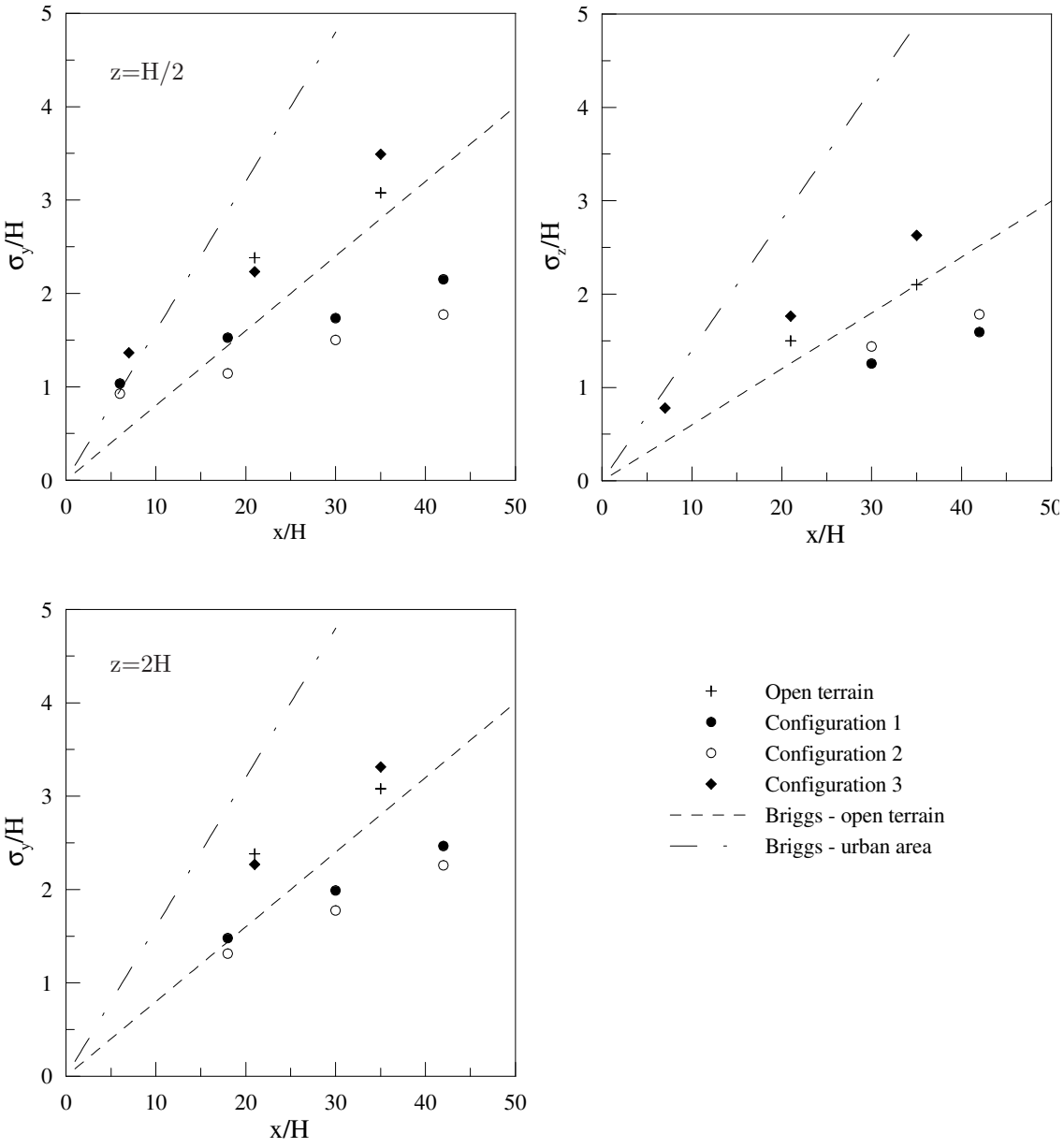

Figure 3.57: Lateral and vertical plume spread as function of distance from the source in the different studied configurations.

3.3.4 Influence of the wind direction

In order to study how the wind direction affects the dispersion, the turning surface on which the group of buildings laid was rotated of various angles. Configuration 1 was investigated for wind incident angles equal to 10^o, 25^o and 45^o. As discussed before, experimental problems did not allow to know exactly the wind direction and so it was defined in the range $\pm 2.5^o$. Configuration 2 was investigated for the wind orientation equal to $45^o \pm 2.5^o$. Our goal was to evaluate how the lateral and the vertical plume spreading evolve with the distance from the source and how they are affected by the local arrangement of the array.

Two coordinate systems are taken into account in order to describe the plume behaviour, one is aligned with the wind direction $\{x_{\mathrm{EFF}}, y_{\mathrm{EFF}}, z\}$ and the other is aligned with the axis of the array $\{x, y, z\}$. If θ is the angle between the wind direction and the axis of the array, the transformation between the coordinate systems is

$$x_{\mathrm{EFF}} = x \cdot cos\theta + y \cdot sin\theta \tag{3.16}$$

$$y_{\mathrm{EFF}} = -x \cdot sin\theta + y \cdot cos\theta \tag{3.17}$$

The concentration measurements have been performed throughout the array and are initially presented for each studied angle referring to the coordinate system of the array. Nevertheless, as the concentration profiles are measured along the street of the array, the calculated moments depend on the angle θ the street forms with the wind direction, as shown in 3.58.

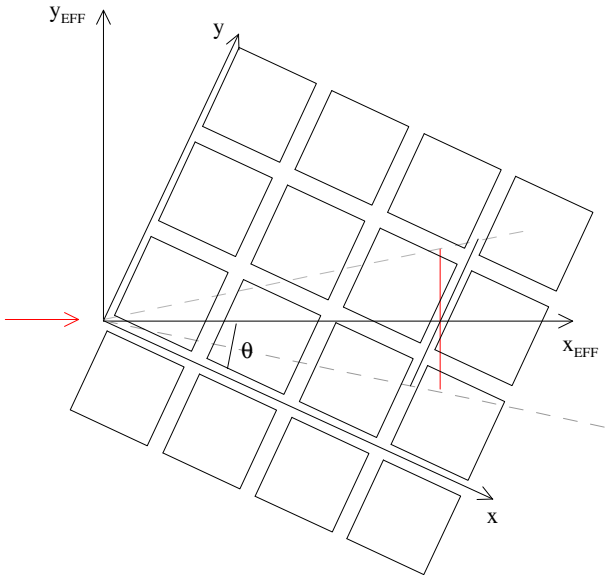

Figure 3.58: Coordinate systems

Successively, the moments of the distribution will be expressed according to the reference system aligned with the wind direction in order to evaluate the effective plume spreading and to allow comparing the effect of the array orientation respect to the incident wind. The effective moments in the coordinate system solidal with the wind can be approximated as:

$$y_{c,\mathrm{EFF}}(x/cos\theta) = y_c \cdot cos\theta \tag{3.18}$$

$$\sigma_{y,\mathrm{EFF}}(x/cos\theta) = \sigma_y \cdot cos\theta \tag{3.19}$$

$$\sigma_{z,\mathrm{EFF}}(x/cos\theta) = \sigma_z \tag{3.20}$$

$$\tag{3.21}$$

In Figure 3.59 the normalized horizontal profiles of the mean concentration within the array for the wind direction equal to $\theta = \mathbf{10^o} \pm 2.5^o$ are plotted and show a totally asymmetric shape, since the pollutants exchanges are dominated by the advection process at the intersection. A mean transversal flow directed towards the street takes place at the intersection as consequence of the external wind orientation and transports few pollutants into the street. It is worth noting that the maximum value of concentration in each profile is confined into the channel that holds the source and the plume deflection is reduced regards to the expected value, both effects of the channelling phenomenon. Figure 3.60 shows that the normalized horizontal profiles above the array are well described by a Gaussian model. This suggests that at the height $z = 2H$ the local inhomogeneities vanished and the obstacle array may be represented by an effective roughness that does not only depend on the geometrical layout but is function of the wind direction. In fact, the dispersion pattern within the array is strongly affected by the direction of the incident wind respect to the obstacles and diffuses above the array. In Figure 3.61 the vertical profiles of mean concentration are shown at different positions along the y-axis and presents different standard deviations. The plume deflection above the array is consistent with the wind orientation $\theta = 10^o \pm 2.5^o$, while within the array the centreline is shifted regards to the expected line because the effect of channelling confines the plume.

Figure 3.62 shows the normalized horizontal profiles of the mean concentration within the array for a wind direction equal to $\theta = \mathbf{25^o} \pm 2.5^o$. It is worth noting that the far-field profiles look like steps, as the concentration is quasi-constant along the street, while at the intersection abrupt variations are observed. This means that what happens in the intersections is determinant to control the dispersion mechanisms within a street network. Figure 3.63 shows that the normalized horizontal profiles above the array are well described by a Gaussian curve. In Figure 3.64 the vertical profiles of mean concentration are shown and their behaviour varies according to the different sampling positions within the array. The standard deviation of the vertical distributions at $x = 24$H is plotted as function of the distance from the theoretical centerline y_c[2] and there are several values of the standard deviation corresponding to a single distance. It should be noted that x does not express the effective distance from the source, as explained at the beginning of this section. The best evaluation of σ_z at the distance x is assumed to be the standard deviation of the distribution that has been measured near as possible to the plume centerline. The best estimation of the standard deviation is plotted as function of the distance x to show the evolution of the vertical dispersion parameter downwind the source. The plume deflection above the array is consistent with the wind orientation $\theta = 25^o \pm 2.5^o$, while within the array the centreline is shifted with respect to the expected line. Conversely to the case of the wind parallel to the x-axis, the plume spreading is more enhanced within the array than above it, since the pollutants are transported into the streets by the mean flow and their concentration remains roughly constant because of the weak vertical mass exchanges along the streets.

Concerning $\theta = \mathbf{45^o} \pm 2.5^o$, the horizontal profiles of mean concentration have been carried within and above the array both along the x-axis and the y-axis of the array and are presented in Figure 3.65, 3.66, 3.67 and 3.68. The profiles along the x-axis correspond to the wind orientation θ, while those along the y-axis correspond to $90^o - \theta$, and if the wind direction was exactly $\theta = 45^o$ the profiles at the same distance from the source should match. However, the expected symmetrical dispersion pattern has not been observed - as in the case of the wind parallel to the x-axis. The condition of symmetry, i.e. $\theta = 0^o$ or $\theta = 45^o$, can be considered an unstable equilibrium state, since the system moves away from the equilibrium after small disturbances. As everything should be stable to be observable, a totally symmetrical dispersion pattern is very hard to be detected. The profiles within the array show the typical 'step' behaviour: the concentration is approximately constant along the street axis and abrupt gradients occur at

[2]The theoretical centerline correspond to the wind direction, i.e. $y_c = x \cdot cos\theta$

the intersection. The profiles above the array are instead well fitted by Gaussian curves and confirm that at $z = 2H$ all the inhomogeneities due to the presence of the obstacles vanish. In Figure 3.69 the moments of the distributions which have been performed along the x-axis, both within and above the array, are plotted as function of the distance from the source, while Figure 3.70 refers to the distributions which have been measured along the y-axis. In both the figures a slight deflection of the plume has been observed that is consistent with the uncertainty in the definition of the angle and is the same within and above the array: the obstacles do not impose any preferred direction in the dispersion of the plume, as confirmed by the small values of the skewness. It is worth noting that the profiles, except at the first row where the release conditions may be not negligible, are rather symmetrical regards to the axis $y = y_{c,th}$ because of the symmetry of the layout regards to the wind direction.

Finally we investigate how the wind orientation $\theta = 45^o \pm 2.5^o$ affects the dispersion pattern in configuration 2. The horizontal profiles of mean concentration have been carried both along the x-axis and the y-axis of the array, as shown in Figure 3.71, 3.72, 3.73 and 3.74. The plume deflection within and above the array is driven by the external wind orientation and any asymmetry related to the asymmetry of the layout is detected. The only effect concerns the shape of the concentration distribution: along the y-axis, i.e. $S_x = H$, the typical step profile is observed - quasi-constant concentration values along the street and abrupt variations at the intersections - while along the x-axis, i.e. $S_y = 2H$, a step profile is present together with a smoother profile. As explanation, the array is divided in two regions regards to the angle $\theta = 45^o$: for $\theta < 45^o$ the intersections contribute to the concentration distribution along the x-axis and a step profile takes place, while for $\theta > 45^o$ the contribution from the intersections becomes negligible and then a smooth profile is present. In Figure 3.75, the vertical profiles at different position downstream the source are plotted and point out the different behaviour according to the position. The standard deviation of the vertical distributions is plotted as function of the distance from the theoretical centerline y_c and as function of the distance x. In Figure 3.76 the moments of the concentration distributions performed along the x-axis within and above the array are plotted as function of the distance from the source, while in Figure 3.77 those of the concentration distributions performed along the y-axis are shown. The plume deflection follows the orientation of the wind, both within and above the array. The plume spreading is larger within the array due to the presence of the obstacles that canalize the pollutants within the streets, where it is captured.

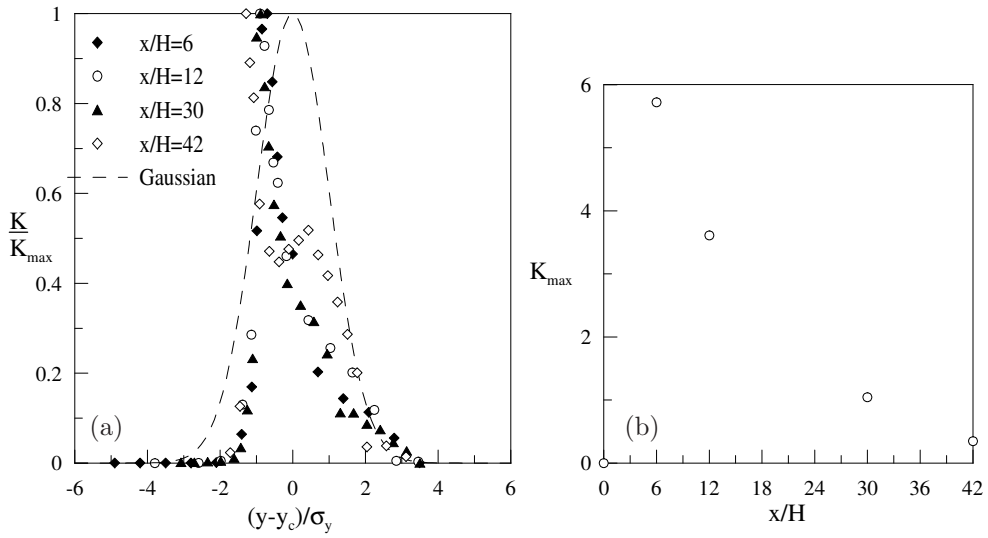

a) Normalized mean concentration profiles at various positions downstream the source and unitarian Gaussian curve (dashed line); b) downwind decay of the maximum value of the mean concentration profile

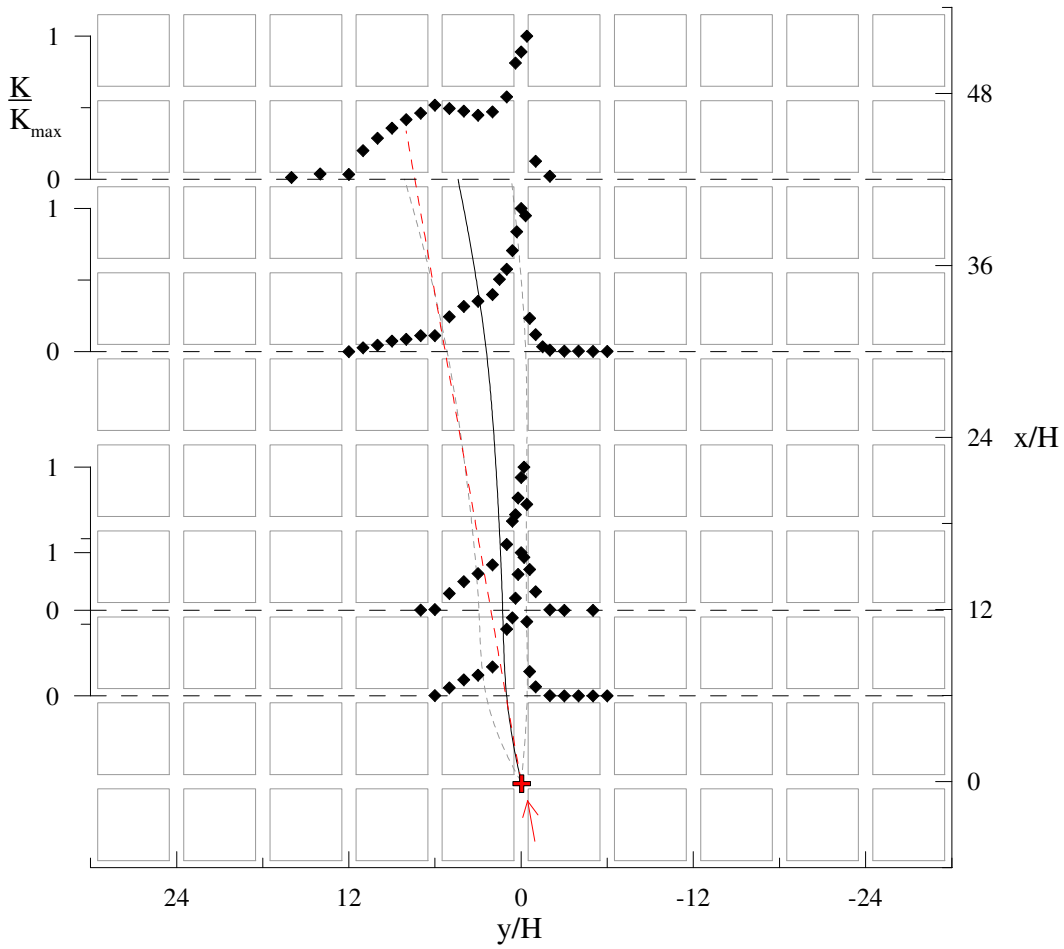

Figure 3.59: Overall plume behaviour within the array (z=H/2) - $\theta = \mathbf{10^o}$

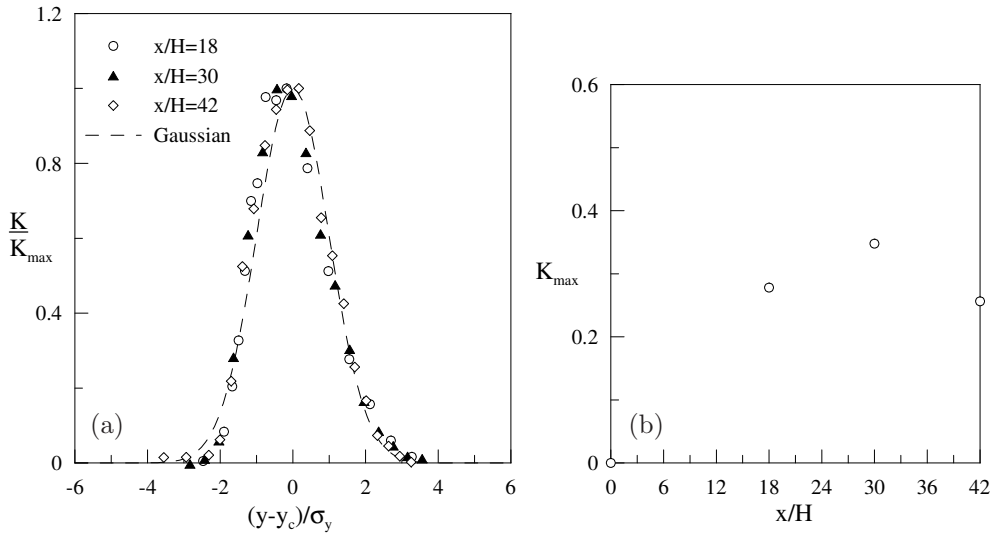

a) Normalized mean concentration profiles at various positions downstream the source and unitarian Gaussian curve (dashed line); b) downwind decay of the maximum value of the mean concentration profile

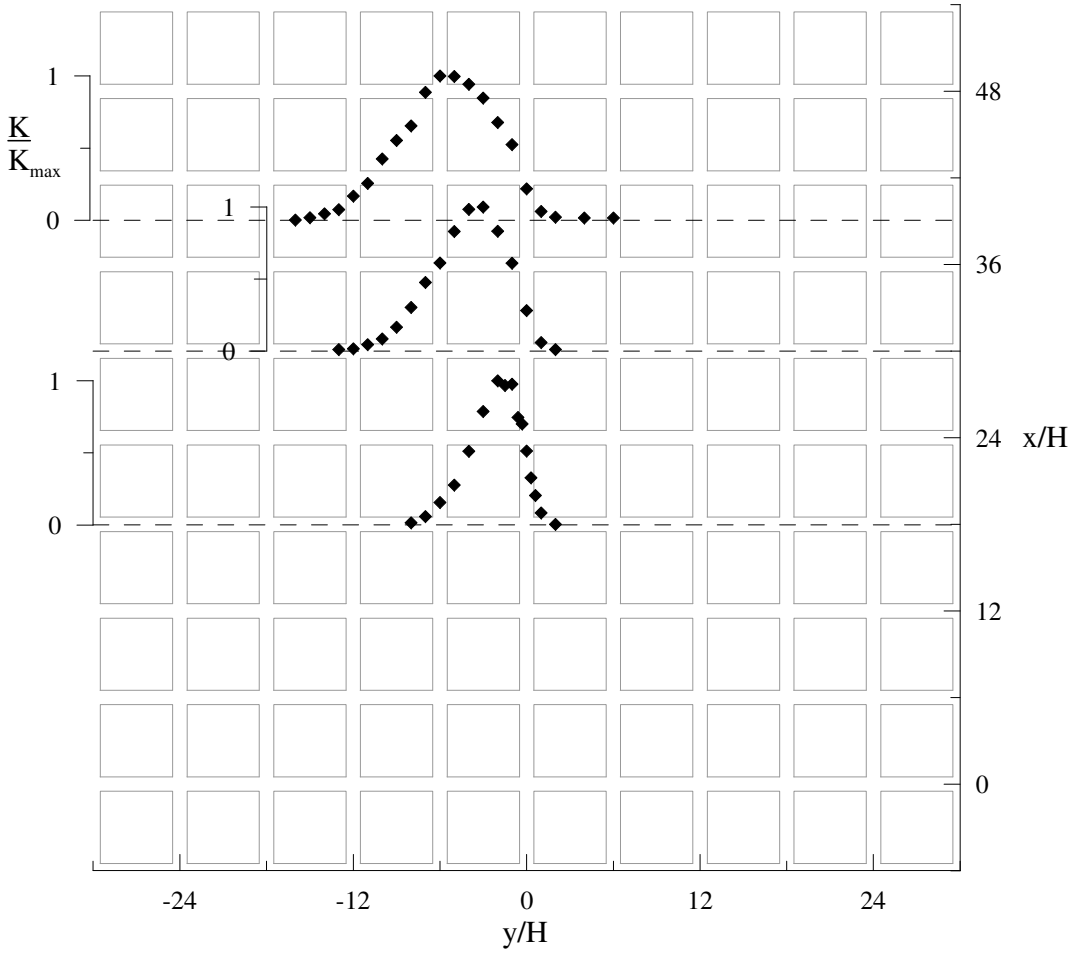

Figure 3.60: Overall plume behaviour above the array (z=2H) - $\theta = \mathbf{10^o}$

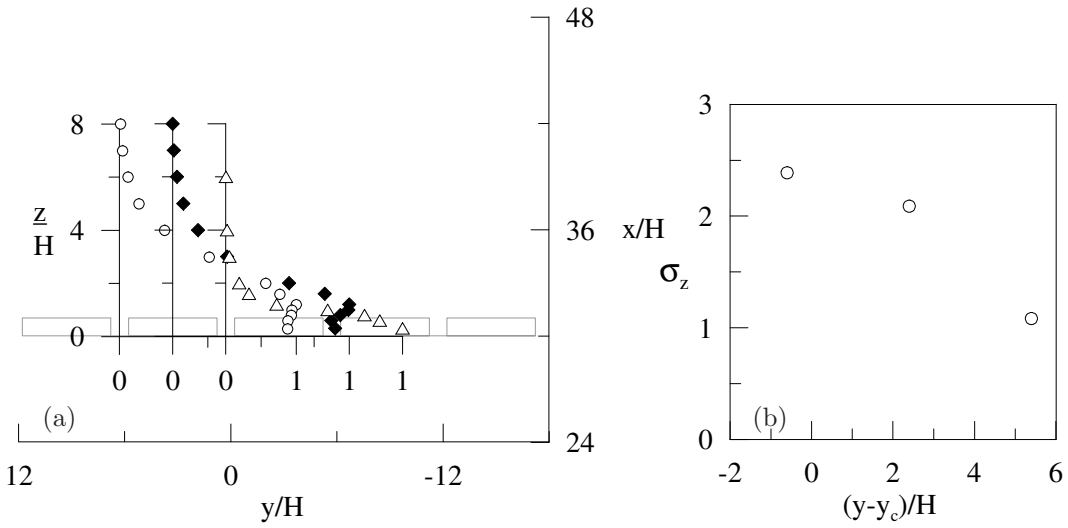

a) Normalized vertical mean concentration profiles at various positions downwind the source; b) evolution of the vertical dispersion parameter

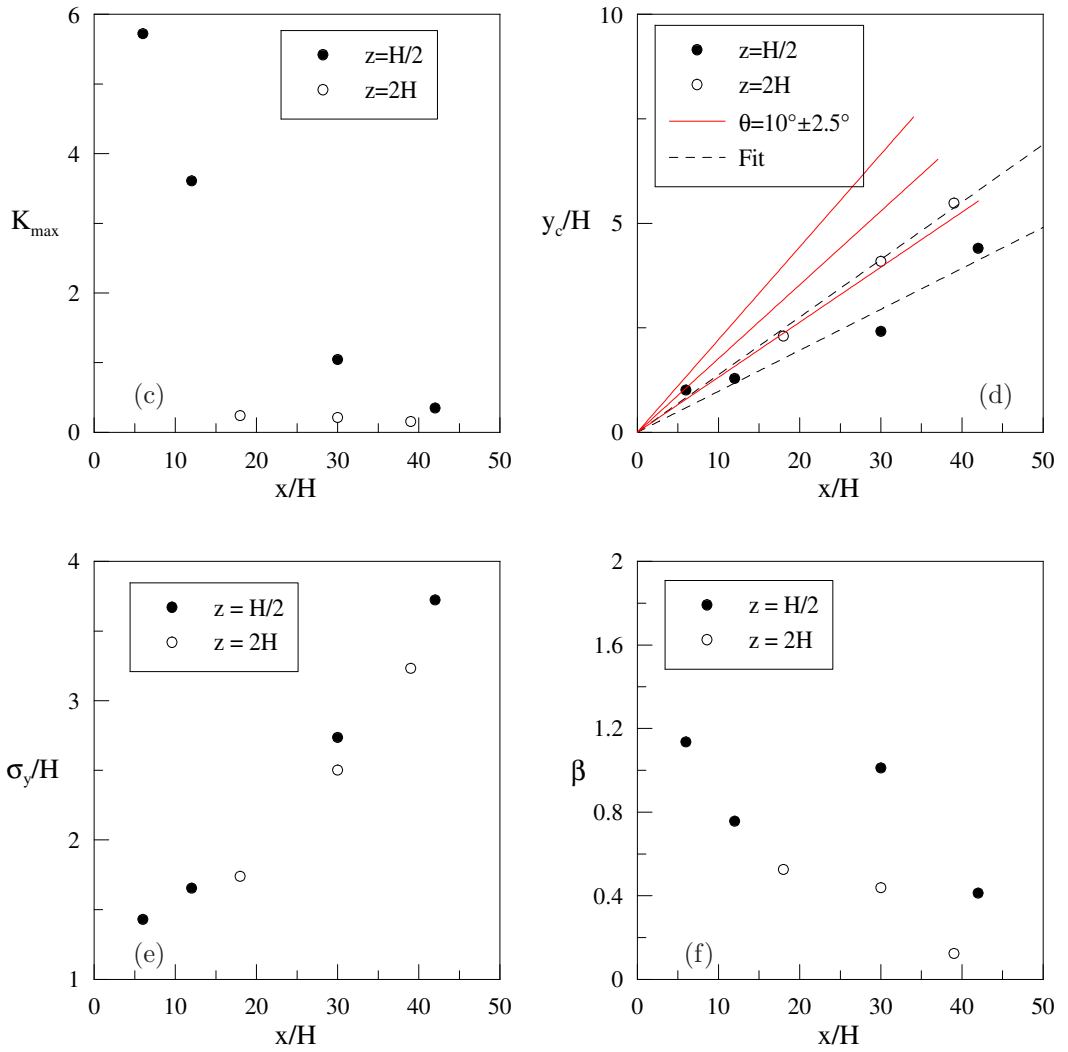

Moments of the horizontal mean concentration profiles at various positions downstream the source: c) mean concentration maximum; d) plume deflection; e) standard deviation; f) skewness.

Figure 3.61: Description of the plume - $\theta = \mathbf{10^o}$

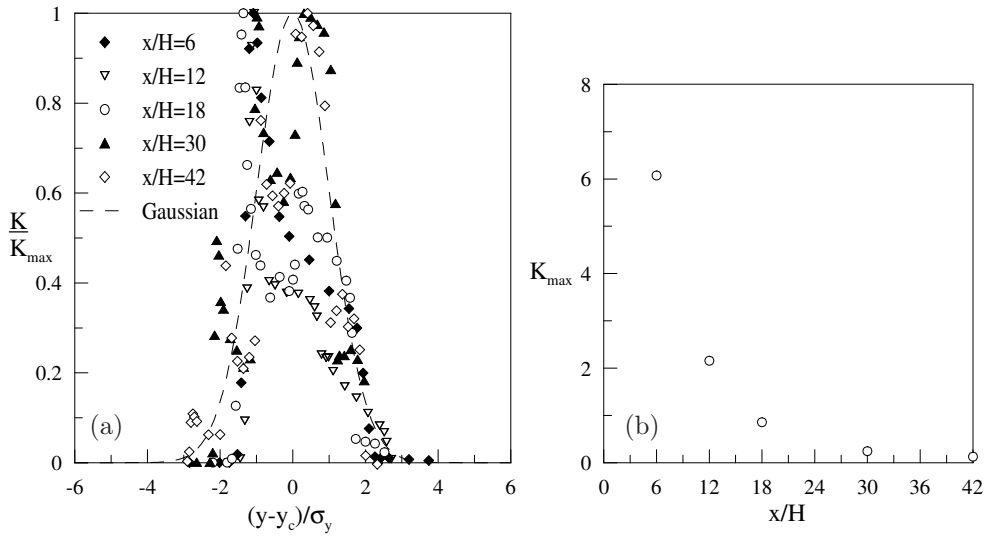

a) Normalized horizontal mean concentration profiles at various positions downstream the source and unitarian Gaussian curve (dashed line); b) downwind decay of the maximum mean concentration value

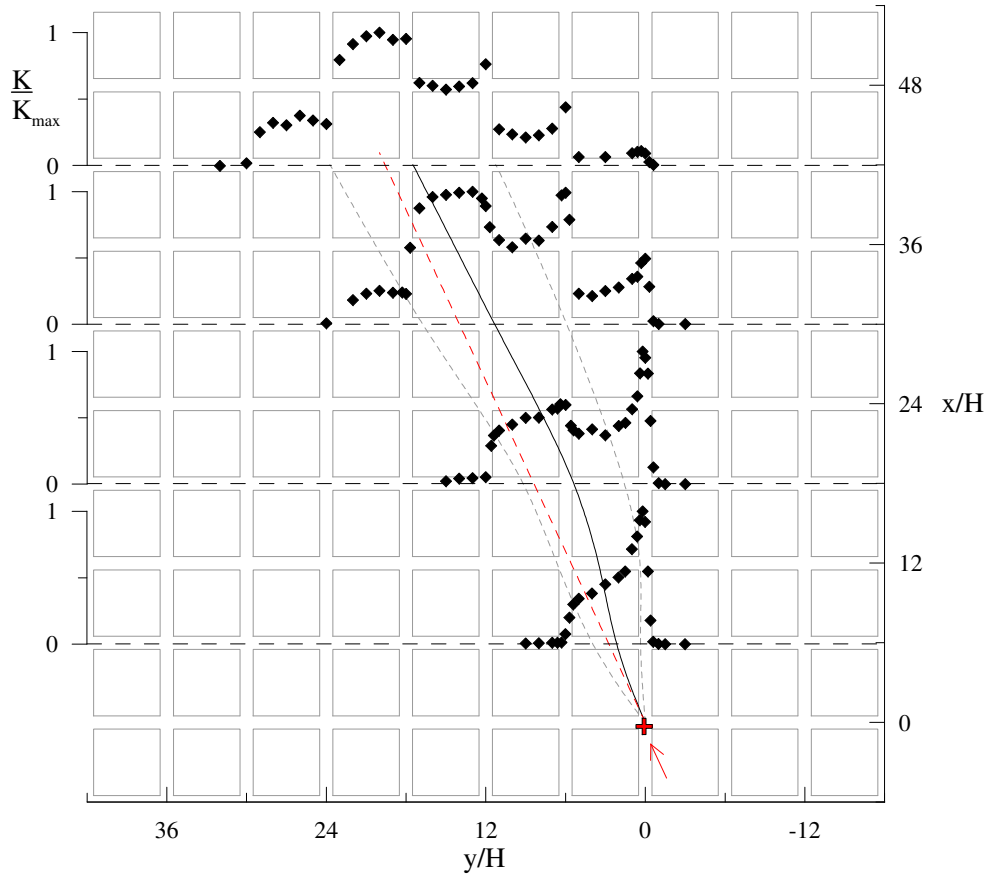

Figure 3.62: Overall plume behaviour within the array (z=H/2) - $\theta = \mathbf{25^o}$

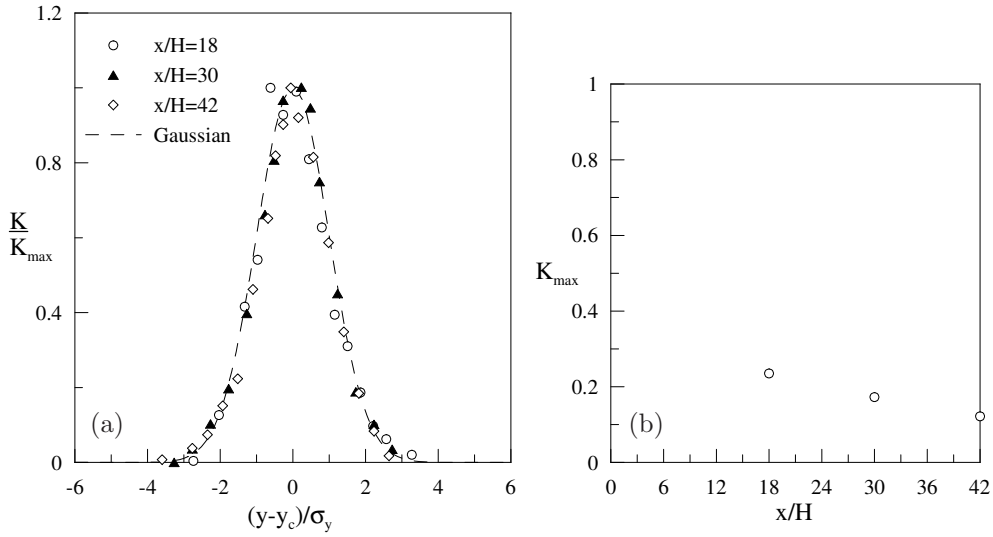

Normalized horizontal mean concentration profiles at various positions downstream the source and unitarian Gaussian curve (dashed line) (a) and downwind decay of the maximum value of the mean concentration profile (b)

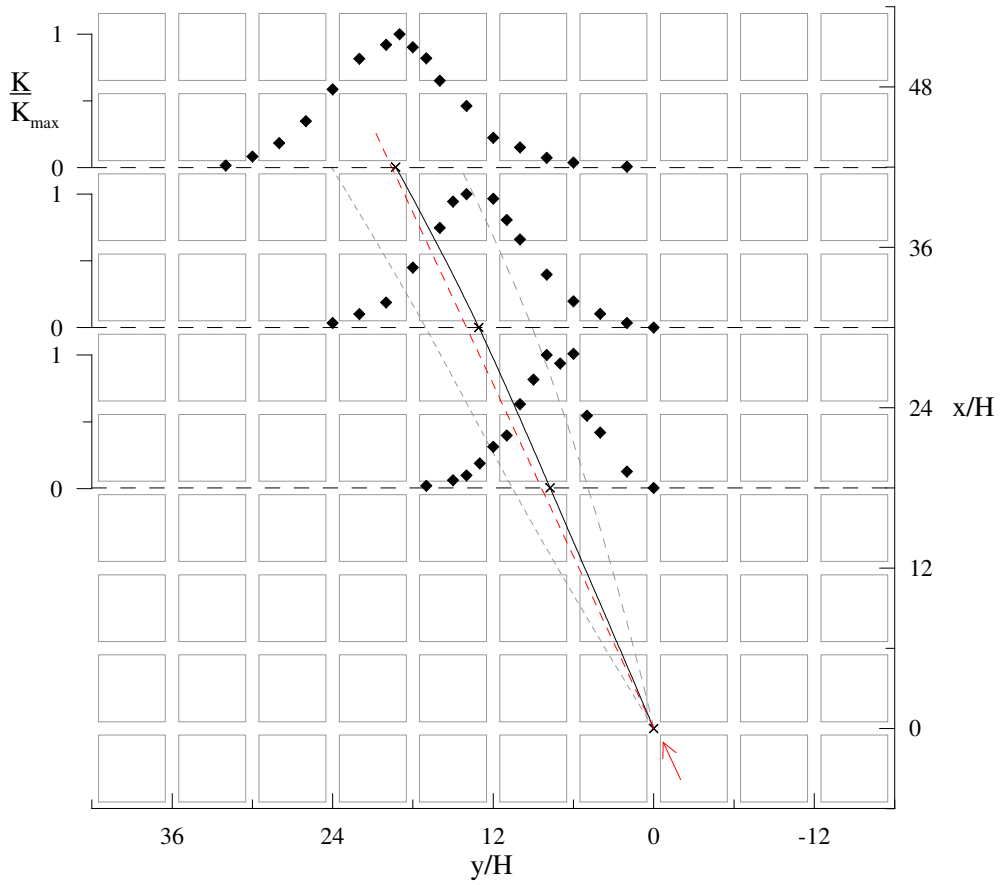

Figure 3.63: Overall plume behaviour above the array (z=2H) - $\theta = \mathbf{25^o}$

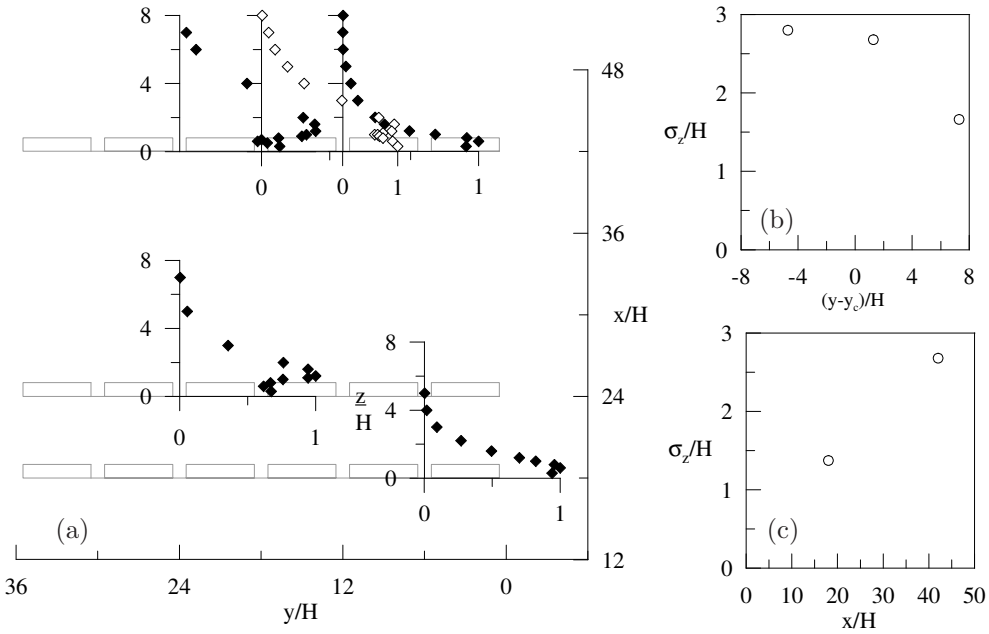

a) Normalized vertical mean concentration profiles at various positions downstream the source; b) vertical dispersion parameter as function of the distance from the theoretical centerline; c) evolution of the vertical dispersion parameter

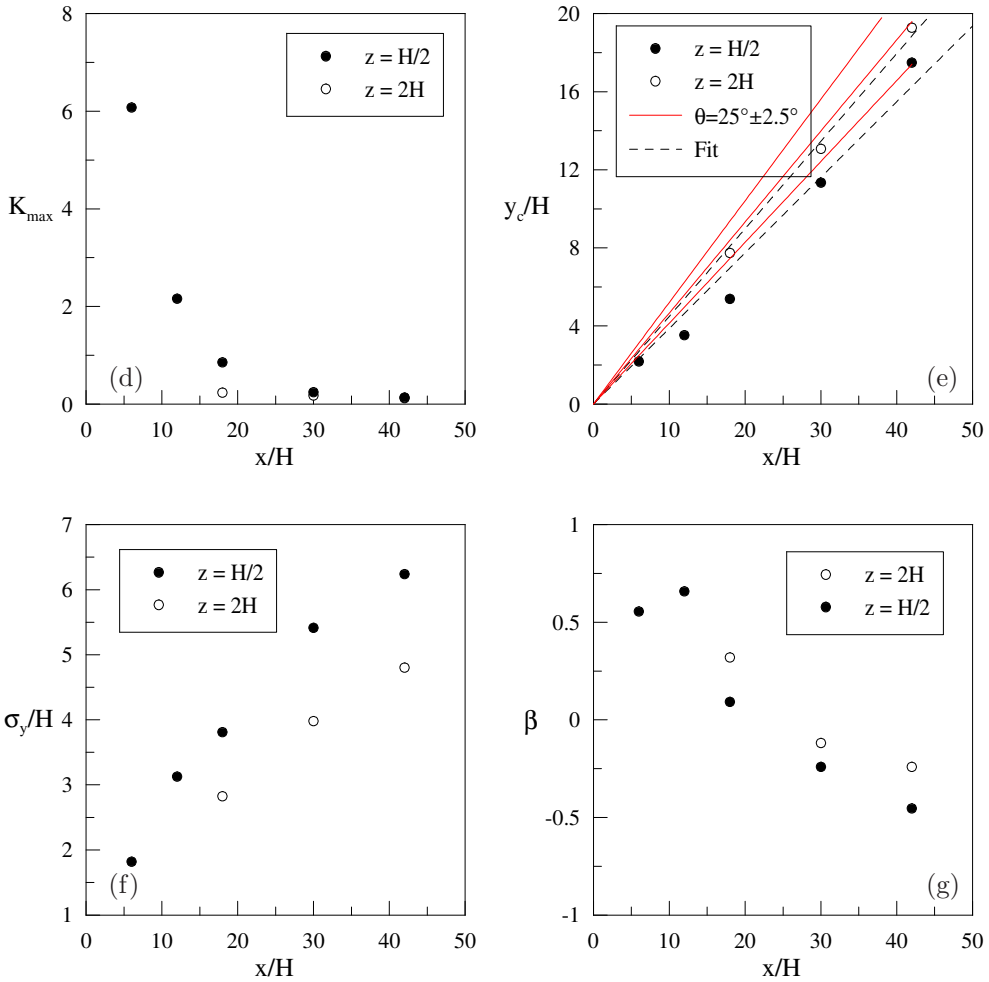

Moments of the horizontal mean concentration profiles at various positions downstream the source: d) mean concentration maximum; e) plume deflection; f) standard deviation; g) skewness.

Figure 3.64: Description of the plume - $\theta = \mathbf{25^o}$

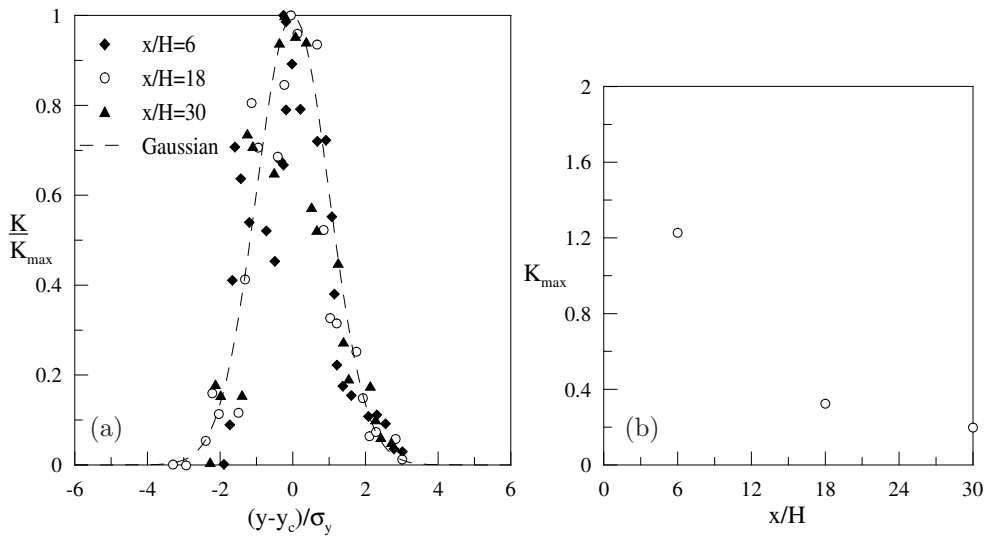

a) Normalized horizontal mean concentration profiles at various positions downstream the source and unitarian Gaussian curve (dashed line); b) downwind decay of the maximum value of the mean concentration profile

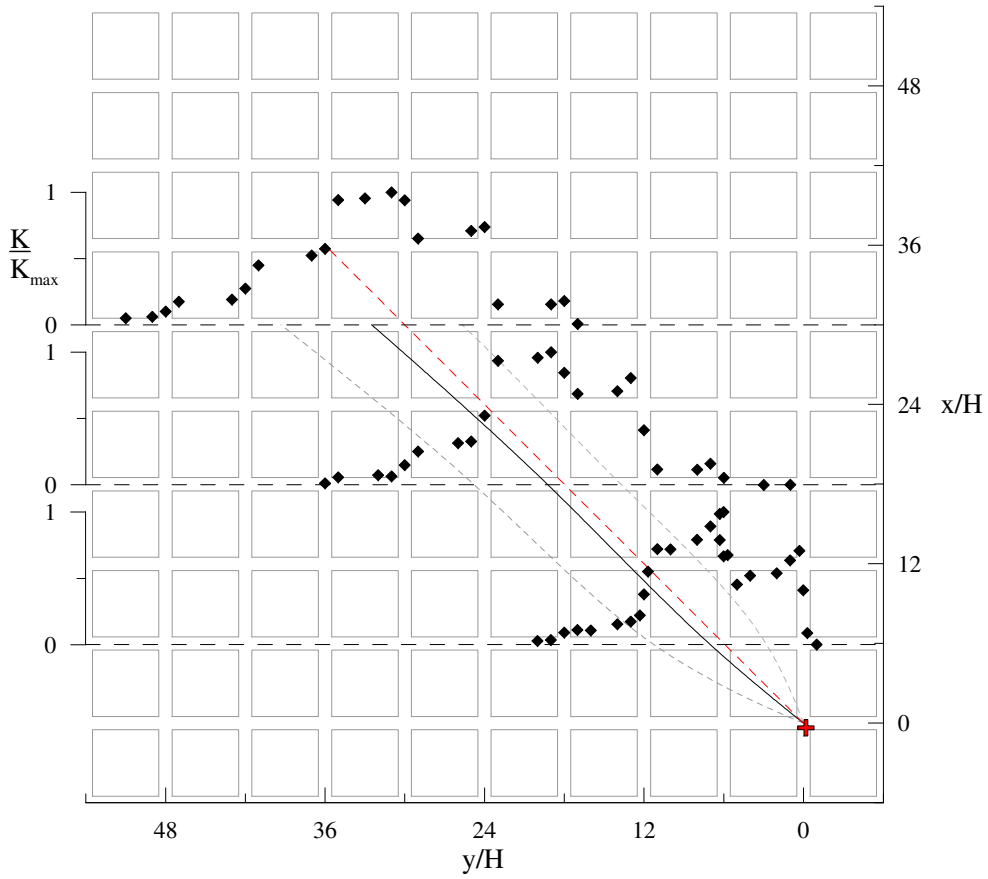

Figure 3.65: Overall plume behaviour within the array (z=H/2) - $\theta = \mathbf{45^o}$

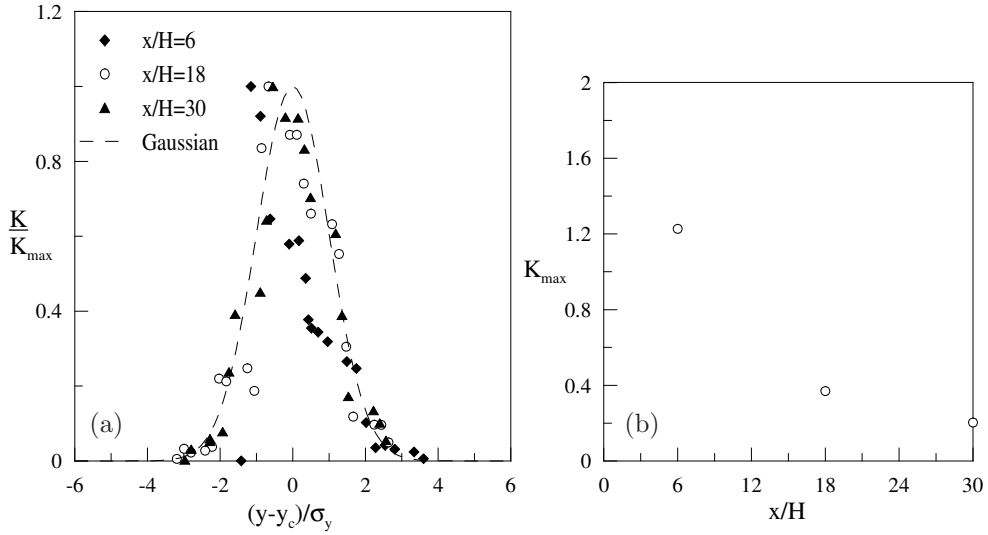

a) Normalized horizontal mean concentration profiles at various positions downstream the source and unitarian Gaussian curve (dashed line); b) downwind decay of the maximum value of the mean concentration profile

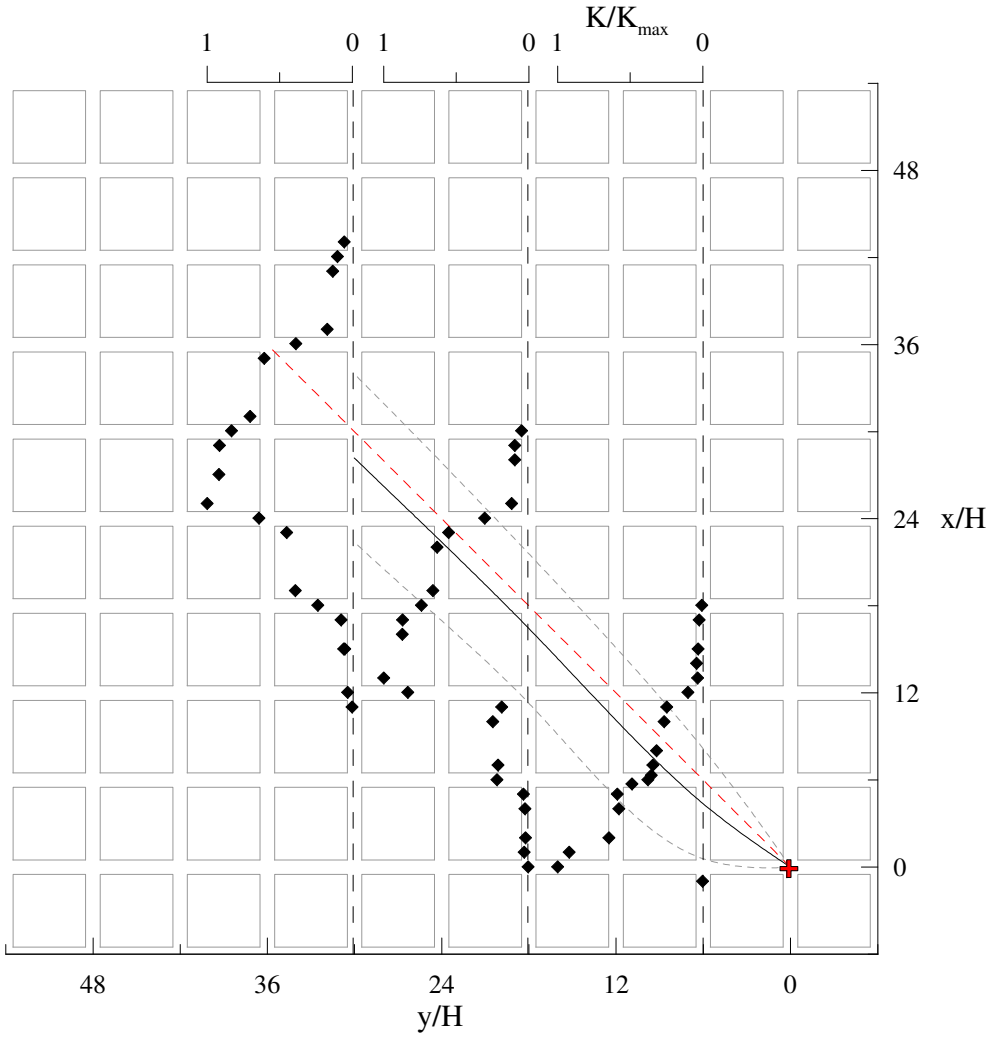

Figure 3.66: Overall plume behaviour within the array (z=H/2) - $\theta = \mathbf{45^o}$

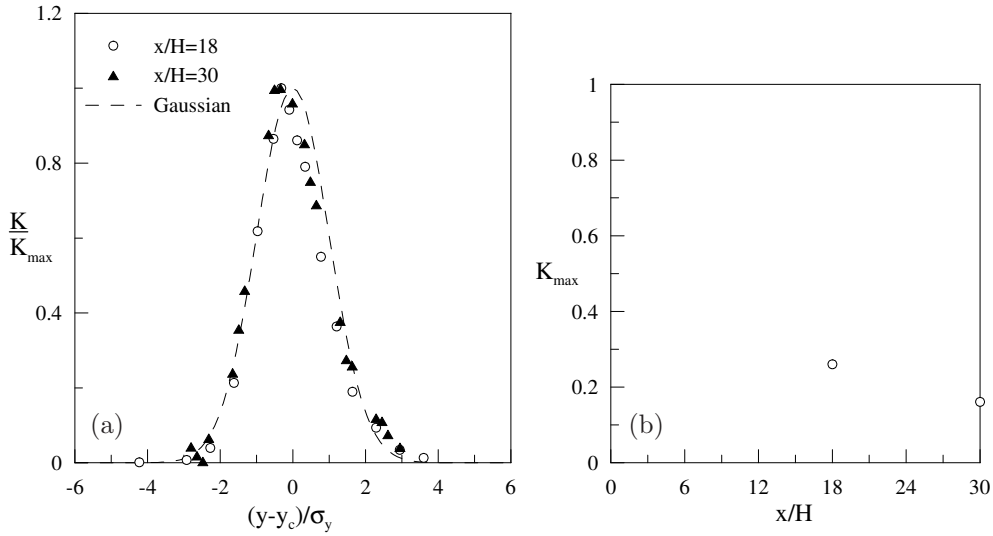

a) Normalized horizontal mean concentration profiles at various positions downstream the source and unitarian Gaussian curve (dashed line); b) downwind decay of the maximum value of the mean concentration profile

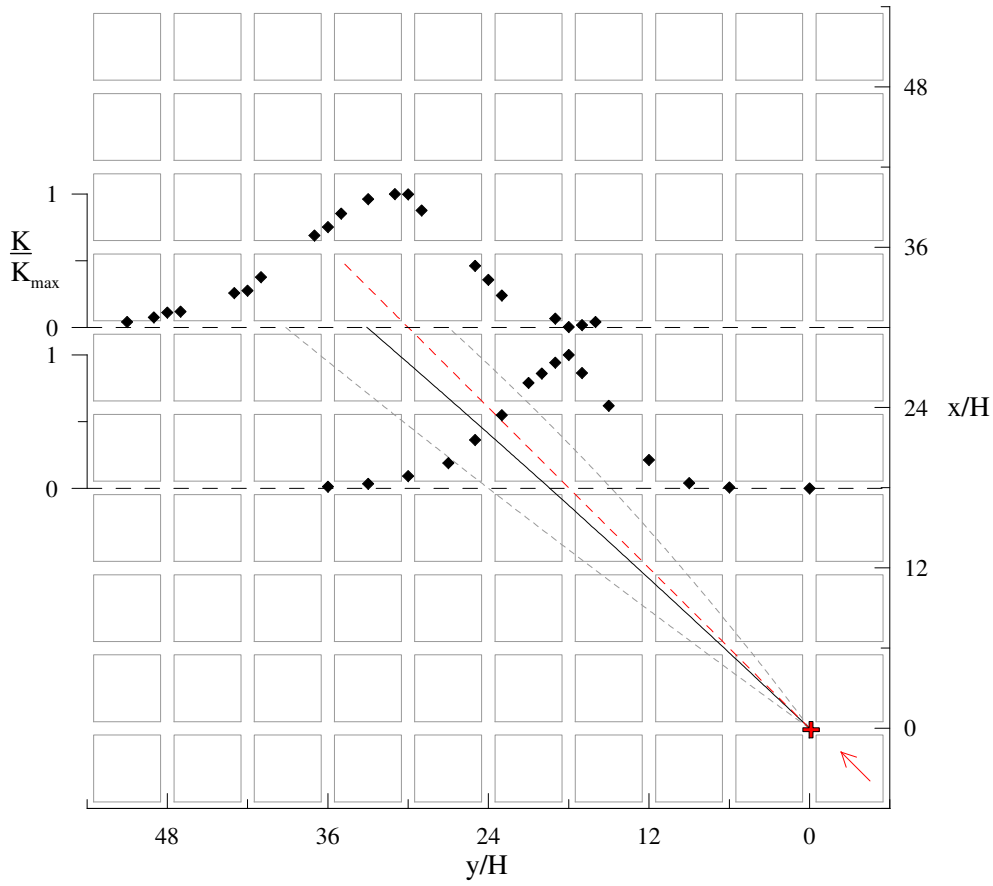

Figure 3.67: Overall plume behaviour above the array (z=2H) - $\theta = \mathbf{45^o}$

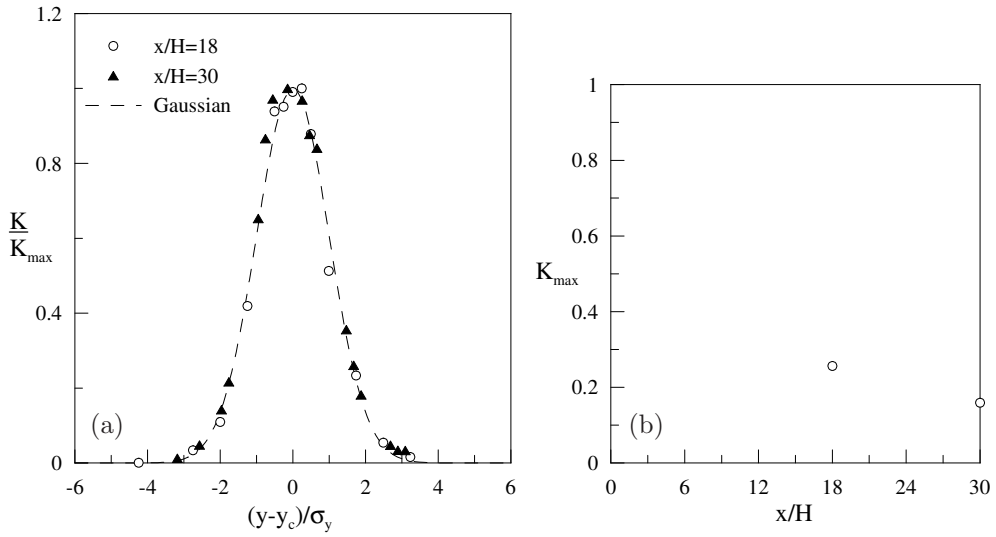

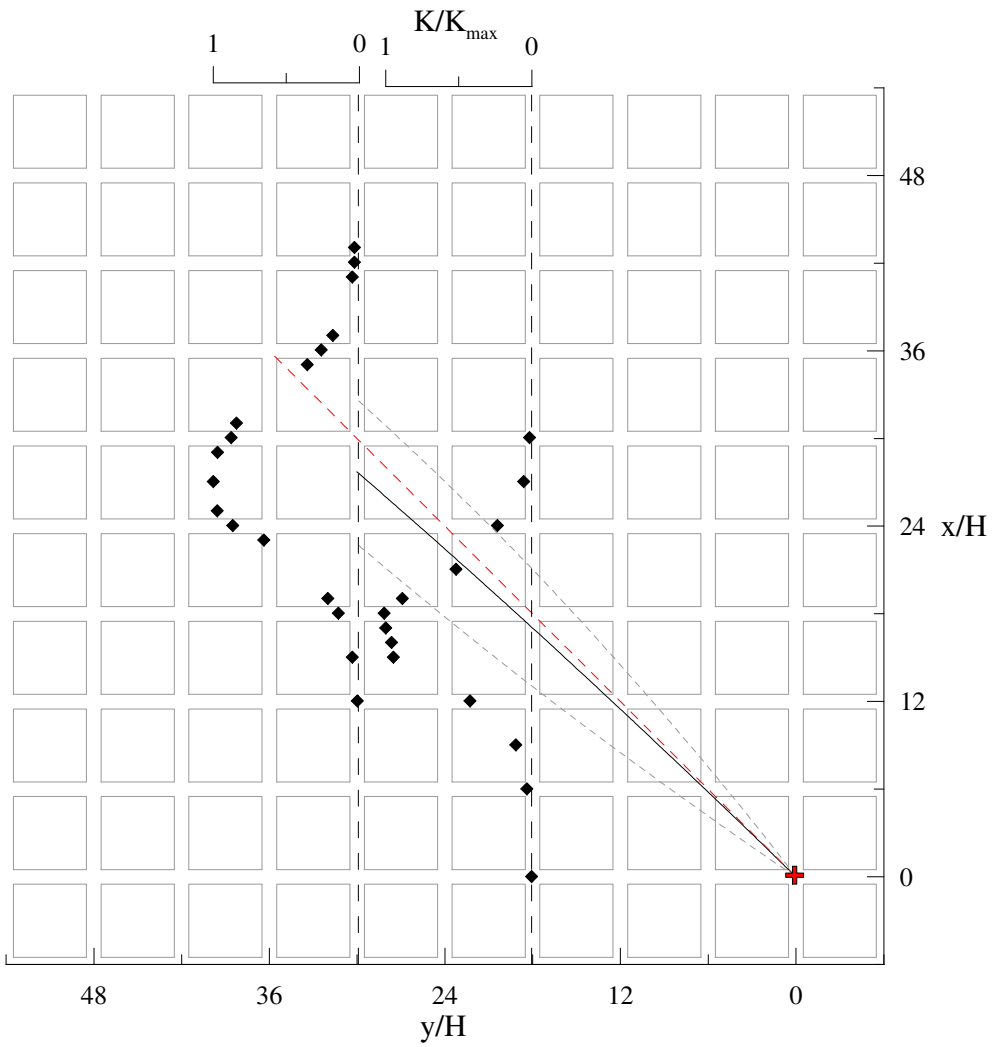

Figure 3.68: Overall plume behaviour above the array (z=2H) - $\theta = \mathbf{45^o}$

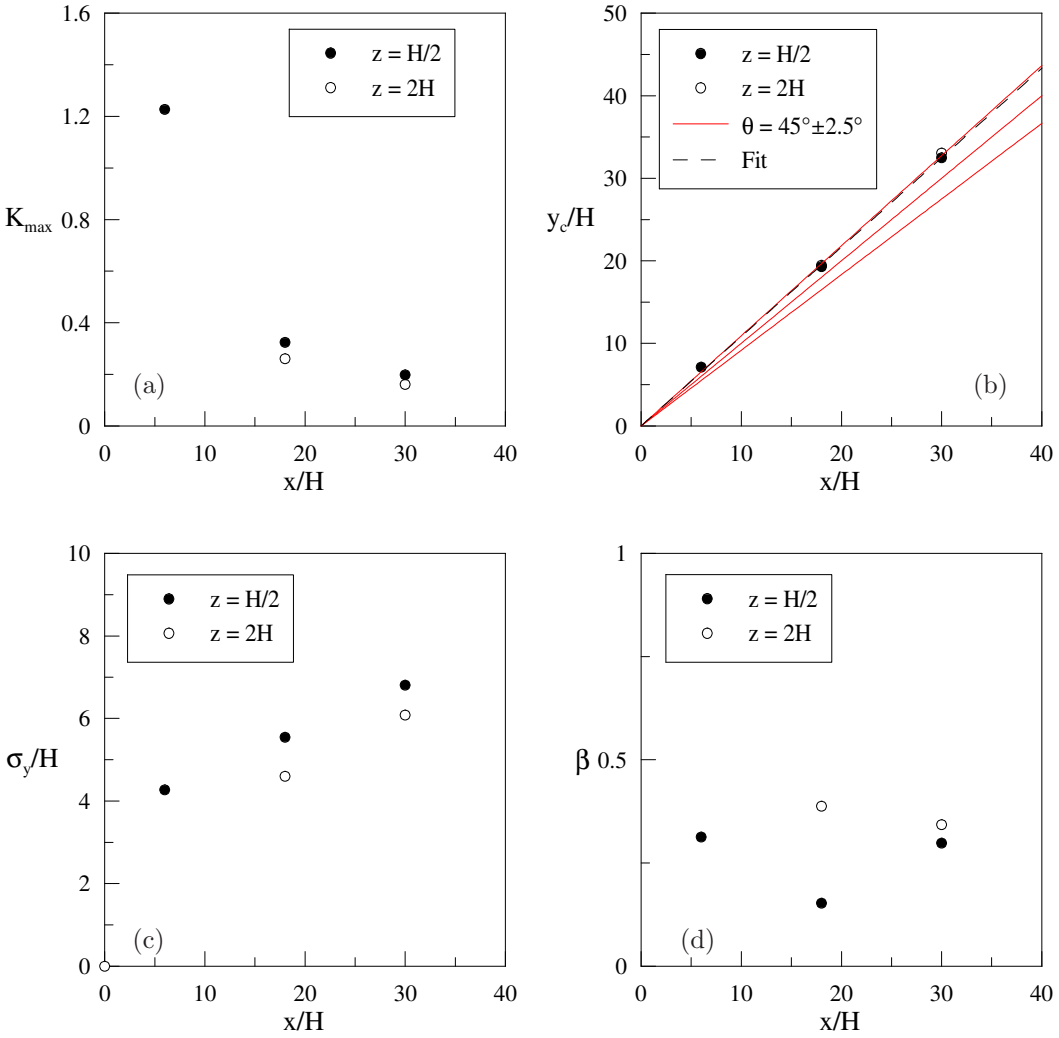

Moments of the horizontal mean concentration profiles at various positions downstream the source: a) mean concentration maximum; b) plume deflection; c) standard deviation; d) skewness.

Figure 3.69: Description of the plume - $\theta = \mathbf{45^o}$

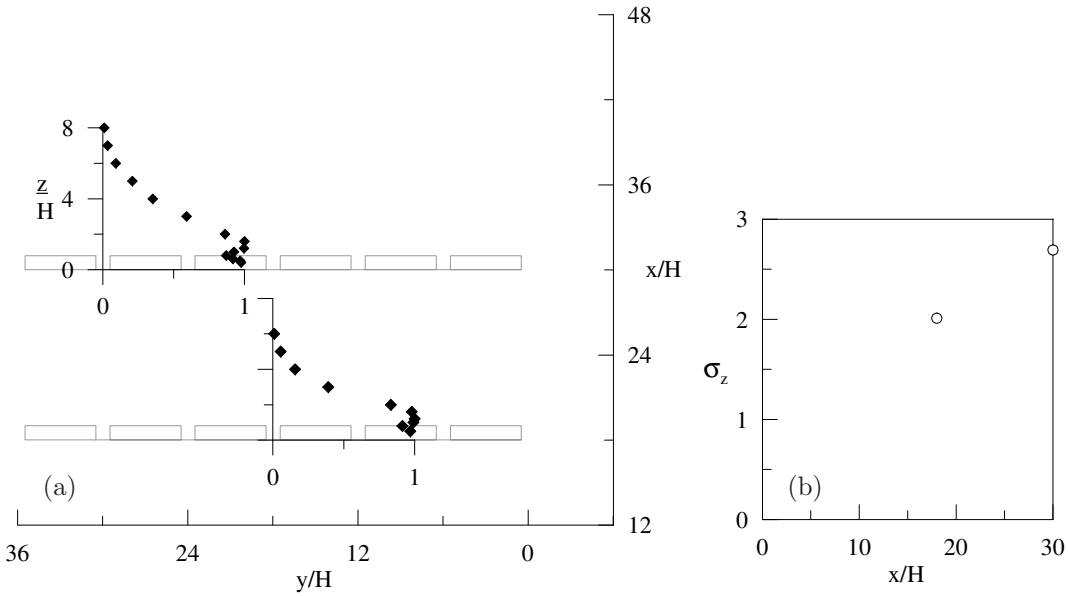

a) Normalized vertical mean concentration profiles at various positions downstream the source; b) Evolution of the vertical dispersion parameter

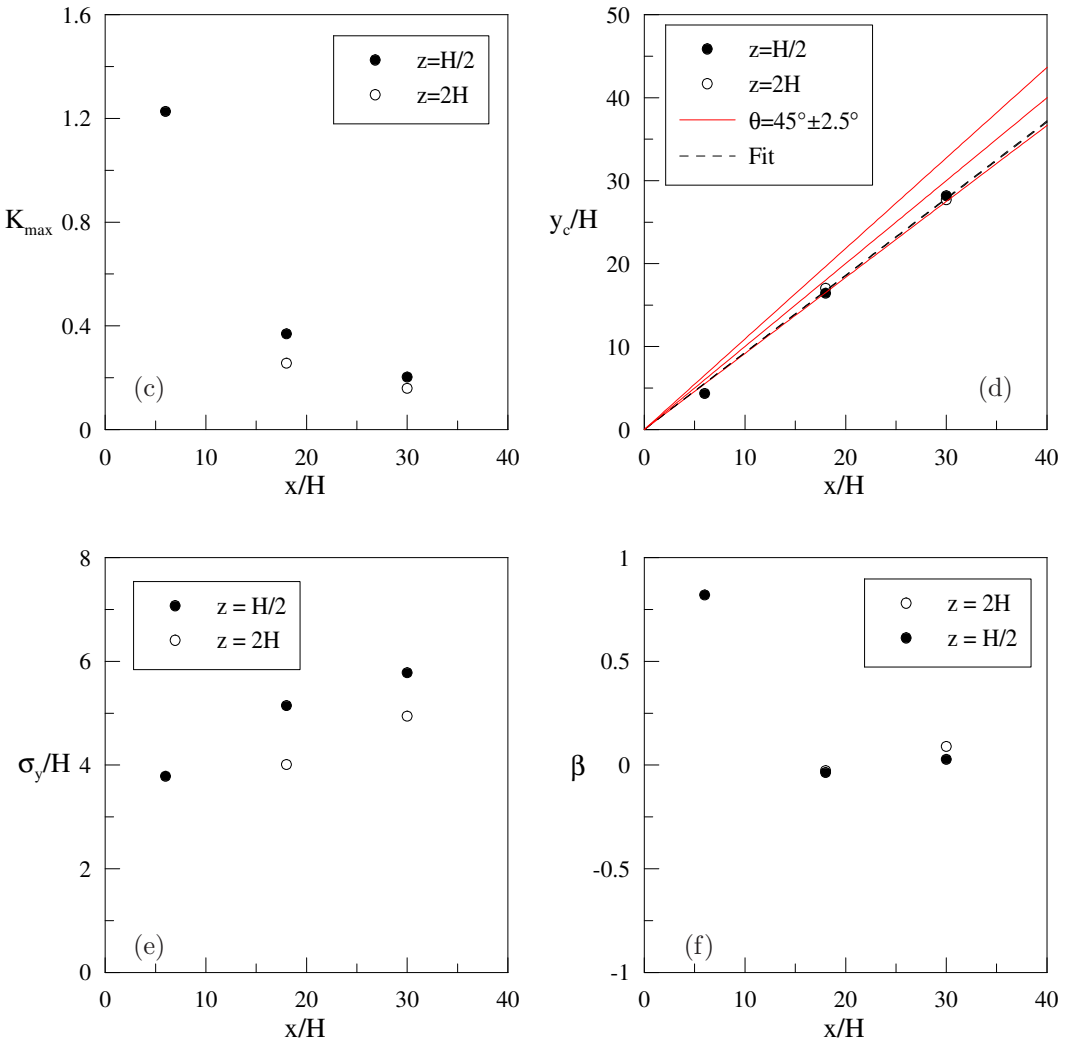

Moments of the horizontal mean concentration profiles at various positions downstream the source: c) mean concentration maximum; d) plume deflection; e) standard deviation; f) skewness.

Figure 3.70: Description of the plume - $\theta = \mathbf{45^o}$

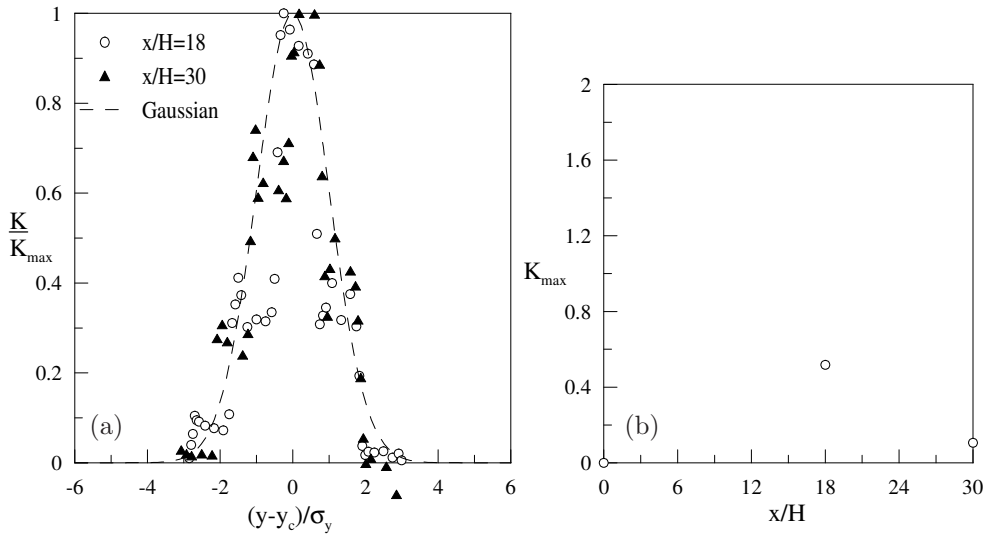

a) Normalized horizontal mean concentration profiles at various positions downstream the source and unitarian Gaussian curve (dashed line); b) downwind decay of the maximum value of the mean concentration profile

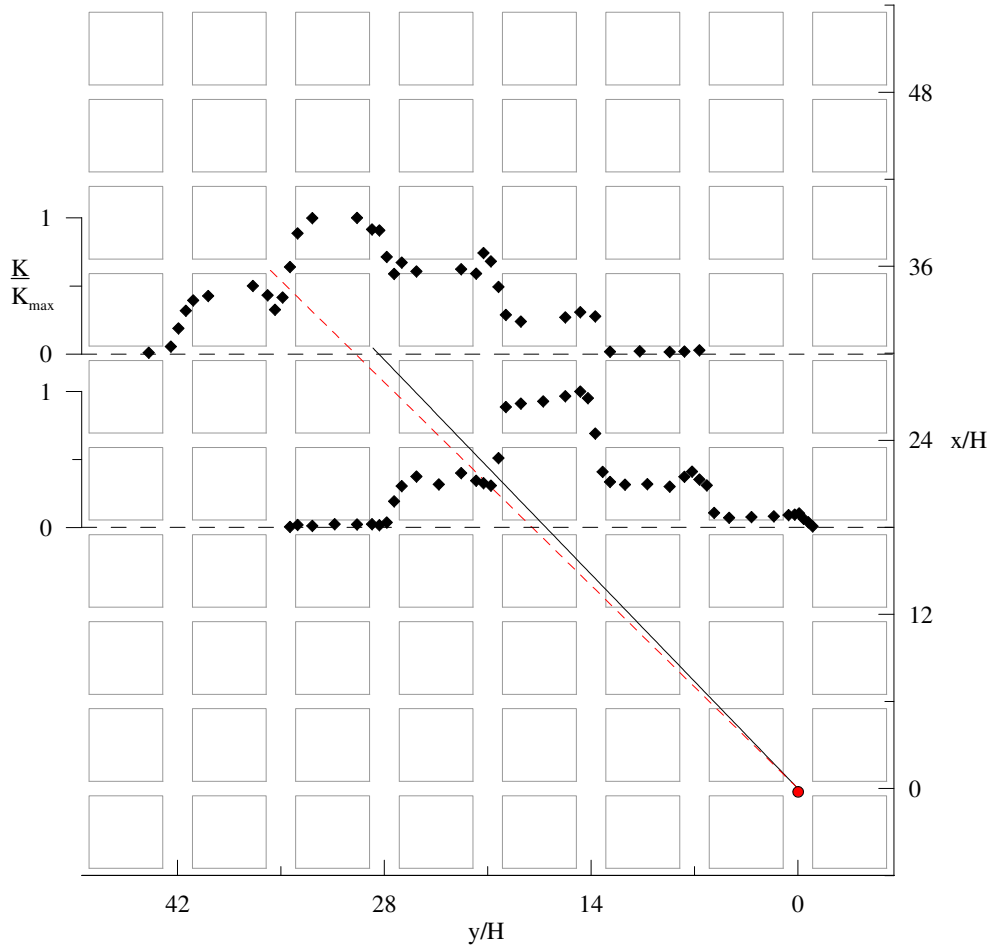

Figure 3.71: Overall plume behaviour within the array - $\theta = \mathbf{45^o}$, configuration 2

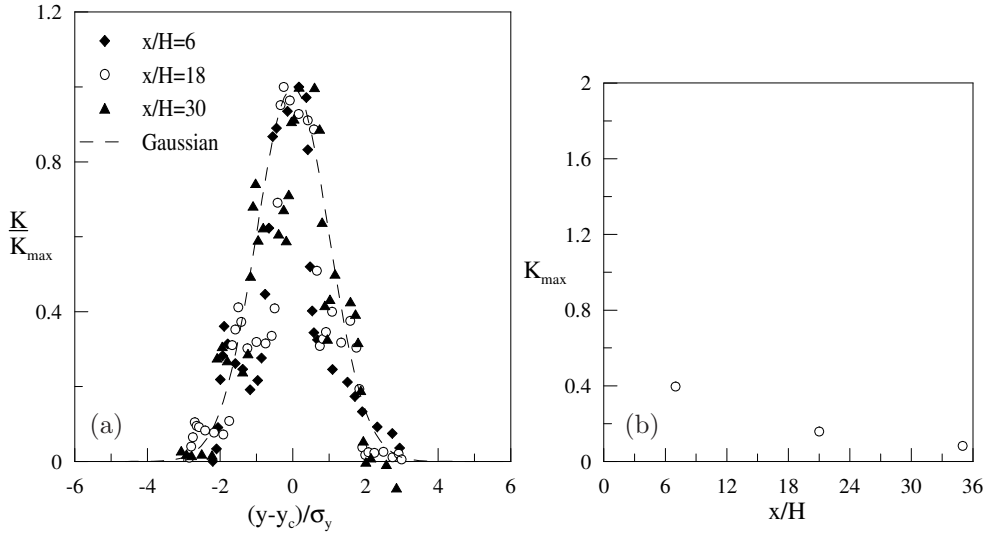

a) Normalized horizontal mean concentration profiles at various positions downstream the source and unitarian Gaussian curve (dashed line); b) downwind decay of the maximum value of the mean concentration profile

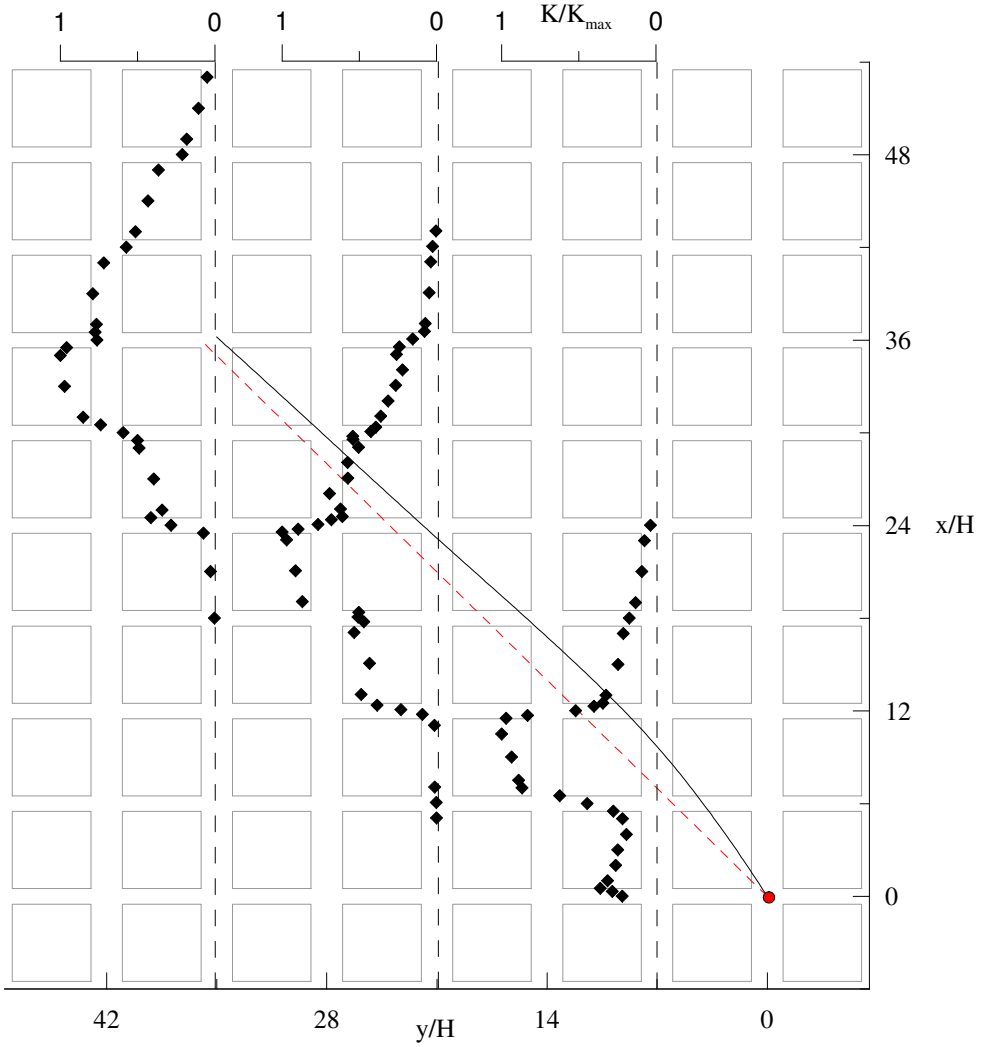

Figure 3.72: Overall plume behaviour within the array - $\theta = \mathbf{45^o}$, configuration 2

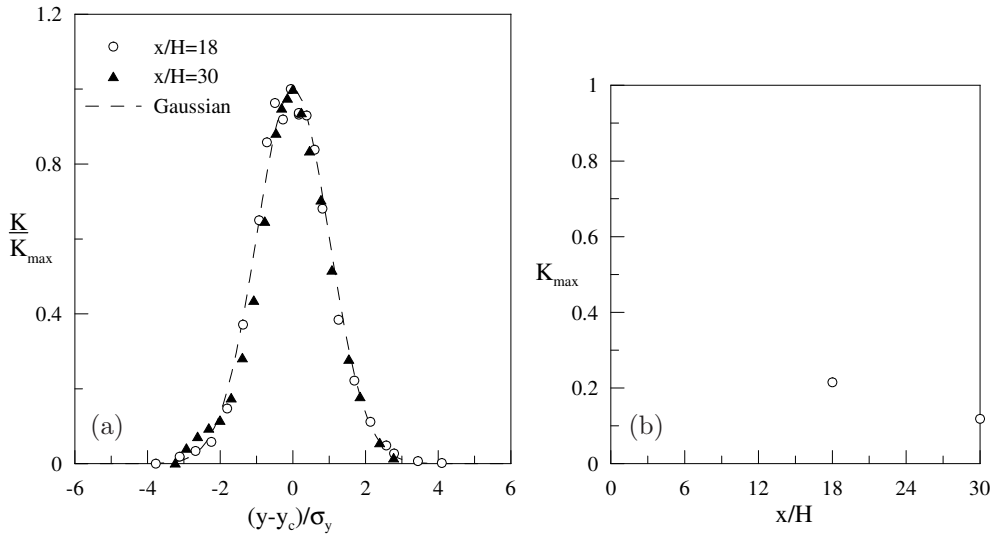

a) Normalized horizontal mean concentration profiles at various positions downstream the source and unitarian Gaussian curve (dashed line); b) downwind decay of the maximum value of the mean concentration profile

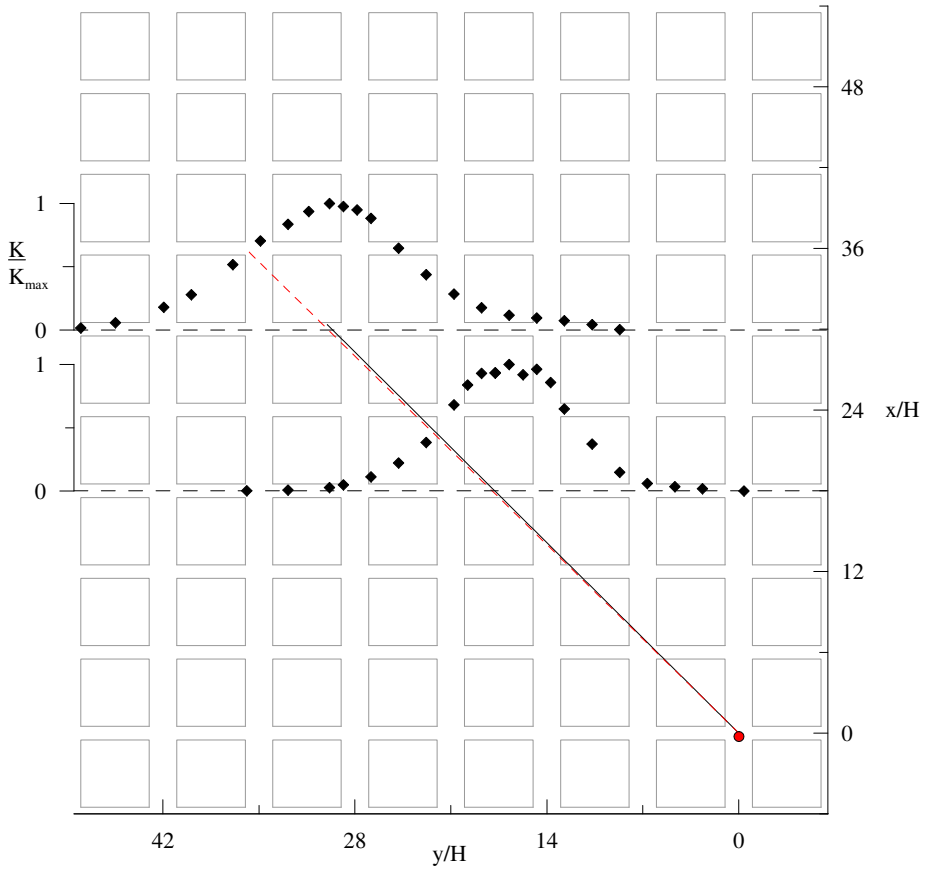

Figure 3.73: Overall plume behaviour above the array - $\theta = \mathbf{45^o}$, configuration 2

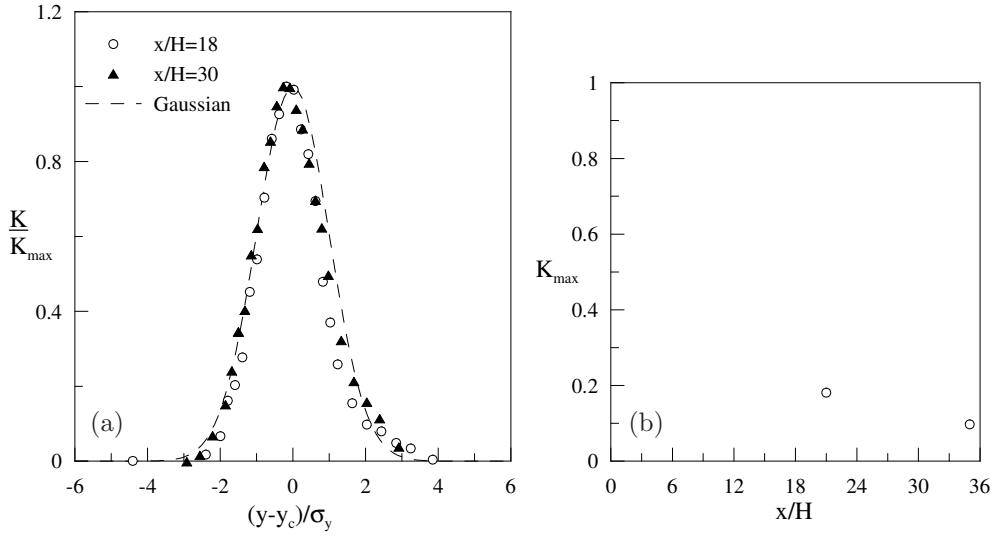

a) Normalized horizontal mean concentration profiles at various positions downstream the source and unitarian Gaussian curve (dashed line); b) downwind decay of the maximum value of the mean concentration profile

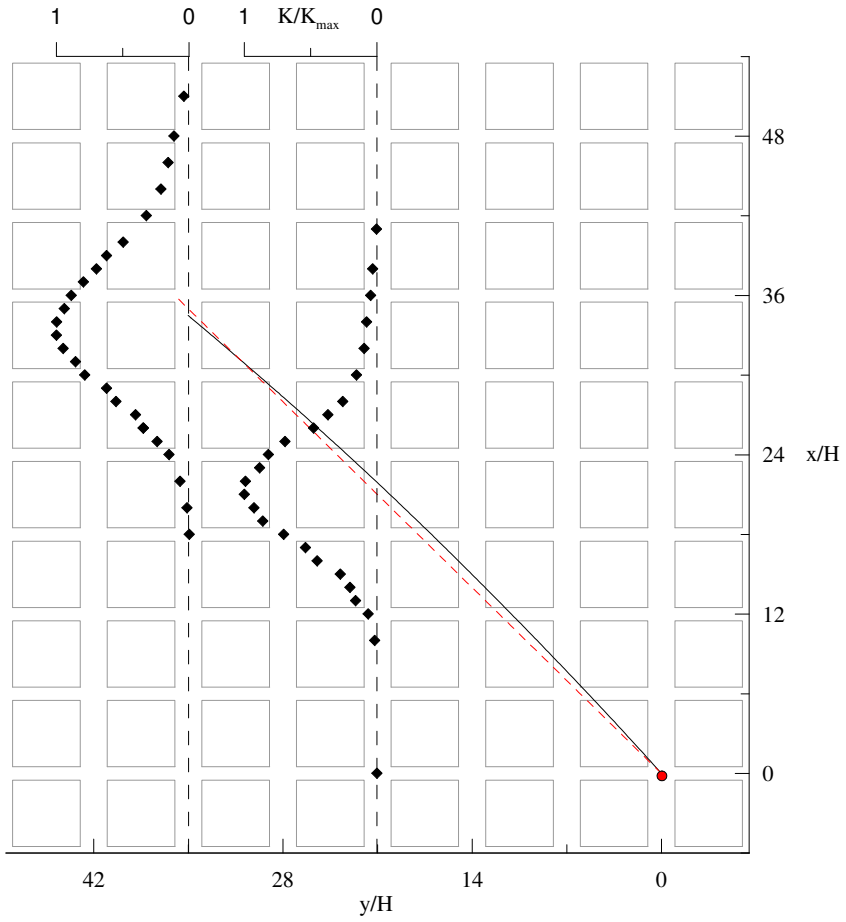

Figure 3.74: Overall plume behaviour above the array - $\theta = \mathbf{45^o}$, configuration 2

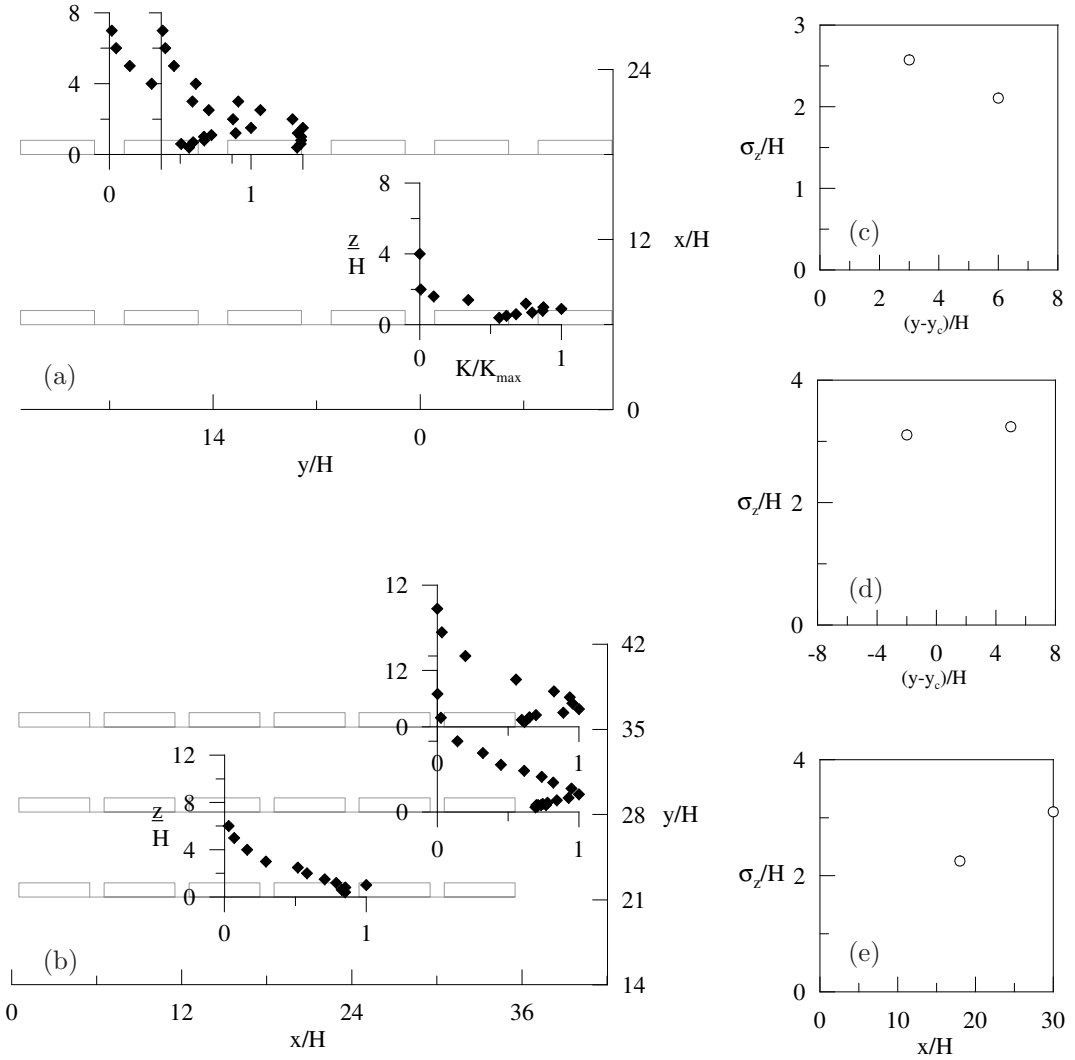

a) and b) Normalized vertical mean concentration profiles at various positions downstream the source; c) and d) vertical dispersion parameter as function of the distance from the theoretical centerline respectively at x=18H and x=30H; e) downwind evolution of the vertical dispersion parameter

Figure 3.75: Description of the plume - $\theta = \mathbf{45^o}$, configuration 2

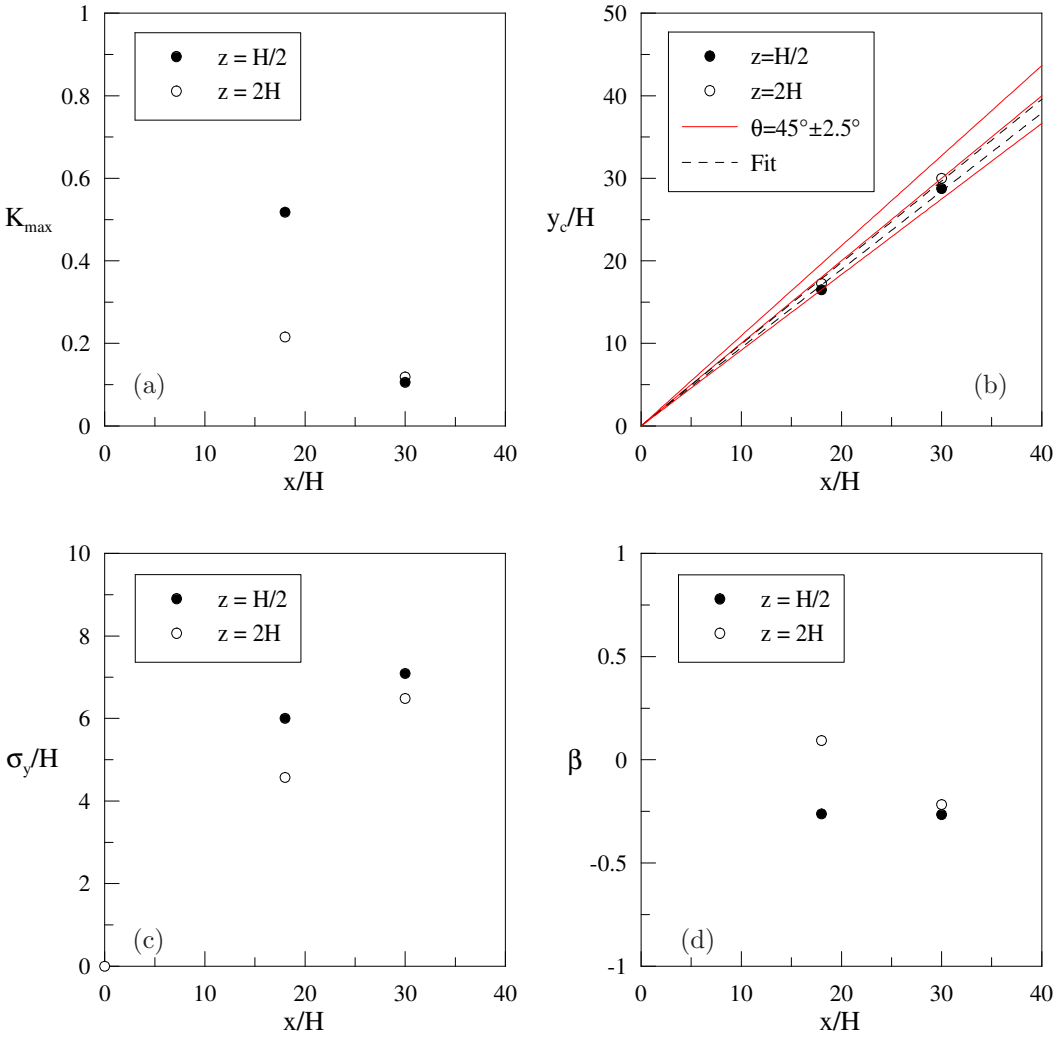

Moments of the horizontal mean concentration profiles at various positions downstream the source: a) mean concentration maximum; b) plume deflection; c) standard deviation; d) skewness.

Figure 3.76: Description of the plume - $\theta = \mathbf{45^o}$, configuration 2

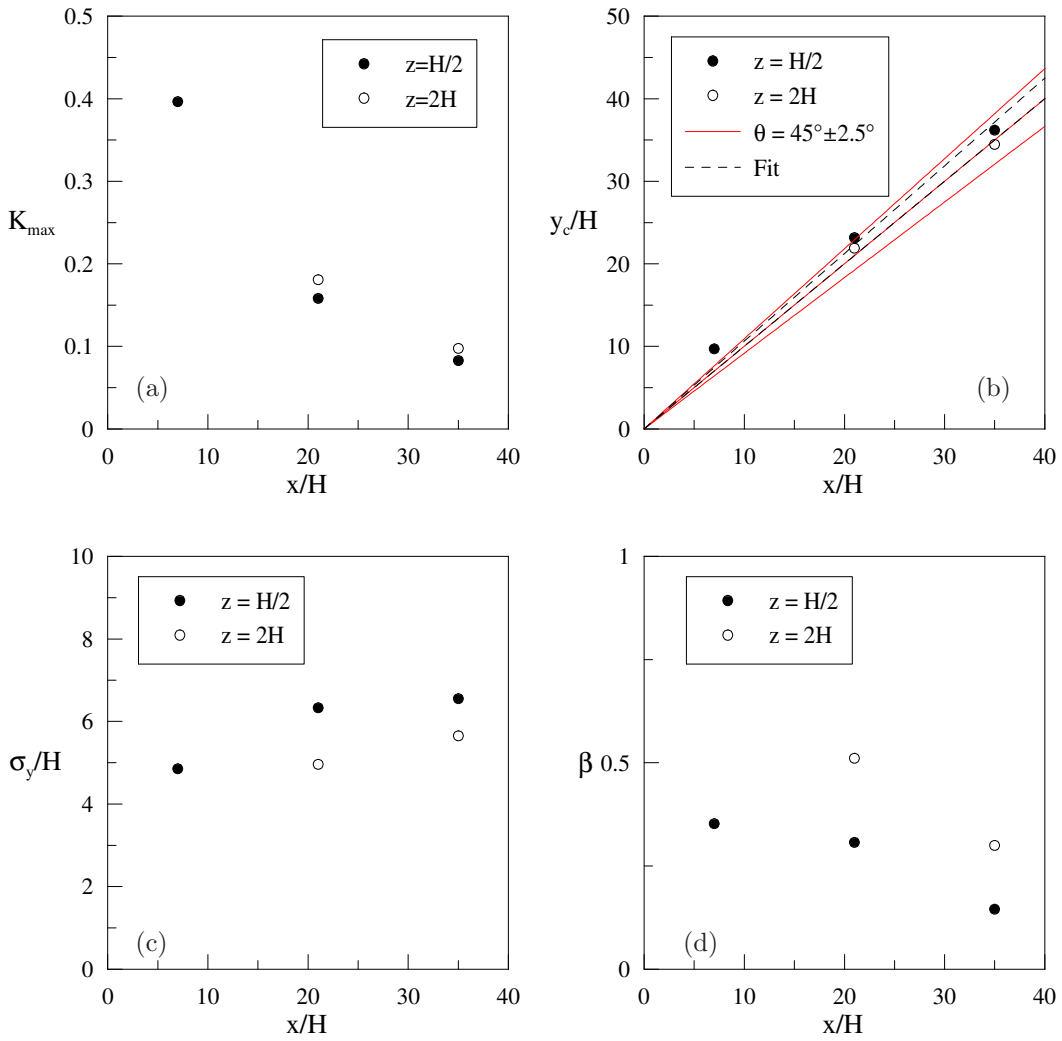

Moments of the horizontal mean concentration profiles at various positions downstream the source: a) mean concentration maximum; b) plume deflection; c) standard deviation; d) skewness.

Figure 3.77: Description of the plume - $\theta = \mathbf{45^o}$, configuration 2

The plume evolution throughout the array for different wind orientations has been described. Now we focus on the plume evolution in the reference system solidal with the wind direction. The deflection and the plume spreading are calculated by means of the transformations 3.18 and are referred to as $y_{c,\mathrm{EFF}}$, $\sigma_{y,\mathrm{EFF}}$ and $\sigma_{z,\mathrm{EFF}}$.

Initially, the plume behaviour through the array of configuration 1 for the different wind directions are compared in Figure 3.78. One differing aspect of the plume dispersion within an obstacle array in comparison to open terrain dispersion is that the orientation of the obstacles may have significant effect on the direction of the dispersing plume. Yee (2004) observed that for incident angles less than approximately 20^o, the centerline of the plume was deflected towards the normal to the front face of the array, while for greater incidence angles, it was deflected away. As seen in Figure 3.78-b) and c), the deviation of the plume centerline towards the parallel to the x-axis of the array is detected for the angles $\theta = 10^o$ and $\theta = 25^o$, due to the channelling effect of the plume, while it vanishes for $\theta = 45^o$ because of the symmetrical layout that does not impose any preferential direction on the plume. In Figure 3.78-a),d) and e), the spatial evolution of the plume spreading is plotted for the different orientations of the array regards to the incident wind. The horizontal plume spreading within the array seems to increases with the angle, except for $\theta = 45^o$ where the plume is characterised by a very large initial value but a reduced growth rate, similar to the case $\theta = 0^o$. The scattering of the horizontal dispersion parameters for the different angles is enhanced within the array but still survives above the array. This observation is quite important because it points out how the dispersion pattern above the array cannot abstract from the dispersion pattern within the array, which works as a virtual source. So, the dynamical conditions of the atmosphere are not sufficient to determine the pollutants dispersion above the roof, but it is essential to know how the pollutants are distributed within the street network. The vertical spreading is suppressed for $\theta = 0^o$, due to the channelling effect that reduces the lateral dispersion and thus the vertical one, whereas it assumes higher values for the other wind incident directions, which are comparable to the value in open terrain.

Then, the plume behaviour through the array of configuration 2 for the different wind directions are compared in Figure 3.79. An important deflection is detected for $\theta = 90^o$[3] within configuration 3, whose origin is difficult to evaluate but is presumably related to the sensitivity of the dispersion mechanisms to the asymmetry both of the wind direction and the array configuration. The horizontal spreading of the plume varies with the incident angle and the higher values match the case $\theta = 45^o$, since for $\theta = 0^o$ and $\theta = 90^o$ the channelling phenomena confine the plume. The vertical spreading varies with the incident wind direction and all the values are larger than the value in open terrain, except the case $\theta = 0^o$, due to the larger exchange surfaces which characterise the array configuration.

Finally, the plume behaviour through the array of configuration 1 and 2 for the wind direction equal to $\theta = 45^o$ are compared in Figure 3.80. The horizontal plume spreadings are similar above the array and comparable to the values in open terrain, while within the array are enhanced. Concerning the vertical dispersion, a more densely packed array (configuration 1) causes a lower vertical spreading and suggests that an enhanced vertical exchange takes place. It is worth noting that the position of the source placed at the intersection within the array certainly affects the plume evolution.

In this section it has been pointed out how complex is the dispersion through an obstacle array, although the array was simplified and few parameters have been investigated, and how many effects have to be taken into account to correctly foresee the dispersion patterns. Further, suitable urban models have to be considered to describe the dispersion in urban areas at neighbourhood scale.

[3]Investigating the configuration 2 for the incident wind direction $\theta = 90^o$ signifies investigating the configuration 3 for the incident wind direction $\theta = 0^o$

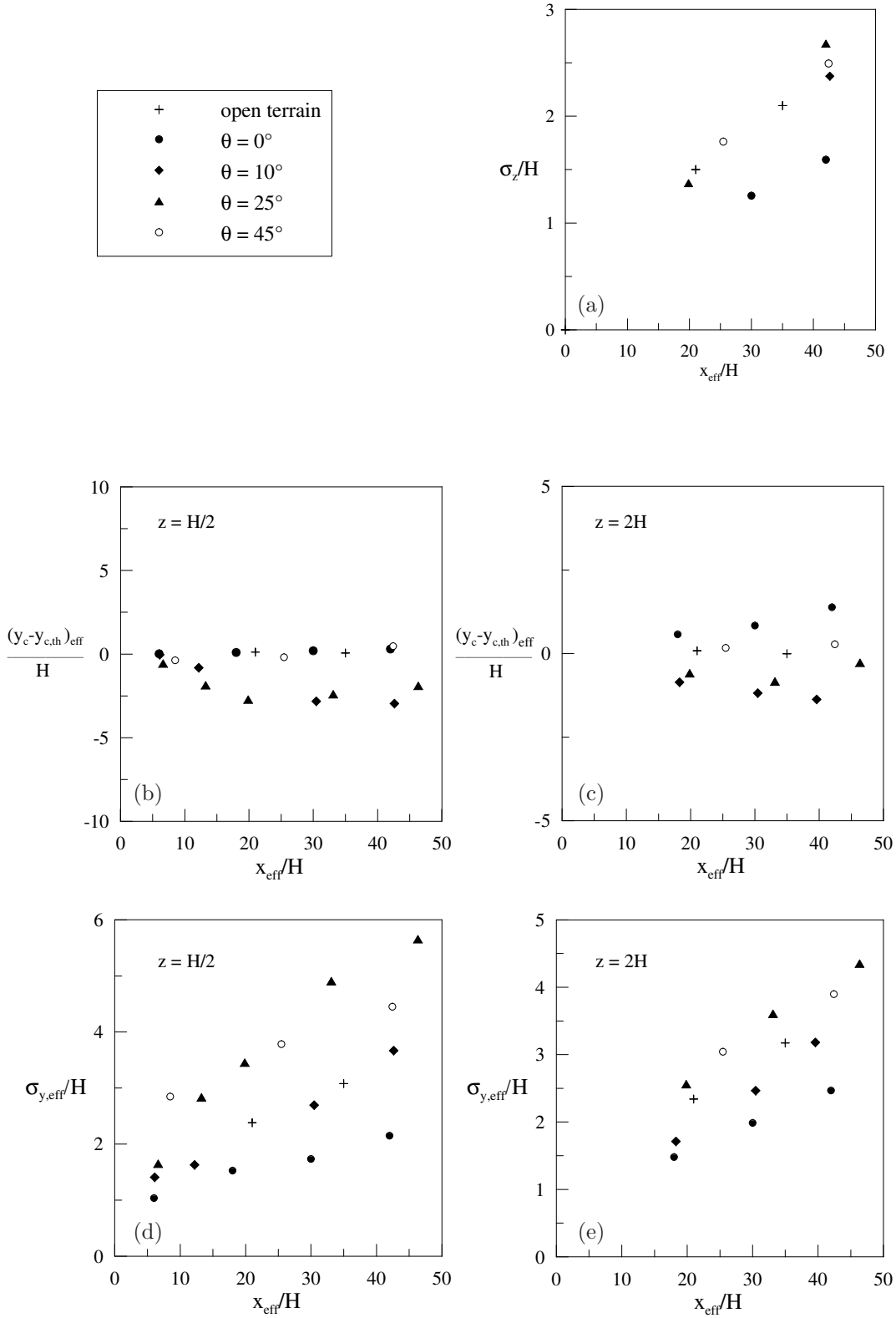

Figure 3.78: Effect of the incident wind orientation on the plume behaviour - configuration 1. a) Vertical plume spreading; b)-c) deflection of the plume within and above the array; d)-e) horizontal spreading of the plume within and above the array.

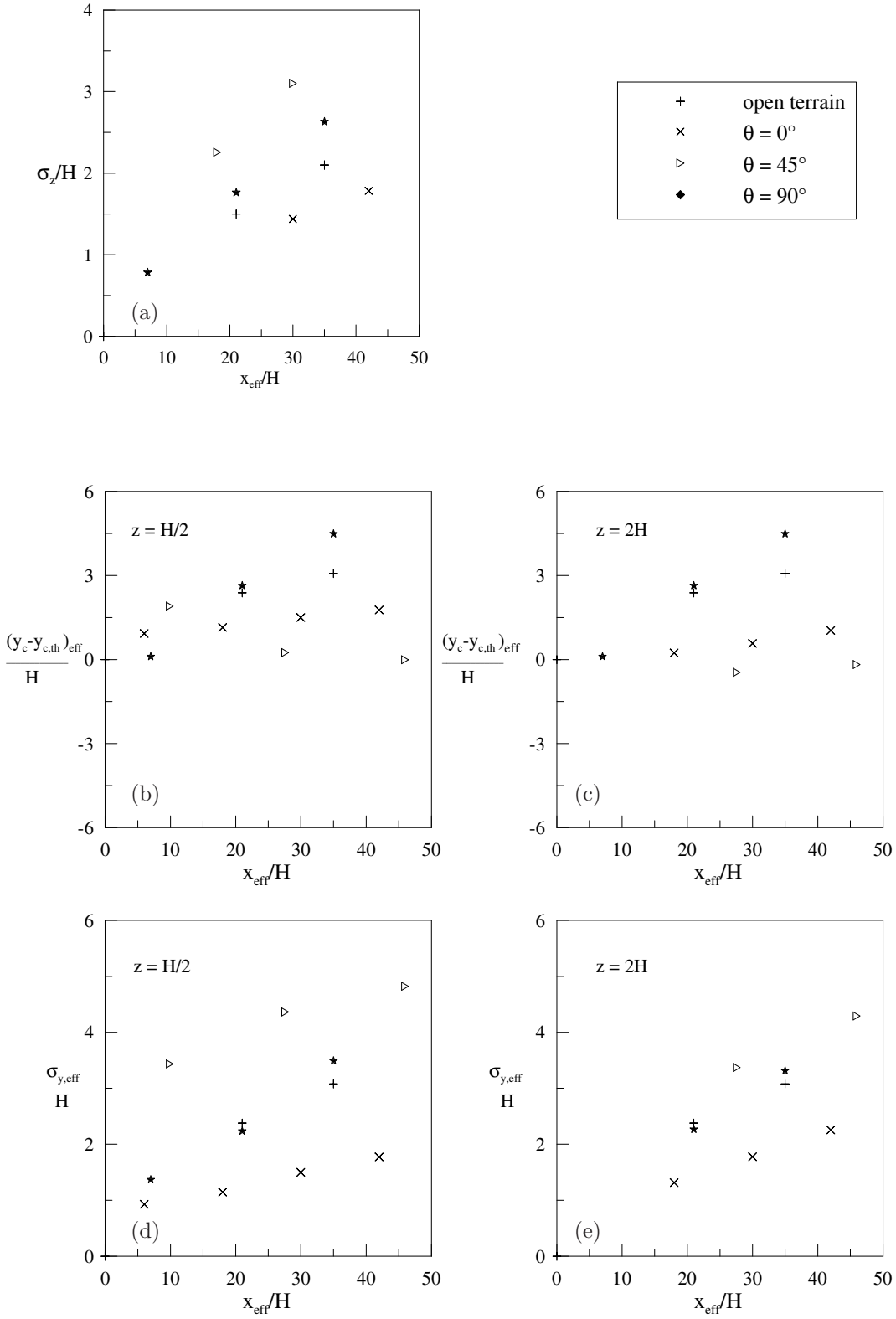

Figure 3.79: Effect of the incident wind orientation on the plume behaviour - configuration 2. a) Vertical plume spreading; b)-c) deflection of the plume within and above the array; d)-e) horizontal spreading of the plume within and above the array.

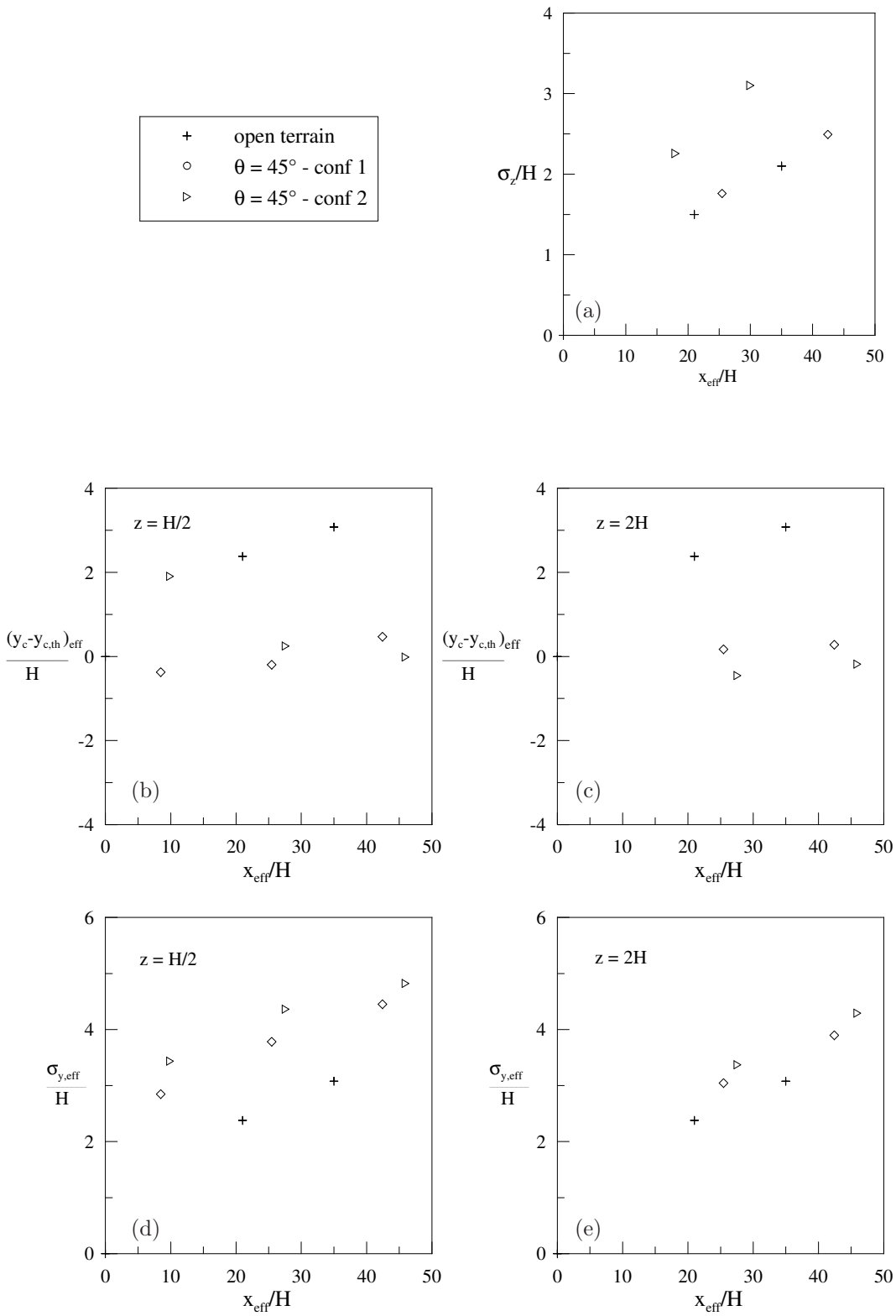

Figure 3.80: Effect of the array configuration on the plume behaviour - $\theta = 45^o$. a) Vertical plume spreading; b)-c) deflection of the plume within and above the array; d)-e) horizontal spreading of the plume within and above the array.

Chapter 4

The street network model SIRANE

4.1 Description of the model

The model SIRANE (Soulhac, 2000) is an urban dispersion model that calculates the pollutants distribution at the neighbourhood scale. It has been developed at LMFA, Ecole Centrale de Lyon, in order to provide a modelling tool that is able to take into account the complexity of the urban area in operational conditions: few input and poor computational means. The model represents the urban canopy as a street network. A box model is applied to each street and turbulent mass fluxes at street intersection and at roof level are parameterized by means of simple relations. The pollutant dispersion above the roof level is modelled by means of a gaussian model. A brief description of the street network approach and of the parametrization implemented in the model is carried out in this section. In the following section, SIRANE simulations are compared to the wind tunnel experimental data in order to show performances, limitations and potentialities of the model.

4.1.1 The street-network approach

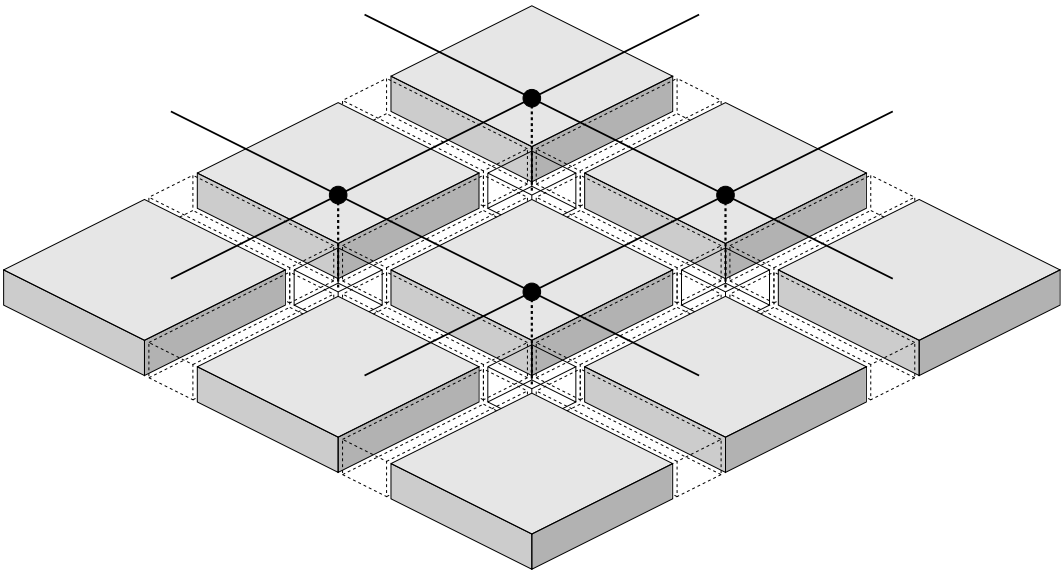

Figure 4.1: Topology of a network of streets: segments and nodes

SIRANE adopts a simplified description of the urban geometry , which is represented as a network of streets, represented by *segments*, connected by intersections, represented by *nodes* (Figure 4.1). The box model approach makes each street segment schematically represented as a parallelepiped of length L, width W and height H (Figure 4.2), and a spatially averaged concentration is computed within each box.

In steady state conditions, the mass balance within the box can be expressed as:

$$\mathcal{Q} + \mathcal{Q}_E - HWU_{street}C_{street} + \mathcal{Q}_s = 0 \tag{4.1}$$

where C_{street} is the average concentration inside the street, $\mathcal{Q}$ is the source strength within the street, $\mathcal{Q}_E$ the pollutant fluxes at street intersection, $\mathcal{Q}_s$ is the turbulent flux through the street-atmosphere interface and $HWU_{street}C_{street}$ represents the flux of pollutants through the downstream section of the street.

Assuming that the geometry of the street and the pollutant emission within it are known, three terms have to be modelled to compute the spatially average concentration: the velocity within the street U_{street}, the pollutant fluxes at street intersection $\mathcal{Q}_E$ and the turbulent flux through the street-atmosphere $\mathcal{Q}_s$.

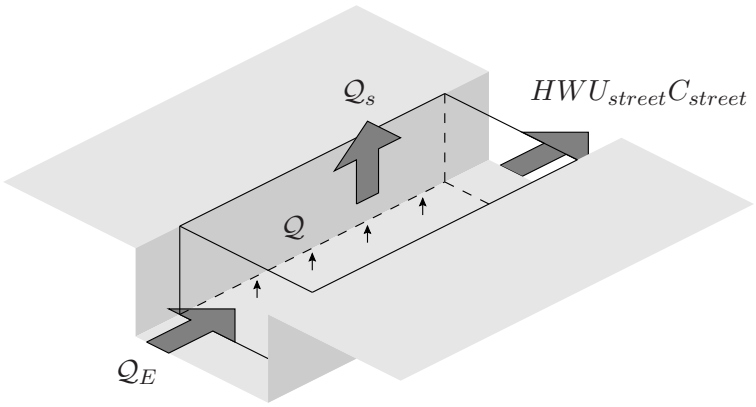

Figure 4.2: Mass balance within a street segment.

4.1.2 Average velocity within the street U_{street}

As it was shown (Soulhac *et al.*, 2007; Dobre *et al.*, 2005) the flow in a street canyon for any external wind direction is characterised by an helicoidal motion. In the plane perpendicular to the street axis a recirculating motion takes place: this means that the average transverse component of the flow in the street is null. The spatially-average velocity component along the street axis U_{street} is assumed to be driven only by the external flow and can be computed adopting the model presented in Soulhac *et al.* (2007). U_{street} is expressed by a relation of the form:

$$U_{street} = u_* cos(\theta_\infty)\ \mathrm{h}(H/W, z_i/W) \tag{4.2}$$

The spatially averaged velocity thus depends on the following parameters:

- the component of the friction velocity that is parallel to the street axis, $u_* \cos(\theta_\infty)$;
- the aspect ratio H/W of the street;
- the ratio z_i/W between the surface roughness of the street wall and the width of the street.

In the Figures 4.3-a and 4.3-b, the dependence of the function h on the two parameters H/W and z_i/W is shown. It is evident that for increasing street aspect ratio and wall roughness, the average longitudinal velocity is reduced.
It is worth noting that this model has been developed to calculate the spatially averaged velocity into a street of infinite length and therefore the influence of the intersection on the canyon flow is neglected. As long as the presence of the intersection clearly modifies the mean flow within the street, it seems unrealistic to consider the flow dynamics within the street independent from the flow in the intersection. For this reason an empirical correction of the velocity has been introduced. The influence of this corrective factor on the pollutant concentration estimations is discussed in the next Section.

4.1.3 Pollutant fluxes at street intersections $\mathcal{Q}_E$

The pollutant dispersion at street intersection implemented in SIRANE has been widely discussed in Soulhac (2000). The main features of the model are here briefly summarized. The calculation of the mass transfer in a street intersection requires a reliable estimate of the fluxes entering and leaving the intersection from the different crossing streets. An essential requirement for the street model is that it should provide a good estimate of the mass flux along the street. Although experimental and numerical data showed that both the flow field and the dispersion phenomena are influenced by the presence of the intersection, a first approximation of

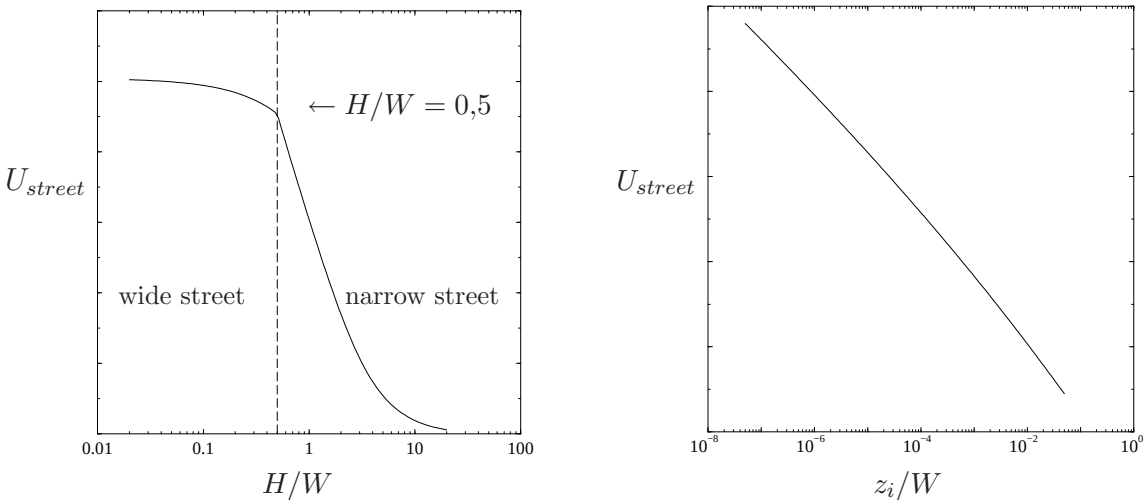

Figure 4.3: Evolution of the velocity according to the aspect ratio H/W (left) and to the surface roughness z_i (right).

U_{street} can be achieved by assuming that the flow in the street is not affected by the presence of the intersection and hence it is dynamically similar to the flow in an infinite length street and calculated by 4.2.

The pollutant fluxes entering in the intersection are computed as $H_i W_i U_{street,i} C_{street,i}$, where the index i indicates the various streets of the intersection.

To quantify the pollutant outwards fluxes $\mathcal{Q}_{E,j}$, a *tensor of turbulent exchange* $\widehat{\boldsymbol{\alpha}}(\theta_0)$ is defined, where $\widehat{\alpha}_{i,j}(\theta_0)$ represents the average air flow from the street i towards the street j. It is worth noting that the tensor $\widehat{\boldsymbol{\alpha}}(\theta_0)$ depends on the direction θ_0 of the external wind. The fluxes $\mathcal{Q}_{E,j}$ outgoing from the street j (counted positively) depends on the tensor of exchange by the relation:

$$\mathcal{Q}_{E,j} = \sum_{i=1}^{N_I} \widehat{\alpha}_{i,j}(\theta_0) C_{street,i} \; + \; \mathcal{Q}_v \tag{4.3}$$

where $\mathcal{Q}_v$ represents the pollutant flux in the vertical direction. The vertical flux depends on the vertical air motion within the intersection, which is computed as the imbalance between the fluxes entering and leaving the intersection. The vertical air flux $\dot{V}_v$ in the intersection is then defined by the relation:

$$\dot{V}_v = \sum_{i=1}^{N_I} H_i W_i U_{street,i} \tag{4.4}$$

When $\dot{V}_v < 0$, the resulting air flux, referred to as $\dot{V}_{ext \to j}$, is directed from the external atmosphere towards the street j. Otherwise, if $\dot{V}_v > 0$, the air flux is directed from the intersection towards the overlying atmospheric flow and is referred here to as $\dot{V}_{j \to ext}$. Concerning the pollutant dispersion, the mass fluxes can be modelled as a sink or a source of pollutants, whose strength $\mathcal{Q}_v$ is determined by the following expressions:

$$\begin{cases} \mathcal{Q}_v = \displaystyle\sum_{i=1}^{N_I} \dot{V}_{i \to ext} \, C_{street,i} & \text{outwards flux.} \\ \\ \mathcal{Q}_v = - \displaystyle\sum_{i=1}^{N_I} \dot{V}_{ext \to i} \, C_{ext} & \text{inwards flux.} \end{cases} \tag{4.5}$$

where C_{ext} represents the concentration in the flow above the canopy.

The model simplifies the dispersion mechanisms by assuming that the pollutant transport in the horizontal plane is decoupled from the pollutant transport in the vertical direction.

The equation 4.3 should allow to determine one of the unknown terms of the mass balance equation (Eq. 4.1). However, it still contains an unknown factor: the concentration C_{ext} in the external flow. The evaluation of C_{ext} requires a model for the pollutant dispersion above the urban canopy that will be discussed in Paragraph 4.1.5.

4.1.4 Turbulent fluxes at street-atmosphere interfaces $\mathcal{Q}_S$

As seen, the mass balance within a street section requires the estimation of the turbulent mass fluxes between the street canyon and the overlying atmospheric flow. The modelling of these turbulent fluxes has to take into account the dynamical conditions of the external flow, which is assumed to be the driving force of the transfer processes between the urban canopy and the atmosphere.

A general expression for the turbulent fluxes through the street-atmosphere interface is

$$\mathcal{Q}_s = LWu_d(C_{street} - C_{ext}) \tag{4.6}$$

where L and W fixes the size of the interface, C_{street} and C_{ext} are the concentration within and above the street respectively and u_d is a mass exchange velocity.

The mass exchange velocity u_d between a street canyon and the overlying atmospheric flow is related to the turbulent fluctuations taking place at the shear layer at the street-atmosphere interface. To date, the mechanisms governing the momentum and mass transfer between a cavity flow and the external atmospheric flow are still poorly understood. In the last years several studies were devoted to clarify the main features of this turbulent exchange (Caton *et al.*, 2003; Barlow *et al.*, 2004). In order to study these phenomena, experimental studies have been carried in the Laboratoire des Mécanique des Fluides et Acoustique of the Ecole Centrale. Several aspects have been investigated to point out the dependence of the velocity exchange on the canyon geometry, on the wall roughness and on the dynamical conditions of the external flow (Salizzoni, 2005). Moving from experimental results, Salizzoni (2005) described the turbulent transport between the cavity and the external flow as determined by two phenomena: on one side by a momentum 'diffusion' induced by the local shear generated turbulence and on the other side by the turbulent kinetic energy fluxes coming from the external flow towards the cavity. It is worth noting that these two mechanisms are not independent of each other. The local shear generated turbulence depends on the velocity difference $\Delta U = U_1 - U_2$ within the shear layer itself, being U_1 and U_2 the mean velocities at the shear layer boundaries. The turbulent kinetic energy fluxes from the external flow toward the cavity depend on the turbulence intensity and on the integral length scale of the external flow.

When the turbulence intensity of the external flow is negligible compared to the local production within the shear layer, ΔU governs the entire transfer process and the mass exchange velocity can be expressed as

$$u_d = \beta \Delta U \qquad \text{with} \qquad \beta = const.$$

However, this never holds for atmospheric flows and the influence of the turbulent kinetic energy fluxes on the shear layer dynamics has to be taken into account. We can write

$$u_d = \beta \Delta U \qquad \text{with} \qquad \beta = \beta \left\{ i, \frac{l}{W} \right\}$$

where i is the turbulence intensity of the external flow, l is the integral length scale of the external flow and W is the canyon width.

It is worth noting that the mechanisms governing these processes are highly intermittent and that any analytical model of this mass transfer requires simplifying assumptions. Assuming the box-model approach, the mean velocity within the street is equal to zero whereas the external velocity U_{ext} is assumed to be uniform in the direction perpendicular to the y-axis. Assuming a first order closure model the function β is expressed as

$$\beta = \sqrt{\frac{\Lambda}{\pi}} \qquad \text{with} \qquad \Lambda = \frac{\mathrm{K}_m}{U_H W} \tag{4.7}$$

where $U_H = U_{ext}/2$ is the wind velocity at roof level. A detailed derivation of Eq. 4.7 is provided in Appendix A. The coefficient Λ depends on the turbulent characteristics k and l of the external flow, where l represent the size of the largest eddies. Adopting the Prandtl mixing length hypothesis we can express the turbulent diffusivity as $\mathrm{K}_m = \sigma_{u_i} l$, where σ_{u_i} represents the scale of the velocity fluctuations; the parameter Λ can then be expressed as:

$$\Lambda = \frac{\sigma_{u_i} l}{U_H W} \tag{4.8}$$

In a boundary layer flow, the size of the larger structures is of the order of the boundary layer depth δ. However, as it was shown by Salizzoni (Salizzoni, 2005) the width of the street acts like a filter on the size of the turbulent structures penetrating into the street. This fixes the maximal size of the eddies which are responsible for the turbulent transfer between the street and the atmosphere. However, in order that an eddy in the external flow carries pollutants within the street, it is not only necessary that it is small enough to penetrate in the street. In fact the turbulent transfer between the canyon and the overlying boundary layer flow is due to the entrainment of external vortical structures which are coupled with the vortices produced in the shear layer. The vortex coupling takes place between turbulent structures whose dimensions are quite the same, otherwise the smaller vortex would be 'advected' by the larger one. In this sense, the street might be not enough large to enable the vortices produced within the shear layer to intercept the larger scale size eddies in the external flow. From that point of view, we can assert that the shear layer acts as a filter on the eddy size getting into the cavity. In other words, the characteristic time scale of an eddy, defined as $t_{turb} = \pi l/\sigma_{u_i}$, has to matches to the characteristic time scale above the street $t_{adv} = W/U_{ext}$, i.e. $t_{turb} = t_{adv}$. This assumption allows to express l as a function of the turbulence intensity at the street-atmosphere interface:

$$\frac{l}{W} = \frac{1}{2\pi}\frac{\sigma_{u_i}}{U_H} \tag{4.9}$$

By introducing this expression into the equation 4.8, we obtain:

$$\Lambda = \frac{1}{2\pi}\left(\frac{\sigma_{u_i}}{U_H}\right)^2 \tag{4.10}$$

So the pollutant fluxes across the street-atmosphere can be finally expressed as

$$\mathcal{Q}_s = LW\sigma_{u_i}\frac{\pi}{\sqrt{2}}(C_{street} - C_{ext}) \qquad \text{where} \qquad u_d = \frac{\pi}{\sqrt{2}}\sigma_{u_i} \tag{4.11}$$

4.1.5 Flow and dispersion above the canopy

The last stage of the modelling is related to the flow and dispersion above the roof level, i.e. in the urban boundary layer.

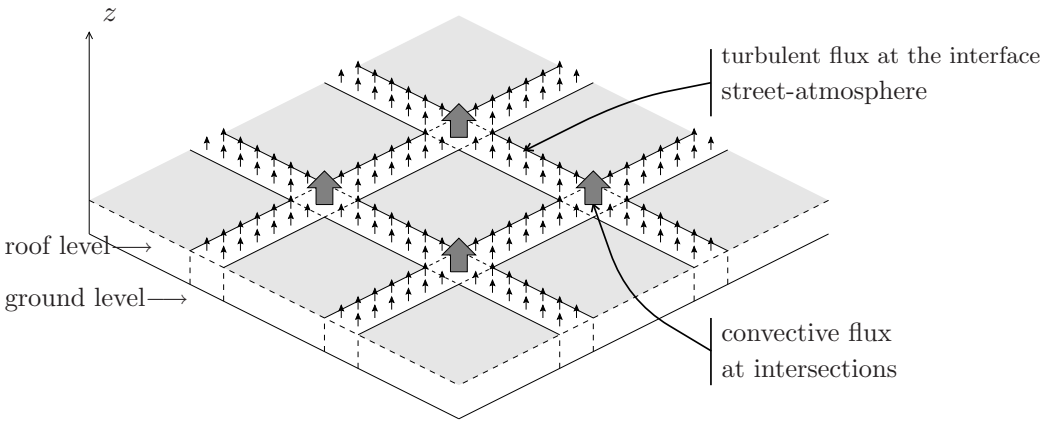

Figure 4.4: Dispersion in external atmosphere; pollutant fluxes at street-atmosphere interface and at intersections.

Similarly to ADMS-Urban, the flow above the street network is described according to the Monin-Obukhov similarity theory. The presence of the roughness sub-layer is neglected and the external flow is assumed to be uniform on the horizontal plane.

Two categories of emissions in the external flow can be identified, as shown in Figure 4.5:

- pollutants emitted within the urban canopy that go beyond the level of the roofs, either by a turbulent flux at the interface street-atmosphere §4.1.4 or by a convective flux at street intersections §4.1.3 (figure 4.4-b).
- any other type of emission due to sources that emits directly in the external atmosphere (chimneys on the roofs, emissions industrial...)

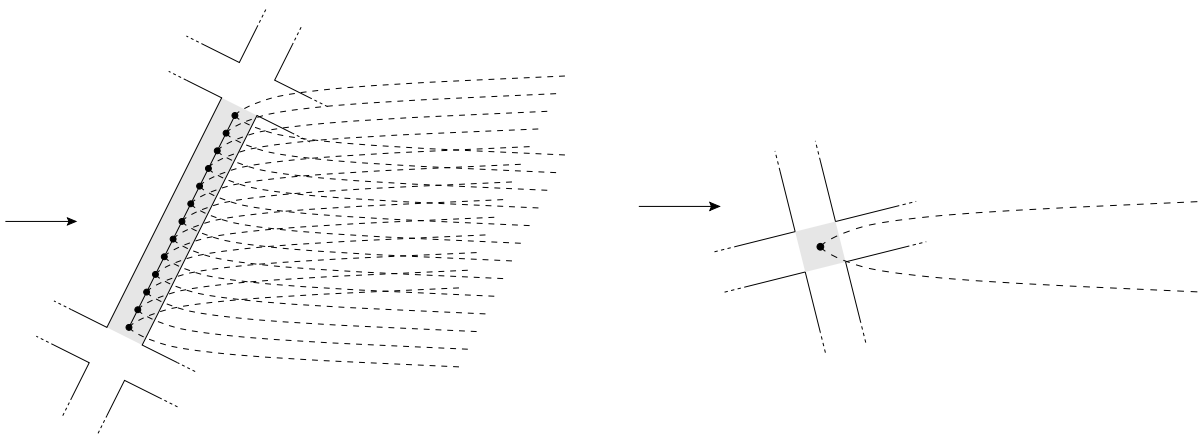

a) Emission from a segment of street. *b) Emission from a node of intersection.*

Figure 4.5: Discretization of the fluxes of emission in the external atmosphere.

To model the concentration field induced by a point source in a uniform flow, the approximate Gaussian solution is adopted:

$$\overline{c}(x,y,z) = \frac{\mathcal{Q}}{\pi\sigma_y\sigma_z U_{ext}} \exp\left[-\frac{1}{2}\left(\frac{y^2}{\sigma_y^2}+\frac{z^2}{\sigma_z^2}\right)\right] \tag{4.12}$$

The standard deviations σ_y and σ_z, are parameterized adopting the Monin-Obukhov similarity theory (Pasquill and Smith, 1983). When a solid boundary limits the lateral plume spreading,

the usual image source technique is used, considering the plane located at $z = H$ as the reflecting surface.

In the model SIRANE a simple discretization of the street section is made and a line source is represented as a series of point sources (Figure 4.5). The concentration induced by each point source is calculated by means of the equation 4.12 and the total concentration in any point of the external atmosphere is calculated as the superposition of all sources. It is now possible to compute the concentration C_{ext} above each street and each intersection, thus determining the last unknown factor of the problem. It is worth noting that the concentration C_{ext} above a street depends on the outgoing fluxes at the top of the urban canopy, which themselves depend on the difference $C_{ext} - C_{street}$.

4.1.6 Numerical resolution

The mass balance within a street can finally be expressed as

$$\mathcal{Q} + \mathcal{Q}_E - HWU_{street}C_{street} + \frac{\sigma_w WL}{\sqrt{2}\pi}(C_{ext} - C_{street}) = 0 \tag{4.13}$$

The equation 4.13 represent the first equation of a coupled system. Assuming that σ_w is known, we dispose of a series of coupled linear equations, where the unknown factors are:

- The concentration $C_{street,i}$ in the street i.
- The concentration $C_{ext,i}$ above the street i.
- The convective flux $\mathcal{Q}_{E,i}$ entering in the street i by the upwind section.
- The concentration $C_{ext,j}$ above the intersection j.

the problem can then be formalized by a matric equation:

$$\boldsymbol{A} \cdot \boldsymbol{x} = \boldsymbol{b} \tag{4.14}$$

where $\boldsymbol{x}$ represents a vector whose components are the unknown factors of the problem. Defined as N_R and N_I the numbers of streets and intersections, the linear system is thus composed by $3N_R + N_I$ equations with $3N_R + N_I$ unknowns. When a district with lateral dimension of about one kilometer is considered, N_R and N_I can be larger than 100 and the size of matrix $\boldsymbol{A}$ becomes very large. It is then difficult to apply exact methods of resolution of linear systems and the adoption of an iterative methods is required.

Those methods are generally based on the properties of the matrix $\boldsymbol{A}$, as the symmetries of the matrix or null elements away from the diagonal. Unfortunately, in our case, this matrix does not have these properties. Since the concentration in a street depends on the concentration within a large number of other streets, most of the elements of the matrix $\boldsymbol{A}$ are different from zero. However, as long as the concentration within any street depends only on the sources located upstream, the linear system can be ordered following the wind direction. In fact, by using an iterative method of the type Gauss-Seidel and by ordering the equations in the direction of the flow, the iterations necessary to obtain a converged solution are reduce of about 30 % compared to the resolution of a disordered system.

4.2 Comparison between SIRANE simulations and experimental data

In order to validate and eventually improve the mass transfer parameterizations implemented in SIRANE, we compare the concentration field calculated by SIRANE within the idealized

array (configuration 1) with the experimental measurements. The experimental conditions are simulated by SIRANE at the wind tunnel scale.
Initially we discuss the values of the parameters which have been used in the simulation.

The street aspect ratio is H/W =1 and the values of velocity at roof height and building roughness are chosen so that the average velocity within the street calculated by Eq. 4.2 matches the experimental values for a wind parallel to the street. Therefore the velocity at roof height U_H is 2.4 m/s and the building roughness is z_i=0.000025 m, which corresponds to the full-scale value z_i=0.01 m. The vertical velocity fluctuation is assumed to be $\sigma_w = 0.35$ m/s, a plausible value. Concerning the average velocity within the street for any wind direction, it has been demonstrated experimentally in this thesis that the model overestimates the average velocity because it does not take into account the influence of the intersection. A correction of the Eq. 4.2 is proposed in order to reproduce the experimental values of the average velocity within the street for the different incident winds:

$$U_{street} = u_* f(\theta_\infty)\, \mathrm{h}(H/W, z_i/W) \tag{4.15}$$

where

$$f(\theta_\infty) = cos(\theta_\infty) \cdot [\alpha + (1-\alpha)\, cos(\theta_\infty)]$$

In the Figure 4.6, the average street velocities as predicted by the two empirical models are compared with the experimental values. The revised model seems to quite well describe the experimental behaviour. An interesting observation is that the percentage decreasing of the average velocity depends on the wind direction: for small $cos\theta$ values the percentage variation of the average street velocity is larger than for high $cos\theta$ values, where the velocity assumes higher values and the percentage variation is therefore less significative. This different behaviour in the variation of the velocity has an important effect, namely the orientation of the wind within the canopy, θ_{in}, is different regards to that above the canopy, θ_∞. We calculate the direction of the wind within the canopy as

$$\theta_{in} = atan\left(\frac{U_{par,x}}{U_{par,y}}\right)$$

where $U_{par,x}$ and $U_{par,y}$ are the average velocity of the street parallel to the x-axis and the y-axis respectively. In Fig. 4.7, it is worth noting that θ_{in} is smaller than θ_∞ for $\theta_\infty < 45^o$ and is larger for $\theta_\infty > 45^o$. The value $\theta_\infty = 45^o$ corresponds to an axis of symmetry related to the symmetrical configuration of the array. This behaviour could explain the channelling effect which has been pointed out by measurements and thus the shifting of the plume centerline regards to the expected value that corresponds to the external wind direction. Thus the introduction of the empirical correction to the average street velocity allows to simulate the channelling effect, whose effect depends on the α parameter. Fig. 4.8 demonstrates the effect of the α parameter on the exchange mechanisms at the intersections by comparing the dispersion patterns within the array calculated for $\alpha = 0.3$ and for $\alpha = 0$. It is worth noting that the higher is α the less significant is the channelling effect, until it disappears at $\alpha = 1$. For $\alpha = 1$ the Eq. 4.15 matches the previous formulation (Eq. 4.2).

Concerning the dispersion in the external flow, the model requires the plume advection velocity and the standard deviation values. Instead of assuming the usual empirical relations for the standard deviation evolution, a new parametrization is proposed:

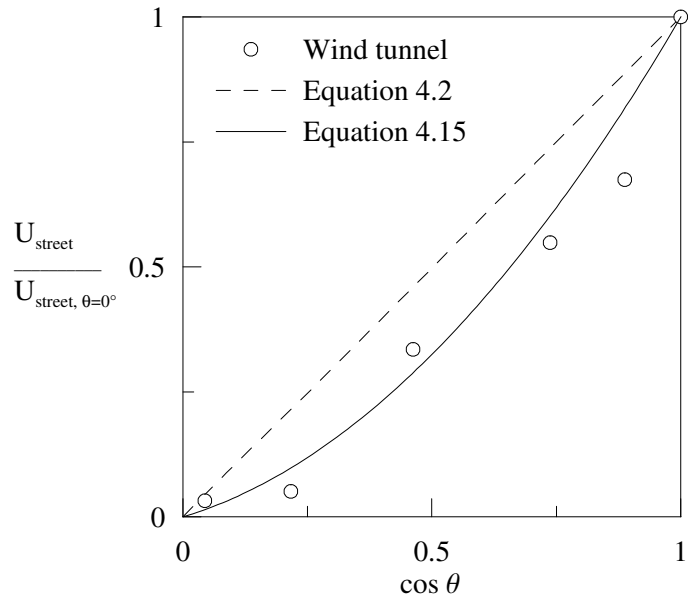

Figure 4.6: Average velocity within the street for different wind directions: experimental and theoretical values

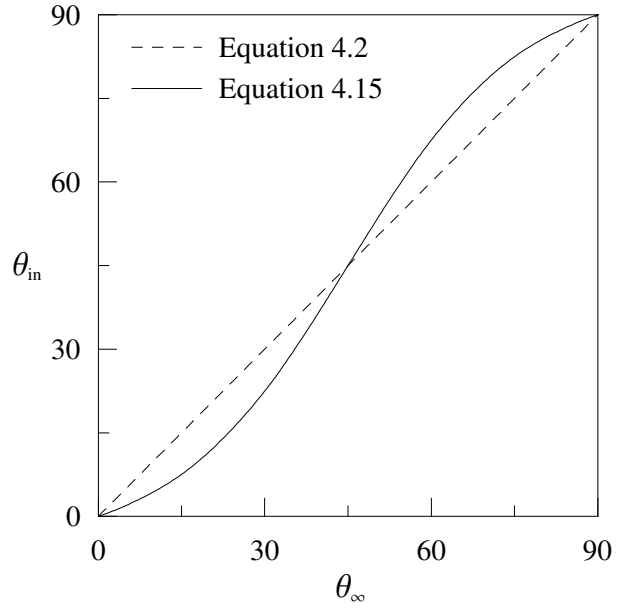

Figure 4.7: Orientation of the velocity vector within the array as function of the external wind orientation

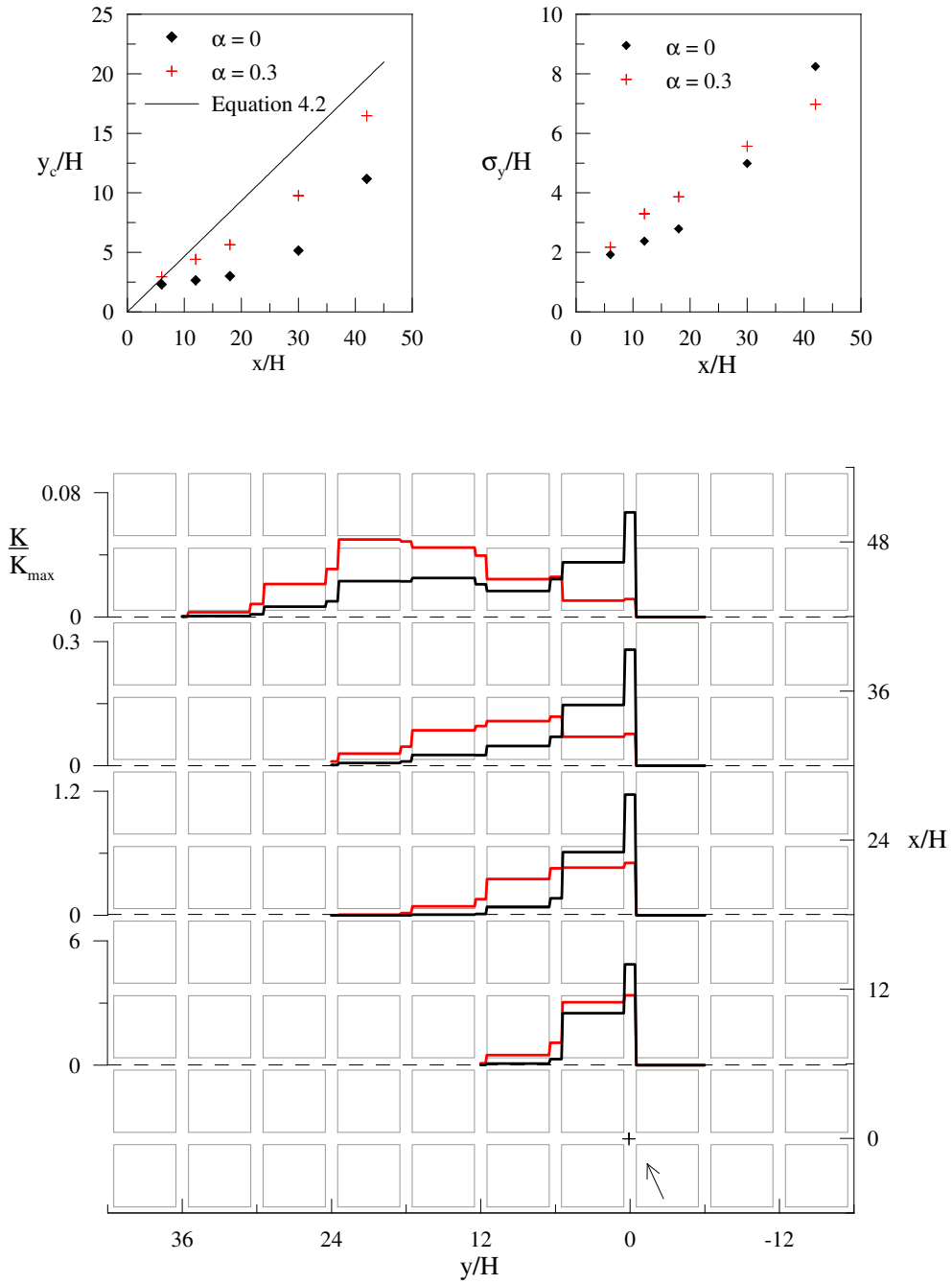

Figure 4.8: Comparison of the dispersion patterns within the array calculated by SIRANE for $\alpha = 0$ and $\alpha = 0.3$

$$\sigma_y = \frac{\sigma_v \cdot t}{\sqrt{1 + \frac{t}{2T_{l,y}}}} \tag{4.16}$$

$$\sigma_z = \frac{\sigma_w \cdot t}{\sqrt{1 + \frac{t}{2T_{l,z}}}} \tag{4.17}$$

$$\tag{4.18}$$

where T_l is the lagrangian time-scale and gives the measure of the maximum correlation time, whiled σ_v and σ_w are the velocity fluctuations. These values have been calibrated by comparing the theoretical behaviour of the standard deviations to the plume evolution observed in open terrain. This way allows to take into account the actual characteristics of the simulated flow. This approach is not generally applicable to real-world dispersion study, because we can not know the spatial evolution of the plume but we have to describe it by means of general relations.

Now we compare the SIRANE results with the experimental data. In Fig. 4.9 and 4.10, the dispersion patterns are compared for the incident wind parallel to the x-axis within and above the array. The results are quite satisfying, except for the concentration values into the lateral streets of the array. This disagreement is due to the limitation of SIRANE in dealing with dispersion mechanisms at intersection. In fact, SIRANE takes into account the advection mechanism due to the mean velocity component but neglects the diffusion processes related to the fluctuating components. However, these processes give the main contribution to the pollutants dispersion within the lateral streets for a wind parallel to the x-axis, that is when there is not a mean flow, and neglecting them causes the observed disagreement. A further step will be to improve the parametrization to take into account this phenomenon. In Fig. 4.11 and 4.12, the concentration fields associated to a wind direction $\theta = 10^0$ are shown within and above the array respectively. The comparisons show a quite good agreement and further the plume centerline shifting and the standard deviation evolution are well reproduced. Fig. 4.13 and 4.14 represents the case $\theta = 25^0$. SIRANE well simulates the experimental concentration pattern, except for the concentration profiles at $z = H/2$ far from the source. However, it is important noting that these profiles are characterised by very low concentration values and, even if the relative errors are rather high, the absolute errors are less important. Fig. 4.15 and 4.16 refers to the incident wind direction $\theta = 45^0$. The comparison above the roof is good whereas within the canopy there is not a very good agreement: the near-field concentration is overestimated, while the far-field is underestimated. However, the plume centerline and the standard deviation evolution are well simulated, as well as the shape of the concentration profile.

The comparison showed an excellent agreement concerning the plume centerline shifting and the standard deviation evolution. Further, even if the concentration values do not match exactly, the shape of the profile is well reproduced. These are encouraging results and indicate that SIRANE is able to model the main dispersion mechanisms, although its intrinsically simple approach.

For this comparison the Briggs relations for the plume standard deviations were replaced by a turbulent diffusivity coefficient K_{ext}.

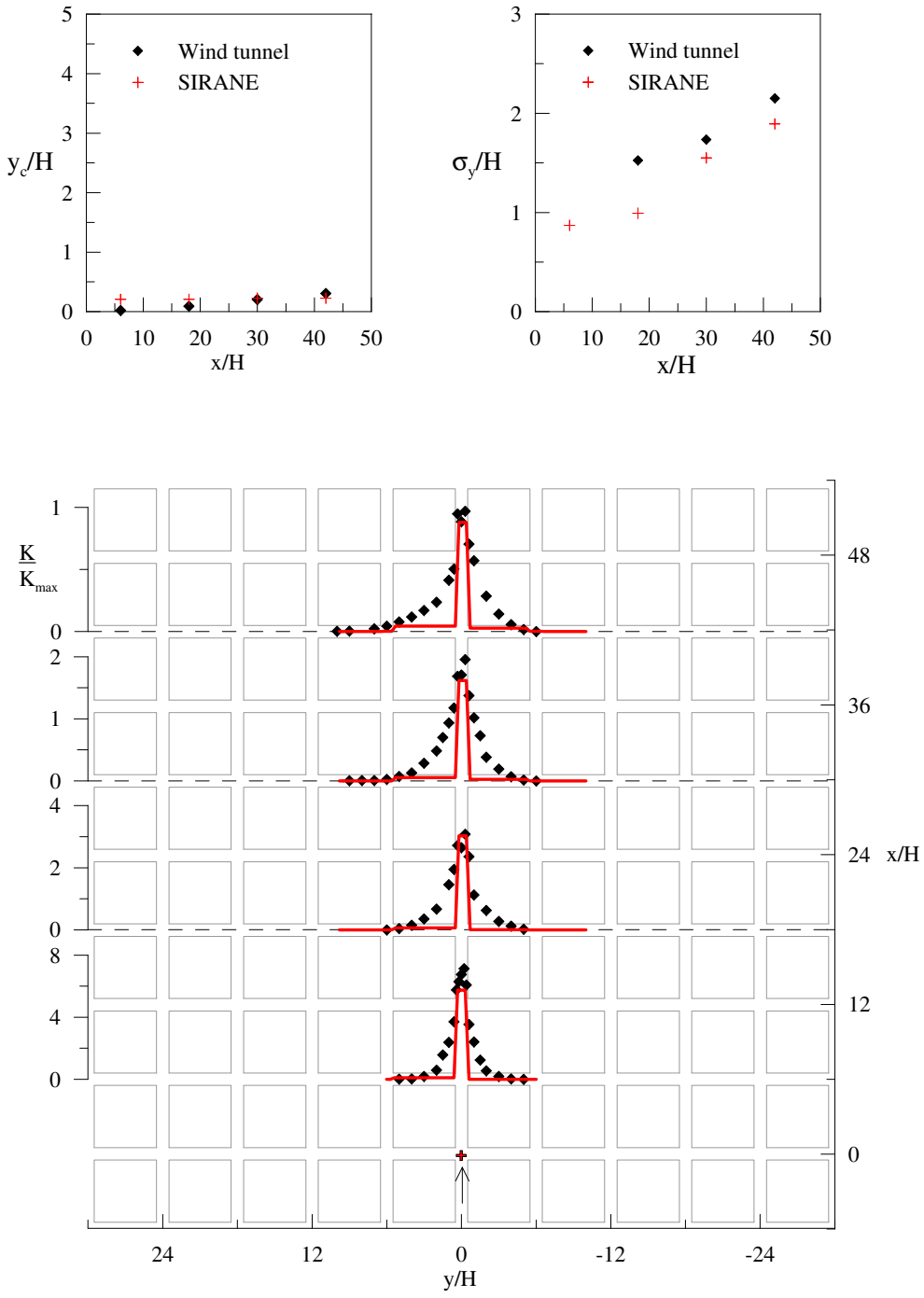

Figure 4.9: Comparison between SIRANE simulations and experimental data within the array, $z = H/2$, for the incident wind direction $\theta = 0^o$

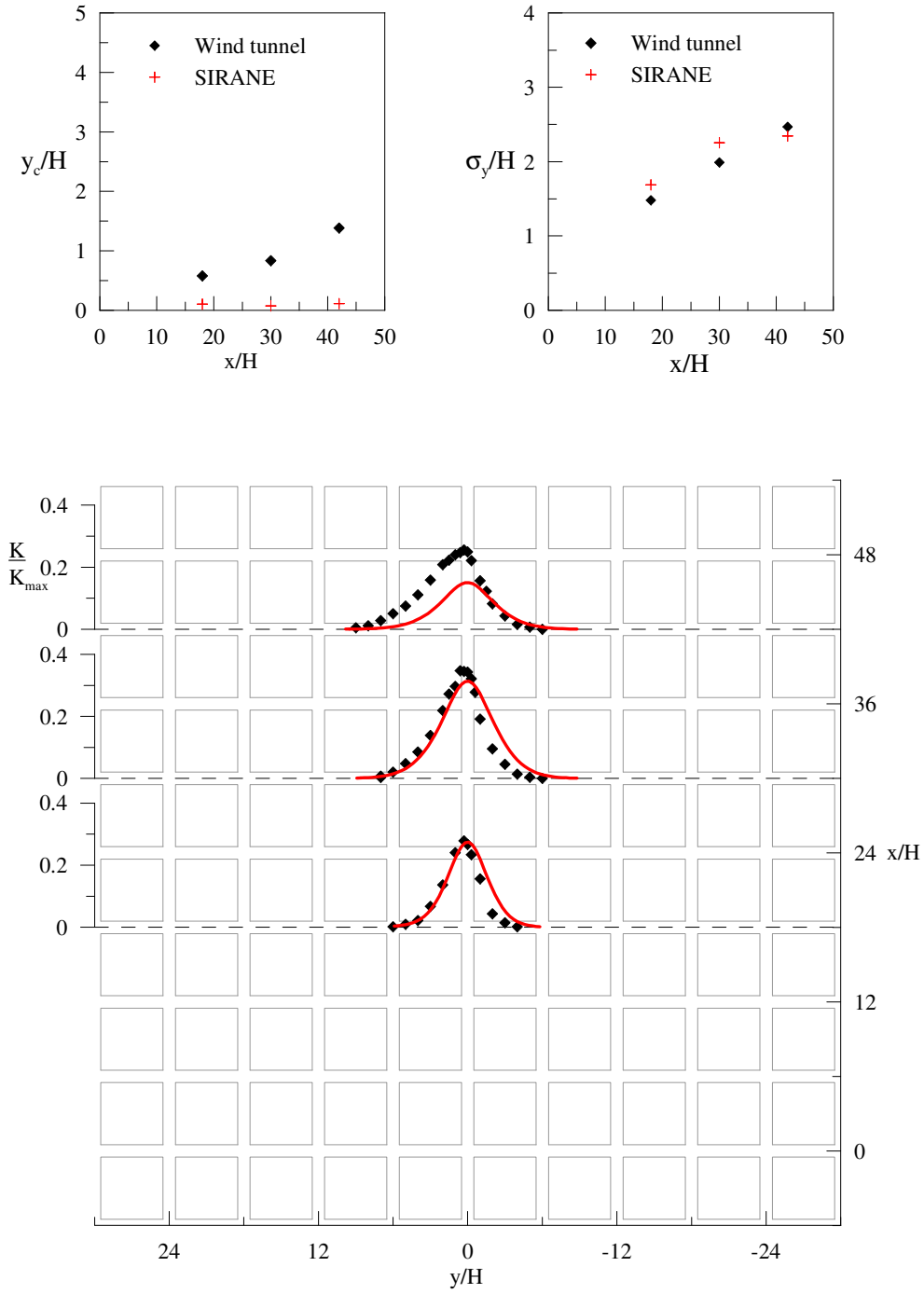

Figure 4.10: Comparison between SIRANE simulations and experimental data above the array, $z = 2H$, for the incident wind direction $\theta = 0^o$

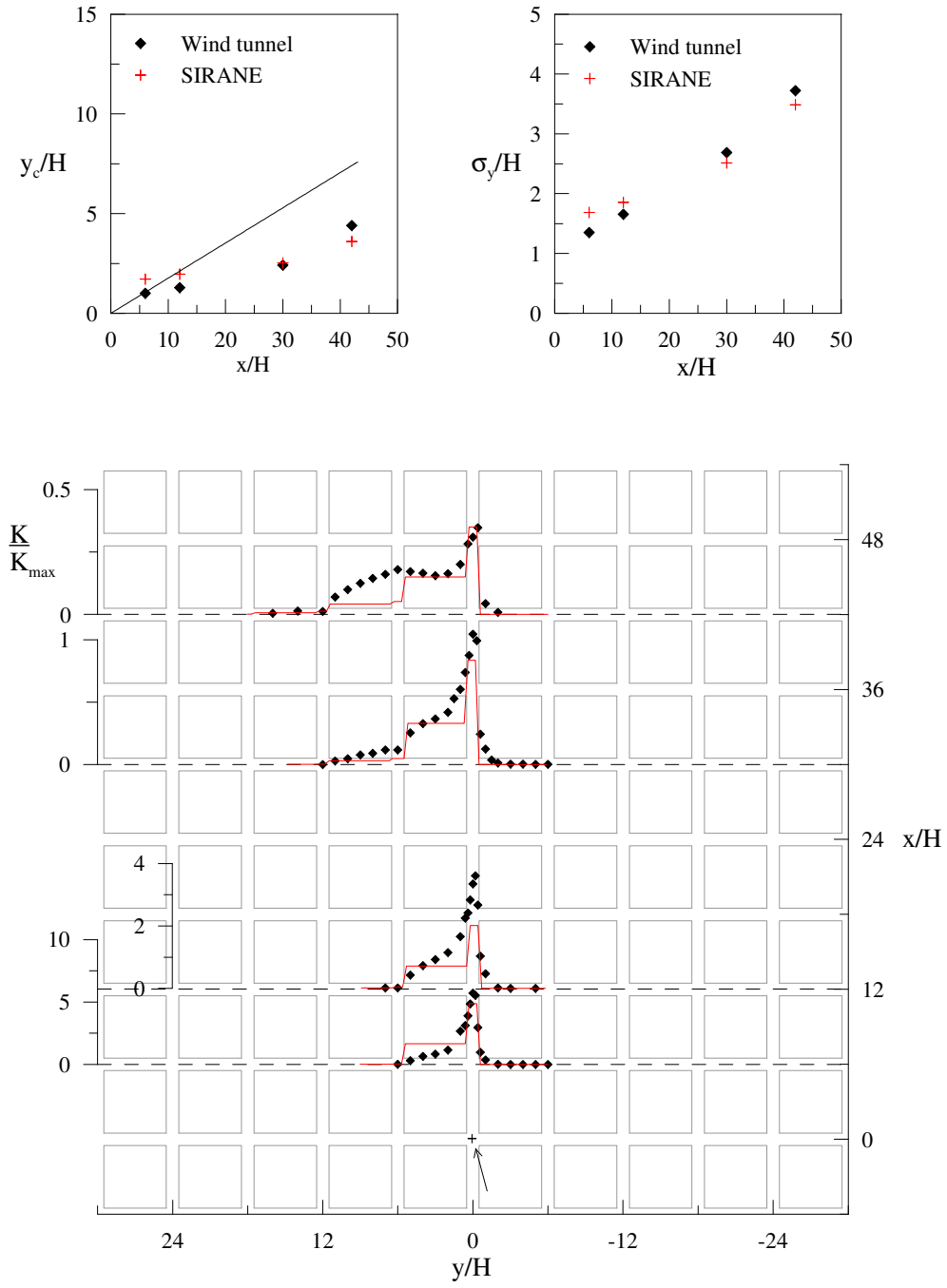

Figure 4.11: Comparison between SIRANE simulations and experimental data within the array, $z = H/2$, for the incident wind direction $\theta = 10^o$

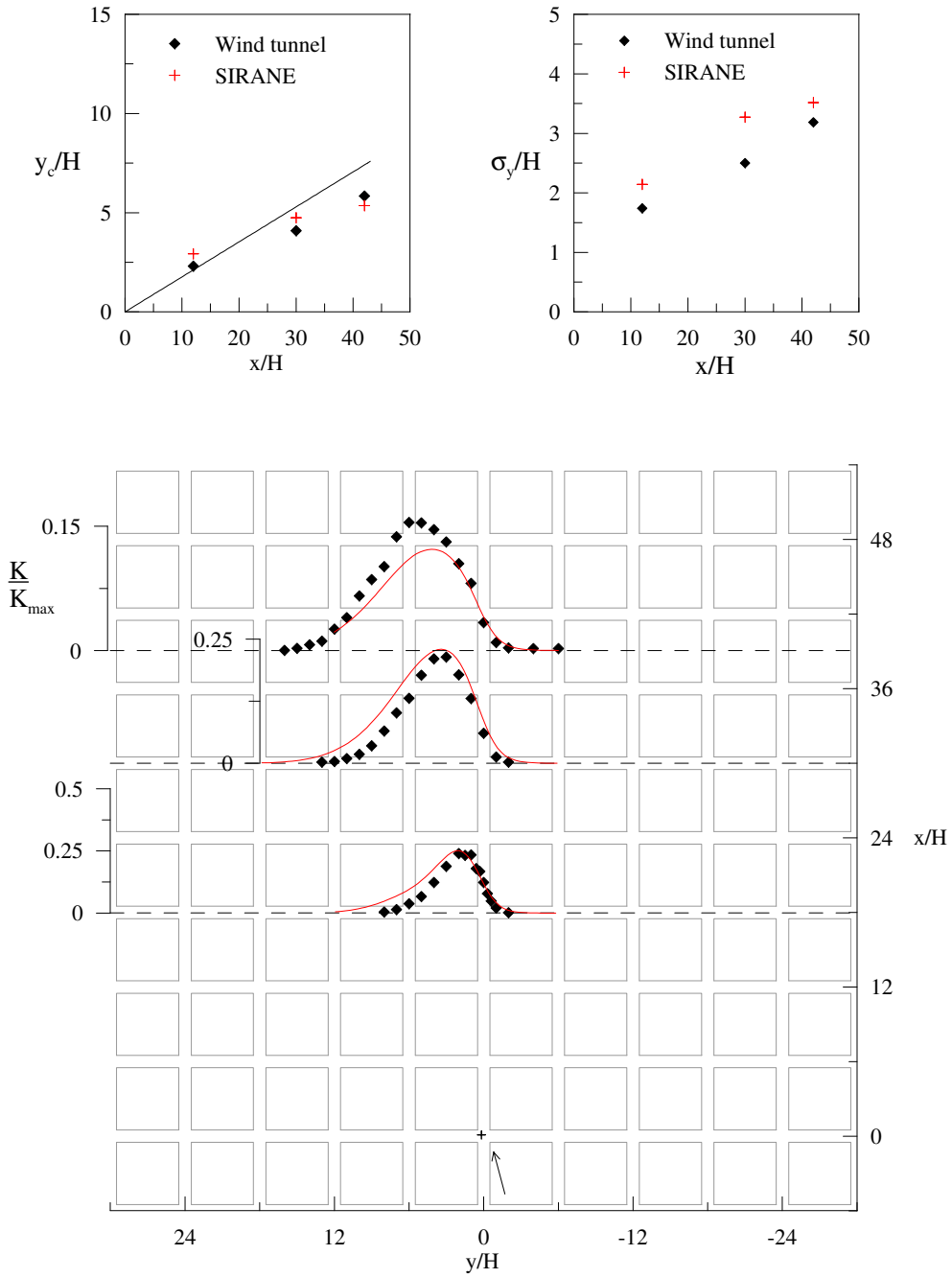

Figure 4.12: Comparison between SIRANE simulations and experimental data above the array, $z = 2H$, for the incident wind direction $\theta = 10^o$

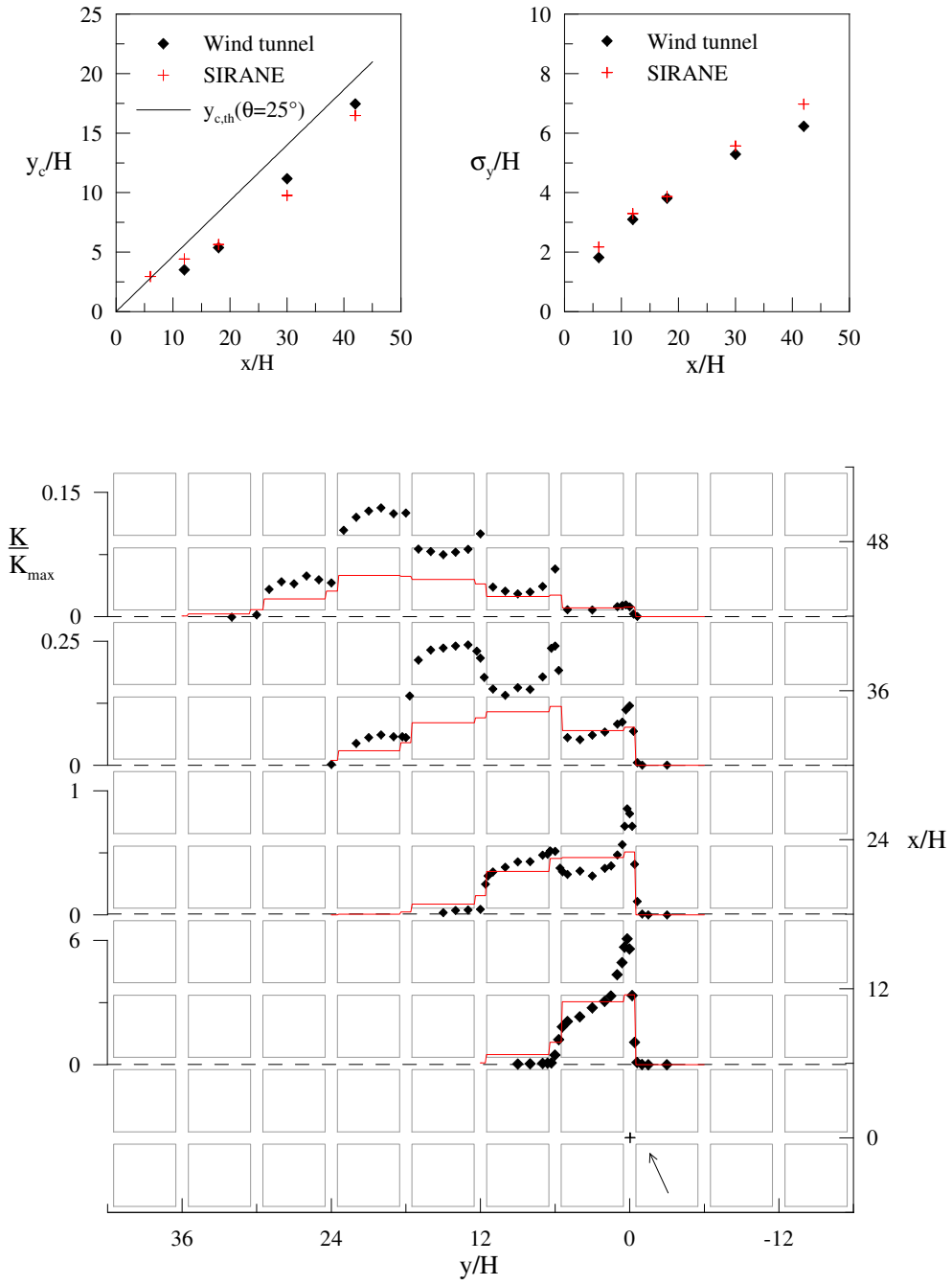

Figure 4.13: Comparison between SIRANE simulations and experimental data within the array, $z = H/2$, for the incident wind direction $\theta = 25^o$

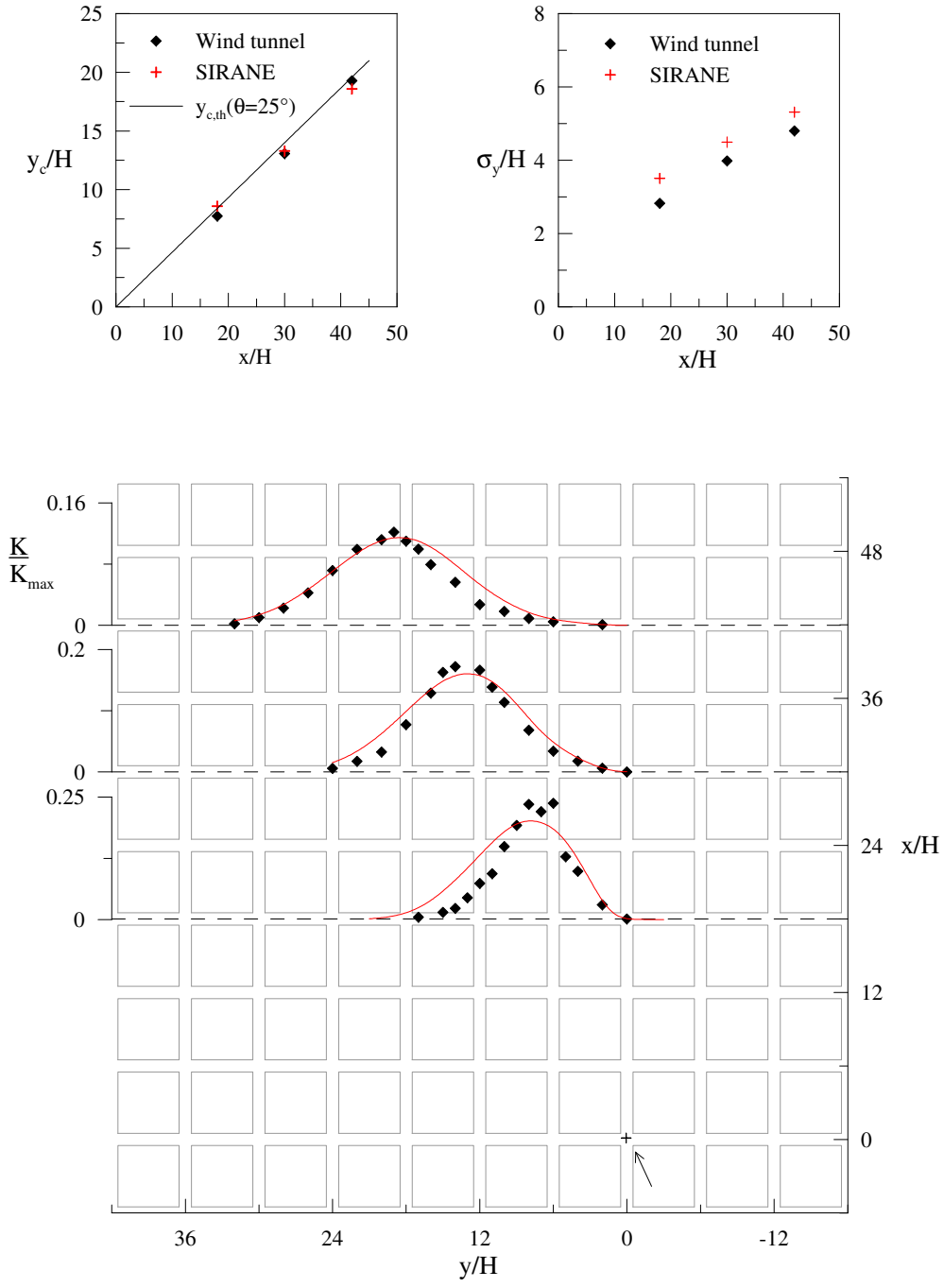

Figure 4.14: Comparison between SIRANE simulations and experimental data above the array, $z = 2H$, for the incident wind direction $\theta = 25^o$

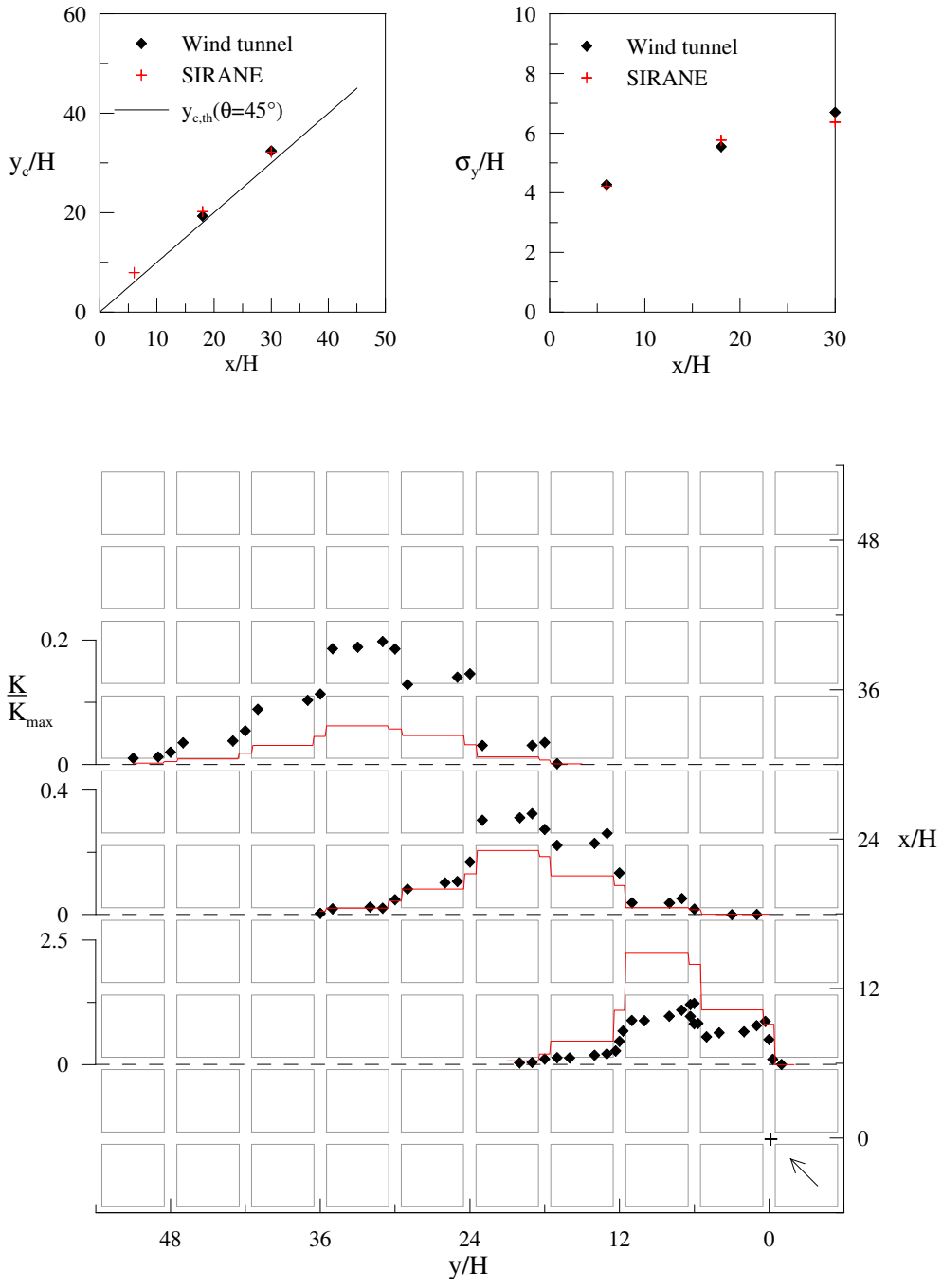

Figure 4.15: Comparison between SIRANE simulations and experimental data within the array, $z = H/2$, for the incident wind direction $\theta = 45^o$

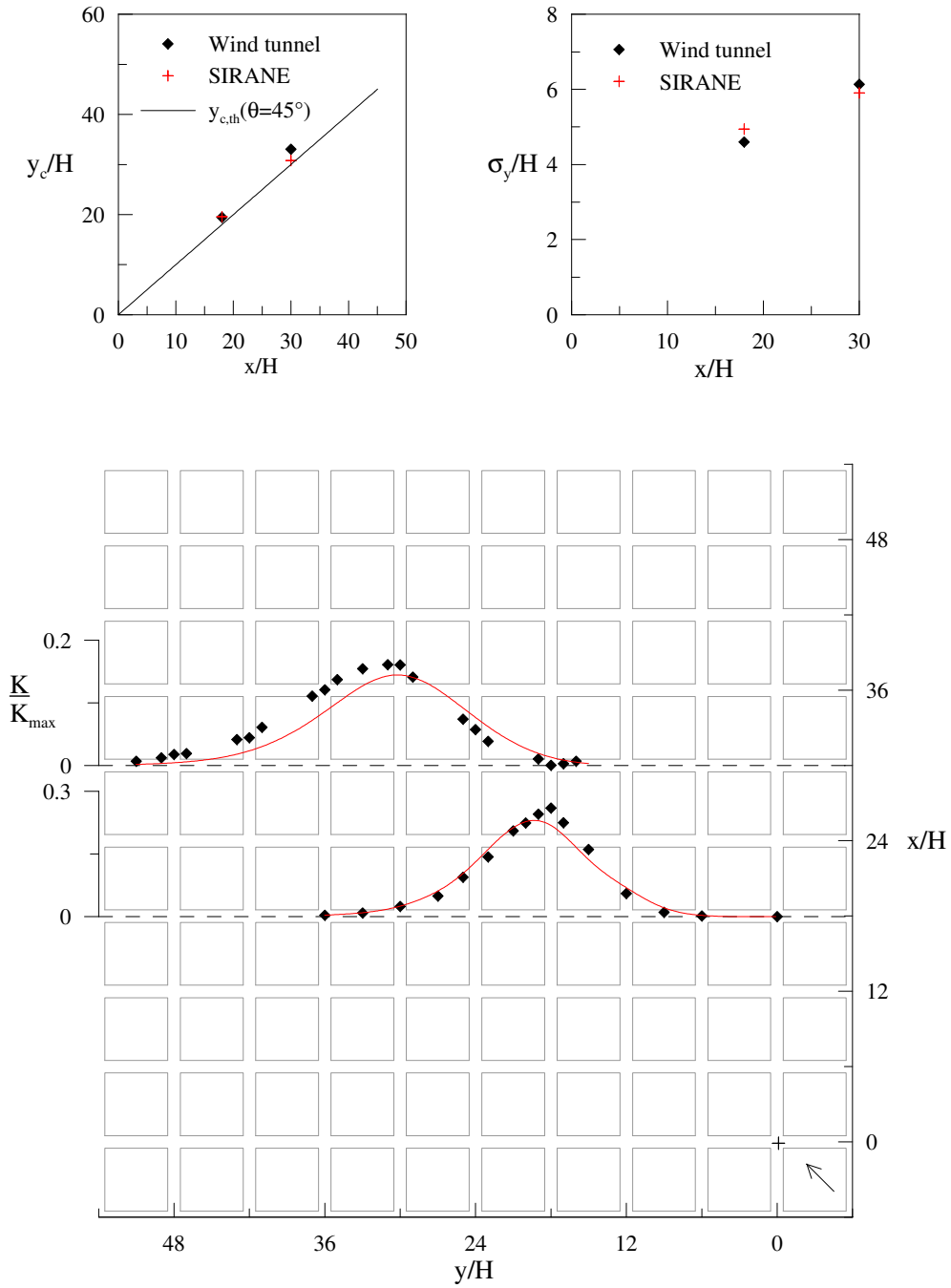

Figure 4.16: Comparison between SIRANE simulations and experimental data above the array, $z = 2H$, for the incident wind direction $\theta = 45^o$

Conclusions and perspectives

Conclusions

Flow and dispersion in urban areas at the scale of the neighborhood is the topic of my research. Most of the local fluid mechanical processes are understood but how these combine through a complex array of structures is less clear. The aim of the present work was thus to identify and study the phenomena associated with the pollutant dispersion through a neighborhood and point out how the exchange mechanisms are affected by the geometrical layout of the neighborhood. At the same time, the goal was to improve the urban dispersion modelling in order to supply operational tools for the management and the control of the urban air quality.

Experimental and numerical simulations have been performed through out an idealized array and the investigation was focused on two aspects:

- how does the geometrical layout of the array affect the flow and the dispersion through the array
- how does the direction of the external wind influence the exchange mechanisms through the array

The flow field within different array configurations was investigated for a wind that is parallel to the street axis through experimental and numerical approach. The study pointed out that the crucial parameter in determining the flow dynamics within the canopy is the aspect ratio of the street perpendicular to the wind direction, rather than the usual *lambda* parameters defining the dimensionless frontal and plan areas. This street aspect ratio, i.e. the width-to-height ratio of the street perpendicular to the wind direction, fixes the size of the exchange surfaces and thus the flow regime. Differently from the streets of infinite length, the current obstacle array consist in a network of finite length streets connected by intersections. Beside the usual interface between the external wind and the flow within the perpendicular street, this configuration produces another exchange surface that separates the flow within the intersection and the flow within the perpendicular street. For the street aspect ratio equal to $S_x/H = 1$, an analogy may be drawn with the flow regime over sufficiently close obstacles, which is usually referred to as the skimming flow regime. The external flow and the flow within the intersection seem to be decoupled from the flow within the perpendicular street and a limited mass and momentum exchange may be supposed. Concerning the street aspect ratio $S_x/H = 2$, the flow dynamics is similar to that occurring over more spaced obstacles, that is a wake interference flow regime. An important interaction between the flow is observed that should enhance the dispersion mechanisms.

The influence of the wind direction on the flow field within streets and intersections of the array was investigated only experimentally, since a wide numerical investigation had been performed by Soulhac (2000). The experimental data seem to confirm that when the orientation of the wind is any the flow field within the street shows a helicoid movement that results from the superposition of an across-street recirculating motion and an along-street channelling. However, the street velocity, namely the longitudinal velocity averaged through the street, is not proportional to the longitudinal projection of the external wind, as proposed by Soulhac for streets of infinite street. The presence of the intersection affects the flow within the adjacent street and part of the energy of the flow is dissipated in the vortical structures originating close to the intersection, thus reducing the averaged street velocity.

Concerning the dispersion phenomena, a plume was released from a point source placed within the array at the intersection and its evolution through the array was detected experimentally.

The study of the plume behaviour through different geometrical array layouts shows that the dispersion patterns are strongly related to the flow dynamics and thus depend on the aspect ratio of the perpendicular street, S_x/H, as seen previously. For $S_x/H = 1$ the channelling phenomenon confines the plume into the street where it is released and limits the lateral diffusion of the plume. Further, the transfer at the top of the canopy is limited and thus also the vertical diffusion is suppressed. For $S_x/H = 2$, the wake interference flow enhances the pollutants exchanges and the lateral and vertical diffusion are larger. The horizontal concentration profiles measured within the array are not fitted by the usual Gaussian curve, indicating that the dispersion mechanisms are strongly influenced by the presence of the obstacles. Contrarily, above the array the local influence of the obstacles vanishes and the usual Gaussian curves well describe the measured horizontal concentration distributions, which are not only the results of the dispersing characteristics related to the dynamical conditions of the flow but depend on the dispersion pattern within the array that works as virtual source.

It is worth noting that the dispersion pattern is not univocally determined by the geometrical characteristics of the array, usually defined through the *lambda* parameters, but an essential parameter appears to be the direction of the incident wind. The horizontal concentration profiles within the array are highly asymmetrical and shows a step behaviour: the mean concentration appears rather uniform within the street, while abrupt variations occur at the intersection, highlighting the essential role of the intersection in the horizontal dispersion processes within the canopy. Concerning the vertical diffusion, it is related to the turbulent exchange between the street and the external atmosphere.

Another important aspect is that the orientation of the obstacles has a significant effect on the direction of the dispersing plume, that is the plume centerline does not follow the direction of the external wind but is deflected towards the normal to the front face of the array for angles $\theta < 45^o$. The lateral diffusion of the plume varies with the direction of the external wind and thus the geometrical parameters of the array are not sufficient to determine the dispersion pattern.

Regarding the dispersion in urban areas, although the concentration distributions above the canopy are well described by Gaussian curves, the usual Gaussian approach is totally inappropriate since it parameterizes the standard deviations by assuming one parameter, i.e. the roughness length, to synthesize the effects of the geometry of the urban canopy. Our work highlights that in order to correctly describe the dispersion above the urban canopy is necessary to know how the pollutants spread within the canopy, which is influenced by both the geometrical disposition of the obstacles and the incident wind direction.

The urban dispersion model SIRANE, which has been developed as tool for the monitoring and the management of the urban air quality, models the main dispersion processes within the canopy, which is represented as a network of streets, and calculates the concentration in each street segment using a box model. SIRANE simulates quite well the measured dispersion

patterns. The agreement between numerical and experimental results is encouraging, as it means that the main dispersion mechanisms are represented.

Perspectives

During this study, we showed the necessity of suitable models to describe pollution in urban areas at the scale of neighborhood. Therefore, it is important to continue the development and the validation of these models, in order to extend their field of application and to improve the quality of the results.

A research orientation could be to study more complex geometries, such as the intersections of streets and the places of big size. During our work, we proposed a model of exchange on the level of a simple intersection. It would be interesting to continue this study and to build a model of dispersion making it possible to determine the distribution of concentration in the intersection. In addition, the modeling of the great places will have to be the subject of a specific study, in which one will consider the interaction with the external flow.

The complexity of the dispersion mechanisms in urban areas required to focus on certain physical processes, neglecting other aspects. This work did not take into account among other things the thermal phenomena and the air motion produced by the traffic, whose effect on the turbulence and on the pollutant mixing should not be negligible. A detailed study on this aspect would constitute certainly an interesting subject of research.

As final step, it would be very interesting to be able to carry out comparisons with field measurements.

Appendix

Appendix A

A first-order closure model for the turbulent transfer

We consider a mixing layer consisting in two flows characterised by different dynamical conditions and different passive scalar concentration, as shown in Figure A.1. The properties of each flow are assumed to be uniform along the streamwise direction: the velocity U, the turbulent kinetic energy k and integral length scale l, as well as the concentration of a passive scalar C.

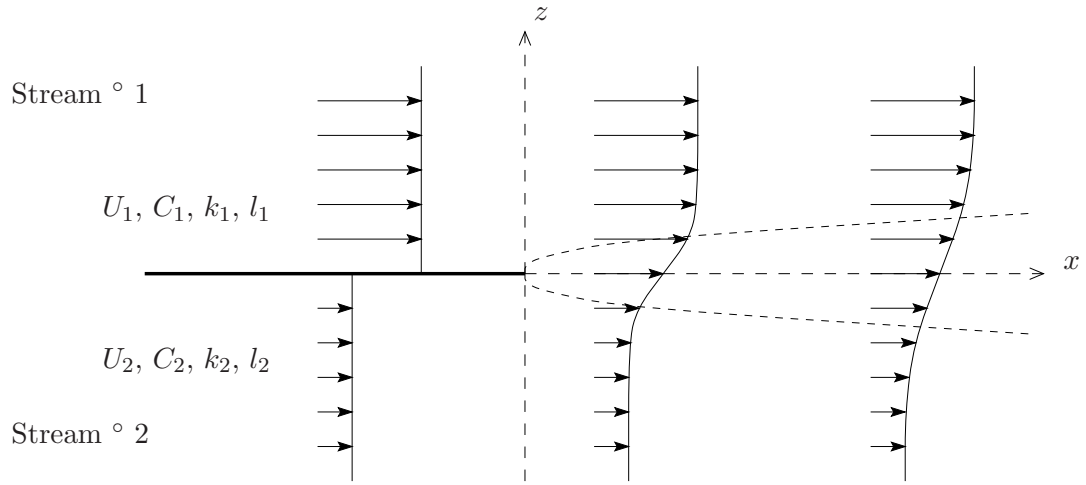

Figure A.1: Characteristic diagram of a mixing layer

In case of a two-dimensional mixing layer, we can write:

$$\begin{cases} \dfrac{\partial \overline{u}}{\partial x} + \dfrac{\partial \overline{w}}{\partial z} = 0 & \text{(A.1)} \\ \overline{u}\dfrac{\partial \overline{u}}{\partial x} + \overline{w}\dfrac{\partial \overline{u}}{\partial z} = \dfrac{\partial}{\partial z}\overline{u'w'} & \text{(A.2)} \\ \overline{u}\dfrac{\partial \overline{c}}{\partial x} + \overline{w}\dfrac{\partial \overline{c}}{\partial z} = \dfrac{\partial}{\partial z}\overline{w'c'} & \text{(A.3)} \end{cases}$$

The time averaged turbulent fluxes through the interface of the mixing layer are given by the correlations $\overline{u'w'}$ for the momentum flux and $\overline{w'c'}$ for the mass flux. We assume a first order closure model to model these correlations, as suggested by the gradient-transport theory, and

we introduce a turbulent diffusivity coefficient K. The correlations can be expressed in the form:

$$\overline{u'w'} = -\mathrm{K}_u \frac{\partial \overline{u}}{\partial z} \quad \text{and} \quad \overline{w'c'} = -\mathrm{K}_c \frac{\partial \overline{c}}{\partial z} \tag{A.4}$$

We assume a turbulent Schmidt number equal to 1, i.e. $\mathrm{K}_u = \mathrm{K}_c = \mathrm{K}$. In order to model the turbulent mass and momentum fluxes, it is necessary to determine the turbulence characteristics at the interface street-atmosphere that depend either on the local shear production and on the advection from one stream to the other. When the two flows are slightly turbulent, the turbulence is mainly locally generated by the Kelvin-Helmotz instabilities: the turbulent diffusivity coefficients K_1 and K_2 are weak regards to the turbulent diffusion generated at the shear-layer interface. When the two flows are sufficiently turbulent, it can be assumed that the locally generated turbulence is negligible compared to the turbulent eddies advected by the flows. The analytical resolution of the problem presented here relies on the method adopted by Goertler (1942) and described by Rajaratnam (1976). The Goertler's solution (Goertler, 1942) is based on the idea that the dimension l of the turbulent structures generated within the mixing layer increases linearly with the distance x. From the assumption that the turbulent diffusivity K is proportional to l and to a velocity scale $U_m = (U_1 + U_2)/2$, Goertler solved the equations A.1 and A.2 and supplied the flow and concentration field. We are interested in atmospheric flows, that is when the two flows are highly turbulent. In this case, the solution of the problem depends on K_1 and K_2. If the turbulent flows are uniform, i.e. $\mathrm{K}_1 = \mathrm{K}_2 = \mathrm{K}_m$, the general behaviour of the fluid is then completely similar to the laminar motion of a fluid of molecular viscosity $\mathrm{K}_m ol$. Dimensional analysis arguments allow to identify a similarity parameter ξ, defined as:

$$\xi = \frac{\sigma z}{\sqrt{x}} \qquad \text{with } \sigma = \sqrt{\frac{U_m}{4\mathrm{K}_m}} \text{ and } U_m = \frac{U_1 + U_2}{2} \tag{A.5}$$

The velocity profile is given by a self-similar solution and can be expressed as:

$$\Psi = U_m \sqrt{x} F(\xi) \tag{A.6}$$

Adopting Cauchy's stream function, we can write:

$$\begin{cases} \overline{u} = \dfrac{\partial \psi}{\partial z} = \sigma U_m F'(\xi) \\ \overline{w} = -\dfrac{\partial \psi}{\partial x} = \dfrac{U_m}{2\sqrt{x}} (\xi F'(\xi) - F(\xi)) \end{cases} \tag{A.7}$$

Substituting these expressions in the equations A.2, the following differential equation is obtained:

$$F''' + 2\sigma F F'' = 0 \tag{A.8}$$

The solution of this equation is obtained by means of a limited development of σF as a function of $\lambda_u = \frac{U_1 - U_2}{U_1 + U_2}$. By keeping only the terms of order 1, the velocity field assumes the following self-similar form:

$$\overline{u} = \frac{U_1 + U_2}{2} + \frac{U_1 - U_2}{2} \operatorname{erf}\left(\frac{\sigma z}{\sqrt{x}}\right) \tag{A.9}$$

where erf is the error function. The analogy of the form of equations A.2 and A.1 allows to express the concentration field in a similar way:

$$\overline{c} = \frac{C_1 + C_2}{2} + \frac{C_1 - C_2}{2} \operatorname{erf}\left(\frac{\sigma z}{\sqrt{x}}\right) \tag{A.10}$$

Assuming a first-order closure model, the turbulent mass flux $d\mathcal{Q}_s$ through an element dx at interface between the two flows ($z = 0$) is given by:

$$d\mathcal{Q}_s = -\mathrm{K} \left.\frac{\partial \overline{c}}{\partial z}\right|_{z=0} dx \tag{A.11}$$

By introducing the velocity and concentration field (Eq. A.9 A.10) in the Eq. A.11, the turbulent flux per unit length can be expressed as:

$$\overline{w'c'} = \frac{\partial \mathcal{Q}_s}{\partial x} = -\sqrt{\frac{U_m \mathrm{K}_m}{4\pi x}}(C_1 - C_2) \tag{A.12}$$

The flux varies as $1/\sqrt{x}$ and depends on the average velocity between the two flows and on the turbulent diffusivity of the flows.

The total turbulent flux $\mathcal{Q}_s$ at the street-atmosphere interface is finally given by:

$$\mathcal{Q}_s = \int_0^L \int_0^W \frac{\partial \mathcal{Q}_c}{\partial x} dxdy = L\sqrt{\frac{U_m \, \mathrm{K}_m W}{\pi}}(C_{street} - C_{ext}) \; = LW u_d (C_{street} - C_{ext}) \tag{A.13}$$

$$\text{being} \qquad u_d = U_m \sqrt{\frac{\Lambda}{\pi}} \tag{A.14}$$

where y represents the co-ordinate parallel to the street axis and x the co-ordinate in the streamwise direction and $\Lambda = \frac{\mathrm{K}_m}{U_H W}$ is an non-dimensional parameter.

Assuming a one-degree of freedom box-model we can assume that $U_1 = U_{ext.}$ and $U_2 = 0$, so that $U_m = U_H = U_{ext.}/2$.

This form for the turbulent mass flux across the interface street-atmosphere is very similar to the analytical model of Hotchkiss and Harlow (Hotchkiss and Harlow, 1973):

$$C_{street} - C_{ext} = C_0 = \frac{\mathcal{Q}}{U_H W L} \frac{1}{\sqrt{\Lambda}} \text{ with } \Lambda = \frac{\mathrm{K}_m}{U_H W} \tag{A.15}$$

where K_m represents an average turbulent diffusivity within the street. In fact, this relation is perfectly equivalent to equations **??** and 4.8, unless for the factor $\sqrt{\pi}$.

Antonia, R. A., and Krogstad, P. A. 2001. Turbulence structure in boundary layers over different types of surface roughness. *Fluid Dynamics Research*, **28**, 139–157.

Barlow, J.F., Harman, I. N., and Belcher, S. E. 2004. Scalar fluxes from urban street canyons. Part I: Laboratory simulation. *Boundary-Layer Meteorol.*, **113**, 369–385.

Benesh, F. 1978. *Carbon monoxide hot spot guidelines, Volume V: User's manual for Interaction-Midblock Model.* EPA-450/3-78-037.

B.J. Legg, P.A. Coppin, M.R. Coppin. 1984. A three-hot-wire anemometer for measuring two velocity components in high intensity turbulent boundary layers. *J. Phys. E: Sci. Instrum.*, **17**, 970–976.

Blackadar, A. K., and Tennekes, H. 1968. Asymptotic similarity in neutral barotropic planetary boundary. *J. Atmos. Sci.*, **25**.

Blocken, B., Stathopoulos T. Carmeliet J. 2007. CFD simulation of the atmospheric boundary layer - wall function problems. *Atmospheric Environment*, **41 - 2**, 238–252.

Bottema, M. 1997. Urban roughness modelling in relation to pollutant dispersion. *Atmos. Env.*, **31 - 18**, 3059–3075.

Boussinesq, J. 1897. *Théorie de l'écoulement tourbillonnant et tumultueux des liquides.* Gauthier-Villars, Paris.

Briggs, G. A. 1973. *Diffusion estimation of small emissions.* Contribution N. 79. Atmospheric Turbulence and Diffusion Laboratory, Oak Ridge, TN.

Britter, R.E., and Hanna, S.R. 2003. Flow and dispersion in urban areas. *Ann. Rev. fluid Mech.*, **35**, 469–96.

Bullin, J. A., Hinz, M., and Bower, S. C. 1982. *Vehicle emissions from intersections.* Texas Transportation Institute, FHWA/SDHPT Project 2250.

Caton, F., Britter, R.E., and Dalziel, S. 2003. Dispersion mechanism in astreet canyon. *Atmospheric Environment*, **37**, 693–702.

Cheng, H., and Castro, I. P. 2002. Near wall flow over urban-like roughness. *Boundary Layer Meteorol.*, **104**, 229–259.

Cheng, H., Hayden P. Robins A. G. Castro I. P. 2007. Flow over cube arrays of different packing densities. *J. of Wind Engineering and Industrial Aerodynamics*, **95**, 715–740.

Coceal, O., Belcher S.E. 2004. A canopy model of mean winds through urban areas. *Q.J.R. Meteorol. Soc.*, **130**, 1349–1372.

Davidson, M. J., Snyder, W. H., Lawson, R. E., and Hunt, J. C. R. 1996. Wind tunnel simulations of plume dispersion through groups of obstacles. *Atmos. Env.*, **30 - 22**, 3715–3731.

Dobre, A., Arnold, S.J., Smalley, R.J., Boddy, J.W.D., Barlow, J.F., Tomlin, A.S., and Belcher, J.F. 2005. Flow field measurements in the proximity of an urban intersection in London, UK. *Atmospheric Environment*, **39**, 4647–4657.

Finnigan, J. J. 1985. Turbulent transport in flexible plant canopies. *Pages 443–480 of:* Hutchinson, B.A., and Hicks, B.B. (eds), *The Forest-Atmosphere Interaction.* Dordrect: D.Reidel Publishing Co.

Gadilhe, A., Janvier, L., and Barnaud, G. 1993. Numerical and experimental modelling of the three-dimensional turbulent wind flow through an urban square. *Jour. of Wind Eng. and Indust. Aerod.*, **vol 46-47**, pp 755–763.

Gailis, R. M., and Hill, A. 2006. A wind tunnel simulation of plume dispersion within a large array of obstacles. *Boundary-Layer Meteorology*, **119**, 289–338.

Goertler, H. 1942. Berechnung von aufgaben der freien turbulenz auf grund eines neuen naherungsansatzes. *Z.A.M.M.*, **22**, 244–254.

Griffin. 1983. *An air quality intersection model.* FHWA Report No. FHWA-CO-RD-83-14, Colorado Department of Highways, Denver, CO.

Grimmond, C. S. B., and Oke, T. R. 1999. Aerodynamic properties of urban areas derived from analysis of surface form. *J. Appl. Met.*, **38**, 1262–1292.

Hanna, S. R., Tehranian, S., Carissimo, B., Macdonald, R. W., and Lohner, R. 2002. Comparisons of model simulations with observations of mean flow and turbulence within simple obstacle arrays. *Atmos. env*, **36**, 5067–5079.

Hertel, O., and Berkowicz, R. 1989. *Modelling pollution from traffic in a street canyon. Evaluation of data and model developement.* DMU Luft A-129, NERI.

Hotchkiss, R. S., and Harlow, F. H. 1973. Air pollution transport in street canyons. *Environmental Protection Agency*, 1–128.

Hoydysh, W. G., and Dabberdt, W. F. 1994. Concentration fields at urban intersections: fluid modeling studies. *Atmos. Env.*, **28 - 11**, 1849–1860.

Hoydysh, W. G., Dabberdt, W. F., Schorling, M., Yang, F., and Holynskyj, O. 1995. Dispersion modeling at urban intersections. *Science of the Total Environment*, **169**, 93–102.

Hunter, L. J., Watson, I. D., and Johnson, G. T. 1990. Modelling air flow regimes in urban canyons. *Energy and Buildings*, **15 - 3**, 315–324.

Irwin, H.P.A.H. 1981. The design of spires for wind simulation. *Journal of Wind Engineering and Industrial Aerodynamics*, **7**, 361–366.

Jimènez, J. 2004. Turbulent flows over rough wall. *Ann. Rev. Fluid Mech.*, **36**, 173–96.

Louka, P., Belcher, S. E., and Harrison, R. G. 2000. Coupling between air flow in streets and the well-developed boundary-layer aloft. *Atmos. Env.*, **34 - 16**, 2613–2622.

L.W.B. Browne, R.A. Antonia, L.C. Chua. 1989. Calibration of X-probes for turbulent flow measurements. *Experiments in Fluids*, **7**, 201–208.

MacDonald, R. W. 2000. Modelling the mean velocity profile in the urban canopy layer. *Boundary-Layer Meteorol.*, **97**, 25–45.

MacDonald, R. W., Griffiths, R. F., and Cheah, S. C. 1997. Field experiments of dispersion through regular arrays of cubic structures. *Atmos. Env.*, **31 - 6**, 783–795.

MacDonald, R. W., Griffiths, R. F., and Hall, D. J. 1998. A comparison of results from scaled field and wind tunnel modelling of dispersion in arrays of obstacles. *Atmos. Env.*, **32 - 22**, 3845–3862.

MacDonald, R. W, Carter, S., and Slawson, P. R. 2000. *Measurements of mean velocity and turbulence statistics in simple obstacle arrays at 1:200 scale.* University of Waterloo, Department of Mechanical Engineering.

McHugh, C. A., Carruthers, D. J., and Edmunds, H. A. 1997. ADMS-urban: an air quality management system for traffic, domestic and industrial pollution. *International Journal of Environment and Pollution*, **8**, 666–674.

Messina, A. 1983. *Estimates of air pollution near signalized intersections.* Federal Highway Administration.

Monin, A. S., and Obukhov, A. M. 1954. Basic laws of turbulent mixing in the ground layer of the atmosphere. *Trans. Geophys. Inst. Akad. Nauk, USSR*, **151**, 163–187.

Namdeo, A. K., and Colls, J. J. 1996. Development and evaluation of SBLINE, a suite of models for the prediction of pollution concentrations from vehicles in urban areas. *Science of the Total Environment*, **189–90**, 311–320.

Oke, T. R. 1987. *Boundary layer climates.* 2nd. London: Methuen.

Oke, T. R. 1988a. Boundary layer climates. *The Meteorological Magazine*, **117 - 1394**, 89–.

Oke, T.R. 1988b. Street design and urban canopy layer climate. *Energy and Buildings*, **11**, 103–113.

O'Toole, D. M., Hilfiker, R. C., and Muldoon, G. 1975. *Evaluation of air quality in the vicinity of the intersection of Wisconsin and Western Avenues N. W.* FHWA Final Report FHWA/DC/OTPP-75/1.

Ott, W. R. 1977. Development of criteria for siting air monitoring stations. *Journal of Air Pollution Control Association*, **27 - 6**, 543–547.

Pasquill, F., and Smith, F. B. 1983. *Atmospheric diffusion.* third. John Wiley & sons.

Perkins, R. J., and Belcher, S. E. (eds). 1997. *Flow and dispersion through gropus of obstacles.* Oxford: Clarendon Press.

Plate, E. J. 1982. *Engineering Meteorology.* Amsterdam: Elsevier.

Rajaratnam, N. 1976. *Turbulent jets.* Elsevier.

Raupach, M. R. 1981. Conditional statistics of Reynolds stress in rough-wall and smooth wall turbulent boundary layers. *J. Fluid Mech.*, **108**, 363–382.

Raupach, M. R., Thom, A. S., and Edwards, I. 1980. A wind-tunnel study of turbulent flow close to regularly arrayed rough surfaces. *Boundary-Layer Meteorol.*, **18**, 373–397.

Raupach, M. R., Coppin, P. A., and Legg, B. J. 1986. Experiments on scalar dispersion within a model plant canopy. Part I : The turbulence structure. *Boundary-Layer Meteorol.*, **35**, 21–52.

Raupach, M. R., Antonia, R.A., and Rajoplan, S. 1991. Rough-wall turbulent boundary layers. *Appl. Mech. Rev.*, **44 - 1**, 1–25.

R.J. Smalley, R.A. Antonia, L. Djenidi. 2001. Self preservation of rough-wall turbulent boundary layers. *Eur. J. Mech. B-Fluids*, **20**, 591–602.

Robins, A., Savory, E., Scaperdas, A., and Grigoriadis, D. 2002. Spatial variability and source-receptor relations at a street intersection. *Water, Air and Soil Pollution: Focus*, **2**, 381–393.

Robins, A.G. 1979. The development and structure of simulated neutrally stable atmospheric boundary layers. *J. Ind. Aerodyn.*, **4**, 71–100.

Rosas, B., Paine, B., Woodruff, J., Halvorson, J., and Berka, J. 1980. *Measuring and modeling carbon monoxide at a high volume intersection.* Federal Highway Administration and Minnesota Department of Transportation.

Rotach, M. W. 1993. Turbulence Close to a Rough Urban Surface. Part I: Reynolds Stress. *Boundary-Layer Meteorol.*, **65**, 1–28.

Rotach, M. W. 1994. Determination of the zero plane displacement in an urban environment. *Boundary-Layer Meteorol.*, **67**, 187–193.

Roth, M. 2000. Review of atmospheric turbulence over cities. *Quart. Jour. of Roy. Met. Soc.*, **126**, 941–990.

Salizzoni, P. 2005. *Mass and momentum transfer in urban boundary layer.* PhD Thesis, Politecnico di Torino - Ecole Centrale de Lyon.

Scaperdas, A., and Colvile, R.N. 1999. Assessing the rapresentativeness of monitoring data from an urban intersection site in central London, UK. *Atmos. Env.*, **33 - 4**, 661–674.

Soulhac, L. 2000. *Modélisation de la dispersion atmosphérique à l'intérieur de la canopée urbaine.* PhD Thesis, Ecole Centrale de Lyon.

Soulhac, L., Perkins, R. J., and Salizzoni, P. 2007. Flow in a street canyon for any external wind direction. *Boundary-Layer Meteorology.*

Taylor, G. I. 1935. Statistical theory of turbulence, Part I. *Proc. Roy. Soc. London, Ser. A*, **105**, 421–444.

Taylor, G.I. 1921. Diffusion by continuous movements. *Proc. Roy. Soc. London, Ser. A.*

Theurer, W., Plate E. J., and Hoeschele, K. 1996. Semi-empirical Models as a Combination of Wind Tunnel and Numerical Dispersion Modeling. *Atmos. Environ.*, **30**, 3583–3597.

Tutu, N.K., and Chevray, R. 1975. Cross-wire anemometry in high intensity turbulence. *J. Fluid Mech.*, **71**, 785–800.

Wieringa, J. 1993. Representative roughness parameters for homogeneous terrain. *Boundary-Layer Meteorol.*, **63**, 323–363.

Wilson, N.R., and Shaw, R.H. 1977. A higher order closure model for canopy flow. *J. Appl. Meteor.*, **16**, 1197–1205.

Yamartino, R. J., and Wiegand, G. 1986. Development and evaluation of simple models for the flow, turbulence and pollutant concentration fields within an urban street canyon. *Atmos. Env.*, **20 - 11**, 2137–2156.

Yee, E., and Biltoft, C. A. 2004. Concentration fluctuation measurements in a plume dispersing through a regular array of obstacles. *Boundary-Layer Meteorology*, **111**, 363–415.

Y.Nakamura, T.R. Oke. 1988. Wind, temperature and stability conditions in an east-west oriented urban canyon. *Atmospheric Environment*, **22**, 2691–2700.

Zamurs, J., and Piracci, R. J. 1982. Modelling of carbons monoxide hot spots. *Journal of Air Pollution Control Association*, **32 - 9**, 947–953.